

**Some pages of this thesis may have been removed for copyright restrictions.**

If you have discovered material in Aston Research Explorer which is unlawful e.g. breaches copyright, (either yours or that of a third party) or any other law, including but not limited to those relating to patent, trademark, confidentiality, data protection, obscenity, defamation, libel, then please read our [Takedown policy](#) and contact the service immediately (openaccess@aston.ac.uk)

An investigation of support effects on the  
Pt-catalysed selective transformation of  
 $\alpha,\beta$ -unsaturated substrates

*Lee James Durndell*

Doctor of Philosophy

Aston University

European Bioenergy Research Institute

February 2015

© Lee James Durndell, 2015

Lee James Durndell asserts his moral right to be identified as the author of this thesis

This copy of the thesis has been supplied on condition that anyone who consults it is understood to recognise that its copyright rests with its author and that no quotation from the thesis and no information derived from it may be published without appropriate permission or acknowledgement

## Abstract

Pt catalyst series were prepared on mesoporous SBA-15, SBA-16, KIT-6, true liquid crystal-templated meso-macroporous SBA-15 and a commercial, low surface area silica support. Support structure can be easily fabricated using surfactant templating as a mode of stringent control on porosity, surface area and internal structure. The impact of varying Pt-support physicochemical properties was systematically studied for the selective transformation of allylic substrates under chemoselective oxidation and hydrogenation regimes, a class of reactions highly applicable to industry. Pt-based heterogeneous catalysts are well-known for their utilisation in the hydrogenation of  $\alpha,\beta$ -unsaturated aldehydes, although the mode of action and lack of systematic studies in the literature fuels continuing debate into the role of Pt nanoparticles and support choice for this area. This project attempts to shed some light on several frequently asked questions in this field.

Successful support synthesis and stability after Pt impregnation is confirmed through HRTEM, XRD and N<sub>2</sub> porosimetry. Decreasing metal loading promoted dispersion values, regardless of support choice, with surface PtO<sub>2</sub> content also showing visible enhancement. Increasing support surface area and mesoporosity exhibited the following trend on Pt dispersion augmentation; low surface area commercial silica < true liquid crystal-templated SBA-15 < SBA-15 < SBA-16 ~ KIT-6. For the selective oxidation of cinnamyl alcohol, increasing PtO<sub>2</sub> surface population confers substantial rate enhancements, with turnover frequencies evidencing PtO<sub>2</sub> to be the active species.

In the Pt-catalysed hydrogenation of cinnamaldehyde, strong support insensitivity was observed towards catalytic activity; as turnover frequencies normalised to Pt metal reveal constant values. However, structure sensitivity to the desired unsaturated alcohol arose, evidencing the requirement of flat, extended Pt (111) facets for C=O hydrogenation. Pt/SBA-15 proved the most selective, reflecting suppressed cinnamyl alcohol hydrogenation, with DRIFTS and *in-situ* ATR-IR evidencing the key role of support polarity in re-orientation of cinnamaldehyde to favour di- $\sigma_{CO}$  adsorption and C=O versus C=C hydrogenation. High pressures increased activity, whilst a dramatic shift in selectivity from dominant C=C (1 bar) to C=O hydrogenation (10 bar) was also observed, attributed to surface crowding and suppression of di- $\sigma_{CC}$  and  $\eta_4$  di- $\sigma_{CO} + \pi_{C=C}$  cinnamaldehyde binding modes.

## Acknowledgements

First off, completion of this thesis would not have been possible without the help, support and patience of a great many people, of which I am very appreciative.

Special thanks go to my supervisors, Professor Adam F. Lee and Professor Karen Wilson, for giving me the opportunity to conduct this research; and for all support and guidance throughout the duration of my PhD and particularly during the relocation from Cardiff University to Aston University. I am also grateful to the EPSRC for the funding of this project; as well as to the Department of Chemistry at Cardiff University and the European Bioenergy Research Institute (EBRI) at Aston University for providing enjoyable environments in which to work!

I must also make a special mention and (thanks!) to Dr Nicole S. Hondow (University of Leeds) for her help collecting the majority of HRTEM images shown in this thesis. Also, to Dr Christopher M.A. Parlett for his help and guidance during the course of this project - especially with instrument training during the first few months. I am extremely appreciative for the continuing support and friendship of the Surface, Materials and Catalysis Group at Aston University, and for the time spent with several visiting researchers – It may have been brief but it was a laugh.

I must recognise the crucial role of my parents, Andrea and Richard Durndell, who guided and consoled me from the very beginning – Stopping me from switching to Pharmacology, when this project seemed to be going nowhere. To Miss Yvonne Wilday, Miss Natalie Soper and Mr Andrew Fox, for their help and understanding during the dark times, when I was truly struggling.

Last but no means least, Dr. Vannia Cristina Dos Santos. Sem você eu não teria feito isso por meio da relocação de Cardiff para Birmingham. Tem sido difícil estar longe , mas eu sou grato que você já esteve lá , sempre que eu preciso de você. Obrigado! Eu te amo!

This work is dedicated in the memory of Mr James “*Jim*” Wilcock (1936-2009) and Mrs Ann-marie Durndell (1943-2013).

## Declaration

I declare that the research conducted and described in this doctoral thesis was carried out between October 2011 and February 2015 and is the sole work of the author. This work has not previously been submitted in whole or part for a degree at any other time or at any other academic institution. I hereby, give my consent as author for my thesis, if accepted, to be made available for photocopying and for inter-library loan, and for the title and summary to be made readily available to outside institutions.

Some of the research reported in this document has been published in peer-reviewed journal articles, which are referenced below:

- 1) L. Durndell, C. M. Parlett, N. S. Hondow, K. Wilson and A. F. Lee, *Nanoscale*, 2013.
- 2) L. Durndell, C. M. Parlett, N. S. Hondow, M. A. Isaacs, K. Wilson and A. F. Lee, *Scientific Reports*, 2015.

## Table of Contents

### ***Chapter 1 - Introduction***

1.1.	Introduction	2
1.1.1.	Green chemistry and heterogeneous catalytic systems	2
1.1.2.	Selective transformation of allylic substrates	4
1.1.2.1.	Catalytic selective oxidation of allylic alcohols	5
1.1.2.2.	Heterogeneous platinum catalysts – Mechanistic aspects of selective aerobic oxidation	6
1.1.2.3.	Catalytic selective hydrogenation of allylic aldehydes	8
1.1.3.	Deactivation	13
1.1.4.	Supports	14
1.1.4.1.	Modification of support properties	15
1.1.4.1.1.	Ordered mesoporous silica	15
1.2.	Thesis aims	21
1.3.	References	22

### ***Chapter 2 - Experimental***

2.1.	Catalyst Preparation	28
2.1.1.	Materials	28
2.1.2.	SBA-15 synthesis	28
2.1.3.	SBA-16 synthesis	28
2.1.4.	KIT-6 synthesis	29
2.1.5.	Polystyrene bead synthesis	29
2.1.6.	TLCT-Macro-mesoporous SBA-15 synthesis	29
2.1.7.	Metal incipient wetness impregnation (all supports)	30
2.2.	Sample Characterisation	30
2.2.1.	Microscopy and elemental composition determination	30
2.2.1.1.	Scanning electron microscopy	30
2.2.1.2.	Energy dispersive x-ray spectroscopy	32
2.2.1.3.	Transmission electron microscopy	32

2.2.2. X-ray analysis	33
2.2.2.1. Powder X-ray diffraction	33
2.2.2.2. X-ray photoelectron spectroscopy	35
2.2.2.3. X-ray adsorption – Synchrotron-based structural studies	38
2.2.3. Bulk Sample Characterisation	40
2.2.3.1. Thermogravimetric analysis	40
2.2.3.2. Carbon monoxide pulse chemisorption	40
2.2.3.3. Diffuse reflection infra-red fourier transform spectroscopy	43
2.2.3.4. Nitrogen Porosimetry	44
2.3. Catalyst Testing	47
2.3.1. Selective oxidation	47
2.3.1.1. Alcohol selective oxidation (standard procedure)	47
2.3.1.2. Role of atmosphere on cinnamyl alcohol selective oxidation	47
2.3.1.3. Role of <i>in-situ</i> reduction pre-treatment	48
2.3.1.4. Identifying reactive intermediate behaviour in selective oxidation	48
2.3.1.5. Effect of O <sub>2</sub> pressure on cinnamyl alcohol selective oxidation	48
2.3.2. Selective hydrogenation	49
2.3.2.1. Cinnamaldehyde hydrogenation (standard procedure)	49
2.3.2.2. Effect of H <sub>2</sub> pressure on cinnamaldehyde selective hydrogenation	49
2.3.3. Active site leaching – Hot filtration	50
2.4. References	50

**Chapter 3 - The selective oxidation of allylic alcohols over platinum/silicas  
– Identification of active site and mesopore effects**

3.1. Introduction	54
3.2. Results and Discussion	55
3.2.1 Characterisation of bare silica supports	55

3.2.1.1.	Powder x-ray diffraction	55
3.2.1.2.	Nitrogen Porosimetry	56
3.2.1.3.	Transmission electron microscopy	58
3.2.2.	Characterisation of Pt impregnated silica supports	59
3.2.2.1.	Energy dispersive x-ray analysis	59
3.2.2.2.	Powder x-ray diffraction	60
3.2.2.3.	Nitrogen porosimetry	63
3.2.2.4.	Carbon monoxide pulse chemisorption	68
3.2.2.5.	X-ray photoelectron spectroscopy	69
3.2.2.6.	X-ray adsorption spectroscopy	76
3.2.3.	Cinnamyl alcohol selox	80
3.2.3.1.	Active site heterogeneity	80
3.2.3.2.	Oxygen vs. Air as primary oxidant	82
3.2.3.3.	The role of catalyst pre-reduction on cinnamyl alcohol selox	88
3.2.4.	Tailoring active species stability	91
3.2.5.	Mapping the reaction pathway	94
3.2.6.	Alternative substrate selox	96
3.3.	Conclusion	98
3.4.	References	99

***Chapter 4 - Platinum-based selective hydrogenation of allylic aldehydes – An investigation of nanoparticle characteristics and support architecture on cinnamyl alcohol selectivity***

4.1.	Introduction	102
4.2.	Results and Discussion	102
4.2.1.	Characterisation of polystyrene spheres	102
	– Scanning electron microscopy	
4.2.2.	Characterisation of parent SBA-16 and TLCT-MM-SBA-15 supports	103
4.2.2.1.	Powder x-ray diffraction	103
4.2.2.2.	Nitrogen porosimetry	105



4.2.2.3.	Transmission electron microscopy – As synthesised supports	108
4.2.3.	Characterisation of Pt impregnated supports	110
4.2.3.1.	Energy dispersive x-ray analysis	110
4.2.3.2.	Powder x-ray analysis	111
4.2.3.3.	Nitrogen porosimetry	113
4.2.3.4.	Carbon monoxide pulse chemisorption	116
4.2.3.5.	Transmission electron microscopy – Pt- impregnated materials	118
4.2.3.6.	X-ray photoelectron spectroscopy	120
4.2.4.	Cinnamaldehyde hydrogenation	123
4.2.4.1.	Probing the reaction pathway	132
4.2.4.2.	Effect of H <sub>2</sub> pressure	135
4.2.4.3.	Active site heterogeneity	138
4.2.5.	Extended characterisation of Pt impregnated silica supports	139
4.2.5.1.	<i>In-situ</i> XRD	139
4.2.5.2.	Diffuse reflectance infra-red fourier transform	142
4.2.6.	Alternate substrates	148
4.2.6.1.	Substituted benzaldehydes	148
4.2.6.2.	α-methyl-trans-cinnamaldehyde hydrogenation	150
4.2.6.3.	Preliminary studies into ketone and derivative aliphatic aldehyde hydrogenation	152
4.3.	Conclusion	155
4.4.	References	157

### ***Chapter 5 – Conclusions and Further work***

5.1.	Conclusions	161
5.1.1.	CinnOH selective oxidation	161
5.1.2.	Cinnamaldehyde selective hydrogenation	163
5.1.3.	Future work	165
5.2.	References	166
	<b><i>Appendix</i></b>	167

## Table of Equations, Figures, Schemes and Tables

### Chapter 1 - Introduction

<b>Figure 1.1</b> – The 12 points of green chemistry as an aid to catalyst design	2
<b>Figure 1.2</b> – Proposed reaction scheme for $\alpha$ , $\beta$ -unsaturated cinnamone derivatives	5
<b>Figure 1.3</b> – Cobalt-doping of Pt nanoparticles demonstrating the “critical size effect”	10
<b>Figure 1.4</b> – Schematic representing molecular re-orientation of cinnamaldehyde by self-assembled monolayer thiolate introduction onto Pt surfaces	12
<b>Figure 1.5</b> – Nanoparticle sintering – Loss of uniform, discrete particles in favour of larger agglomerated masses	14
<b>Scheme 1</b> – Representation of SBA-15 mesoporous framework formation	17
<b>Scheme 2</b> – Visual representation of the interactions between sol-gel species and the surfactant template in various media	18
<b>Scheme 3</b> – The mechanism of hydrolysis and condensation of alkoxy silane precursors to form silica in acid catalysed conditions	19

### Chapter 2 - Experimental

<b>Figure 2.1</b> – A representation of signal generation from beam-specimen interactions	31
<b>Figure 2.2</b> – An illustrative representation of x-ray generation	32
<b>Figure 2.3</b> – The FEI Tecnai CM200 TEM in the LENNF facility at the University of Leeds	33
<b>Figure 2.4</b> – Schematic representation of in-phase x-ray diffraction phenomena	34
<b>Equation 2.1</b> – Bragg’s Law	34
<b>Equation 2.2</b>	34
<b>Equation 2.3</b> – The Scherrer equation	35
<b>Equation 2.4</b> – Binding energy	36
<b>Figure 2.5</b> – Schematic representation of photoelectron generation	36
<b>Equation 2.5</b> – Determination of total angular momentum	37
<b>Figure 2.6</b> – Schematic representation of XAS spectrum for the Pt L <sub>III</sub> -edge	38
<b>Equation 2.6</b> – EXAFS equation	39
<b>Figure 2.7</b> – Molecular orbital diagrams for CO on Pt and free gaseous CO	41
<b>Equation 2.7</b> – Metal dispersion	42
<b>Equation 2.8</b> – Average particle size	42
<b>Equation 2.9</b> – Hooke’s Law	43
<b>Figure 2.8</b> – A schematic representation of the parabolic mirrors utilised for infra-red beam focussing in diffuse reflectance IR	43
<b>Figure 2.9</b> – Typical adsorption isotherms and hysteresis loops for type IV and V isotherms	45
<b>Equation 2.10</b> – BET (Linear)	46
<b>Equation 2.11</b> – Definition of constant, C	46
<b>Equation 2.12</b> – BET surface area calculation	46
<b>Equation 2.13</b> – Kelvin equation	46
<b>Table 2.1</b> – GC column oven method for cinnamyl alcohol analysis	47
<b>Table 2.2</b> – GC column oven method for cinnamaldehyde analysis	49
<b>Figure 2.10</b> – Schematic representation of Parr 5500 series autoclave	50

**Chapter 3 - The selective oxidation of allylic alcohols over Platinum/silicas  
– Identification of active site and mesopore effects**

<b>Figure 3.1</b> – A schematic representation and TEM images of 2-Dimensional SBA-15 and interconnected 3-Dimensional KIT-6 mesoporous silica	54
<b>Figure 3.2</b> – Stacked low angle XRD pattern of parent SBA-15 and KIT-6 supports	55
<b>Table 3.1</b> – Textural properties of parent silica supports	56
<b>Figure 3.3</b> – Stacked isotherm plot of KIT-6, SBA-15 and amorphous silica	57
<b>Figure 3.4</b> – Stacked BJH pore size distributions for the mesoporous silica supports	58
<b>Figure 3.5</b> - Representative dark field HRTEM images of (a) SBA-15 and (b) KIT-6	58
<b>Table 3.2</b> – A comparison of targeted and actual bulk platinum loadings	59
<b>Figure 3.6</b> – Stacked low angle XRD plots for Pt/SBA-15 and Pt/KIT-6	60
<b>Figure 3.7</b> – Stacked wide angle XRD plots for Pt/amorphous, Pt/SBA-15 and Pt/KIT-6	61
<b>Table 3.3</b> – Pt nanoparticle size calculated from Pt(111) reflection	62
<b>Figure 3.8 (a)</b> – Stacked N <sub>2</sub> isotherm plot for Pt/amorphous silica series	63
<b>Figure 3.8 (b)</b> – Stacked N <sub>2</sub> isotherm plot for Pt/SBA-15	64
<b>Figure 3.8 (c)</b> – Stacked N <sub>2</sub> isotherm plot for Pt/KIT-6 series	65
<b>Figure 3.9</b> – Tracking changes in BET support surface area with metal loading	66
<b>Figure 3.10</b> – Changes in mesopore and micropore surface area with metal loading	66
<b>Figure 3.11</b> – BJH pore size distributions for Pt impregnated SBA-15 and KIT-6	67
<b>Table 3.4</b> – Dispersion and average Pt particle size calculated from CO titration	68
<b>Figure 3.12</b> – Influence of Pt loading and support architecture on Pt dispersion	69
<b>Figure 3.13 (a)</b> – Stacked Pt 4f XPS plot of Pt/amorphous silica series	70
<b>Figure 3.13 (b)</b> – Stacked Pt 4f XPS plot of Pt/SBA-15 series	71
<b>Figure 3.13 (c)</b> – Stacked Pt 4f XPS plot of Pt/KIT-6 series	72
<b>Figure 3.14</b> – Influence of Pt loading and support architecture on surface PtO <sub>2</sub> content	73
<b>Figure 3.15</b> – Relationship between surface PtO <sub>2</sub> content and metal dispersion	74
<b>Equation 3.1a and Equation 3.1b</b>	74
<b>Equation 3.2a and Equation 3.2b</b>	75
<b>Equation 3.3</b> – Estimation of oxide thickness	75
<b>Figure 3.16</b> – Stacked XAS normalised Pt L <sub>III</sub> -edge spectra Pt/ amorphous silica series	76
<b>Table 3.5</b> – A direct comparison between PtO <sub>2</sub> determination using XPS and XANES	77
<b>Figure 3.17</b> – XANES fitting, EXAFS K <sup>3</sup> weighted data and Fourier transform data fittings for 2.10 and 0.09 wt. % Pt/aSiO <sub>2</sub>	76-78
<b>Table 3.6</b> – Pt L <sub>III</sub> -edge EXAFS fitting parameters	79
<b>Figure 3.18</b> – Influence of stirring rate on cinnamyl alcohol selective oxidation	80
<b>Figure 3.19</b> – Hot filtration tests to determine the extent of Pt leaching in cinnamyl alcohol selective oxidation	81
<b>Figure 3.21</b> – Cinnamyl alcohol reaction profiles	83
<b>Figure 3.22</b> – Initial rate dependence of cinnamyl alcohol selox on (a) Pt loading and support architecture and (b) surface PtO <sub>2</sub> concentration	84
<b>Figure 3.23</b> – Cinnamyl alcohol aerobic selox turnover frequencies expressed	85

as a function of surface Pt metal or PtO <sub>2</sub> content	
<b>Figure 3.24</b> – Representative selectivity profile as a function of reaction time showing major cinnamyl alcohol selox products	86
<b>Figure 3.25</b> – Detrimental impact of surface Pt <sup>(0)</sup> on selectivity to oxidation versus hydrogenation products	87
<b>Figure 3.26</b> – Cinnamyl alcohol selox reaction profiles over in-situ reduced 0.11 wt. % Pt/SBA-15 and control “fresh” catalyst	88
<b>Figure 3.27</b> – The effect of reaction atmosphere on cinnamyl alcohol initial activity	89
<b>Figure 3.28</b> – Representative selectivity profile as a function of reaction time showing major cinnamyl alcohol selox products over <i>in-situ</i> reduced 0.11 wt. % Pt/SBA-15 catalyst	90
<b>Figure 3.29</b> – Influence of O <sub>2</sub> reaction pressure on cinnamyl alcohol conversion and oxidation:hydrogenation product selectivity over a 0.05 wt. % Pt/aSiO <sub>2</sub> catalyst	91
<b>Figure 3.30</b> – Stacked Pt 4f XPS plots of fresh vs. spent Pt/aSiO <sub>2</sub> catalyst over variable reaction time and O <sub>2</sub> pressure	92
<b>Figure 3.31</b> – Influence of cinnamyl alcohol reaction time and O <sub>2</sub> pressure on surface PtO <sub>2</sub> concentration for a 0.54 wt. % Pt/aSiO <sub>2</sub> catalyst	93
<b>Scheme 1</b> – Reaction network for cinnamyl alcohol selox	94
<b>Table 3.7</b> – Selox performance of 0.05 wt. % Pt/SBA-15 towards saturated and unsaturated oxygenates	96

**Chapter 4 - Platinum-based selective hydrogenation of allylic aldehydes – An investigation of nanoparticle characteristics and support architecture on cinnamyl alcohol selectivity**

<b>Figure 4.1</b> – SEM image of synthesised polystyrene spheres and associated particle size distribution	103
<b>Figure 4.2</b> – Low angle XRD patterns of parent SBA-16 and TLCT-MM-SBA-15 supports	104
<b>Table 4.1</b> – Textural properties of parent silica supports	105
<b>Figure 4.3 (a)</b> – Isotherm plot and BJH pore size distribution of parent SBA-16 support	106
<b>Figure 4.3 (b)</b> – Isotherm plot and BJH pore size distribution of parent TLCT-MM-SBA-15 support	106
<b>Figure 4.4 (a)</b> – Representative HRTEM images of SBA-16	108
<b>Figure 4.4 (b)</b> – Representative HRTEM images of TLCT-MM-SBA-15	108
<b>Table 4.2</b> – A comparison of targeted and actual bulk platinum loadings	110
<b>Figure 4.5 (a)</b> – Stacked wide angle and low angle XRD plots for Pt/SBA-16	111
<b>Figure 4.5 (b)</b> – Stacked wide angle and low angle XRD plots for Pt/TLCT-MM-SBA-15	111
<b>Table 4.3</b> – Pt nanoparticle size calculated from Pt(111) reflection	112
<b>Figure 4.6 (a)</b> – Stacked N <sub>2</sub> isotherm plot for Pt/SBA-16	113
<b>Figure 4.6 (b)</b> – Stacked N <sub>2</sub> isotherm plot for Pt/TLCT-MM-SBA-15	114
<b>Figure 4.7</b> – Tracking changes in BET support surface area with metal loading	115
<b>Figure 4.8</b> – Changes in micropore surface area with metal loading	115
<b>Figure 4.9</b> – BJH pore size distributions for Pt/SBA-16 and Pt/TLCT-MM-SBA-15	116
<b>Table 4.4</b> – Dispersion and average Pt particle size calculated from CO	117

chemisorption

<b>Figure 4.10 (a)</b> – Representative HRTEM images of approx. 2 wt. % Pt/SBA-16 and particle size distribution	118
<b>Figure 4.10 (b)</b> – Representative HRTEM images of approx. 2 wt. % Pt/TLCT-MM-SBA-15 and particle size distribution	119
<b>Figure 4.11 (a)</b> – Stacked 4f XPS plot of Pt/SBA-16	120
<b>Figure 4.11 (b)</b> – Stacked 4f XPS plot of Pt/TLCT-MM-SBA-15	121
<b>Figure 4.12</b> – Influence of Pt loading and support architecture on surface PtO <sub>2</sub> content	121
<b>Figure 4.13</b> – Relationship between surface PtO <sub>2</sub> content and metal dispersion	122
<b>Figure 4.14</b> – Influence of stirring rate on cinnamaldehyde hydrogenation	123
<b>Figure 4.15 (a)</b> – Cinnamaldehyde hydrogenation reaction profiles for amorphous silica and SBA-15 series under ambient conditions	124
<b>Figure 4.15 (b)</b> – Cinnamaldehyde hydrogenation reaction profiles for KIT-6 and SBA-16 series under ambient conditions	124
<b>Figure 4.15 (c)</b> – Cinnamaldehyde hydrogenation reaction profiles for TLCT-MM-SBA-15 series under ambient conditions	125
<b>Figure 4.16 (a)</b> – Initial rate dependence of cinnamaldehyde hydrogenation at 1 bar as a function of Pt particle size	125
<b>Figure 4.16 (b)</b> – Turnover frequencies for cinnamaldehyde hydrogenation	126
<b>Figure 4.17</b> – Influence of catalyst:substrate ratio on cinnamaldehyde hydrogenation initial rate and turnover frequency	127
<b>Figure 4.18</b> – Cinnamyl alcohol selectivity over silica supported platinum catalysts for cinnamaldehyde hydrogenation after 7 hrs as a function of Pt particle size	128
<b>Figure 4.19 (a)</b> – Evolution of product selectivity as a function of cinnamaldehyde conversion over approx. 2 wt. % Pt/amorphous silica and Pt/SBA-15 catalysts	129
<b>Figure 4.19 (b)</b> – Evolution of product selectivity as a function of cinnamaldehyde conversion over approx. 2 wt. % Pt/KIT-6 and Pt/TLCT-MM-SBA-15 catalysts	129
<b>Figure 4.20</b> – Cinnamyl alcohol and 3-phenylpropionaldehyde hydrogenation over approx. 2 wt. % silica supported platinum catalysts at 1 bar H <sub>2</sub>	132
<b>Figure 4.21</b> – 3-phenylpropan-1-ol hydrogenation over approx. 2 wt. % silica supported platinum catalysts at 1 bar H <sub>2</sub>	133
<b>Scheme 1</b> – Kinetic network for cinnamaldehyde hydrogenation	134
<b>Figure 4.22 (a)</b> – H <sub>2</sub> pressure dependence of CinnALD hydrogenation over amorphous silica, SBA-15 and TLCT-MM-SBA-15 at approx. 2 wt. % platinum	135
<b>Figure 4.22 (b)</b> – H <sub>2</sub> pressure dependence of CinnALD hydrogenation over KIT-6 and SBA-16 at approx. 2 wt. % platinum	135
<b>Figure 4.23</b> – Relationship between $p_{H_2}$ and reaction order over amorphous silica, SBA-15 and TLCT-MM-SBA-15; KIT-6 and SBA-16 supported platinum catalysts for CinnALD hydrogenation	136
<b>Figure 4.24</b> – H <sub>2</sub> pressure dependence on C=O versus C=C hydrogenation pathways during CinnALD hydrogenation	137
<b>Figure 4.25</b> – Hot filtration tests to determine the extent of Pt leaching in cinnamaldehyde hydrogenation	139
<b>Figure 4.26</b> – Hydrogen pressure dependence of fcc platinum lattice parameter of approx. 2 wt. % silica supported platinum catalysts at room temperature	140
<b>Figure 4.27</b> – Hydrogen pressure independence Pt (111):(200) x-ray reflections	141

over approx. 2 wt. % Pt/SBA-15 catalysts	
<b>Scheme 2</b> - CinnALD adsorption over carbon nanofiber-supported Pt nanoparticles – Elucidation of activity and selectivity effects over polar and non-polar surfaces	142
<b>Figure 4.28</b> – In vacuo DRIFT spectra of 2 wt. % silica supported platinum catalysts	143
<b>Scheme 3</b> – Schematic representation of silanol functionalities with associated stretching frequencies	144
<b>Figure 4.29</b> – <i>In-situ</i> ATR-IR spectra confirming the temperature independence of approx. 2 wt. % Pt/aSiO <sub>2</sub> and 2 wt. % Pt/SBA-15 catalyst films under flowing cinnamaldehyde/anisole solution at 25 °C and 90 °C	145
<b>Figure 4.30</b> – <i>In-situ</i> ATR-IR spectra of approx. 2 wt. % Pt impregnated silica catalyst films under flowing cinnamaldehyde/anisole solution at 90 °C and an illustration of unfavorable aromatic-surface interaction arising from adoption of di-σ <sub>C=C</sub> versus di-σ <sub>C=O</sub> CinnALD adsorption on Pt nanoparticles over a polar SBA-15 surface	146
<b>Figure 4.31</b> – Arrhenius plots for CinnALD hydrogenation over approx. 2 wt. % Pt impregnated on amorphous, SBA-15 and KIT-6 silica's at 1 bar H <sub>2</sub>	147
<b>Scheme 4</b> – Chemical structure of screened benzylic aldehydes	148
<b>Figure 4.32</b> – Performance of approx. 2 wt. % Pt/SBA-15 and 2 wt. % Pt/aSiO <sub>2</sub> catalysts for the hydrogenation of substituted benzaldehydes	149
<b>Scheme 5</b> – Chemical structure of α-methyl-trans-cinnamaldehyde	150
<b>Figure 4.33</b> - Influence of methyl substitution alpha to the carbonyl in CinnALD for the rates of C=C versus C=O hydrogenation over large and small Pt nanoparticles supported on silica analogues	151
<b>Figure 4.34</b> – α-methyl- <i>trans</i> -cinnamyl alcohol hydrogenation over approx. 2 wt. % silica supported platinum catalysts at 1 bar H <sub>2</sub>	152
<b>Scheme 6</b> – Chemical structure of crotonaldehyde derivatives and ketones	153
<b>Table 4.5</b> – Catalytic performance of allylic substrates and aromatic ketones under ambient conditions	153

### **Chapter 5 – Conclusions and Further work**

<b>Figure 5.1</b> – Cinnamyl alcohol aerobic selox turnover frequencies expressed as a function of surface Pt metal or PtO <sub>2</sub> content for Pt/aSiO <sub>2</sub> , Pt/SBA-15 and Pt/KIT-6 catalysts	162
<b>Figure 5.2</b> – H <sub>2</sub> pressure dependence of cinnamaldehyde hydrogenation	164
<b>Figure 5.3</b> – In vacuo DRIFT spectra of 2 wt. % silica supported platinum catalysts	165

### **Appendix**

<b>Figure 6.1</b> - Stacked Si 2p XPS plot of all parent silica supports	167
<b>Figure 6.2</b> - Stacked O 1s XPS plot of all parent silica supports	168

# *Chapter 1*

## *Introduction*

## 1.1 Introduction

### 1.1.1 Green chemistry and heterogeneous catalytic systems

The progression towards a clean and efficient synthesis route for the formation of  $\alpha,\beta$ -unsaturated species is paramount to a sustainable chemical economy, due to the value placed on such classes of compounds as intermediates or final products utilised in the pharmaceutical, agrochemical and fine chemical sectors. For example, cinnamaldehyde is both a food and fragrance additive,<sup>1</sup> conferring the flavour and aroma of cinnamon, whilst also serving as an insect repellent.<sup>2</sup> Such aldehydes are typically derived by the selective oxidation of their corresponding allylic alcohols. Historically, stoichiometric amounts of hazardous/toxic oxidants were employed to drive such oxidations (permanganate and chromate containing oxidants),<sup>3,4</sup> with often poor final product yield and the unfortunate generation of harmful waste in multi-tonne quantities.<sup>5</sup> The 12 principles of green chemistry, shown in **Figure 1.1**, outline the key aspects for the understanding and effective design of next-generation catalysts urgently needed to attain the aspirations of a cleaner, sustainable chemical industry.<sup>6,7</sup>

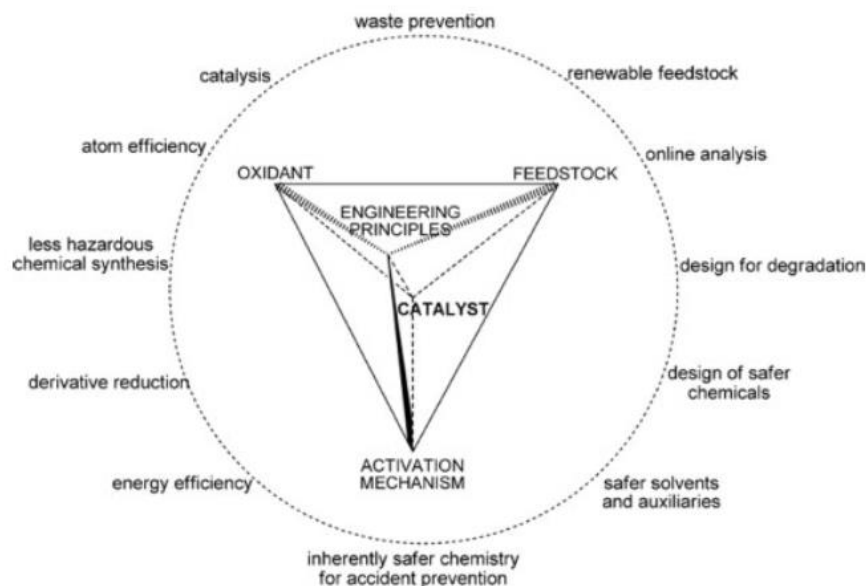


**Figure 1.1 – The 12 points of green chemistry as an aid to catalyst design**  
(modified from reference 3)

Heterogeneous catalysts capable of such chemoselective transformations have thus attracted great interest.<sup>7</sup> The co-existence of reactive  $\text{H}_2\text{C}-\text{OH}$  or  $\text{HC}=\text{O}$  groups in close proximity to  $\text{C}=\text{C}$  moieties is a challenge to high unsaturated product selectivity in many



reaction schemes.<sup>8,9</sup> Consequently, a fundamental understanding of the active site and reaction network is pivotal for improving catalyst design.

The definition of a catalyst is any reagent or material which increases the rate of chemical reaction by the lowering the activation energy barrier for the rate determining step of said reaction, without being consumed. This rate enhancement is achieved by providing an alternative mechanism, proceeding through a transition state of lower energy. In doing so, this can enable reactions normally hindered by slow reaction kinetics/barriers, to proceed with enhanced rate under more amiable conditions, wrt to the uncatalysed reaction. However, as substrate complexity increases, multiple reaction pathways present themselves resulting in the possibility of various side products. As each product has an inherent activation energy barrier, the presence of a catalyst can be used as a tool to drive the formation of specific products, based solely on energetic favourability.<sup>10,11</sup> In this instance, intelligent design must be employed to tune final product selectivity and improve system efficiency. Applying this fundamental property, catalytic systems are utilised in a wide array of situations, from large-scale cracking of long-chain alkanes and crude oil in the petrochemical sector,<sup>12</sup> to the promotion of the *Heck*<sup>13</sup> and *Friedel-Crafts*<sup>14</sup> reactions in fine chemical synthesis, but perhaps most famously in the after-treatment of partially converted emission gases in internal combustion engines.<sup>15,16</sup> Unaided such processes could not be implemented on such a substantial scale without catalyst exploitation.

For simplicity's sake, catalysts can be defined as one of two classes; Heterogeneous and Homogeneous. Catalyst-reaction mixture relationships determine which subdivision the catalyst falls into, a catalyst in the same phase as the reaction mixture can be defined as a homogeneous catalyst; if the two phases are different the term heterogeneous applies. Homogeneous motifs typically employ soluble, metal complexes in the liquid phase with the active site clearly identifiable, allowing for a more efficient, stream-lined protocol to be adopted during catalyst design. Tuning ligand structure and the presence of auxiliary compounds can be used to adapt final product selectivity and introduce chirality effects into complex reaction pathways.<sup>17,18,19</sup> An abundance of literature reviews encompassing a scope of transformations, focusing on  $\alpha,\beta$ -unsaturated substrates, highlight the interest in this field.<sup>20,21,22,23,24</sup> The ability to produce catalysts with a defined active site is highly desirable in all fields of catalytic design; however homogeneous systems come with several fundamental drawbacks. Acute toxicity, complex multi-step preparation procedures and high initial expense fly in the face of "green chemistry" concepts, whilst separation and recycling

of the active phase from the final product is often difficult and ultimately costly at a commercial level.<sup>25</sup> Heterogeneous catalysts do not suffer from such drawbacks, with solid catalyst used for liquid and gas phase reactions alike. Product-catalyst separation is often simplistic aiding product purity and active phase recyclability. Synthesis routes for such materials are often rudimentary, with reproducibility and ease of scale-up earning increased interest from commercial/industrial sectors.<sup>26</sup> Deactivation phenomena and positive elucidation of the active site present fresh complications, with modulation of surface characteristics, *in-situ*, adding an additional layer of frustration.<sup>27,28</sup> Recent developments in surface-sensitive and operando/*in-situ* time resolved analytical instrumentation, in tandem with computational modelling, have yielded greater insight into catalytic behaviour.<sup>29,30,31,32</sup> Unfortunately, procedures such as synchrotron analyses remain a prerequisite for a comprehensive understanding of active species generation, reactive intermediate and surface species determination,<sup>29,33,34,35,36</sup> with any hope of achieving this via in-house characterisation (*e.g XPS, XRD, DRIFTS etc.*) still remote. These drawbacks are, for now, only intellectual limitations but as research evolves the understanding and versatility of these systems become more apparent.

### 1.1.2 Selective transformation of allylic substrates

In continuation of the theme, a number of approaches have been implemented and evaluated in a bid towards enhancing the understanding of structure-performance relationships and heterogeneous active site identification and activity. These approaches have been reviewed in subsequent sections of this thesis. The selective oxidation of cinnamyl alcohol to cinnamaldehyde over supported platinum catalysts has been used as a model reaction to reveal the active site, under “*benign*” conditions. In parallel, the selective hydrogenation of cinnamaldehyde to cinnamyl alcohol explores metal particle size and support surface effects, as an attempt to dictate the final reaction pathway. **Figure 1.2** highlights the proposed reaction scheme for these transformations. It is hoped that understanding catalyst behaviour for both protocols, will permit the design of a truly bi-functional material, minimising waste and optimising atomic economy.

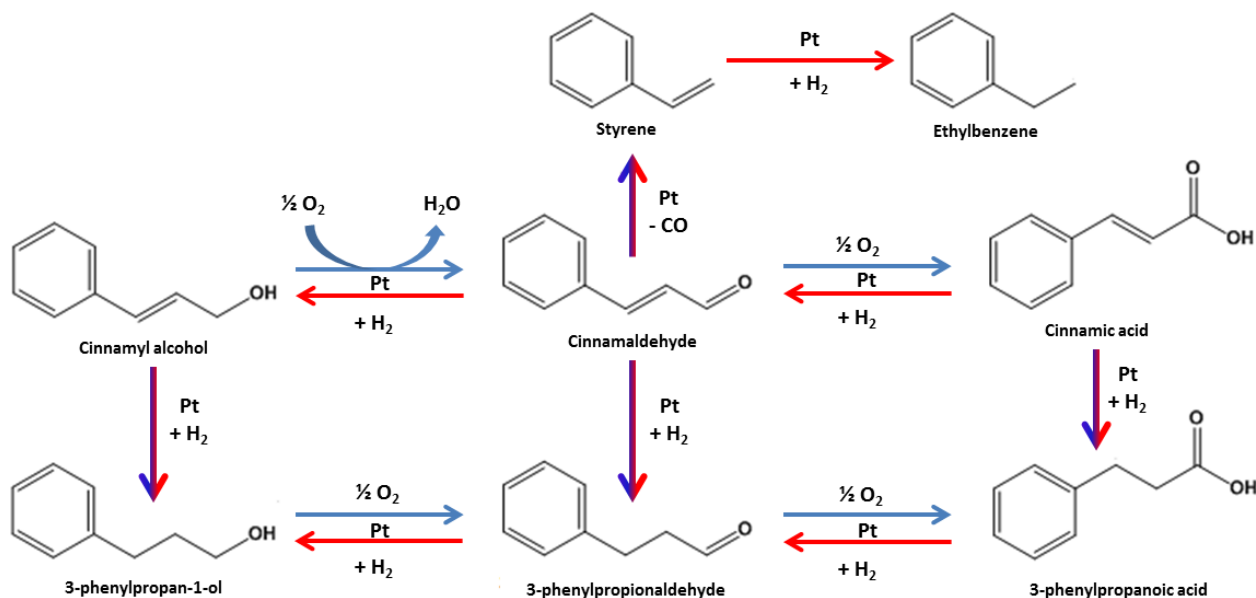


**Figure 1.2 – Proposed reaction scheme for  $\alpha,\beta$ -unsaturated cinnamyl derivatives**

*(Blue indicates oxidation, Red indicates hydrogenation)*

Selective hydrogenation and oxidation reactions are fundamental for the synthesis of many organic compounds including amines, nitrates, alcohols, esters and carbonyl-containing species.<sup>37,38</sup> In order to meet the demands of an ever-growing population, the need to optimise current syntheses, moving away from “*non-green*” practices (*i.e.* the use of stoichiometric reagents and extreme reaction conditions), is imperative. Heterogeneous catalysis is a relatively new and exciting field with numerous materials and systems available. However, for the purpose of this study, heterogeneous platinum will be the principle focus of discussion.

### 1.1.2.1 Catalytic selective oxidation of allylic alcohols

The selective oxidation of alcohols (*selox*) to carbonyl and carboxylic acid moieties, utilising air/molecular oxygen as the oxidant, is a mainstay of organic chemistry and catalysis. High priority has been placed on the optimisation of this process, due to its importance in all levels of chemical manufacturing. Reaction rate and selectivity can be dictated by the complexity of the substrate. Increasing steric demands and intermediate stabilisation provide greatly diminished reaction characteristics.<sup>39, 40</sup> Allylic and benzylic-based substrates are typically more active than their saturated counterparts in heterogeneous catalysis.  $\alpha,\beta$ -unsaturation introduces multiple functional groups, allowing for new catalyst-substrate binding regimes, aiding product conversion.<sup>41</sup> However, this may cause much diminished selectivity, due to the different reactivity of C=O and C=C bonds, leading to problems in over-oxidation or loss of  $\alpha,\beta$  unsaturation entirely.<sup>41</sup> High rates and excellent

aldehyde selectivity have been achieved by tailoring active site density and support effect introduction. The selective oxidation of primary alcohols to the aldehyde equivalent is challenging.<sup>42</sup> These substrates exhibit reduced reactivity (vs. secondary and unsaturated alcohols), due to low carbocation stability in the resulting transition state.

Platinum group metals (PGM) are widely employed as heterogeneous catalysts for oxidative dehydrogenation, hydrogen transfer and oxygen insertion reactions.<sup>43,44,45</sup> Palladium has been extensively studied for the selective oxidation of allylic alcohols,<sup>7,39,46</sup> wherein sophisticated *in-situ*/operando spectroscopic and kinetic measurements have identified surface PdO as the active site responsible for crotyl and cinnamyl alcohol oxidation.<sup>27,34,47</sup> Ruthenium supported on TiO<sub>2</sub>,<sup>48</sup> CeO<sub>2</sub>,<sup>49</sup> Al<sub>2</sub>O<sub>3</sub>,<sup>50</sup> and hydrotalcite,<sup>51</sup> has also demonstrated efficiency towards allylic alcohol selox. Nanoparticulate gold also exhibits high carbonyl selectivity, in the presence of an auxiliary base. Many studies have been dedicated towards understanding the origin of this activity with strong nanoparticle size dependence and metal–support interactions attributed to such behaviour.<sup>52</sup> Studies by Schmidt show that the discrete electronic structure of Au clusters (below 2.5 nm) impart reactivity properties, not otherwise expressed by bulk gold nanoparticles.<sup>53</sup> Biomass-derived polyfunctional alcohols, such as 5-hydroxymethylfurfural (5-HMF) can also be selectively oxidised by supported gold nanoparticles,<sup>54</sup> providing routes to exciting renewable polymers such as PEF (derived from 2,5-furan dicarboxylic acid, FDCA).<sup>41,55</sup> Bimetallic variants, such as Au/Pd<sup>56</sup> and Au/Pt<sup>57</sup> catalysts have evidenced strong synergies in alcohol selox, resulting in enhanced activity, selectivity and lifetime.

### **1.1.2.2 Heterogeneous platinum catalysts – Mechanistic aspects of selective aerobic oxidation**

Although, there are numerous examples of monometallic Pt nanoparticles being utilised effectively in the chemoselective hydrogenation of  $\alpha,\beta$ -unsaturated substrates; the same cannot be stated for the reverse pathway. Prati *et al* report the selective oxidation of CinnOH over PVA-stabilised Pt colloidal particles supported on carbon. High selectivity to the desired product, cinnamaldehyde, is reported but with poor overall activity (TOF = approx. 60-90 h<sup>-1</sup> in H<sub>2</sub>O). In this study, the PVA structural stabilising agent was deemed to partially inhibit catalytic activity, through active site blocking.<sup>57</sup> A common theme in literature reports of Pt-catalysed oxidation processes is the poor selectivity of said

nanoparticles to the desired aldehyde/acid products.<sup>41, 58-61</sup> There is much debate into the relative stability and modes of deactivation for these materials. As with Pd-based systems, many authors attribute over-oxidation of Pt and Pd nanoparticles as the origin of diminished catalytic activity - though experimental evidence to support this is shaky at best. Mallat and Baiker hypothesise that reduced Pd<sup>(0)</sup> and Pt<sup>(0)</sup> centres provide the active site for alcohol dissociate adsorption and  $\beta$ -hydride elimination to the associate aldehyde.<sup>62, 63</sup> The regeneration of catalysts, deemed to be “over-oxidised,” by exposure to alcohols in an inert atmosphere or re-reduction through introduction of H<sub>2</sub> was used as the basis to this argument. It must be noted that catalyst deactivation could be attributed to factors other than “over-oxidation,” such as *in-situ* surface substrate/product build-up (sometimes referred to as “Coking”) or through active site leaching. In numerous studies, these factors are not investigated and so stating deactivation through metallic active site degradation, due to on-line loss of activity, provides an overly simplistic explanation to a more complicated scenario. In the selective oxidation of glucose, Abbadi *et al* observed significant deactivation of 5% Pt/C catalysts exclusively at pH's below 7, with negligible deactivation observed in alkaline conditions. Deactivation through over-oxidation does not explain this loss activity, especially when the author attempted catalyst “re-activation” through *in-situ* reduction by molecular H<sub>2</sub>.<sup>64</sup> Instead, deactivation was accredited to a build-up of strongly bound CO, formed through the decarbonylation of gluconic acid, or through direct adsorption of gluconic acid to Pt(111) surfaces. Similarly, the decarbonylation of benzaldehyde, in the selective oxidation of benzyl alcohol, led to the direct observation of CO bound to Pd/Al<sub>2</sub>O<sub>3</sub> surfaces by ATR-IR spectroscopy, through Pd(111) facets – in tandem with similar levels of catalyst deactivation.<sup>65</sup> Wang and co-workers screened a series of soluble Pt nanoclusters in the aqueous phase selective oxidation of various alcohol substrates. In the selective oxidation of cyclohexanol, soluble colloidal Pt nanoparticles synthesised from H<sub>2</sub>, glycol, NaBH<sub>4</sub> and ethanol reducing treatments, respectively, reported excellent conversion (>97%) and yield (> 90%) values. However, samples reduced in the presence of H<sub>2</sub> aggregated after the first reaction cycle, with NaBH<sub>4</sub> and ethanol treated catalysts showing significant aggregation after the second cycle.<sup>61</sup> A direct activity comparison between these Pt nanoclusters and comparable supported Pt systems shows very little promotion in catalytic activity for these unsupported nanoclusters. At first glance this seems an odd finding; the theoretical number of accessible active sites for substrate oxidation is much greater in this regime (by rationale of greater exposed external metal surface areas), thus greater catalytic activities are expected.<sup>66</sup> As this is not the case, it stands to reason that site-blocking or destabilising and/or repulsive

interactions between PVP and alcohol substrates prevent optimal catalyst activity from being achieved (inhibition of alcohol dissociative adsorption, alcoholate formation or product desorption steps). Pt nanoparticle aggregation in this study led to catastrophic losses in catalytic activity.

The selective oxidation of CinnOH to CinnALD over heterogeneous Pt systems has the potential to form a plethora of by-products (**Figure 1.2**).<sup>42, 44</sup> The most substantial reflecting the labile hydrogenation of the C=C functionality, through the presence of surface hydrogen species. Subsequent competing hydrogenolysis of the C-O bond<sup>60</sup> and decarbonylation<sup>67</sup> pathways can also take place. As stated above, reactively formed CO, through decarbonylation, can lead to poisoning of surface active sites. Altering reaction conditions such as the utilisation of batch versus flow reactors,  $pO_2$  and temperature can significantly alter product distribution.<sup>68</sup> The addition of pure flowing oxygen (wrt air) through the reaction solution can lead to a substantial promotion in activity and selectivity towards the desired carbonyl product.<sup>69</sup>

Further understanding into the Pt-catalysed selective oxidation of alcohol substrates, through positive identification of the true active site and modes of deactivation, can provide an avenue to more robust catalytic systems in the future.

### 1.1.2.3 Catalytic selective hydrogenation of allylic aldehydes

With the need for sustainable, environmentally-benign processes widely debated amongst academic and industrial communities, the use of gaseous hydrogen vs. novel *in-situ* generation of hydrogen species has taken centre stage. In traditional organic chemistry, reducing agents, *i.e.*  $NaBH_4$ ,  $LiAlH_4$  and tin compounds, are utilised to great effect allowing for the reproducible transformation of challenging substrates. However, enantiomeric selectivity, persistent toxicity and disposal issues tarnish any plans for their continued long-term use. The future looks to gaseous hydrogen, not only as a potential replacement for such practices, but also as a prospective clean energy carrier.<sup>70</sup> Hydrogen can be manufactured in high abundance from the splitting of water, via electrolysis, from dry biomass and biomass-derived liquid fuels (*i.e.* methanol or biodiesel).<sup>71,72,73</sup> However, high-capacity storage and safety considerations remain a concern.

Platinum finds use in almost all aspects of industrial and commercial heterogeneously catalysed hydrogenation processes, due to its ability to reduce a wide variety of

functionalities, including C=C,<sup>74, 75</sup> C≡C,<sup>76, 77</sup> C≡N,<sup>78</sup> C=O,<sup>79</sup> NO<sub>2</sub><sup>80</sup> and aromatics<sup>78</sup> utilising molecular hydrogen. As stated previously, the hydrogenation of allylic and benzylic aldehydes to unsaturated alcohols is commercially important, however efforts to develop highly active and selective heterogeneous catalysts have been stalled by the inherent thermodynamic stability of C=O relative to C=C bonds; and poor understanding into mode of action and structure-function parameters.<sup>20, 81</sup>

Early (albeit simplistic) mechanistic work for hydrogenation procedures was conducted in 1996-1998 by Zaera *et al.* In this study, the selective hydrogenation of ethylene over Pt(111) single-crystal surfaces was chosen as a representative model for olefin-based substrates over metallic surfaces. Although in vacuum, ethylene hydrogenation proceeded via stepwise addition of hydrogen over a clean catalyst surface; at higher pressures deposition of carbonaceous species actively played a role in substrate adsorption kinetics. It may be obvious to say, but under reaction conditions, build-up of carbon on any catalyst surface has a negative effect on reaction rate (active site blocking by carbon prevents subsequent substrate hydrogenation). However the most important factor controlling ethylene hydrogenation is intermediate stability and strength of substrate binding. For this model system, Zaera concluded that the presence of co-adsorbed surface hydrogen permitted an increased formation in weakly-adsorbed ethylene species on the Pt(111) surface - subsequently leading to an increased rate of ethane generation (reaction orders were approximately 1 with respect to weakly-adsorbed ethylene and hydrogen surface coverage). Deuteration of the ethene starting material reinforces the positive role of surface hydrogen – through evidence of H incorporation in the final product and a “first-order” rate constant (as said above).<sup>82, 83</sup> Tailoring substrate binding strength and mode through intelligent catalyst design is one possible method to producing more selective hydrogenation catalysts.

In order to determine the role of geometric and electronic contributions to the selective hydrogenation of commercially valuable substrates, Tsang and co-workers investigated the oleic acid/oleylamine stabilised mono- and bimetallic Pt-catalysed conversion of cinnamaldehyde (CinnALD) to cinnamyl alcohol (CinnOH).<sup>84, 85</sup> In this study, colloidal Pt nanoparticles were prepared in a range of sizes (2.8-14.4 nm) and decorated with an additive metal, Cobalt, prior to impregnation onto a carbon support.

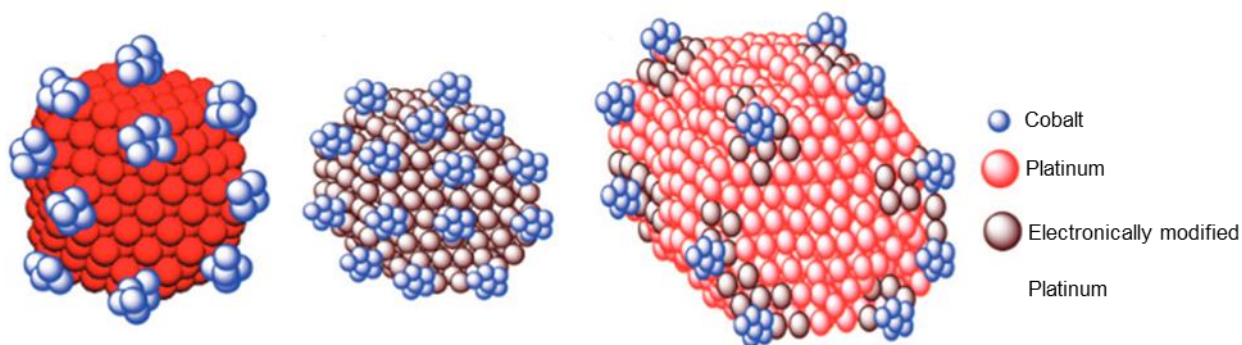


**Figure 1.3** – Cobalt-doping of Pt nanoparticles demonstrating the “critical size effect”  
(modified from reference 84)

**Figure 1.3** provides a pictorial representation of the geometric arrangement of the cobalt atoms on the Pt nanoparticle surface, as a function of Pt size. It is clearly shown and evidenced by Tsang et al that cobalt adatoms preferentially begin to populate coordinatively unsaturated edge and step sites as Pt nanoparticle size increases (the author references this as “*The critical size effect*”). Doped and un-doped Pt nanoparticles were screened in parallel for the chemoselective hydrogenation of CinnALD, in which selectivity towards CinnOH demonstrated a strong dependence on geometric size and cobalt adatom location. It was proposed that low coordination edge and step sites favour C=C hydrogenation - Blockage of these sites, *in combination with electronic effects*, instilled by Co decoration was thus suggested as the origin to a promotion in C=O hydrogenation. Silva and Zheng both utilised bimetallic systems, either through additive doping or a one-pot synthesis, to further enhance Pt nanoparticle selectivity towards CinnOH.<sup>86, 87</sup> Silva et al investigate the one-pot addition of Sn and Fe precursors to a solution of hexachloroplatinic acid, impregnated on TiO<sub>2</sub>. In this study, monometallic Pt nanoparticles display high selectivity to the unsaturated alcohol (87%) but show significant catalyst deactivation very early into the reaction. Pt-Fe/TiO<sub>2</sub> systems demonstrated the highest activity, reaching full conversion after 90 minutes and 97% desired product selectivity. In this study, the role of TiO<sub>2</sub> as a reducible support has not been discussed. Introduction of the Strong-Metal-Support-Interaction (SMSI) has been used to great effect for selectivity promotion in other systems.<sup>88-92</sup> Such a substantial promotion of the C=O pathway over monometallic Pt seems to indicate the activation of SMSI phenomena – It could be theorised that surface reduction of TiO<sub>2</sub> to a suboxide species, TiO<sub>x</sub> (where x is an oxidation state < 2), plays a crucial role in triggering support migration, playing a similar role to Co additives in the selective blocking of unselective sites.<sup>89, 93, 94</sup> Zheng and co-workers follow a similar route to Tsang; doping Pt/SiO<sub>2</sub> catalysts with Co and Cu separately.



As shown in Tsang's previous work, Co-doping preferentially promotes the C=O pathway (76%) - attributed to blocking of C=C selective edge and corner sites. Cu-doping demonstrates a detrimental effect on product selectivity, switching off C=O dominant pathways (35%) in favour of C=C formation (60%). In these studies it is very clear that bimetallic systems can afford superior selectivity towards CinnOH, however no clear physiochemical analyses have been conducted to further elucidate the role of promoters in the blocking of coordinatively unsaturated, unselective sites and/or the electronic modification of platinum by additive metals or reducible supports in this study. Recently, Zhu and Zaera found, if somewhat in contrast to the work described above, that CinnOH selectivity was insensitive to silica-supported Pt nanoparticle size.<sup>95</sup> This seems suspect and may be attributed to the small Pt size regime used in this study (1.3-2.4 nm particles). The ratio of Pt facets with size may not change significantly to observe a substantial change in final product selectivity or substrate adsorption mode.<sup>8</sup> Although, CinnALD hydrogenation rates were demonstrated to be structure sensitive, with Pt(111) facets accounting for a 5-fold increase in turnover frequency – It must be noted that extended Pt(111) facets become a more significant feature as Pt nanoparticle size increases and increasing the range of sizes studied may aid in structure dependant activity and selectivity determination.

Surface studies of crotonaldehyde, an aliphatic derivative of CinnALD, show the critical nature of adsorption geometry on product determination over Pt(111) facets. High Pt(111) facet population led to minor repulsion of the alkene functionality away from the Pt surface, favouring close approach of the C=O bond in a more atop fashion.<sup>96-98</sup> Using this principle as a stepping stone, there have been several studies into the use of surface modification of support and metal nanoparticles to achieve increased selective C=O activation.

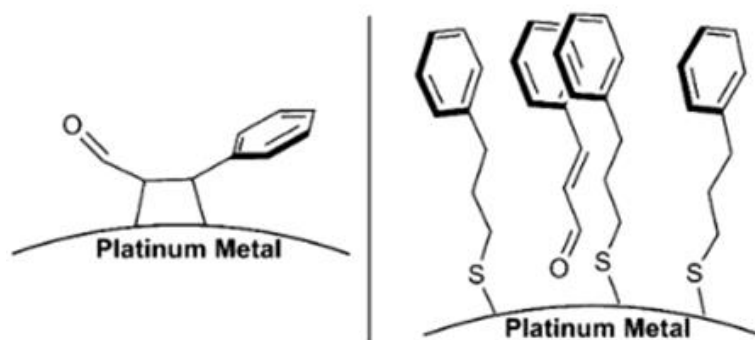


**Figure 1.4** – Schematic representing molecular re-orientation of cinnamaldehyde by self-assembled monolayer thiolate introduction onto Pt surfaces (modified from reference 85)

Medlin *et al* employed thiolate adsorption onto Pt surfaces as one such approach, controlling phenylated thiol structure aided in direct tuning of specific, non-covalent interactions with CinnALD (**Figure 1.4**). As a consequence of such interactions, molecular re-orientation of the CinnALD substrate to permit C=O centric end-on bonding, with respect to the Pt/Al<sub>2</sub>O<sub>3</sub> surface, enhanced CinnOH selectivity by approx. 70%.<sup>99, 100</sup> Promotion was found to originate from favourable  $\pi$ -stacking interactions between thiol self-assembled monolayers and the phenyl ring of CinnALD, increasing desired product selectivity without compromising rates of formation.<sup>99</sup> Continuing this theme, in work adapted from Baiker and Mallat,<sup>18</sup> Zaera and co-workers employed surface tethering of cinchonidine to silica sites adjacent to Pt nanoparticles, in an effort to add molecular functionality and substrate adsorption mode control to the Pt-catalysed hydrogenation of ethyl pyruvate on silica supports.<sup>101</sup> Ethyl pyruvate contains two C=O functionalities in close proximity and thus chemoselective transformation of either one of these groups becomes a matter of enantioselectivity and steric control. The authors devised a protocol for defined Cd tethering to specific sites and thus screened catalytic activity in acidic and aromatic solvents. Solvent choice seems to express only minor fluctuations in performance (100% yield, 30% ee in many cases), however controlling the Cd:Pt ratio led to a flip in enantioselectivity. The fundamentals of this study provide a clear indication that enantioselective hydrogenation through surface modification is possible and should be pursued in future work, but the paper itself draws much scepticism due to poor characterisation of Pt sites (Pt dispersion levels drawn from TEM exclusively) and expression of product yields with no written identification of product identity, *i.e.* 1-ethoxy-1-hydroxy-propan-2-one versus 2-hydroxy-propionic acid ethyl ester and/or (R)/(S) enantiomers of either product. Surface functionalization provides an

effective route to enhancing and controlling product selectivity; Guo *et al* confine Pt nanoclusters (1.7 nm) within cavities of a metal-organic framework, thus applying the aforementioned steric principles to pre-formed support architectures.<sup>102</sup> To confirm successful internal Pt confinement, the authors compared external versus internal CinnALD hydrogenation catalytic performance of said nanoparticles highlighting dramatically increased conversion (99%) and unsaturated alcohol selectivity (92%) for confined Pt nanoparticles; with high recyclability. This study is interesting due to the level of catalytic enhancement afforded by this method. In previous literature studies, it has been established that small Pt nanoparticles systematically exhibit poor selectivity towards any product with high levels of unsaturation, due an elevated surface population of unselective, coordinatively unsaturated facets. This dramatic promotion in unsaturated alcohol selectivity was credited to strict control of CinnALD adsorption geometry to Pt sites in a C=O centric atop fashion, lowering Pt-C=C group exposure – preserving  $\alpha$ ,  $\beta$ -unsaturation, even in the presence of such facets.

These studies explain the importance of controlled substrate adsorption geometry and Pt facet population on final product selectivity. Tuning size and support physicochemical properties could provide beneficial improvements in product dictation, without the need for complex synthetic pre-formation of shaped Pt nanoparticles or post-modification with potentially Pt active site deactivating surface additives (*i.e.* thiols).

### 1.1.3 Deactivation

Regardless of reaction type, the deactivation of heterogeneous catalysts can be divided into five categories.<sup>103,104,28</sup>

- 1) Poisoning via chemisorbed by-products on catalyst surface (*typically CO*);
- 2) Coking of active site/support by carbonaceous species;
- 3) Chemical transformation of active species (*i.e. reduction of PtO<sub>2</sub> to Pt<sup>(0)</sup>*);
- 4) Nanoparticle sintering or mechanical degradation (**Figure 1.5**);
- 5) Active species migration via in-solution leaching;

The mechanism of catalyst poisoning has been postulated as a three-fold process and can be classed as thermal, mechanical and chemical processes. Reaction conditions often dictate the type and rate of deactivation phenomena, with types 1-3 widely reported for chemoselective hydrogen transfer and dehydrogenation reactions.

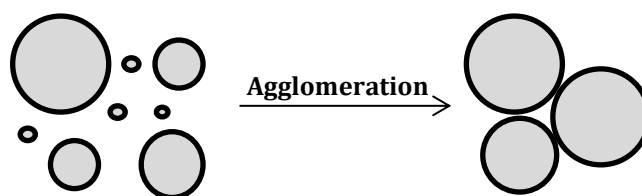


**Figure 1.5 – Nanoparticle sintering – Loss of uniform, discrete particles in favour of larger agglomerated masses**

Until very recently, the nature of the active site for Pt-based liquid phase alcohol selenol had been disputed. Where a metallic site has been postulated, deactivation can be attributed to the over-oxidation of the catalyst surface. The level of oxygen coverage has two effects; poisoning by physical blocking of adsorption sites, thus limiting substrate conversion, or inducing electronic and/or geometric changes in surface structure.<sup>105,106</sup> Where an oxidic basis for the active site is theorised, metal oxide stability determines catalytic behaviour and rate of poisoning.<sup>107,108,109</sup> Synchrotron studies of heterogeneous PdO systems, performed by Lee et al, have established that in circumstances where oxygen is absent, reduction of PdO to metallic Pd occurs.<sup>27,110</sup> Promotion of decarbonylation pathways has been postulated, due to the promotion of carbon-coking over the metallic surface. This has found to be in direct correlation with Pt-based catalysts, where preferential carbon coverage over Pt (111) facets hinders catalyst performance lifetime.<sup>20,111</sup> Selective poisoning of catalyst active sites is often overcome by pre-reduction treatments, prior to recycling, however changes in active sites through irreversible poisoning phenomena, such as deposition of carbonaceous deposits, does provide additional considerations when tailoring catalyst suitability. Sintering and leaching of the active species are not predominant for the principal reactions covered in this thesis, due to the utilisation of organic solvents and temperatures lower than 373K.<sup>42,112,113,114</sup> However, leaching tests were performed as confirmation.

### 1.1.4 Supports

Issues with catalyst recovery and active site stability plague the use of homogeneous catalysts, hindering viability in commercial and industrial environments.<sup>25</sup> The deposition of catalyst precursor onto solid supports has been suggested as an alternative. Implementation of post-reduction and/or oxidation treatments afford *in-situ* generation of specific active sites whilst maintaining variable facet control, without the need for auxiliaries and ligand stabilisation, and most beneficially straightforward catalyst recovery can all be achieved. The most commonly exploited support materials are carbonaceous, silica, alumina, titania and

ceria species, artificial incorporation of mesoporous networks and surface area enhancements allow for further customisation.<sup>115,116,117</sup> Strict control of synthesis and preparation parameters can be applied, tuning the chemical and physical properties of each support material. Surface area, morphology and inherent porosity (*i.e.* mesoporous and ordered architectures) all play a pivotal role in dictating active site dispersion, nanoparticle size and substrate diffusion kinetics.<sup>118,119,120</sup> The introduction of acid/base or metal support interaction properties, in tandem with the above provides additional versatility.<sup>88,121</sup> Desired selectivity and reaction kinetics can be targeted via knowledge of support behaviour, allowing for smart catalyst design.

### 1.1.4.1 Modification of support properties

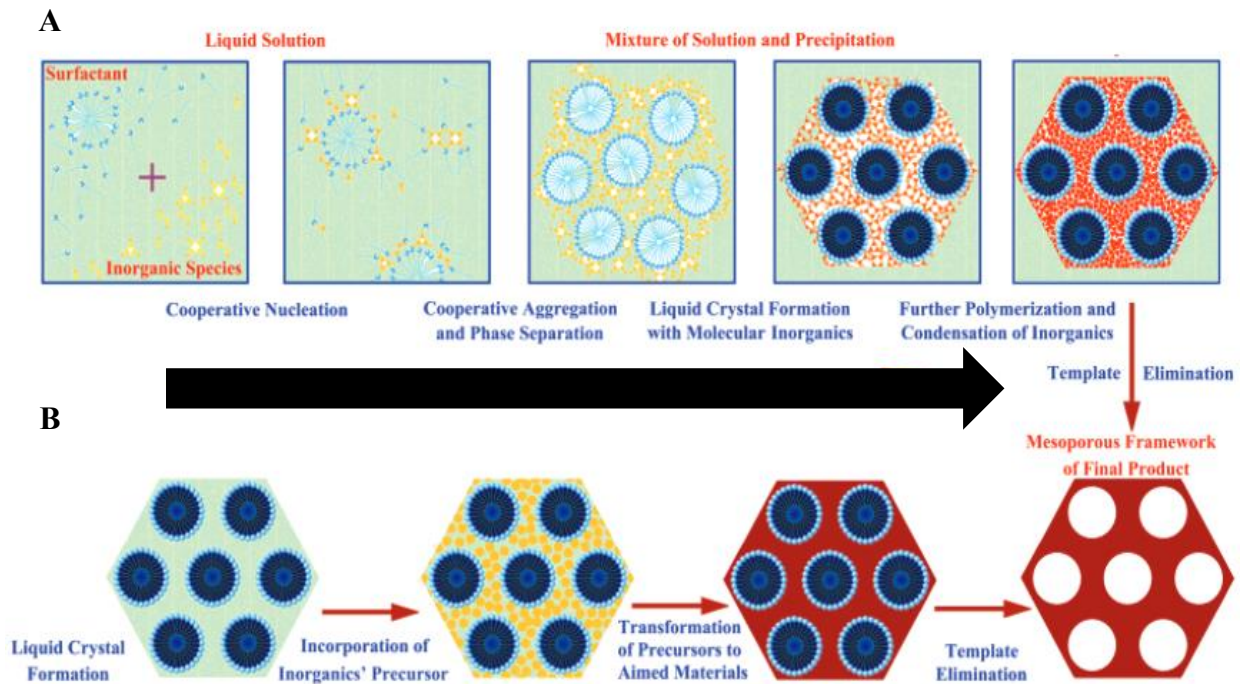
There are many synthetic avenues available to maximise active site dispersion and nanoparticle size control. Tailoring support surface area and internal porosity is most widely reported throughout many literature sources.<sup>122,123</sup> Three types of porosity have been identified; microporosity (pore diameters <2 nm), mesoporosity (pore diameters between 2-50 nm) and macroporosity (pore diameters >50 nm). Studies tend to shy away from microporous materials due to relatively small pore sizes, and hence significantly diminished internal substrate-product diffusion characteristics exhibited.<sup>124,125</sup> On the other hand, macroporosity completely overcomes this problem, at the expense of lowered surface areas and active site dispersion.<sup>126</sup> The utilisation of templated mesoporous and dual macro-mesoporous systems has been suggested as a viable alternative to surface area vs. pore size disputes. The choice of surfactant type and preparation parameters promotes the regulation of pore size and tuneable fabrication of interpenetrating and non-interpenetrating ordered and disordered architectures.<sup>127,128</sup> Channel interconnectivity (*i.e.* KIT-6) has been shown to encourage *in-situ* mass transfer kinetics,<sup>47</sup> whilst enhancing metal dispersion<sup>109</sup> and reducing sintering phenomena,<sup>129</sup> with respect to non-interconnected systems. Controlling product selectivity through size-specific, directed substrate diffusion is achievable through the interplay of narrow micro-mesopores. However, mass transfer effects and increased probability of channel blockage hinder reaction rates.<sup>130,131</sup>

#### 1.1.4.1.1 Ordered mesoporous silica

The arrival of the M41S family of mesoporous silicas and aluminosilicates in the early 1990's was heralded as a breakthrough in heterogeneous catalyst support design.

Synthesis protocols using templating species opened the door for tunable pore architectures, long-range ordering and surface area adaptation with an extraordinary degree of reproducibility.<sup>132,133</sup> Owing to the versatility of this protocol, a multitude of new mesoporous silicates have been reported and reviewed by Corma,<sup>127,130</sup> Schuth<sup>134</sup> and Slowing,<sup>135</sup> with applications ranging from nanoparticle support to carriers for directed drug transport. SBA-derived materials are widely reported as ideal support manifolds,<sup>136,137</sup> with emphasised importance placed on their tuneable internal structure, high surface areas and chemical/thermal stability. Subtle adaptations to synthesis conditions permits dictation of resultant pore architectures; the expression of 2D non-interconnected hexagonal  $P6mm$  (SBA-15) and 3D interconnected internal channels  $Im3m$  (SBA-16) and  $Ia3d$  (KIT-6) have been established.<sup>138,139</sup> The additional functionality, inherent to a flexible internal pore structure, coupled with chemical inertness of silica-based supports,<sup>140</sup> provides the basis for an accurate determination of support physical characteristics on catalytic performance, in the absence of induced support-metal interactions<sup>141</sup> or support reduction.

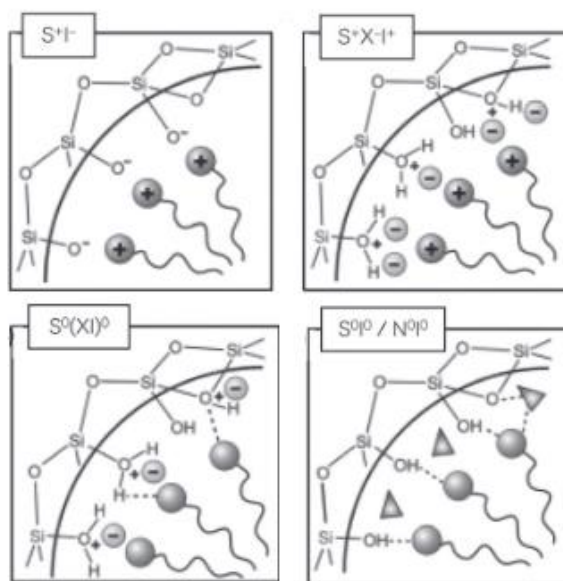
In order to successfully synthesise hierarchical silica materials, the presence of structural directing agents are key as promoters for the initial formation and stabilisation of the silica mesophase. Dependant on the required architecture and support properties, a choice of neutral, anionic and cationic surfactants are available. Cationic surfactants exhibit excellent solubility and stability in preparations employing acidic or basic media; however expense and toxicity limit their wide-scale application. Examples of carboxylate, sulfate and phosphate-derived anionic surfactants have been used to synthesise mesoporous silicas, in the presence of “*co-structure-directing agents*,” typically aminosilanes. The low price, lack of toxicity and inherent biodegradability of non-ionic surfactants have attracted considerable interest from industry. Tailoring non-ionic surfactant functionality affords the formation of adaptable mesophases, *via self-assembly*, leading to bespoke support geometries and assemblies.<sup>142</sup> Formation of surfactant micelles, driven by entropic effects, is promoted by the elimination of “*water of crystallisation*” situated around each surfactant molecule. This results in the formation of a mesophase, this mechanism is accepted as cooperative self-assembly due to its prevalence as low as 5% surfactant concentration (Represented in **Scheme 1**).<sup>130</sup> Stability can be augmented further by hydrogen-bonding and ionic interactions between surfactant micelles, *as-formed* silica and silicate precursors. Surfactant type and pH can be adapted to dictate internal fine structure.



**Scheme 1** – Representation of SBA-15 mesoporous framework formation via (A) Cooperative self-assembly and (B) “True” liquid-crystal templating (TLCT) methodologies (Adapted from reference 142)

There are four common types of silicate – surfactant head group interactions described in the literature for hierarchical silica generation<sup>143, 144</sup>:

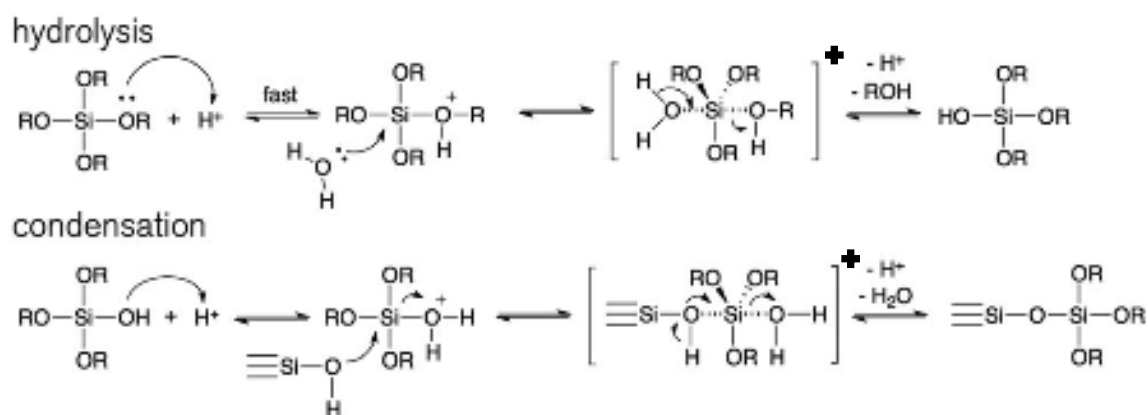
- 1) Electrostatic - Ionic surfactant (S) and silicate (I) with opposite charge e.g.  $S^+I^-$
- 2) Electrostatic - Ionic surfactant and silicate with matching charge in the presence of a counter-ion (X) such as sulphate, nitrate or halogen e.g.  $S^+X^-I^+$
- 3) Electrostatic – Non-ionic surfactant, silicate and acid e.g.  $S^0H^+X^-I^+$
- 4) Hydrogen Bonding – Non-ionic surfactant and hydrated silicate e.g.  $S^0I^0$



**Scheme 2** – Visual representation of the interactions between sol-gel species and the surfactant template in various media (acidic/neutral) (Adapted from reference 143)

As the mesophase begins to take shape, silica polymerisation occurs at the interface (**Scheme 3**), as micellar systems agglomerate, thus leading to fabrication and self-assembly of a mesoporous architecture.<sup>145,146</sup> Following this stage, the silica mesophase undergoes precipitation from solution; further polymerisation across the interface promotes the condensation of silicate agglomerates, resulting in the fabrication of the silica walls. The application of polar, protic solvents with heightened volatility (*i.e. EtOH, MeOH etc.*) permits strict control of polymerisation rates and surfactant assembly at the interface.<sup>142</sup> Solvent evaporation creates an artificially increased local surfactant concentration, further polymerisation of inorganic species ensues improving stability of the precipitated silica phase, and aiding truly liquid crystalline phase construction.





**Scheme 3** – The  $S_N2$  mechanism of hydrolysis and condensation of alkoxy silane precursors to form silica in acid-catalysed conditions

The choice of structural directing agent can heavily impact micelle formation and adopted geometry, and in turn mesopore properties can be tuned according to desired characteristics. In using non-ionic tri-block copolymers, the ratio of hydrophilic to hydrophobic groups is critical for controlling pore shape and ultimately pore architecture. As the phase diagrams for these systems are well-known, surfactant effects are easily tunable as demonstrated by the synthetic methodologies employed in SBA-15/16 and KIT-6 syntheses.<sup>147</sup> Increasing said ratio to favour hydrophilic domains, encourages the formation of spherical surfactant micelles. Lower ratios institute less curved geometries, with disk-shaped structures assembling to form rods. Adjusting this ratio and contemplating surfactant packing phenomena provides the basis for SBA-15 and SBA-16 preparations.<sup>147</sup> In the formation of SBA-15 by a tri-block copolymer P123 ( $EO_{20}PO_{70}EO_{20}$ ), Khodakov *et al* proposed the initial formation of a micellar disk-shaped structure with a hydrophobic PPO core and a PEO-water-silicate corona (*or edge*). Subsequent packing of these cylindrical micelles into extended rod structures provides the foundation for the characteristic structure of SBA-15.<sup>148</sup>

Although the choice of surfactant demonstrates a pivotal role in the dictation of support mesostructure and porosity, altering hydrothermal treatment parameters and the presence of certain additives, *i.e.* *n*-butanol in KIT-6 synthesis, permit added levels of structural control. Microporosity has been postulated to originate from substantial interactions between the silica framework and the more hydrophilic ethylene oxide regions (EO) of the utilised tri-block copolymer, leading to interconnectivity between mesopores (especially in SBA-15).<sup>149</sup> Altering of hydrothermal temperature and duration can lead to

tailoring of pore size. For example, in the synthesis of SBA-15, increasing treatment temperature causes an increased hydrophobicity in the PEO regions of the Pluronic P123 copolymer, thus causing a subsequent withdrawal from the silicate walls.<sup>150</sup> As cross-linkage and silicate hydrolysis continues well into the hydrothermal stage, an increased hydrothermal temperature leads to larger surfactant micelles – resulting in larger pore SBA-15 with thin walls and diminished microporosity.<sup>149, 151</sup> Kim *et al* report a similar effect for mesoporous, body-centered cubic SBA-16 silicates; in which increasing the hydrothermal treatment parameters from 45°C and 1 day to 100°C and 2 days also yielded larger mesopores, decreased mesopore wall thickness and microporosity.<sup>138</sup> Two explanations have been given for the loss of microporosity with increasing hydrothermal temperature. Firstly, dehydration<sup>152</sup> or deprotonation<sup>150</sup> of the ethylene oxide moieties decreases their hydrophilic character leading to diminished interaction at the inorganic interface. Secondly, induced swelling of the micropores into the mesopore domain, through higher hydrothermal temperatures, permits decreased accuracy in microporosity detection through t-plot calculations etc.<sup>149</sup> Altering the synthesis protocols used for SBA-15 generation, Ryoo and co-workers show the addition of *n*-butanol and low acidic concentration (0.5 M HCl) produces a drastic change in the adopted interfacial curvature of tri-block copolymer P123 micelles and slows the rate of inorganic condensation; leading to the formation of the interpenetrating bicontinuous 3D cubic mesostructure of KIT-6 (a phase transition from *P6mm* to *Ia3d*).<sup>138, 153</sup>

Two alternatives to the cooperative assembly mechanism for mesostructured silica generation are: (1) True liquid crystal templating (TLCT)<sup>154</sup> and (2) Evaporation induced self-assembly (EISA).<sup>155</sup> Typically, in TLCT strategies a significantly elevated surfactant concentration (~50 %) is used, resulting in favourable lyotropic liquid phase formation (formation of hexagonal long-range order for P123 upon solvent addition), providing a platform for which silica can be templated and mesostructure generated.<sup>155</sup> EISA is commonly used to form films and membranes and can be applied to materials other than silica, *i.e.* titania,<sup>156</sup> in instances where the rate of inorganic precursor hydrolysis must be slow and strictly controlled. The production of inorganic oligomers is controlled by directed polymerisation in a volatile polar protic solvent (such as MeOH), improving inorganic assembly at the surfactant interface.<sup>142, 147</sup> Subsequent solvent evaporation permits continued inorganic species polymerisation combined with further liquid crystalline phase formation, as

local surfactant concentration increases with solvent loss, allowing greater templating to occur.

Upon completion, removal of the structure directing template is commonly achieved by calcination,<sup>137, 157</sup> owing to the relatively high thermal stability of the final mesostructured silica.<sup>137</sup> In order to avoid localised overheating within the material, slow heating ramp rates are required. Calcination treatments between 500-550 °C are used to completely remove the surfactant, whilst maintaining support structure integrity. Surfactant template extraction can also be accomplished through solvent extraction in organic solvents such as ethanol or toluene; however complete removal of the tri-block copolymer is not always possible, with approximately a residual 4% post-treatment.<sup>158, 159</sup> Yang et al report that directed decomposition of the surfactant template can also be achieved through stepwise treatment with concentrated H<sub>2</sub>SO<sub>4</sub> and subsequent calcination at 200°C, generating mesoporosity and micropores respectively.<sup>160</sup>

## 1.2 Thesis aims

The aims of this investigation are:

- To investigate the influence of silica hierarchical support structure on the final physiochemical properties of supported Pt nanoparticles; highlighting any effect brought about by the introduction of mesoporous architectures to said supports.
- To identify the principle catalytic behaviour of these materials in the selective transformation of  $\alpha$ ,  $\beta$ -unsaturated substrates for oxidation and hydrogenation reaction schemes. Establishing the adopted reaction mechanism and active species for each catalytic transformation is critical, whilst determining the cause of catalyst deactivation phenomena.

## 1.3 References

1. J. Cocchiara, C. S. Letizia, J. Lalko, A. Lapczynski and A. M. Api, *Food Chem Toxicol*, 2005, 43, 867-923.
2. S.-S. Cheng, J.-Y. Liu, K.-H. Tsai, W.-J. Chen and S.-T. Chang, *Journal of Agricultural and Food Chemistry*, 2004, 52, 4395-4400.
3. N. Mizuno, *Modern Heterogeneous Oxidation Catalysis*, Wiley, 2009.
4. P. V. Prabhakaran, S. Venkatachalam and K. N. Ninan, *European Polymer Journal*, 1999, 35, 1743-1746.
5. J. H. Clark, *Green Chemistry*, 1999, 1, 1-8.
6. I. Hermans, E. Spier, U. Neuenschwander, N. Turrà and A. Baiker, *Topics in Catalysis*, 2009, 52, 1162-1174.
7. C. P. Vinod, K. Wilson and A. F. Lee, *Journal of Chemical Technology & Biotechnology*, 2011, 86, 161-171.
8. P. Sautet and F. Delbecq, *Journal of Catalysis*, 1995, 152.
9. P. G. N. Mertens, J. Wahlen, X. Ye, H. Poelman and D. E. Vos, *Catal Lett*, 2007, 118, 15-21.
10. P. Atkins and J. de Paula, *Elements of Physical Chemistry*, Macmillan, 2009.
11. M. Bowker, *The basis and applications of heterogeneous catalysis*, Oxford University Press New York, 1998.
12. P. B. Venuto and E. T. J. Habib, *Fluid catalytic cracking with zeolite catalysts*, 1979.
13. W. Cabri and I. Candiani, *Accounts of chemical research*, 1995, 28, 2-7.
14. J. Groves, *Chemical Society Reviews*, 1972, 1, 73-97.
15. K. C. Taylor, *Catalysis Reviews—Science and Engineering*, 1993, 35, 457-481.
16. J. Kašpar, P. Fornasiero and N. Hickey, *Catalysis Today*, 2003, 77, 419-449.
17. D. Enders, H. Wahl and W. Bettray, *Angewandte Chemie International Edition in English*, 1995, 34, 455-457.
18. K. Borszky, T. Mallat and A. Baiker, *Tetrahedron: Asymmetry*, 1997, 8, 3745-3753.
19. X. Wang, L. Shi, M. Li and K. Ding, *Angewandte Chemie International Edition*, 2005, 44, 6362-6366.
20. P. Gallezot and D. Richard, *Catalysis Reviews*, 1998, 40, 81-126.
21. V. Ponec, *Applied Catalysis A: General*, 1997, 149, 27-48.
22. E. Fache, C. Mercier, N. Pagnier, B. Despeyroux and P. Panster, *Journal of molecular catalysis*, 1993, 79, 117-131.
23. M. Bandini, A. Melloni and A. Umani-Ronchi, *Angewandte Chemie International Edition*, 2004, 43, 550-556.
24. J. M. Grill, J. W. Ogle and S. A. Miller, *The Journal of Organic Chemistry*, 2006, 71, 9291-9296.
25. D. J. Cole-Hamilton, *Science*, 2003, 299, 1702-1706.
26. D. Astruc, F. Lu and J. R. Aranzaes, *Angewandte Chemie International Edition*, 2005, 44, 7852-7872.
27. A. F. Lee, C. V. Ellis, J. N. Naughton, M. A. Newton, C. M. Parlett and K. Wilson, *J Am Chem Soc*, 2011, 133, 5724-5727.
28. C. H. Bartholomew, *Applied Catalysis A: General*, 2001, 212, 17-60.
29. A. I. Frenkel, J. A. Rodriguez and J. G. Chen, *ACS Catalysis*, 2012, 2, 2269-2280.
30. M. Chen, N. Maeda, A. Baiker and J. Huang, *ACS Catalysis*, 2012, 2, 2007-2013.
31. X.-M. Cao, R. Burch, C. Hardacre and P. Hu, *The Journal of Physical Chemistry C*, 2011, 115, 19819-19827.
32. S. Jung, K. L. Shuford and S. Park, *The Journal of Physical Chemistry C*, 2011, 115, 19049-19053.
33. D. E. Ramaker and D. C. Koningsberger, *Phys Chem Chem Phys*, 2010, 12, 5514-5534.
34. A. F. Lee, *Australian Journal of Chemistry*, 2012, 65, 615.

35. Q. Jia, E. A. Lewis, C. Grice, E. S. Smotkin and C. U. Segre, *Journal of Physics: Conference Series*, 2009, 190, 012157.
36. G. A. Somorjai and C. Aliaga, *Langmuir*, 2010, 26, 16190-16203.
37. I. T. Horváth and P. T. Anastas, *Chemical reviews*, 2007, 107, 2169-2173.
38. P. Gallezot, *Chemical Society Reviews*, 2012, 41, 1538-1558.
39. K. P. Peterson and R. C. Larock, *The Journal of Organic Chemistry*, 1998, 63, 3185-3189.
40. C. M. A. Parlett, P. Keshwalla, S. G. Wainwright, D. W. Bruce, N. S. Hondow, K. Wilson and A. F. Lee, *ACS Catalysis*, 2013, 3, 2122-2129.
41. S. E. Davis, M. S. Ide and R. J. Davis, *Green Chemistry*, 2013, DOI: 10.1039/c2gc36441g.
42. T. Mallat and A. Baiker, *Chemical Reviews*, 2004, 104, 3037-3058.
43. T. Mallat and A. Baiker, *Catalysis Today*, 1995, 24, 143-150.
44. C. Keresszegi, T. Burgi, T. Mallat and A. Baiker, *Journal of Catalysis*, 2002, 211, 244-251.
45. G. Kyriakou, S. K. Beaumont and R. M. Lambert, *Langmuir*, 2011, 27, 9687-9695.
46. E. Gómez-Bengoá, P. Noheda and A. M. Echavarren, *Tetrahedron Letters*, 1994, 35, 7097-7098.
47. C. M. A. Parlett, D. W. Bruce, N. S. Hondow, M. A. Newton, A. F. Lee and K. Wilson, *ChemCatChem*, 2012, DOI: 10.1002/cctc.201200301, n/a-n/a.
48. A. Köckritz, M. Sebek, A. Dittmar, J. Radnik, A. Brückner, U. Bentrup, M. M. Pohl, H. Hugl and W. Mägerlein, *Journal of Molecular Catalysis A: Chemical*, 2006, 246, 85-99.
49. H. Ji and K. Kaneda, *Tetrahedron Letters*, 2002, 43.
50. K. Yamaguchi and N. Mizuno, *Angewandte Chemie International Edition*, 2002, 41, 4538-4542.
51. T. Matsushita, K. Ebitani and K. Kaneda, *Chemical Communications*, 1999, DOI: 10.1039/A809082C, 265-266.
52. G. J. Hutchings, *Chemical Communications*, 2008, DOI: 10.1039/B712305C, 1148-1164.
53. G. Schmid and B. Corain, *European Journal of Inorganic Chemistry*, 2003, 2003, 3081-3098.
54. S. E. Davis, B. N. Zope and R. J. Davis, *Green Chemistry*, 2012, 14, 143.
55. J. J. Bozell and G. R. Petersen, *Green Chemistry*, 2010, 12, 539-554.
56. J. A. Lopez-Sanchez, N. Dimitratos, N. Glanville, L. Kesavan, C. Hammond, J. K. Edwards, A. F. Carley, C. J. Kiely and G. J. Hutchings, *Applied Catalysis A: General*, 2011, 391, 400-406.
57. N. Dimitratos, A. Villa, D. Wang, F. Porta, D. Su and L. Prati, *Journal of Catalysis*, 2006, 244, 113-121.
58. A. F. Lee and K. Wilson, *Green Chemistry*, 2004, 6, 37.
59. T. Mallat, Z. Bodnar, P. Hug and A. Baiker, *Journal of Catalysis*, 1995, 153, 131-143.
60. M. Caravati, D. M. Meier, J.-D. Grunwaldt and A. Baiker, *Journal of Catalysis*, 2006, 240, 126-136.
61. T. Wang, C.-X. Xiao, L. Yan, L. Xu, J. Luo, H. Shou, Y. Kou and H. Liu, *Chemical Communications*, 2007, DOI: 10.1039/B710845A, 4375-4377.
62. T. Mallat and A. Baiker, *Catalysis Today*, 1994, 19, 247-283.
63. I. V. Delidovich, O. P. Taran, L. G. Matvienko, A. N. Simonov, I. L. Simakova, A. N. Bobrovskaya and V. N. Parmon, *Catal Lett*, 2010, 140, 14-21.
64. A. Abbadi and H. Van Bekkum, *Journal of Molecular Catalysis A: Chemical*, 1995, 97, 111-118.
65. D. Ferri and A. Baiker, *Topics in Catalysis*, 2009, 52, 1323-1333.
66. A. Biffis and L. Minati, *Journal of Catalysis*, 2005, 236, 405-409.
67. N. Hoffman and T. Puthenpurackal, *J. Org. Chem.*, 1962, 27.
68. G. A. Somorjai and J. Y. Park, *Angewandte Chemie International Edition*, 2008, 47, 9212-9228.
69. T. Yasu-eda, R. Se-ike, N.-o. Ikenaga, T. Miyake and T. Suzuki, *Journal of Molecular Catalysis A: Chemical*, 2009, 306, 136-142.
70. I. Fecheté, Y. Wang and J. C. Védrine, *Catalysis Today*, 2012, 189, 2-27.
71. I. K. Kapdan and F. Kargi, *Enzyme and Microbial Technology*, 2006, 38, 569-582.

72. J. A. Turner, *Science*, 2004, 305, 972-974.
73. M. Ni, M. K. Leung, D. Y. Leung and K. Sumathy, *Renewable and Sustainable Energy Reviews*, 2007, 11, 401-425.
74. V. V. Zhivonitko, K. V. Kovtunov, I. E. Beck, A. B. Ayupov, V. I. Bukhtiyarov and I. V. Koptug, *The Journal of Physical Chemistry C*, 2011, 115, 13386-13391.
75. I. Lee, F. Delbecq, R. Morales, M. A. Albitzer and F. Zaera, *Nature materials*, 2009, 8, 132-138.
76. G. Attard, J. Bennett, I. Mikheenko, P. Jenkins, S. Guan, L. Macaskie, J. Wood and A. Wain, *Faraday discussions*, 2013, 162, 57-75.
77. D. Kennedy, G. Webb, S. Jackson and D. Lennon, *Applied Catalysis A: General*, 2004, 259, 109-120.
78. C. Poupin, R. Maache, L. Pirault-Roy, R. Brahmi and C. Williams, *Applied Catalysis A: General*, 2014, 475, 363-370.
79. K. An, N. Musselwhite, G. Kennedy, V. V. Pushkarev, L. Robert Baker and G. A. Somorjai, *Journal of Colloid and Interface Science*, 2013, 392, 122-128.
80. P. Lara, A. Suárez, V. Collière, K. Philippot and B. Chaudret, *ChemCatChem*, 2014, 6, 87-90.
81. P. Claus, *Topics in Catalysis*, 1998, 5.
82. H. Öfner and F. Zaera, *The Journal of Physical Chemistry B*, 1997, 101, 396-408.
83. F. Zaera, *Catal Lett*, 2003, 91, 1-10.
84. S. C. Tsang, N. Cailuo, W. Oduro, A. T. S. Kong, L. Clifton, K. M. K. Yu, B. Thiebaut, J. Cookson and P. Bishop, *ACS Nano*, 2008, 2, 2547-2553.
85. W. O. Oduro, N. Cailuo, K. M. Yu, H. Yang and S. C. Tsang, *Phys Chem Chem Phys*, 2011, 13, 2590-2602.
86. A. Silva, E. Jordao and P. Fouilloux, *Applied Catalysis A: General*, 1997, 148.
87. R. Zheng, M. D. Porosoff, J. L. Weiner, S. Lu, Y. Zhu and J. G. Chen, *Applied Catalysis A: General*, 2012, 419-420, 126-132.
88. M. Abid, V. Paul-Boncour and R. Touroude, *Applied Catalysis A: General*, 2006, 297, 48-59.
89. L. Ono, B. Yuan, H. Heinrich and B. R. Cuenya, *The Journal of Physical Chemistry C*, 2010, 114, 22119-22133.
90. L. R. Baker, G. Kennedy, M. Van Spronsen, A. Hervier, X. Cai, S. Chen, L.-W. Wang and G. A. Somorjai, *Journal of the American Chemical Society*, 2012, 134, 14208-14216.
91. D. Goodman, *Catal Lett*, 2005, 99, 1-4.
92. A. Bruix, J. A. Rodriguez, P. J. Ramírez, S. D. Senanayake, J. Evans, J. B. Park, D. Stacchiola, P. Liu, J. Hrbek and F. Illas, *Journal of the American Chemical Society*, 2012, 134, 8968-8974.
93. S. Tauster, *Accounts of Chemical Research*, 1987, 20, 389-394.
94. B. C. Beard and P. N. Ross, *The Journal of Physical Chemistry*, 1986, 90, 6811-6817.
95. Y. Zhu and F. Zaera, *Catalysis Science & Technology*, 2014, 4, 955-962.
96. A. J. Urquhart, F. J. Williams, O. P. Vaughan, R. L. Cropley and R. M. Lambert, *Chem Commun (Camb)*, 2005, DOI: 10.1039/b500590f, 1977-1979.
97. J. C. de Jesús and F. Zaera, *Surface science*, 1999, 430, 99-115.
98. F. Delbecq and P. Sautet, *Journal of Catalysis*, 2002, 211, 398-406.
99. K. R. Kahsar, D. K. Schwartz and J. W. Medlin, *Journal of the American Chemical Society*, 2013, 136, 520-526.
100. K. R. Kahsar, S. Johnson, D. K. Schwartz and J. W. Medlin, *Topics in Catalysis*, 1-7.
101. J. Hong, I. Lee and F. Zaera, *Catalysis Science & Technology*, 2015, DOI: 10.1039/C4CY00844H.
102. Z. Guo, C. Xiao, R. V. Maligal-Ganesh, L. Zhou, T. W. Goh, X. Li, D. Tesfagaber, A. Thiel and W. Huang, *ACS Catalysis*, 2014, DOI: 10.1021/cs400982n, 1340-1348.
103. M. Besson and P. Gallezot, *Catalysis Today*, 2000, 57, 127-141.
104. A. P. Markusse, B. F. M. Kuster, D. C. Koningsberger and G. B. Marin, *Catal Lett*, 1998, 55.
105. T. Mallat, A. Baiker and L. Botz, *Applied catalysis A: General*, 1992, 86, 147-163.
106. K. Van der Wiele, *Journal of Catalysis*, 1988, 112.

107. C. Keresszegi, *Journal of Catalysis*, 2004, 225, 138-146.
108. A. F. Lee, Z. Chang, P. Ellis, S. F. Hackett and K. Wilson, *The Journal of Physical Chemistry C*, 2007, 111, 18844-18847.
109. L. Durndell, C. M. Parlett, N. S. Hondow, K. Wilson and A. F. Lee, *Nanoscale*, 2013.
110. C. M. A. Parlett, D. W. Bruce, N. S. Hondow, A. F. Lee and K. Wilson, *ACS Catalysis*, 2011, 1, 636-640.
111. V. Fouche, P. Magnoux and M. Guisnet, *Applied catalysis*, 1990, 58, 189-198.
112. A. Abad and H. Garcia, *Angewandte Chemie*, 2005, 44.
113. Y. Dai, B. Lim, Y. Yang, C. M. Cobley, W. Li, E. C. Cho, B. Grayson, P. T. Fanson, C. T. Campbell, Y. Sun and Y. Xia, *Angewandte Chemie*, 2010, 122, 8341-8344.
114. B. Li, W.-Z. Weng, Q. Zhang, Z.-W. Wang and H.-L. Wan, *ChemCatChem*, 2011, 3, 1277-1280.
115. R. J. White, R. Luque, V. L. Budarin, J. H. Clark and D. J. Macquarrie, *Chemical Society Reviews*, 2009, 38, 481-494.
116. P. Van Der Voort, C. Vercaemst, D. Schaubroeck and F. Verpoort, *Phys Chem Chem Phys*, 2008, 10, 347-360.
117. P. Serp, *Applied Catalysis A: General*, 2003, 253, 337-358.
118. C. M. A. Parlett, L. J. Durndell, K. Wilson, D. W. Bruce, N. S. Hondow and A. F. Lee, *Catalysis Communications*, DOI: <http://dx.doi.org/10.1016/j.catcom.2013.07.005>.
119. S. Chytil, W. R. Glomm, E. Vollebakk, H. Bergem, J. Walmsley, J. Sjöblom and E. A. Blekkan, *Microporous and Mesoporous Materials*, 2005, 86, 198-206.
120. S.-H. Liu, R.-F. Lu, S.-J. Huang, A.-Y. Lo, S.-H. Chien and S.-B. Liu, *Chemical communications*, 2006, 3435-3437.
121. J. C. Vedrine, *Topics in catalysis*, 2002, 21, 97-106.
122. M. E. Davis, *Nature*, 2002, 417, 813-821.
123. M. Grün, K. K. Unger, A. Matsumoto and K. Tsutsumi, *Microporous and Mesoporous Materials*, 1999, 27, 207-216.
124. R. Hurt, A. Sarofim and J. Longwell, *Energy & fuels*, 1991, 5, 290-299.
125. J. H. Clark and D. J. Macquarrie, *Chemical Society Reviews*, 1996, 25, 303-310.
126. P. M. Price, J. H. Clark and D. J. Macquarrie, *Journal of the Chemical Society, Dalton Transactions*, 2000, 101-110.
127. A. Corma, *Topics in Catalysis*, 1997, 4, 249-260.
128. V. Meynen, P. Cool and E. Vansant, *Microporous and Mesoporous Materials*, 2009, 125, 170-223.
129. H. I. Lee, S. H. Joo, J. H. Kim, D. J. You, J. M. Kim, J.-N. Park, H. Chang and C. Pak, *Journal of Materials Chemistry*, 2009, 19, 5934-5939.
130. A. Corma, *Chemical reviews*, 1997, 97, 2373-2420.
131. I. Hoek, T. Nijhuis, A. Stankiewicz and J. Moulijn, *Chemical engineering science*, 2004, 59, 4975-4981.
132. J. Beck, J. Vartuli, W. Roth, M. Leonowicz, C. Kresge, K. Schmitt, C. Chu, D. Olson and E. Sheppard, *Journal of the American Chemical Society*, 1992, 114, 10834-10843.
133. C. Kresge, M. Leonowicz, W. Roth, J. Vartuli and J. Beck, *nature*, 1992, 359, 710-712.
134. F. Schüth and W. Schmidt, *Advanced Materials*, 2002, 14, 629-638.
135. I. I. Slowing, J. L. Vivero-Escoto, C.-W. Wu and V. S.-Y. Lin, *Advanced drug delivery reviews*, 2008, 60, 1278-1288.
136. P. Yang, D. Zhao, D. I. Margolese, B. F. Chmelka and G. D. Stucky, *Chemistry of Materials*, 1999, 11, 2813-2826.
137. D. Zhao, Q. Huo, J. Feng, B. F. Chmelka and G. D. Stucky, *Journal of the American Chemical Society*, 1998, 120, 6024-6036.
138. T.-W. Kim, F. Kleitz, B. Paul and R. Ryoo, *Journal of the American Chemical Society*, 2005, 127, 7601-7610.
139. F. Kleitz, S. H. Choi and R. Ryoo, *Chemical Communications*, 2003, 2136-2137.

140. L. Gucci, A. Beck and Z. Pászti, *Catalysis Today*, 2012, 181, 26-32.
141. N. Tsubaki and K. Fujimoto, *Topics in Catalysis*, 2003, 22.
142. Y. Wan and D. Zhao, *Chemical reviews*, 2007, 107, 2821-2860.
143. J. Y. Ying, C. P. Mehnert and M. S. Wong, *Angewandte Chemie International Edition*, 1999, 38, 56-77.
144. J. E. Lofgreen and G. A. Ozin, *Chemical Society Reviews*, 2014, 43, 911-933.
145. K. Flodström, H. Wennerström and V. Alfredsson, *Langmuir*, 2004, 20, 680-688.
146. P. Linton and V. Alfredsson, *Chemistry of Materials*, 2008, 20, 2878-2880.
147. Y. Wan, Y. Shi and D. Zhao, *Chemical Communications*, 2007, DOI: 10.1039/B610570J, 897-926.
148. A. Y. Khodakov, V. L. Zholobenko, M. Impérator-Clerc and D. Durand, *The Journal of Physical Chemistry B*, 2005, 109, 22780-22790.
149. A. Galarneau, H. Cambon, F. Di Renzo, R. Ryoo, M. Choi and F. Fajula, *New journal of Chemistry*, 2003, 27, 73-79.
150. A. Galarneau, H. Cambon, F. Di Renzo and F. Fajula, *Langmuir*, 2001, 17, 8328-8335.
151. P. F. Fulvio, S. Pikus and M. Jaroniec, *Journal of Materials Chemistry*, 2005, 15, 5049-5053.
152. M. Kruk, M. Jaroniec, C. H. Ko and R. Ryoo, *Chemistry of materials*, 2000, 12, 1961-1968.
153. S. Ruthstein, J. Schmidt, E. Kesselman, R. Popovitz-Biro, L. Omer, V. Frydman, Y. Talmon and D. Goldfarb, *Chemistry of Materials*, 2008, 20, 2779-2792.
154. S. G. Wainwright, C. Parlett, R. A. Blackley, W. Zhou, A. F. Lee, K. Wilson and D. W. Bruce, *Microporous and Mesoporous Materials*, 2013, 172, 112-117.
155. G. Wanka, H. Hoffmann and W. Ulbricht, *Macromolecules*, 1994, 27, 4145-4159.
156. I. Tamiolakis, I. N. Lykakis, A. P. Katsoulidis and G. S. Armatas, *Chemical Communications*, 2012, 48, 6687-6689.
157. J. S. Beck, J. C. Vartuli, W. J. Roth, M. E. Leonowicz, C. T. Kresge, K. D. Schmitt, C. T. W. Chu, D. H. Olson and E. W. Sheppard, *Journal of the American Chemical Society*, 1992, 114, 10834-10843.
158. R. Van Grieken, G. Calleja, G. D. Stucky, J. A. Melero, R. A. García and J. Iglesias, *Langmuir*, 2003, 19, 3966-3973.
159. C.-M. Yang, H.-A. Lin, B. Zibrowius, B. Spliethoff, F. Schüth, S.-C. Liou, M.-W. Chu and C.-H. Chen, *Chemistry of materials*, 2007, 19, 3205-3211.
160. C.-M. Yang, B. Zibrowius, W. Schmidt and F. Schüth, *Chemistry of Materials*, 2004, 16, 2918-2925.



## *Chapter 2*

### *Experimental*

## 2.1 Catalyst Preparation

### 2.1.1 Materials

Ammonium tetrachloroplatinate (II) and 3-phenylpropanoic acid were supplied by Alfa Aesar. Pluronic P123, Pluronic F127, tetraethyl orthosilicate, tetramethyl orthosilicate ethanol (absolute) and anisole were purchased from Sigma Aldrich. Cinnamaldehyde, hydrochloric acid (37.5 %) and nitric acid (37.5 %) were purchased from Fisher Scientific. All remaining reaction substrates and intermediates, required for GC calibration, were procured from Sigma Aldrich. Deionised water was utilised throughout.

### 2.1.2 SBA-15 synthesis

Mesoporous SBA-15 supports were synthesised using the method developed by G. D. Stucky and co-workers.<sup>1</sup> In this synthesis, the surfactant Pluronic P123 (20 g), used as a structural templating agent, was dissolved in deionised water (151 cm<sup>3</sup>) and hydrochloric acid (2M, 583 cm<sup>3</sup>) stirring at 35 °C. The silica precursor, tetraethyl orthosilicate (138.8 mmol, 28.92 g, 31 cm<sup>3</sup>) was added to the solution and left for 20 hours with agitation. The resulting gel was sealed and aged for 24 hours at 80 °C without agitation. The precipitate was filtered and washed with deionised water (1000 cm<sup>3</sup>) and dried at room temperature, before a calcination treatment at 500 °C for 6 hours in air (ramp rate 1°C min<sup>-1</sup>). A successful synthesis produces approximately 15.0 g of white solid.

### 2.1.3 SBA-16 synthesis

Mesoporous SBA-16 was successfully manufactured using the parameters clearly set out by Zhao et al.<sup>1</sup> An alternate structural directing agent, Pluronic F127, a reduced synthesis temperature and an increased hydrothermal treatment duration; are the only differences applied to the protocol utilised for SBA-15. Pluronic F127 (20g) was dissolved in deionised water (151 cm<sup>3</sup>) and hydrochloric acid (2M, 583 cm<sup>3</sup>) stirring at 25 °C. The silica precursor, tetraethyl orthosilicate (138.8 mmol, 28.92 g, 31 cm<sup>3</sup>) was added to the solution and left for 20 hours with agitation. The resulting gel was sealed and aged for 48 hours at 80 °C without agitation. The precipitate was filtered and washed with deionised water (1000 cm<sup>3</sup>) and dried at room temperature, before a calcination treatment at 500 °C for 6 hours in air (ramp rate 1°C min<sup>-1</sup>). A successful synthesis produces approximately 15.0 g of white solid.

### 2.1.4 KIT-6 synthesis

In order to correctly synthesise KIT-6, a protocol devised by Kim and co-workers was followed.<sup>2</sup> Pluronic P123 (20 g) was dissolved in deionised water (723.2 cm<sup>3</sup>), butan-1-ol (24.6 cm<sup>3</sup>) and hydrochloric acid (35%, 33.4 cm<sup>3</sup>) with stirring at 35 °C. Tetraethyl orthosilicate (139.7 mmol, 29.11 g, 31.2 cm<sup>3</sup>) was added to the solution and left for 20 hours with agitation. The resulting gel was sealed and aged for 24 hours at 80 °C without agitation. The precipitate was filtered and washed with deionised water (1000 cm<sup>3</sup>) and dried at room temperature, before a calcination treatment at 500 °C for 6 hours in air (ramp rate 1 °C min<sup>-1</sup>). A successful synthesis produces approximately 14.5 g of white solid.

### 2.1.5 Polystyrene bead synthesis

Polystyrene bead synthesis was conducted by a modified polymerisation method developed by Vaudreuil and co-workers.<sup>3</sup> In this preparation, styrene (Sigma Aldrich, > 99%) was used as a monomer source and potassium persulphate (Sigma Aldrich, >99%) was the applied polymerisation initiator. The reaction was performed in batch via a 2 L jacketed Radley's reactor ready system at 80 °C. Prior to deionised water (1.275 L) addition, the reactor was fitted with a thermocouple, Leibig condenser and a N<sub>2</sub> line set to 1.5 bar pressure. The reactor solution was stirred at 300 rpm overnight to ensure complete solution outgassing. In order to fully extract polymerisation inhibitors from the as-supplied monomer reagent, styrene (898 mmol, 93.6 g, 103 cm<sup>3</sup>) was washed five times with NaOH (0.1M) followed by five additional deionised water washings. Potassium persulphate (1.2 mmol, 0.33 g) was dissolved in deionised water (50 cm<sup>3</sup>) at 70 °C. The washed organic monomer phases were added to the purged water phase, followed by the potassium persulphate solution. After stirring under N<sub>2</sub> for 22 hours, the resultant solid was recovered, filtered and washed three times with deionised water and a further three times with ethanol. The beads were dried overnight at 80 °C, yielding approximately 70 grams.

### 2.1.6 TLCT-Macro-mesoporous SBA-15 synthesis

Polystyrene bead addition to the SBA-15 synthesis protocol described in **Section 2.1.2** permitted the successful macropore incorporation into the support framework. Macroporous-mesoporous SBA-15 was synthesised using the "True Liquid Crystal Templating" methodology, adapted from Attard and co-workers.<sup>4</sup> Pluronic P123 (2 g) was mixed with hydrochloric acid acidified water (pH 2, 2 g, 2M) and sonicated for 3 hours at

40 °C to yield a homogeneous gel. Tetramethoxysilane (27.6 mmol, 4.21 g, 4.08 cm<sup>3</sup>, a 1:4 mole ratio to H<sub>2</sub>O) was then added and mixed to produce a homogeneous liquid. Polystyrene beads (6g, synthesis described in **Section 2.1.5**) were then added to the liquid. The sample was placed under vacuum (100 mbar) at 40 °C overnight, resulting in the formation of a viscous gel. The gel was aged for 24 hours at room temperature to complete condensation, before a calcination treatment at 500 °C for 6 hours in air (ramp rate 1 °C min<sup>-1</sup>). A successful synthesis produces approximately 2.0 g of white solid.

### **2.1.7 Metal incipient wetness impregnation (all supports)**

All supports were impregnated with Pt metal precursor using the incipient wetness methodology.<sup>5</sup> Commercial (2.0 g Sigma, 200 m<sup>2</sup>g<sup>-1</sup>), mesoporous SBA-15, macro-mesoporous SBA-15, SBA-16 and KIT-6 silica supports (2.0 g) were wetted with aqueous ammonium tetrachloroplatinate (II) solution (12 cm<sup>3</sup> with precursor concentrations adjusted to achieve nominal Pt loadings of 0.05-2 wt. %). The slurry was stirred for 18 hours at room temperature before heating to 50 °C. After approximately 6 hours agitation ceased and the solids left at 50 °C for a period of 24 hours in order to dry to a powder. These powders were calcined at 500 °C for 4 hours in air (ramp rate 1 °C min<sup>-1</sup>) prior to reduction at 400 °C for 2 h (ramp rate 10 °C min<sup>-1</sup>) under flowing hydrogen (10 cm<sup>3</sup> min<sup>-1</sup>).

## **2.2 Sample Characterisation**

### **2.2.1 Microscopy and elemental composition determination**

#### **2.2.1.1 Scanning electron microscopy**

Scanning electron microscopy (SEM) is a surface sensitive technique often used to study surface or near surface structural features of bulk materials. In this technique, an electron beam is generated from a tungsten filament cathode situated on top of the microscope, via thermionic electron emission.<sup>6</sup> A series of electromagnetic lenses and scanning coils focus and direct the beam, which is subsequently deflected at various angles upon interaction with the sample surface. A variety of signals can be generated dependant on the energy of the primary electrons; this can be controlled by an applied accelerating voltage, typically 1-30kV via the scanning coils, and dependant on the analysis mode. The detection of secondary electrons, produced by inelastic scattering of a primary electrons from the point of impact, allows for the initial formation of the SEM image.<sup>7,8</sup> As these electrons are characteristically of low-energy (<50eV, predominantly 3-5 eV) they are typically localised

within a few nanometres of the sample surface. Due to this reason, secondary electrons are usually not detectable from bulk sample as their escape is greatly hindered. The topography of the sample can be mapped in 3-dimensional space as the extent of secondary electron generation is dependent on the orientation of surface sample facets with the incident beam. Regions at 90° to the beam appear brightest; this decreases as regions move parallel to the beam. Controlling secondary electron generation and contrast allow for optimisation of the image. High energy backscattered electrons are generated through elastic scattering of the incident electron beam with atoms on the sample surface, contributing to the quality of the final image. The higher the atomic mass (or Z number) of the interacting nucleus, the stronger the diffraction effect and the brighter the image.<sup>8</sup> This theory allowed for accurate imaging of high atomic weight platinum nanoparticles and clusters, via impregnation (described in **Section 2.1.7**), on support materials with lower molecular weights and hence diminished Z contrast.

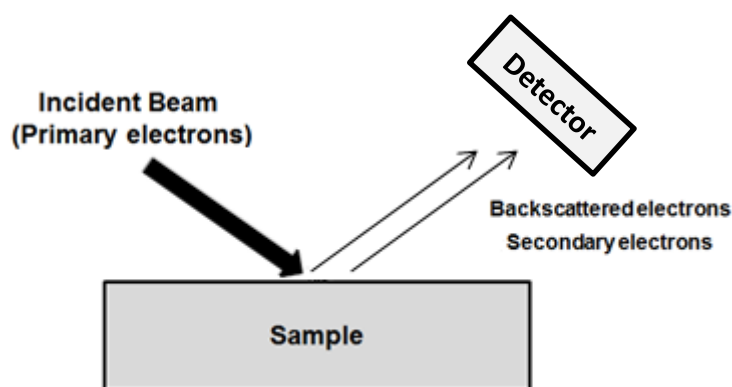


**Figure 2.1 – A representation of signal generation from beam-specimen interactions**

SEM images of bare and impregnated supports were recorded on a Carl Zeiss Evo-40 SEM operating at 10 KV, with an i probe value of 1 nA. Samples were mounted on to aluminium stubs using adhesive carbon tape. Elemental analysis was conducted using an EDX detector attached to the instrument. In order to generate a sufficient level of x-rays needed for an accurate and reliable analysis, the operating voltage was increased to 25KV with an approximate i probe value of 25 nA. EDX analysis was performed six times per sample using a sample collection time of 300 s.

### 2.2.1.2 Energy dispersive x-ray spectroscopy

It is often common practice for electron microscopy techniques (SEM and TEM etc.) to be accompanied with an x-ray detector in order to perform elemental analysis on bulk samples. By adjusting the accelerating voltage of the electron beam, excitation of specimen core electrons can be accomplished. In a principle akin to XPS and XRF techniques, the resulting hole, left via the ejection of the core electron, causes a subsequent destabilisation of the once occupied orbital. In order for stability to be retained, a higher energy electron is demoted, moving into the now empty shell. In doing so an x-ray, associated with the change in energy between the two electron shells, is generated. The wavelength of this x-ray is element-specific, allowing for a positive and quantitative characterisation of the bulk sample.<sup>9,10</sup>



**Figure 2.2 – An illustrative representation of x-ray generation<sup>11</sup>**

### 2.2.1.3 Transmission electron microscopy

As with SEM, transmission electron microscopy (TEM) utilises a beam of electrons for imaging, however key differences between the two techniques are apparent. The electron beam is transmitted through an ultra-thin sample, any apparent absorption by the sample resulting in a change in transmitted beam intensity. This effect is focussed and magnified by an objective lens, with an image formed on a phosphorescent screen.<sup>12</sup> Because of this TEM images are two-dimensional in nature and must be prepared with greater precision. Sample thickness greatly affects final image resolution, though superior magnification levels can be achieved allowing for alternative structural characteristics to be deduced (wrt SEM).

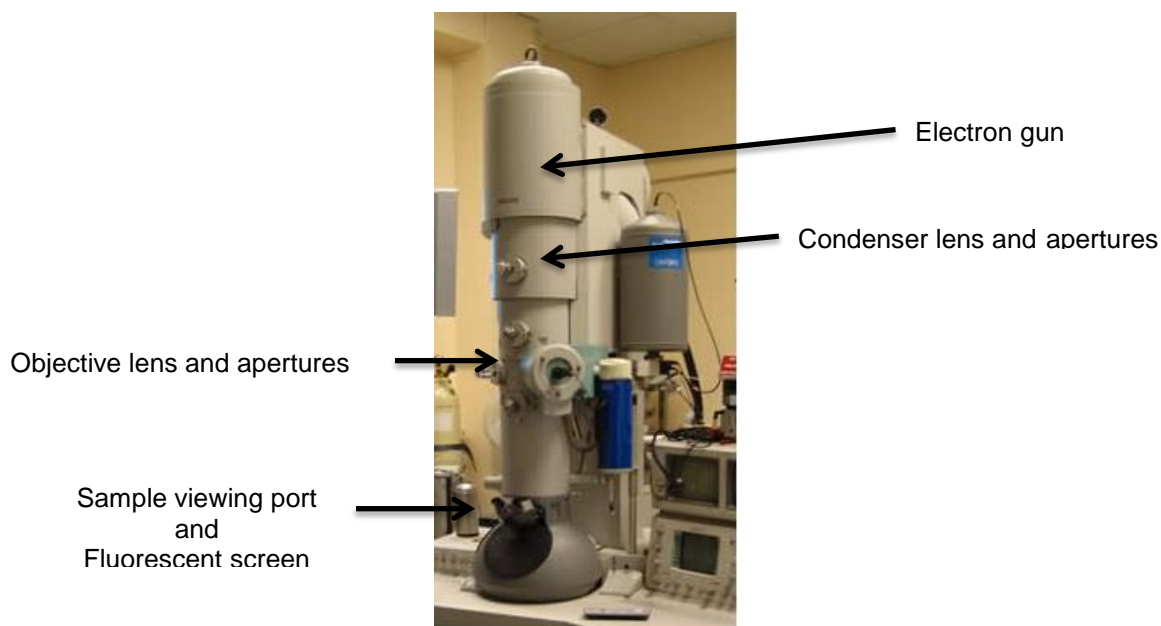


**Figure 2.3 – The FEI Tecnai CM200 TEM in the LENNF facility at the University of Leeds**

High resolution TEM images were recorded on an FEI Tecnai F20 field emission gun TEM operating at 200 kV equipped with a Gatan charge-coupled device (CCD) Orius SC600A camera at the University of Leeds. Powdered samples were prepared via dispersion in ethanol (absolute), sonicated for 15 minutes before dropcasting onto a continuous or holey carbon film atop a copper grid (Agar Scientific Ltd.). All images were processed and analysed with ImageJ version 1.41 software.

## 2.2.2 X-ray Analysis

### 2.2.2.1 Powder x-ray diffraction

Powder x-ray diffraction (XRD) is a non-destructive analytical technique, which due to the wavelengths within the Ångström range, can be used to great effect to probe the physical properties of materials. Revealing internal crystal structure can allow for the identification of bulk phases, sample transformations and an accurate, qualitative estimation of particle size<sup>13</sup>. In the case of this investigation, x-ray photons are generated from a Cu  $K_{\alpha}$  (1.54 Å, 8.04 keV) anode via the ejection of a primary electron from the K-shell causing the subsequent formation of a core hole. Demotion of a higher energy electron, typically from the L-shell, fills this “hole” with subsequent  $K_{\alpha}$  photon emission. These photons are directed towards a homogeneous (finely ground powder) solid sample. Although the bulk of most sample materials are polycrystalline, and hence consist of many randomly orientated crystal domains and orientations, the homogeneous nature of the sample gives rise to a sufficient

level of short-range order to allow the constructive interference of incident x-rays with ordered pore structures and lattice planes.<sup>14,15</sup> The constructive interference, arising from in-phase reinforcement of elastically scattered x-rays, gives rise to fingerprint diffraction patterns unique to each material as shown in **Figure 2.4**.



**Figure 2.4 – Schematic representation of in-phase x-ray diffraction phenomena<sup>16</sup>**

According to Bragg’s Law (**Equation 2.1**), diffraction patterns can only be observed at set reflection angles if the spacing between crystal planes,  $d$ , is equal to the x-ray wavelength multiplied by an integer,  $n$ .

$$n\lambda = 2d\sin\theta \quad \text{Equation 2.1: Bragg’s Law}$$

$n$  = order of reflection (multiplication integer);  $\lambda$  = incident x-ray wavelength;  
 $d$  = lattice spacing and  $\theta$  = diffraction angle

This equation can be adapted in order to determine unit cell parameters and pore spacing for mesoporous materials, calculated from the most intense diffraction peak (**Equation 2.2**).

$$a = \frac{\sqrt{(h^2+k^2+l^2)}}{2\sin\theta} \quad \text{Equation 2.2}$$

$a$  = lattice parameter;  $\lambda$  = wavelength of Cu K $\alpha$  radiation (0.1541 nm);  $h,k,l$  = miller indices and  $\theta$  = diffraction angle

Selection rules dictate the presence of certain peaks, dependant on crystal structure. Face centred cubic (FCC) assemblies, such as Pt and Pd, only exhibit peaks if all miller indices are odd or even.<sup>14</sup> Body centred cubic structures, including SBA-16, Li, Na or K, do not produce peaks when the sum of all miller indices is odd, or additionally at  $d_{100}$  and  $d_{111}$ , due to atoms or pores at  $\frac{1}{2}$  miller indices. At these positions, refractions 180° out of phase



are produced and are thus cancelled out.<sup>17</sup> Unfortunately, particle size analysis is limited to a minimum particle size detection of approx. 2 nm. As particle size diminishes, line broadening occurs due to incomplete removal of destructive interference of scattered x-rays, causing an increase in peak width. In larger crystallites, an increased number of lattice planes allows for a compensation of this effect, but as particle size decreases this phenomenon becomes more severe, eventually cancelling out diffraction peaks entirely.<sup>18</sup> However, the Scherrer equation can be applied to determine particle size if diffraction peaks are present (**Equation 2.3**)<sup>19</sup>.

$$L = \frac{k\lambda}{\left(\sqrt{(B^2 - S^2)}\cos\theta\right)} \quad \text{Equation 2.3: The Scherrer equation}$$

L = crystallite size (nm); B = FWHM of diffraction peak; S = 0.15 (systematic broadening caused by diffractometer); k = 0.9

XRD patterns were recorded on a Panalytical X'PertPro diffractometer equipped with an X'celerator detector using a Cu K $\alpha$  (1.54 Å) source and nickel filter, calibrated against a Si (Panalytical) standard. Low angle patterns were recorded over a range of  $2\theta = 0.3-8^\circ$  (step size  $0.01^\circ$ , scan speed  $0.014^\circ \text{ s}^{-1}$ ) and wide angle patterns over a range of  $2\theta = 10-90^\circ$  (step size  $0.02^\circ$ , scan speed  $0.040^\circ \text{ s}^{-1}$ ).

### 2.2.2.2 X-ray photoelectron spectroscopy

X-ray photoelectron spectroscopy (XPS) is a surface sensitive, analytical technique that provides information regarding the oxidation state, empirical formula, species population and local chemical environment of a wide array of materials. x-rays are often produced from a monochromated source, usually Al K $\alpha$  (1486.6 eV) or Mg K $\alpha$  (1253.6 eV), resulting in low energy, “*Soft x-rays*.”<sup>20,21</sup> In order to produce higher energy, “*hard x-rays*,” electrons typically need to be accelerated to energies of 1-6 GeV requiring synchrotron radiation. Although this method does allow for greater enhancement in signal intensity and more detailed examination of atomic and electronic sample structure, wrt XPS, this technique is much less widely available and subject to limitations (equipment availability, cost etc.).<sup>22</sup> XPS analyses are conducted under high-vacuum conditions in order to minimise collisions between gas-phase molecules and liberated core electrons, maximising the probability of detection. As core electrons have energies which lie in the x-ray region, the introduction of incident photons to the sample material, above the electron binding energy, favours the emission of a photoelectron with kinetic energy related to the binding energy. The binding

energy ( $E_B$ ) is the energy required to promote an electron to the Fermi level from a specific electronic level, and is unique to each element and its local environment. Knowing this, the intensity and energy position of each photoelectron yields an XPS spectrum. The binding energy can be deduced using the kinetic energy of the emitted electrons and applied to **(Equation 2.4)**.<sup>23</sup>

$$E_B = h\nu - E_{kin} - \phi_{sp} \quad \text{Equation 2.4: Binding energy}$$

$E_B$  = binding energy of emitted electron;  $h\nu$  = incident x-ray photon energy;  
 $E_{kin}$  = kinetic energy of emitted electron;  $\phi_{sp}$  = spectrometer work function

As a consequence of emission, a core hole is left and an excited state formed. This new electronic configuration is relatively unstable and so the ionised atom must *relax* in order to return to the ground state. Outer electrons are demoted to fill the core holes and the target atom gains electronic stability **(Figure 2.5)**. Liberated photoelectrons have a very small escape depth and hence give rise to the surface sensitive nature of this technique. Interactions between the ejected photoelectron and other sample electrons/environmental factors typically limit the free electron path to approx. 1-3 nm, over an electron energy range of 0-1000 eV.<sup>24</sup>

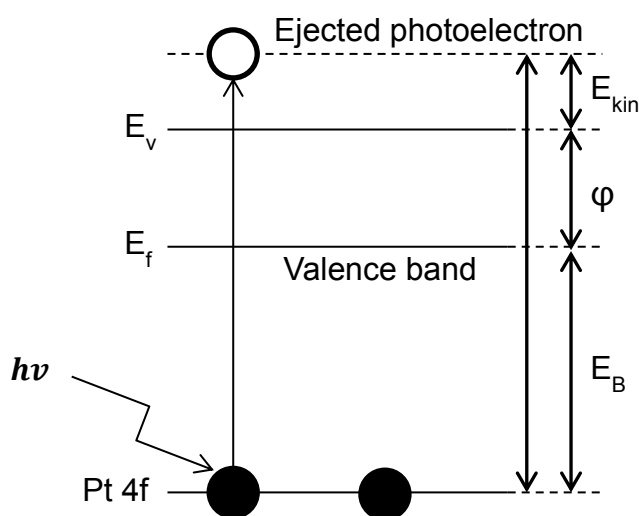


**Figure 2.5 – Schematic representation of photoelectron generation**  
 ( $E_v$  = vacuum level;  $E_f$  = Fermi level)

The final appearance of the XPS spectrum is greatly affected by the orbital in which a photoelectron is generated. When emission occurs from a non-s orbital ( $l > 0$ ), spin coupling interactions between orbital angular momentum ( $l$ ) and the spin of the ejected electron ( $m_s$ ) arise, the sum of which is known as the total angular momentum ( $j$ ) **(Equation 2.5)**.

$$j = l + s$$

**Equation 2.5: Determination of  
total angular momentum**

As the spin of the electron can be clockwise (+ 1/2) or anti-clockwise (- 1/2), two  $j$  values are produced. S orbitals do not possess any distinct orbital angular momentum ( $l = 0$ ), thus appearing as singlet peaks, but for all other orbitals the effect of spin coupling splits the resultant XPS peak into doublet form. These new peaks have a defined ratio equal to  $2j + 1$ . For the 4f orbital, used most commonly for platinum in this study,  $l = 3$  giving rise to  $j$  values of 7/2 and 5/2, and a peak ratio of 4:3.

The local atomic environment for the same element within a sample can produce additional orbital peaks with altered binding energies, shifted from the parent peak. These shifts in binding energy are often attributed to initial and final state effects relating to the oxidation state of the atom being analysed. As the atom becomes more electron-deficient, inherent to increasing oxidation state, the binding energy of an electron within this system also increases, due to a greater attractive force exerted by the nucleus over this electron. Probing the outermost filled orbitals is common practice as these components are more sensitive to any shifts in binding energy, yielding an enhanced level of resolution.<sup>25</sup> Sample surface charging can present an additional complexity for binding energy determination. This effect is especially prevalent when analysing insulating samples, such as silica, where an accumulation of surface positive charge results in a shift to higher binding energy values. Instruments are equipped with charge neutralisers to combat this problem, but as a safeguard binding energies are often charge corrected to the C 1s peak or Si 2p peaks.<sup>23</sup>

XPS analysis was performed on a Kratos Axis HSi x-ray photoelectron spectrometer fitted with a charge neutraliser and magnetic focusing lens employing Al K $\alpha$  monochromated radiation (1486.6 eV). Spectral fitting was performed using CasaXPS version 2.3.14. Binding energies were corrected to the Si 2p peak at 103.4 eV. Pt 4f XP spectra were fitted using a common asymmetric peak shape. Errors were estimated by varying the Shirley background-subtraction procedure across reasonable limits and re-calculating the component fits. Characteristic binding energies and doublet peak separations for different component species can be obtained from the National Institute of Standards and Technology (NIST) XPS database.<sup>21</sup>

### 2.2.2.3 X-ray adsorption spectroscopy – Synchrotron-based structural studies

X-ray adsorption spectroscopy (XAS) is a non-destructive technique employing monochromatic high energy x-rays, generated via synchrotron radiation sources, to obtain detailed bulk structural information, by following the level of x-ray adsorption with increasing photon energy. A typical XAS spectrum for Pt is shown in **Figure 2.6**. Although the need for synchrotron radiation is a disadvantage for this technique, the nature of the liberated x-ray photons negates the need for ultra-high vacuum environments. This in turn, allows for in-depth characterisation of samples under in-situ or atmospheric conditions, permitting the possibility to track real-time spatial and oxidation state changes in active site properties.<sup>26</sup>

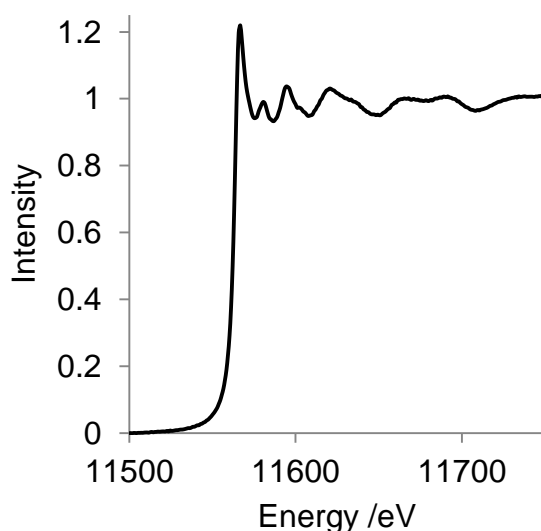


**Figure 2.6 – Schematic representation of XAS spectrum for the Pt L<sub>III</sub>-edge, using Pt<sup>0</sup> foil as a representative example**

In a similar manner to XPS, photoelectron generation occurs via the adsorption of x-ray photons of sufficient energy (energy greater than electron binding energy). Core electrons are typically probed, with the Pt L<sub>III</sub>-edge located at 11585 eV being most useful in analysis.<sup>27</sup> In this case, core 2p electrons are promoted into the higher energy, unoccupied 5d orbital and can be used to identify Pt oxidation state. In theory, as oxidation state increases, the occupation of the higher energy 5d orbitals will diminish, implying an increasing intensity in the absorbance peak just above the edge jump. As the Pt-species becomes more reduced, lowered absorbance is exhibited due to increased initial high energy orbital occupation.<sup>28</sup> Scattering of the photoelectron by neighbouring atoms can produce constructive or

deconstructive interference effects, with respect to final photon adsorption. Such interactions are reflected in the final spectra, via periodic changes in amplitude, and can be used to determine local geometric information, aiding in scattering distance and coordination number calculations.<sup>29</sup> Modified from reference 30, **Equation 2.6** can be used to determine key physicochemical parameters such as oxidation state, coordination numbers and local environment etc.



### **Equation 2.6: EXAFS equation<sup>30</sup>**

An XAS spectrum is typically split up into two distinct regions, the x-ray Adsorption Near Edge Structure (XANES) and Extended x-ray Adsorption Fine Structure (EXAFS) regions. For each sample, photon energies are scanned across a pre-set range from ~ 300 eV below to ~ 1000 eV above the adsorption edge, allowing for sufficient photoelectron generation to arise. The XANES region, situated in the first 100 eV after the adsorption edge, directly relates to oxidation state.<sup>28</sup> The EXAFS region, due to photoelectron scattering, protrudes outward for ~ 1000 eV or until oscillations cease to be observable. The higher kinetic energy of such photoelectrons allows increased propagation, only due to steadily increasing incident x-ray energy. EXAFS spectra can be plotted in “k-space” and with the aid of a mathematically determined model, the atomic environment can be mapped.<sup>31</sup>

XANES and EXAFS measurements were performed at station B18 of the Diamond Light Source facility (Harwell, UK) utilising a Si(111) double crystal fixed exit monochromator. Transmission spectra were collected on a 13-element Ge detector. Pt (11585 eV) L<sub>III</sub>-edge spectra were attained of powder catalyst samples mounted on PTFE washers. Spectra were processed using the IFEFFIT version 1.2.11d open source software suite, employing Athena version 0.9.1 for normalisation, background subtraction and linear

combination fitting of XANES, and Artemis version 0.9.1 for EXAFS fitting. Reference spectra of a PtO<sub>2</sub> powder and a Pt foil standard were also recorded.

## **2.2.3 Bulk Sample Characterisation**

### **2.2.3.1 Thermogravimetric analysis**

Observation of sample behaviour, under gas flow and thermal treatment, is often used as a means to identify and assess a wide variety of material characteristics. These can range from thermal stability, phase transitions to absorption and desorption phenomena, allowing for optimisation of final catalyst properties for certain processes and conditions. Thermogravimetric analysis (TGA) clearly shows any change in sample mass with changes in time upon heat application. Surface absorbed species, water of crystallisation or any sample fluctuations resulting in a mass change or liberation of gases can be identified and quantified using this technique. TGA is typically conducted under an inert gas flow. However, this technique can be adapted for reductive and oxidative treatments.<sup>32,33</sup>

Thermogravimetric analysis was conducted using a Stanton Redcroft STA-780 series thermoanalyser, complete with 706 temperature controller, DC amplifier and balance control. Samples (approx. 7-15 mg) were loaded into an alumina crucible and heated to 800 °C at 10 °C min<sup>-1</sup> under a 20 cm<sup>3</sup> min<sup>-1</sup> helium flow. An identical reference crucible was used, during all analyses, containing pre-treated, inert  $\gamma$ -alumina. A linked computer containing PicoLog data capture software was used to monitor and determine sample mass differences with temperature, allowing for differential temperature analysis to be applied. For the purpose of this work, a 20% Hydrogen / 80% Helium mixture, commonly known as “*Temperature Programmed Reduction*” analysis (TPR), was also employed to determine platinum precursor reduction temperature prior to support impregnation.

### **2.2.3.2 Carbon monoxide pulse chemisorption**

CO Chemisorption relies on the formation of covalent-type bonds between the adsorbate metal and CO. Due to this substantially higher enthalpies of adsorption are predominant, with respect to physisorption processes (**Section 2.2.3.4**), limiting adsorption to monolayer coverage with site specific selectivity being predominant.<sup>20</sup> Bond formation via modulation of charge in both species causes a subsequent reduction in metal surface energy. The M-CO bond strength is far stronger at metal surfaces than when compared with equivalent metal complexes, with group 10 metals exhibiting high bond strengths.<sup>34</sup> This

increased bond strength augments adsorbate thermal stability (eliminating the need for analysis at temperatures below the adsorbate boiling point), and so increases residence time.<sup>35</sup>

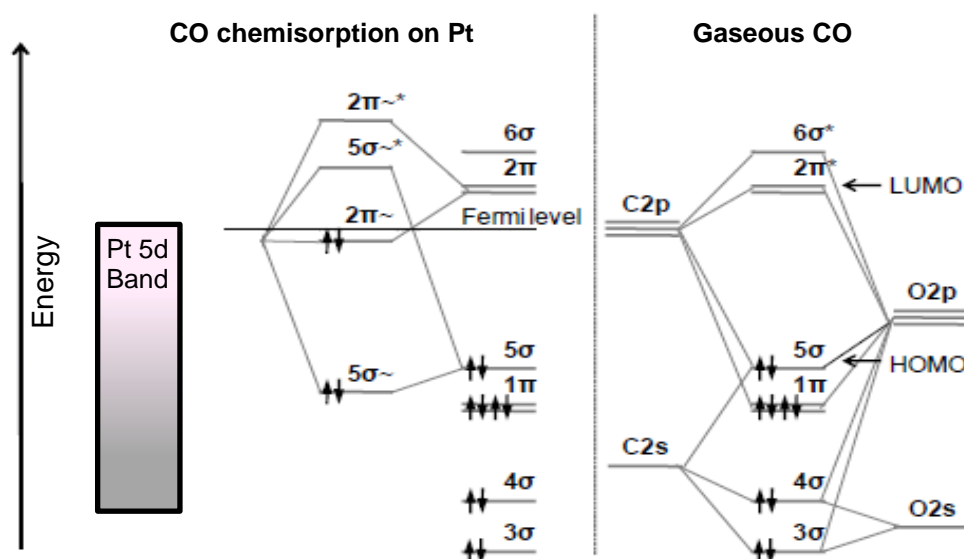


**Figure 2.7 – Molecular orbital diagrams for CO on Pt and free gaseous CO**  
(modified from reference 19)

**Figure 2.7** demonstrates the molecular orbital structure present in the carbon monoxide molecule. Bonding with Pt occurs via the Pt(111) facet,<sup>36</sup> in which the non-bonding  $5\sigma$  molecular orbital interacts with the unoccupied, perpendicular Pt  $d_z^2$  orbital to create two new adsorbate bonding and antibonding orbitals,  $5\sigma^-$  and  $5\sigma^{*-}$ . As the Pt d-band interacts with the highest occupied and lowest unoccupied CO molecular orbitals simultaneously, two additional bonding and antibonding adsorbate orbitals are formed,  $2\pi^-$  and  $2\pi^{*-}$ , originating from the CO  $2\pi^*$  orbital. The  $5\sigma^-$  orbital lies below the Fermi level and so electron filling is energetically favoured. The corresponding anti-bonding orbital, above the Fermi level, is left unoccupied. Electron population in this manner causes a depletion of charge in the C=O bond, weakening it via  $5\sigma$  adsorption orbital electron depletion, simultaneously enhancing Pt-C bond strength. An effect known as “ $\sigma$ -donation”. Further reinforcement of the Pt-C bond takes place via increased population of the  $2\pi^*$  CO anti-bonding molecular orbital, through  $\pi$ -back donation. As the  $2\pi^-$  adsorbate orbital sits just below the Fermi level, preferential charge transfer into this orbital increases the anti-bonding nature of this orbital, thus lowering the bond order and strength of the C=O bond.<sup>20, 37</sup> The Fermi level controls chemisorption bond strength with a higher Fermi level, e.g. Au, causing a decrease in bond strength as partial occupation of anti-bonding adsorbate orbitals arises.<sup>14</sup>

<sup>38</sup> Metals, such as platinum, which contain 5d valence orbitals experience relativistic effects known as lanthanide contraction. This effect drastically decreases the energy difference between 5d and 6s states, allowing for increased electron mobilisation between the two levels, subsequently aiding Pt-CO bonding (metal-ligand charge transfer) and stabilisation of the Pt<sup>4+</sup> oxidation state.<sup>20,34</sup>

CO chemisorption upon Pt occurs via the Pt(111) facet via a terminal orientation without dissociation.<sup>36</sup> A CO:Pt<sub>surface</sub> stoichiometry of 0.68 was assumed and a maximum <sup>7</sup>/<sub>10</sub> monolayer coverage has been postulated for Pt(111) at 25 °C, since the formation of a fully saturated monolayer is energetically unfavourable under the measurement conditions used. Only terminal CO binding is witnessed on Pt (111) surfaces, in order to minimise the the repulsive lateral interaction and thus maximising total intermolecular distance between neighbouring CO molecules. The successive adsorption of each CO molecule contributes to a lowering of the total system energy, until at approx 0.7-075 monolayer coverage, it is no longer energetically favourable to introduce additional CO onto the surface.<sup>39,40,41,36,42</sup> Pt dispersions and average particle sizes were determined using **Equation 2.7**,<sup>20</sup> and **Equation 2.8**.<sup>43</sup>

$$D_m = \left( \frac{\text{mol}_{\text{COads}} S_{\text{av}}}{\text{mol}_{\text{Pt}}} \right) \times 100 \quad \text{Equation 2.7: Metal dispersion}$$

$D_m$  = metal dispersion;  $\text{mol}_{\text{COads}}$  = moles of CO adsorbed;  $S_{\text{av}}$  = average stoichiometry;  
 $\text{mol}_{\text{Pt}}$  = total number of moles of Pt

$$PS_{\text{ave}} = \left( \frac{5C_m f_m}{2.7e^{12} s_{\text{av}} d_m V_g} \right) \quad \text{Equation 2.8: Average particle size}$$

$PS_{\text{ave}}$  = particle size (nm);  $C_m$  = metal surface density (atoms  $\text{cm}^{-1}$ );  
 $f_m$  = metal loading ( $\text{g}_{\text{met}}/\text{g}_{\text{cat}}$ );  $S_{\text{av}}$  = stoichiometry;  $d_m$  = metal density ( $\text{g}_{\text{met}}/\text{cm}^3$ );  
 $V_g$  = chemisorbed gas volume ( $\text{cm}^3/\text{g}_{\text{cat}}$ )

Pt metal dispersions were quantified by CO pulse chemisorption using a Quantachrome ChemBET 3000 and analysed using TPRWin software. Approximately 100 mg of sample was accurately weighed into a sample tube, before outgassing at 150 °C under flowing He ( $20 \text{ cm}^3 \text{ min}^{-1}$ ) for 1 hour. Samples were then reduced at 150 °C under flowing H<sub>2</sub> ( $10 \text{ cm}^3 \text{ min}^{-1}$ ) for 1 hour before analysis at room temperature. This treatment was deemed mild enough to inhibit sintering phenomena. Pulses of CO ( $0.05 \text{ cm}^3$ ) were passed over the sample with subsequent sample adsorption logged. Sequential injections were completed



until 6 equivalent recorded detector responses were acquired. At this point, the surface is considered saturated, no CO is adsorbed by the sample and the total volume of absorbed CO can be calculated.

### 2.2.3.3 Diffuse reflection infra-red fourier transform spectroscopy

Diffuse reflection infra-red fourier transform spectroscopy (DRIFTS) is an infra-red spectroscopic technique, used to probe the bonding mode of surface species. For the purpose of this work, infra-red radiation absorption causes an excitation of the vibrational modes of surface functional groups, either stretching or bending modes, through the adsorption of photons at a specific energy. This results in the generation of a dipole moment, which has a bond-specific wavenumber. Hooke's law (**Equation 2.9**) can be applied in order to ascertain the relationship between the frequency ( $\nu$ ) of vibration with the associated bond strength ( $k$ ) and reduced mass of the target functional group ( $\mu$ ).

$$\nu = \frac{1}{2\pi} \sqrt{\frac{k}{\mu}} \quad \text{Equation 2.9: Hooke's law}$$

Photons can either be reflected (*partially*) by the sample or transmitted through. Due to the random nature of the sample, signal reflection from the sample surface proceeds through various scattering angles. In order to overcome this, a parabolic mirror is utilised in order to focus the reflected beam, thus increasing sensitivity and signal to noise ratios (**Figure 2.8**).<sup>44</sup>

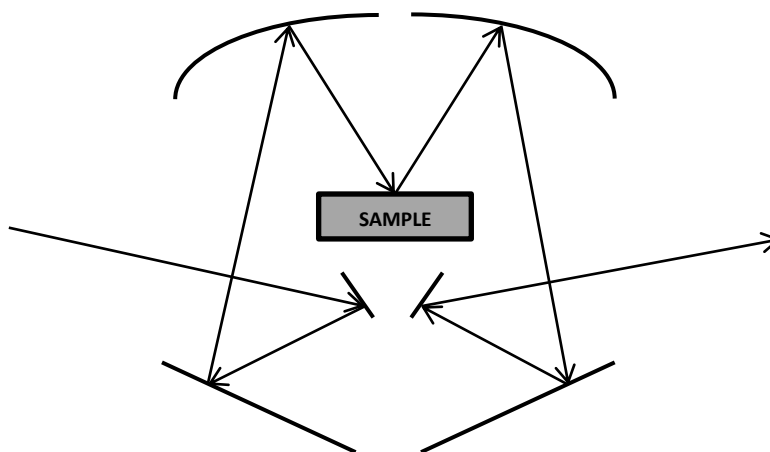


**Figure 2.8** – A schematic representation of the parabolic mirrors utilised for infra-red beam focussing in diffuse reflectance IR (modified from reference 42)

DRIFTS can be used to analyse the surface species of solid powders and rough surfaces, but also demonstrates a high affinity for the detection of surface-chemisorbed species and the direct titration of CO upon metallic surfaces.<sup>45</sup> In this thesis, silanol concentration and type was investigated (discussion and results presented in **Chapter 4**).

DRIFTS measurements were collected on a Thermo-Fisher Nicolet Avatar iS50 FT-IR equipped with a Smart Collector Accessory, Polaris<sup>TM</sup> infrared source and mercury cadmium telluride (MCT-A) photon detector cooled to -196 °C. A gold-coated in-situ cell with temperature control and gas manifold was used to probe the evolution of sample spectra upon variation of these parameters. Background spectra were collected over dried KBr at 200 °C, prior to the collection of sample spectra at 200 °C. In order to ensure well-defined sample spectra, bare silica and Pt/silica samples were diluted in KBr (to 10 wt. %). Spectra were collected using OMNIC software and processed off-line using OPUS 6 software.

### **2.2.3.4 Nitrogen porosimetry**

Optimisation of surface area and pore size characteristics allows for the production of superior catalytic systems. If reactant transport and subsequent product diffusion is deemed faster than the rate of reaction, then it can be quoted that the apparent rate should be proportional to the surface area of the active catalyst.<sup>46</sup> The addition of a well-ordered pore system to an support material, not only increases effective surface area, but also the rate of reactant/product diffusion, theoretically increasing the rate of catalysed reaction.<sup>47</sup>

Nitrogen adsorption arises due to the formation of temporarily induced dipoles, via the variation of electron density within the adsorbate molecule (otherwise known as “London dispersion forces”).<sup>35</sup> During analysis, temperature is kept at a constant, with the N<sub>2</sub> pressure increased stepwise. As N<sub>2</sub> is dosed at varying pressure, the total volume absorbed at each step is recorded and an equilibrium between the rate of adsorption and desorption is assumed. Overall, six distinct isotherm types can be generated (**Figure 2.9**), each providing a high level of detail pertaining to adsorbent surface structure and properties.



**Figure 2.9 – Typical adsorption isotherms<sup>48</sup> and hysteresis loops for type IV and V isotherms<sup>49</sup>**

Type I arises due to strong interactions between the adsorbate gas and adsorbent within microporous materials; Type II is the most common isotherm often exhibited by nonporous and macroporous samples; Type III is unusual as the evaporation of gas condensed within the micropores is more difficult than the initial condensation of said gas, thus leading to adsorbate interactions being greater in the micropores than on the adsorbate surface. Types IV and V are symptomatic of mesoporous supports; and Type VI yielded by uniform multilayer adsorbate adsorption. Hysteresis loops, depicted in **Figure 2.9**, are produced by samples with mesoporous structures (Isotherms IV and V), varying greatly in shape as dictated by subtle changes in adsorption and desorption phenomena within the mesopores.<sup>37</sup> The incorporation of meso-domain channels allow for a new mode of adsorption, across the pore wall (capillary condensation). The distance between the pore wall and adsorbate is substantially decreased, with respect to non-mesoporous materials, amplifying any attractive interactions. Desorption, subsequently occurs across the surface of the liquid adsorbate. The curvature of this liquid (meniscus within the filled pore), hinders evaporation due to surface tension effects, effectively lowering the pressure that gas evaporation can occur relative to the adsorption step. Hysteresis phenomena can be subdivided into four shapes; Type H1 indicates the presence of a material with uniform, regular pore size, Type H2 represents non-uniform ink bottle pore shapes, Types H3-H4 can be attributed to slit shaped pores.<sup>49</sup>

The BET equation (**Equation 2.10**)<sup>50</sup> is used to calculate the total sample surface area and has been modified from traditional Langmuir theory, in order to account for the presence

of multilayer N<sub>2</sub> adsorption. Adsorbent molecules from the monolayer act as adsorption sites for the next layer. The adsorption behaviour of all subsequent layers is assumed to be the same. The constant C is introduced to highlight any differences between the monolayer and multilayer interactions. The specific surface area is calculated from the linear region of the BET plot, corresponding to monolayer coverage, with the assumption of close N<sub>2</sub> molecule packing (1.62 nm<sup>2</sup>), shown in **Equation 2.12**.<sup>35, 37, 49</sup>

$$\frac{P}{V_a(P_0 - P)} = \frac{1}{V_m C} + \frac{C-1}{V_m C} \left( \frac{P}{P_0} \right) \quad \text{Equation 2.10: BET (Linear)}$$

P = pressure; P<sub>0</sub> = saturation pressure; V<sub>a</sub> = volume adsorbed; V<sub>m</sub> = monolayer volume; C = multilayer adsorption parameter

$$C \propto \exp \frac{q_1 - q_L}{RT} \quad \text{Equation 2.11: Definition of constant, C}$$

q<sub>1</sub> = Heat of adsorption of the first layer; q<sub>L</sub> = heat of adsorption for subsequent layers; R = gas constant; T = Analysis temperature

$$a(\text{BET}) = \frac{V_m \sigma N_a}{mv} \quad \text{Equation 2.12: BET surface area calculation}$$

a(BET) = BET specific surface area; N<sub>a</sub> = Avogadro's number; σ = N<sub>2</sub> molecule area (1.62 nm<sup>2</sup>); m = sample mass; v = gas molar volume

Mesopore diameters were calculated from the desorption branch, applying the Barrett, Joyner and Halenda (BJH) method. Modification of the Kelvin equation (**Equation 2.13**)<sup>37</sup> accounts for increased adsorbate desorption difficulty for mesoporous materials, relative to condensation processes, allowing a relationship to be determined between pore diameter and spontaneous adsorbate evaporation. Monitoring any pressure change at each step allows for pore size distribution determination.

$$\ln \left( \frac{P}{P_0} \right) = - \left( \frac{2\gamma v}{RT r_m} \right) \quad \text{Equation 2.13: Kelvin equation}$$

P/P<sub>0</sub> = Relative change in pressure in equilibrium with condensed gas meniscus; γ = liquid surface tension; v = molar volume for condensed adsorbate; r<sub>m</sub> = mean radius of condensed gas meniscus

Adsorption and desorption isotherms were recorded on a Quantachrome Nova 4000 porosimeter at 77K using Novawin v2.2 analysis software. 100 mg catalyst samples (approx.) were weighed into a sample tube before degassing for a period of 2 hours at 393K, prior to N<sub>2</sub> adsorption. Surface area calculations were determined from the Brunauer, Emmett and Teller

(BET) isotherm using a relative pressure range of  $P/P_0 = 0.05-0.2$ . Microporosity values were quoted from the t-plot method using a relative pressure range of  $P/P_0 = 0.2-0.5$ . The pressure ranges utilised for BET surface area and microporosity determination were sufficient to maintain a linear relationship.

## 2.3 Catalyst Testing

### 2.3.1 Selective oxidation

#### 2.3.1.1 Alcohol selective oxidation (standard procedure)

All catalyst testing was conducted using a Radleys Starfish carousel batch reactor under atmospheric pressure at 90 °C. A stock solution of cinnamyl alcohol (84 mmol, 11.23 g, 10.80 cm<sup>3</sup>), mesitylene (7.19 mmol, 0.86 g, 1 cm<sup>3</sup>) and toluene (944 mmol, 87 g, 100 cm<sup>3</sup>) was prepared. Each 25 cm<sup>3</sup> reactor was charged with 10 cm<sup>3</sup> stock solution, to which catalyst (50 mg) was added under 700 rpm stirring, to remove any apparent diffusion limiting effects. In order to correctly identify *true* catalyst activity, blank reactions were performed in parallel using stock solution with, and without, bare support addition. Reactions were sampled (0.25 cm<sup>3</sup>) at fixed intervals (t=0, 10, 20, 30, 40, 50 mins and 1, 2, 3, 5, 7 and 24 hrs) and diluted with toluene (approx. 1.75 cm<sup>3</sup>) for kinetic profiling. Samples were analysed, in triplicate, with subsequent data averaging applied, using off-line gas chromatography on a Varian 3900GC equipped with a CP-8400 autosampler, fitted with a CP-Sil5 CB column (15m x 0.25 mm x 0.25 µm) and FID detector. Column oven ramp rates and oven temperatures are summarised in **Table 2.1**. As stated, reactions were run for a period of 24 hrs, where initial rates were determined from the initial linear region (0 – 1 hrs) of the conversion plot. All products/reactants were calibrated prior to GC analysis, with final selectivities and conversions reported to ±3% error.

Temperature / °C	Rate / °C min <sup>-1</sup>	Hold / min	Total / min
80	<i>initial</i>	0.00	0.00
123	10.0	0.00	4.30
290	40.0	5.00	13.47

**Table 2.1 – GC column oven method for cinnamyl alcohol analysis**

#### 2.3.1.2 Role of atmosphere on cinnamyl alcohol selective oxidation

Catalyst testing was also conducted under N<sub>2</sub> and O<sub>2</sub> atmospheres, in order to determine the effect of reaction atmosphere, if any, on the final conversion and selectivity

profiles of all Pt-based catalysts. The procedure described in **Section 2.3.1.1** was adhered to, with the exception that, either, N<sub>2</sub> or O<sub>2</sub> (5 cm<sup>3</sup> min<sup>-1</sup>) flowed through the reaction solution.

### **2.3.1.3 Role of in-situ reduction pre-treatment**

High and low Pt loading catalysts (50 mg, approx. 2 and 0.10 wt% respectively) were reduced under flowing H<sub>2</sub> (10 cm<sup>3</sup> min<sup>-1</sup>) in toluene (47.2 mmol, 4.35 g, 5 cm<sup>3</sup>) at 90 °C for 1 hr. The solution was then purged with N<sub>2</sub> (10 cm<sup>3</sup> min<sup>-1</sup>) for 30 minutes prior to initiating the reaction via the addition of cinnamyl alcohol (8.4 mmol, 1.123g, 1.08 ml), mesitylene (0.72 mmol, 86 mg, 0.1 cm<sup>3</sup>) and toluene (47.2 mmol, 4.35 g, 5 cm<sup>3</sup>), swapping for an O<sub>2</sub> flow (5 cm<sup>3</sup> min<sup>-1</sup>). Control reactions using N<sub>2</sub> instead of H<sub>2</sub> during the reduction pre-treatment, and N<sub>2</sub> throughout were also performed.

### **2.3.1.4 Identifying reactive intermediate behaviour in selective oxidation**

High and low metal loading samples (50 mg, approx. 2 and 0.05 wt.% respectively) on all silica-supported platinum catalysts were investigated under standard conditions with the exception of O<sub>2</sub> (5 cm<sup>3</sup> min<sup>-1</sup>) flowed through each reaction solution over a 7 hour period. 3-phenylpropan-1-ol (8.4 mmol, 1.144 g, 1.14 cm<sup>3</sup>), 3-phenylpropionaldehyde (8.4 mmol, 1.127 g, 1.12 cm<sup>3</sup>), cinnamic acid (8.4 mmol, 1.245 g, 1.01 cm<sup>3</sup>) and cinnamaldehyde (8.4 mmol, 1.110 g, 1.06 cm<sup>3</sup>) were each tested to determine catalytic behaviour.

### **2.3.1.5 Effect of O<sub>2</sub> pressure on cinnamyl alcohol selective oxidation**

A series of cinnamyl alcohol selective oxidation reactions were completed over a range of metal loadings (50 mg, approx. 2, 0.5 and 0.05 wt. % respectively) on all supported platinum catalysts. The effect of O<sub>2</sub> pressure (5, 10 and 15 bar) on final substrate conversion and product selectivity was investigated. Cinnamyl alcohol (8.4 mmol, 1.123g, 1.08 ml), mesitylene (0.72 mmol, 86 mg, 0.1 cm<sup>3</sup>) and toluene (94 mmol, 8.7 g, 10 cm<sup>3</sup>) were loaded with catalyst into a Büchi limbo autoclave, stirring at 700 rpm to replicate previous testing protocols. Reactor stirring was achieved by a Büchi glasuster Cyclone 075 overhead stirrer with CC3000 controller, reaction temperature and O<sub>2</sub> pressure were continuously regulated by a Büchi glasuster TC 450 temperature controller and Büchi glasuster BPC 9901 pressure flow gas controller. Reactions were run for a period of 7 hours, with samples (0.25 cm<sup>3</sup>) taken and diluted (1.75 cm<sup>3</sup>) with toluene at t=0 and 7h for final conversion and product selectivity determination. Off-line gas chromatography and methodology follows the procedure described in **Section 2.3.1.1**.

## 2.3.2 Selective hydrogenation

### 2.3.2.1 Cinnamaldehyde hydrogenation (standard procedure)

Catalyst screening was performed using Radleys Starfish carousel batch reactors on a 10 cm<sup>3</sup> scale at 90 °C flowing H<sub>2</sub> (5 cm<sup>3</sup> min<sup>-1</sup>) through each reaction solution. Catalyst (100 mg) was added to a reaction mixture containing cinnamaldehyde (8.4 mmol, 1.110 g, 1.06 cm<sup>3</sup>), mesitylene (0.72 mmol, 86 mg, 0.1 cm<sup>3</sup>) and anisole (92 mmol, 9.95 g, 10 cm<sup>3</sup>) at 90 °C under stirring. Reactions were sampled (0.25 cm<sup>3</sup>) for kinetic profiling, at regular intervals (t=0, 10, 20, 30, 40 and 50 mins, 1, 2, 3, 5 and 7 hrs) and diluted (approx. 1.75 cm<sup>3</sup>) with anisole, using off-line gas chromatography with a Varian 3800GC with CP-8400 autosampler fitted with a VF-5ms factor four column (30 m x 0.25 mm x 0.25 μm) and FID detector. Column oven ramp rates and oven temperatures are summarised in **Table 2.2**. Reactions were run for a period of 7 hours; initial rates were calculated from the linear region of the reaction profile (initial 0.1-1.0h). All products/reactants were calibrated prior to GC analysis, with final selectivities and conversions reported to ±3% error.

Temperature / °C	Rate / °C min <sup>-1</sup>	Hold / min	Total / min
50	<i>initial</i>	0.00	0.00
120	4.0	0.00	17.50
260	40.0	10.00	31.00

**Table 2.2 – GC column oven method for cinnamaldehyde analysis**

Additionally, 3-phenylpropan-1-ol (8.4 mmol, 1.144 g, 1.14 cm<sup>3</sup>), 3-phenylpropionaldehyde (8.4 mmol, 1.127 g, 1.12 cm<sup>3</sup>) and cinnamyl alcohol (8.4 mmol, 1.123g, 1.08 ml) were each tested to determine their role in the reaction mechanism.

### 2.3.2.2 Effect of H<sub>2</sub> pressure on cinnamaldehyde selective hydrogenation

A series of cinnamaldehyde selective hydrogenation reactions were completed over a range of metal loadings (100 mg, approx. 2 and 0.1 wt. % respectively) on all supported catalysts. The effect of H<sub>2</sub> pressure (1, 5 and 10 bar) on cinnamaldehyde conversion and product selectivity was investigated. A reaction mixture of cinnamaldehyde (8.4 mmol, 1.110 g, 1.06 cm<sup>3</sup>), mesitylene (0.72 mmol, 86 mg, 0.1 cm<sup>3</sup>) and anisole (92 mmol, 9.95 g, 10 cm<sup>3</sup>) was loaded into a Parr 5500 series autoclave equipped with diptube and overhead stirrer (controlled by a 4848 controller), with reactions conducted at 90 °C under stirring for a period of 7 hours. Reactions were sampled (0.25 cm<sup>3</sup>) for kinetic profiling, at regular intervals (t=0, 10, 20, 30, 40 and 50 mins, 1, 2, 3, 5 and 7 hrs) and diluted (approx. 1.75 cm<sup>3</sup>)

with anisole, using off-line gas chromatography with a Varian 3800GC with CP-8400 autosampler fitted with a VF-5ms factor four column (30 m x 0.25 mm x 0.25  $\mu\text{m}$ ) and FID detector for final conversion and product selectivity determination. Off-line gas chromatography and methodology follows the procedure described in **Section 2.3.1.1**.



**Figure 2.10 – Schematic representation of Parr 5500 series autoclave**

### **2.3.3 Active site leaching analysis – Hot filtration**

A hot filtration test was conducted, modifying the methodology developed by Corma *et al.*<sup>51</sup> This test was used to determine the level of active site leaching under reaction conditions. Catalyst was removed, via filtration of the hot reaction solution under vacuum, after an initial 60 minutes. Upon completion, the filtrate was returned to reaction conditions and reaction sampling resumed.

## **2.4 References**

1. D. Zhao, Q. Huo, J. Feng, B. F. Chmelka and G. D. Stucky, *Journal of the American Chemical Society*, 1998, 120, 6024-6036.
2. T.-W. Kim, F. Kleitz, B. Paul and R. Ryoo, *Journal of the American Chemical Society*, 2005, 127, 7601-7610.
3. S. Vaudreuil, M. Bousmina, S. Kaliaguine and L. Bonnevot, *Advanced Materials*, 2001, 13, 1310-1312.
4. G. S. Attard, J. C. Glyde and C. G. Goltner, *Nature*, 1995, 378, 366-368.



5. R. J. White, R. Luque, V. L. Budarin, J. H. Clark and D. J. Macquarrie, *Chemical Society Reviews*, 2009, 38, 481-494.
6. D. McMullan, *Scanning*, 1995, 17, 175-185.
7. K. K. Kolasinski, *Surface Science: Foundations of Catalysis and Nanoscience*, Wiley, 2012.
8. J. Kinder, *Materials and Corrosion*, 1995, 46, 550-550.
9. R. J. Keyse, *Introduction to Scanning Transmission Electron Microscopy*, Bios Scientific Publishers, 1998.
10. J. Goldstein, *Scanning Electron Microscopy and X-Ray Microanalysis*, Springer London, Limited, 2003.
11. T. Scientific, <http://tawadascientific.com/images/technology/incident-radiation-from-pri.jpg> Accessed March 2013, 2013.
12. J. John W. Heckman and K. L. Klomparens, *Scanning and Transmission Electron Microscopy: An Introduction*, Oxford University Press, Incorporated, 1993.
13. B. Cullity and J. W. Weymouth, *American Journal of Physics*, 1957, 25, 394.
14. J. W. Niemantsverdriet, in *Spectroscopy in Catalysis*, Wiley-VCH Verlag GmbH & Co. KGaA, 2007, DOI: 10.1002/9783527611348.ch6, pp. 147-177.
15. H. P. Myers, *Introductory solid state physics*, CRC Press, 1997.
16. X-ray diffraction - Bruker D8 Discover, <http://fys.kuleuven.be/iks/nvsf/experimental-facilities/x-ray-diffraction-2013-bruker-d8-discover>, Accessed April 2013, 2013.
17. C. Suryanarayana and G. Norton, *X-Ray Diffraction: A Practical Approach*, Plenum Press, 1998.
18. C. Hammond, *The Basics of Crystallography and Diffraction*, OUP Oxford, 2009.
19. A. L. Patterson, *Physical Review*, 1939, 56, 978-982.
20. G. A. Somorjai and Y. Li, *Introduction to Surface Chemistry and Catalysis*, John Wiley & Sons, 2010.
21. NIST X-Ray Photoelectron spectroscopy database, <http://srdata.nist.gov/xps/>, Accessed March 2013, 2013.
22. F. R. Elder, A. M. Gurewitsch, R. V. Langmuir and H. C. Pollock, *Physical Review*, 1947, 71, 829-830.
23. J. F. Watts and J. Wolstenholme, *An Introduction to Surface Analysis by XPS and AES*, Wiley, 2003.
24. I. Chorkendorff and J. W. Niemantsverdriet, *Concepts of Modern Catalysis and Kinetics*, Wiley, 2007.
25. G. Moretti, *Journal of Electron Spectroscopy and Related Phenomena*, 1995, 76, 365-370.
26. M. A. Newton and W. van Beek, *Chemical Society Reviews*, 2010, 39, 4845-4863.
27. F. Behafarid, L. K. Ono, S. Mostafa, J. R. Croy, G. Shafai, S. Hong, T. S. Rahman, S. R. Bare and B. R. Cuenya, *Phys Chem Chem Phys*, 2012, 14, 11766-11779.
28. D. E. Ramaker and D. C. Koningsberger, *Phys Chem Chem Phys*, 2010, 12, 5514-5534.
29. R. Richards, *Surface and Nanomolecular Catalysis*, CRC/Taylor & Francis, 2006.
30. D. C. Koningsberger and R. Prins, *X-ray absorption: principles, applications, techniques of EXAFS, SEXAFS, and XANES*, 1988.
31. B. Ravel and K. Gallagher, *Physica Scripta*, 2005, 2005, 606.
32. E. Brown, *Introduction to Thermal Analysis: Techniques and Applications*, Springer, 2001.
33. P. J. Haines and R. S. o. Chemistry, *Principles of Thermal Analysis and Calorimetry*, Royal Society of Chemistry, 2002.
34. G. C. Bond, *Platinum Metals Review*, 2000, 44, 146-155.
35. R. P. H. Gasser, *An introduction to chemisorption and catalysis by metals*, Clarendon Press, 1987.
36. S. R. Longwitz, J. Schnadt, E. K. Vestergaard, R. T. Vang, E. Laegsgaard, I. Stensgaard, H. Brune and F. Besenbacher, *Journal of Physical Chemistry B*, 2004, 108, 14497-14502.

37. P. A. Webb, C. Orr and M. I. Corporation, *Analytical methods in fine particle technology*, Micromeritics Instrument Corporation, 1997.
38. D. Lovrić and B. Gumhalter, *physica status solidi (b)*, 1987, 139, 423-432.
39. B. Shan, Y. Zhao, J. Hyun, N. Kapur, J. B. Nicholas and K. Cho, *The Journal of Physical Chemistry C*, 2009, 113, 6088-6092.
40. K. B. Rider, K. S. Hwang, M. Salmeron and G. A. Somorjai, *J Am Chem Soc*, 2002, 124, 5588-5593.
41. R. Chen, Z. Chen, B. Ma, X. Hao, N. Kapur, J. Hyun, K. Cho and B. Shan, *Computational and Theoretical Chemistry*, 2012, 987, 77-83.
42. H. Baltruschat and S. Ernst, *ChemPhysChem*, 2011, 12, 56-69.
43. N. Pernicone, *Cattech*, 2003, 7, 196-204.
44. H. Günzler and H.-U. Gremlich, 2002.
45. A. Guerrero-Ruiz, A. Maroto-Valiente, M. Cerro-Alarcón, B. Bachiller-Baeza and I. Rodríguez-Ramos, *Topics in catalysis*, 2002, 19, 303-311.
46. G. C. Bond, *Heterogeneous catalysis: principles and applications*, Clarendon Press, 1974.
47. C. M. A. Parlett, D. W. Bruce, N. S. Hondow, M. A. Newton, A. F. Lee and K. Wilson, *ChemCatChem*, 2012, DOI: 10.1002/cctc.201200301, n/a-n/a.
48. P. B. Balbuena and K. E. Gubbins, *Langmuir*, 1993, 9, 1801-1814.
49. K. S. W. Sing, D. H. Everett, R. A. W. Haul, L. Moscou, R. A. Pierotti, J. Rouquerol and T. Siemieniowska, *Pure and Applied Chemistry*, 1985, 57, 603-619.
50. S. Brunauer, P. H. Emmett and E. Teller, *Journal of the American Chemical Society*, 1938, 60, 309-319.
51. A. Corma, D. Das, H. García and A. Leyva, *Journal of Catalysis*, 2005, 229, 322-331.

## *Chapter 3*

*The selective oxidation of  
allylic alcohols over platinum/silicas*

—

*Identification of active site  
and mesopore effects*

### 3.1 Introduction

The identification of the active site responsible for Pt-catalysed selective oxidation (selox) of allylic substrates is crucial for the future optimisation of Pt-based catalytic systems. Recent studies employing palladium demonstrate the pivotal role PdO active sites play in reaction dynamics.<sup>1</sup> It is still uncertain whether metallic<sup>2,3</sup> or oxidic<sup>4,5,6</sup> Pt species dictate reaction characteristics, or whether an interplay between the two allow for the activation of distinct reaction pathways. A combination of XPS, XAS and reaction telemetry under varying conditions, suggest the presence of a Pt<sup>4+</sup> species is responsible for selox performance.<sup>4</sup>

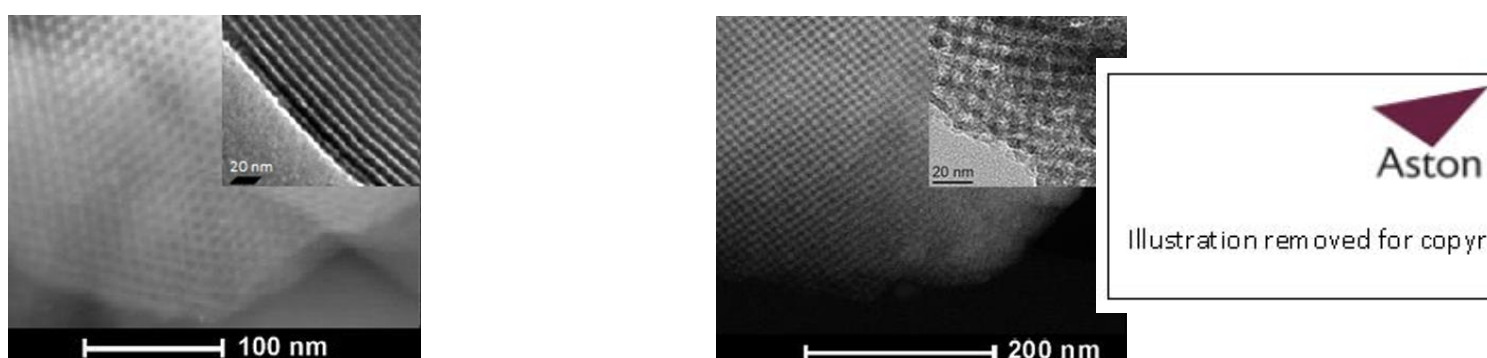


**Figure 3.1 – A schematic representation and TEM images of 2-Dimensional SBA-15 and interconnected 3-Dimensional KIT-6 mesoporous silicas**

A high, inherent chemical stability and lack of support interactions for silica supports provide an ideal basis for probing the effect of support surface area, mesoporous architecture incorporation and variable pore characteristics. The aim of this chapter is to catalogue these effects in allylic alcohol selox, identifying the catalytically active Pt species for this reaction and the possible role of these supports on their overall stability. Commercial, amorphous silica (aSiO<sub>2</sub>) was compared against 2D non-interconnecting and 3D interconnecting mesoporous silicas. SBA-15 consists of hexagonally close-packed, parallel channels without connecting mesopores<sup>7</sup>. KIT-6 introduces interconnected mesopores in a 3-Dimensional array<sup>8</sup>. It is hoped that by exploring the introduction of a pore network and interconnectivity between channels, mass transfer restrictions could be evaluated and eliminated, and “true” non-rate-limited catalytic activity obtained.

## 3.2 Results and Discussion

### 3.2.1 Characterisation of bare silica supports

Two mesoporous silicas, SBA-15 and KIT-6, were successfully prepared utilising the methods reported by Zhao<sup>7</sup> and Ryoo<sup>8</sup> respectively. A range of characterisation techniques were employed to confirm this conclusion. An amorphous silica (aSiO<sub>2</sub>) support (Sigma Aldrich) was used as a point of comparison.

#### 3.2.1.1 Powder x-ray diffraction

The successful formation of SBA-15 (*P6mm*)<sup>7</sup> and KIT-6 (*Ia3d*)<sup>8</sup> pore architectures can be confirmed via indexing the major peaks apparent in the associated low angle powder XRD spectra. **Figure 3.2** shows a stacked plot of these mesoporous supports. All reflections observed at low angles can be associated with well-defined pore structures and long-range support order.

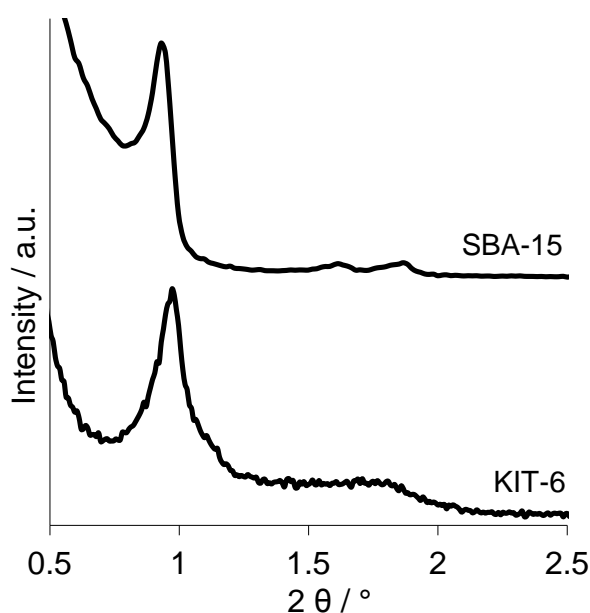


**Figure 3.2** – Stacked low angle XRD patterns of parent SBA-15 and KIT-6 supports

Bragg's Law (**Chapter 2 Equation 2.2**) was used to determine unit cell parameters for each support, with the position of the most intense peak used as a central basis. These values are shown in **Table 3.1**, and are in accordance with associated literature values for identical systems. Information on these space groups is well-known and readily available and so the position and identity of additional reflections can be calculated, reinforcing the correct identification of each pore network. The hexagonally packed *P6mm* space group,

a fundamental feature of SBA-15, exhibits three reflections. The strongest is categorised as the d10 reflection, with two smaller d11 and d20 peaks also present. KIT-6 demonstrates a major d211 reflection with a smaller shoulder stemming from the d220 reflection. An additional broad feature is observed, arising from d420 and d322 reflections. Due to the absence of ordered porosity in the amorphous silica support, no low angle reflections could be collected.

**Table 3.1** - Textural properties of parent silica supports

Sample	Surface area / m <sup>2</sup> g <sup>-1(a)</sup>	Mesopore diameter / nm <sup>(b)</sup>	Micropore surface area / m <sup>2</sup> g <sup>-1(c)</sup>	Cell Lattice parameter / nm <sup>(d)</sup>	Pore separation / nm <sup>(d)</sup>
aSiO <sub>2</sub>	208 (± 25)	31.3	37 (± 4)	n/a	n/a
SBA-15	882 (± 88)	5.7	441 (± 41)	9.0 (± 0.2)	10.4 (± 0.3)
KIT-6	918 (± 92)	6.4	485 (± 49)	22.2 (± 0.2)	15.6 (± 0.3)

<sup>a</sup>N<sub>2</sub> BET, <sup>b</sup>BJH desorption isotherm, <sup>c</sup>N<sub>2</sub> t-plot, <sup>d</sup>Low angle XRD via Bragg's law

### 3.2.1.2 Nitrogen porosimetry

Probing support characteristics with N<sub>2</sub> porosimetry allows for enhanced assessment of support surface area and mesopore characteristics. Type IV adsorption isotherms with intrinsic hysteresis loops are present for SBA-15 and KIT-6, further evidence towards successful mesoporous support synthesis. Isotherms for all three silica supports can be found in **Figure 3.3**. The presence of mesopores within SBA-15 and KIT-6 architectures activates capillary condensation phenomena. A dramatic increase in N<sub>2</sub> adsorption over a relative pressure range of 0.4-0.8 highlights this effect. Furthermore, due to altered dynamics within the mesopore, condensation and evaporation processes will differ during adsorption and desorption steps, yielding hysteresis of the final isotherm.<sup>9,10</sup> SBA-15 and KIT-6 express type H1 hysteresis, indicating a pore shape with consistent diameter throughout. Due to the lack of mesoporosity in amorphous silica, a type II isotherm is shown.

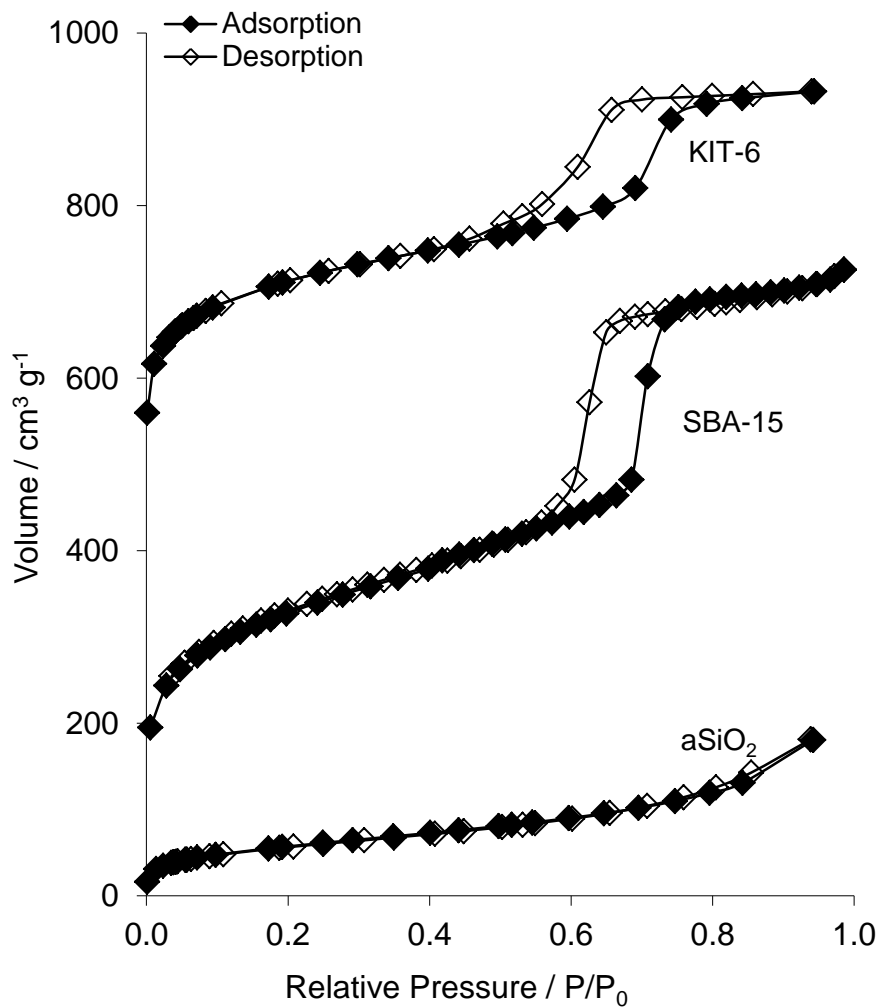


**Figure 3.3 – Stacked isotherm plot of KIT-6 (Offset by 500 cm<sup>3</sup> g<sup>-1</sup>), SBA-15 (Offset by 200 cm<sup>3</sup> g<sup>-1</sup>) and amorphous silica**

BET and BJH treatments have been used to calculate surface area and pore diameters respectively and this data can be found in **Table 3.1**. All readings adhere to literature stated values for similar materials, under the same preparation conditions.

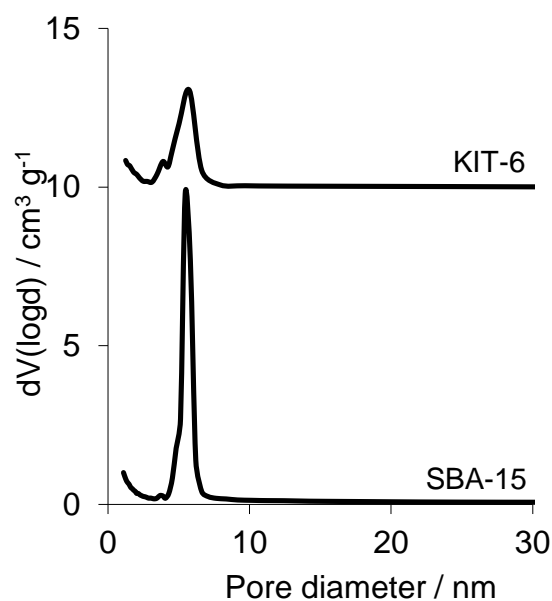


**Figure 3.4 – Stacked BJH pore size distributions for the mesoporous silica supports (KIT-6 offset by 5)**

Narrow BJH pore size distributions are shown for both mesoporous systems, with similar pore sizes also indicated. A common structural templating agent (Pluronic P123) is utilised for both preparations, most likely leading to comparable surfactant micelle sizes prior to silica-surfactant mesophase formation. BJH pore size distributions are shown in **Figure 3.4**. The BET surface areas of KIT-6 and SBA-15 are substantially elevated versus amorphous silica due to the introduction of ordered, internal mesopore networks.

### 3.2.1.3 Transmission electron microscopy

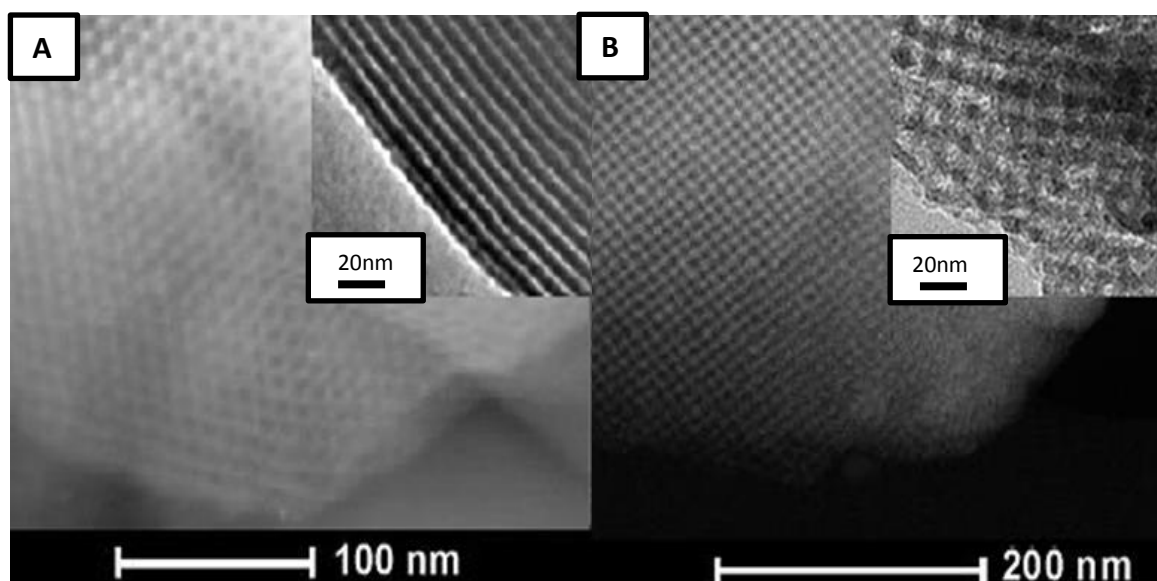


**Figure 3.5 – Representative dark field HRTEM images of (a) SBA-15 and (b) KIT-6**



**Figure 3.5** reinforces the previous evidence for the successful generation of mesoporous supports. The representative TEM images clearly show the hexagonal packing and ordered channels presented by SBA-15  $P6mm$  space groups.<sup>7</sup> Images of KIT-6 samples also highlight the cubic pore structure inherent to  $Ia3d$  unit cell.<sup>8</sup> The average pore diameters, verified from direct measurement of approximately 80 pores, express values of 5.7 ( $\pm$  0.3 nm) and 6.4 ( $\pm$  0.3 nm), for SBA-15 and KIT-6 respectively. Pore spacing and cell lattice parameters are in excellent agreement with calculated low angle XRD values.

### 3.2.2 Characterisation of Pt impregnated silica supports

Upon successful characterisation of bare support, impregnation onto the three silica supports was implemented using the incipient wetness protocol, aiming for bulk Pt loadings of 2-0.05 wt.%.

#### 3.2.2.1 Energy dispersive x-ray analysis

**Table 3.2** – A comparison of targeted and actual bulk platinum loadings

Support	Targeted loading / wt. %	Calculated loading <sup>a</sup> / wt. %
aSiO <sub>2</sub>	2.00	2.10
aSiO <sub>2</sub>	1.00	0.96
aSiO <sub>2</sub>	0.50	0.54
aSiO <sub>2</sub>	0.10	0.09
aSiO <sub>2</sub>	0.05	0.05
SBA-15	2.00	2.01
SBA-15	1.00	1.00
SBA-15	0.50	0.52
SBA-15	0.10	0.11
SBA-15	0.05	0.06
KIT-6	2.00	1.81
KIT-6	1.00	0.87
KIT-6	0.50	0.47
KIT-6	0.10	0.12
KIT-6	0.05	0.06

<sup>a</sup>EDX analysis

EDX analysis was conducted at Cardiff University to accurately ascertain metal loadings on Pt/Silica systems. **Table 3.2** shows an excellent correlation between the desired

and actual bulk metal loadings, thus highlighting the accuracy and reproducibility of the synthesis protocol.

### 3.2.2.2 Powder x-ray diffraction

The impregnation of platinum species onto the support structure demonstrates negligible change in support long-range pore order for SBA-15 and KIT-6, shown in **Figure 3.6**. All peaks present in the parent support low angle XRD are observed (**Figure 3.2**), with no discernible shift in peak position, shape or intensity. Cell lattice parameters remain consistent with parent support values, indicating a preservation of mesopore structural integrity.

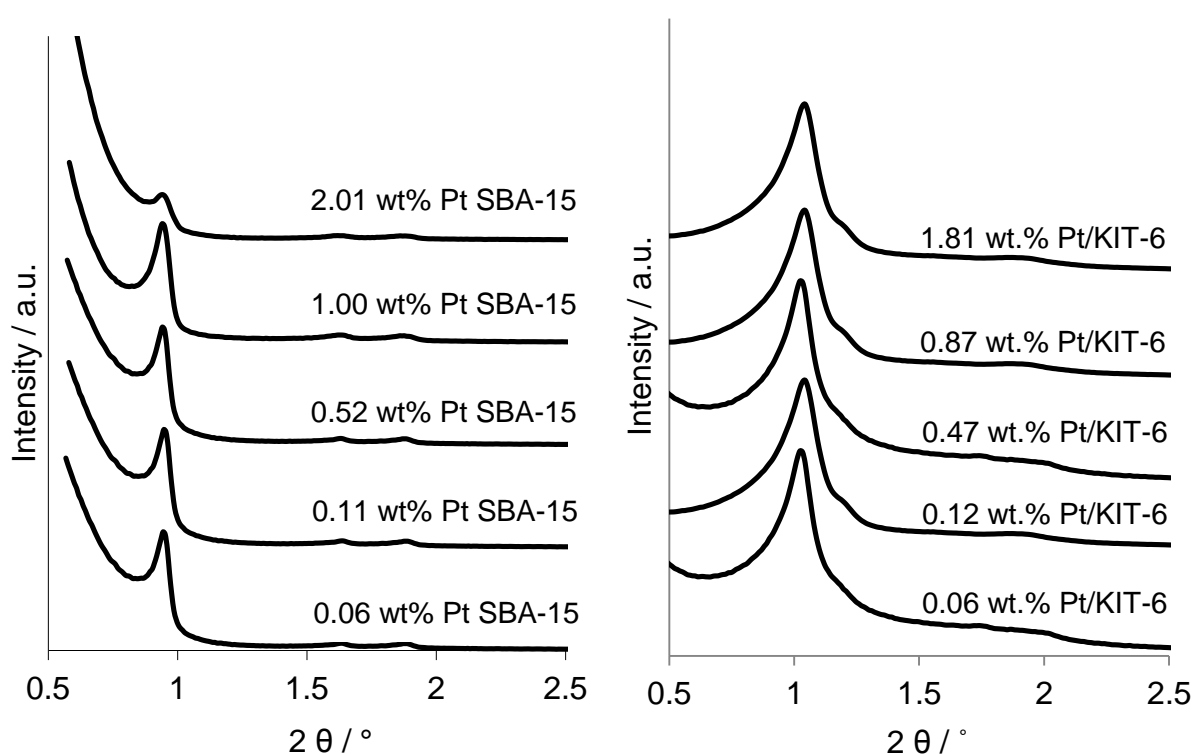


**Figure 3.6 – Stacked low angle XRD plots for Pt/SBA-15 and Pt/KIT-6**

Wide angle XRD serves as a vital tool in the determination of crystalline Pt size and phase determination. Four main reflections can be observed for all Pt/silica systems, arising from large, highly ordered crystallites on the support surface. **Figure 3.7** shows the wide angle diffraction patterns for all impregnated silicas. At bulk Pt loadings, greater than 0.5 wt.%, reflections at  $39.7^\circ$  and  $45.9^\circ$  are characteristic of the Pt(111) and Pt(200) reflections. These indicate the presence of metallic Pt nanoparticles. Further reflections at  $67.5^\circ$  and  $81.1^\circ$ , assigned as (220) and (311) reflections respectively, further support this conclusion.

Due to an inherent crystallite size dependency of this technique, as metal loadings decrease such reflections become absent from the spectra suggesting sub-3 nm crystallite domains.<sup>11</sup> A broad tail-off can be seen on all plots, at less than 35°, attributed to the presence of amorphous silica and disordered frameworks.<sup>12</sup> The Scherrer equation was used to determine nanoparticle size (**Chapter 2 Equation 2.3**),<sup>13</sup> corresponding results are expressed in **Table 3.3**.

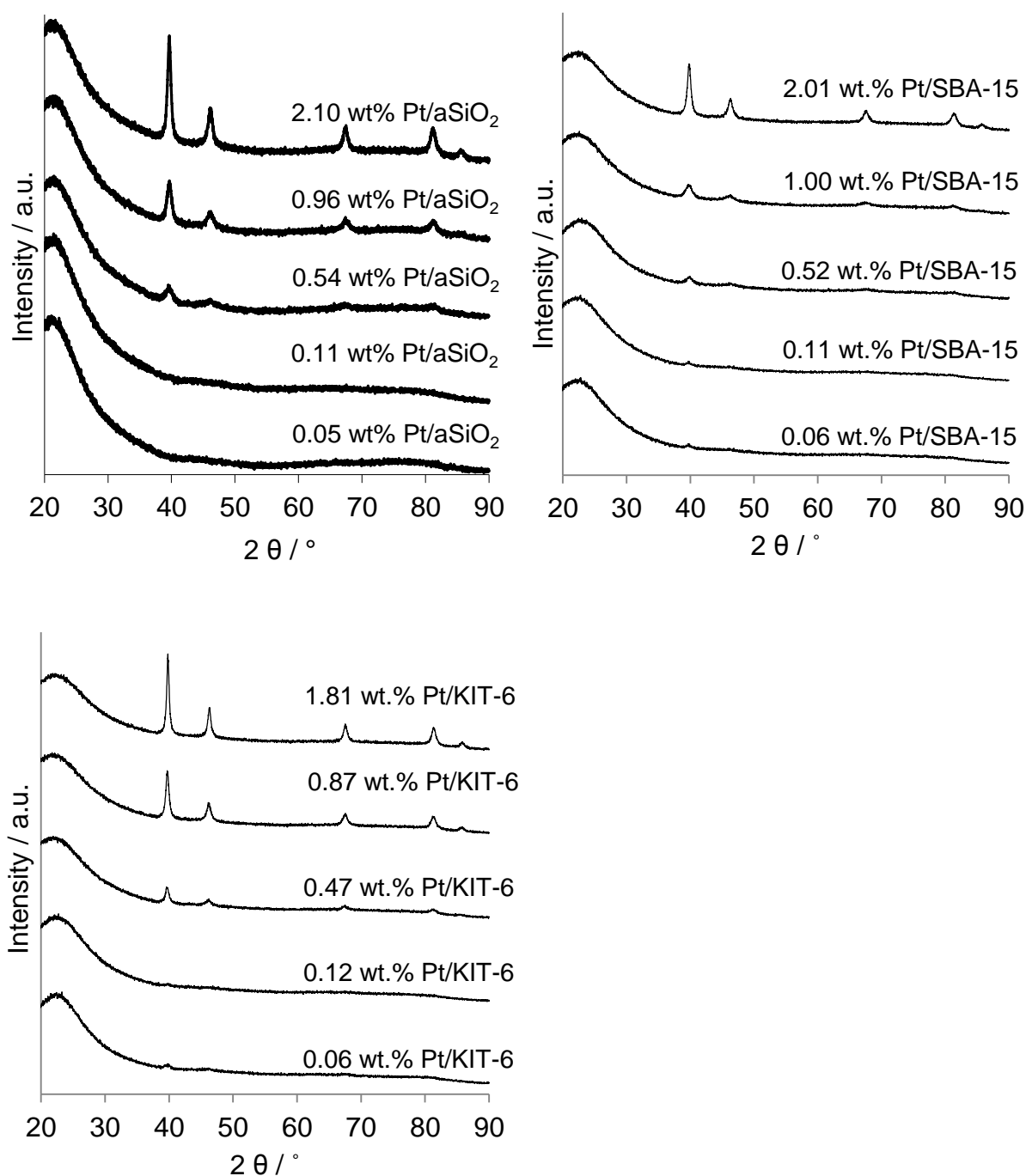


**Figure 3.7 – Stacked wide angle XRD plots for Pt/amorphous silica, Pt/SBA-15 and Pt/KIT-6**

**Table 3.3** – Pt nanoparticle size calculated from Pt(111) reflection

Support	Pt loading / wt. %	Pt particle size / nm
aSiO <sub>2</sub>	2.10	16.6
aSiO <sub>2</sub>	0.96	9.5
aSiO <sub>2</sub>	0.54	8.4
SBA-15	2.01	15.1
SBA-15	1.00	9.0
SBA-15	0.52	5.4
KIT-6	1.81	13.9
KIT-6	0.87	10.3
KIT-6	0.47	5.1

**Table 3.3** shows a clear decrease in Pt nanoparticle size with loading; however this effect is dramatically increased upon enhancement of support surface area and the introduction of hierarchical mesostructure. As stated above, no reflections could be collected for bulk metal loadings <0.5 wt. % across all Pt/silica samples, thus indicating the presence of crystallites smaller than 3 nm.

### 3.2.2.3 Nitrogen porosimetry

Figure 3.8 shows the N<sub>2</sub> isotherms for all three Pt/silica series.

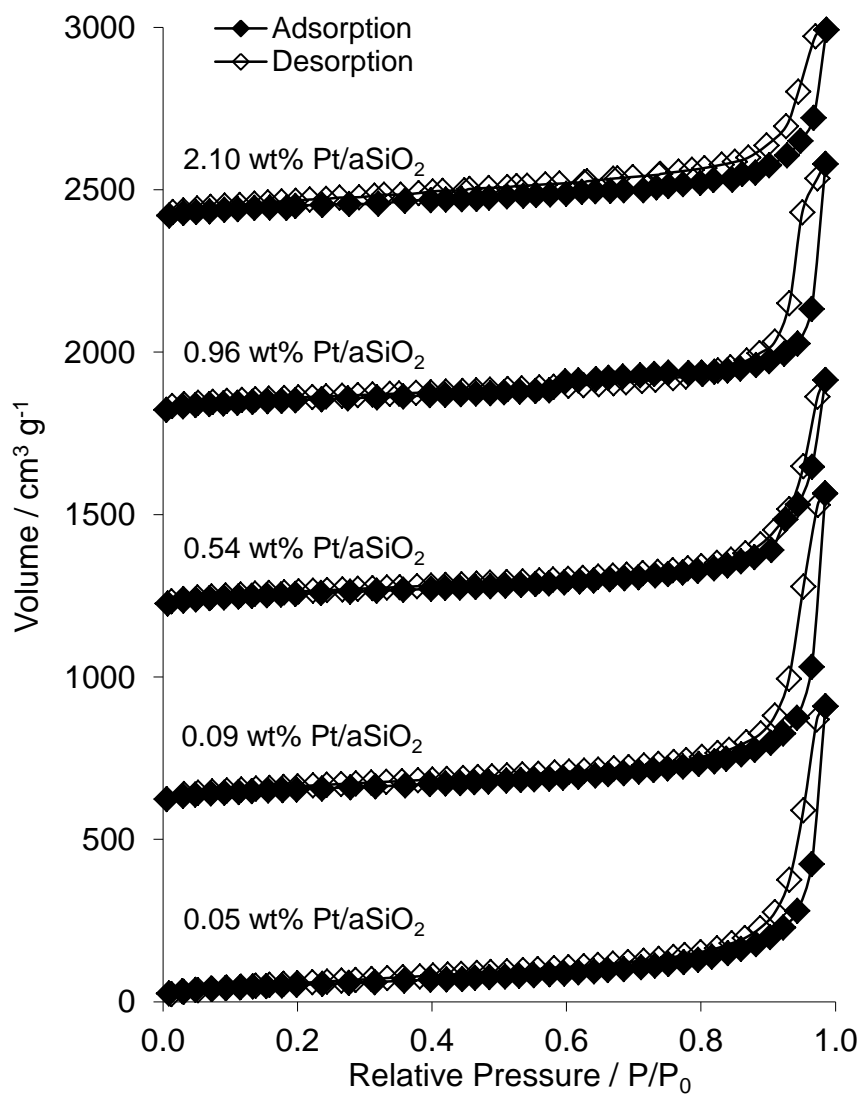
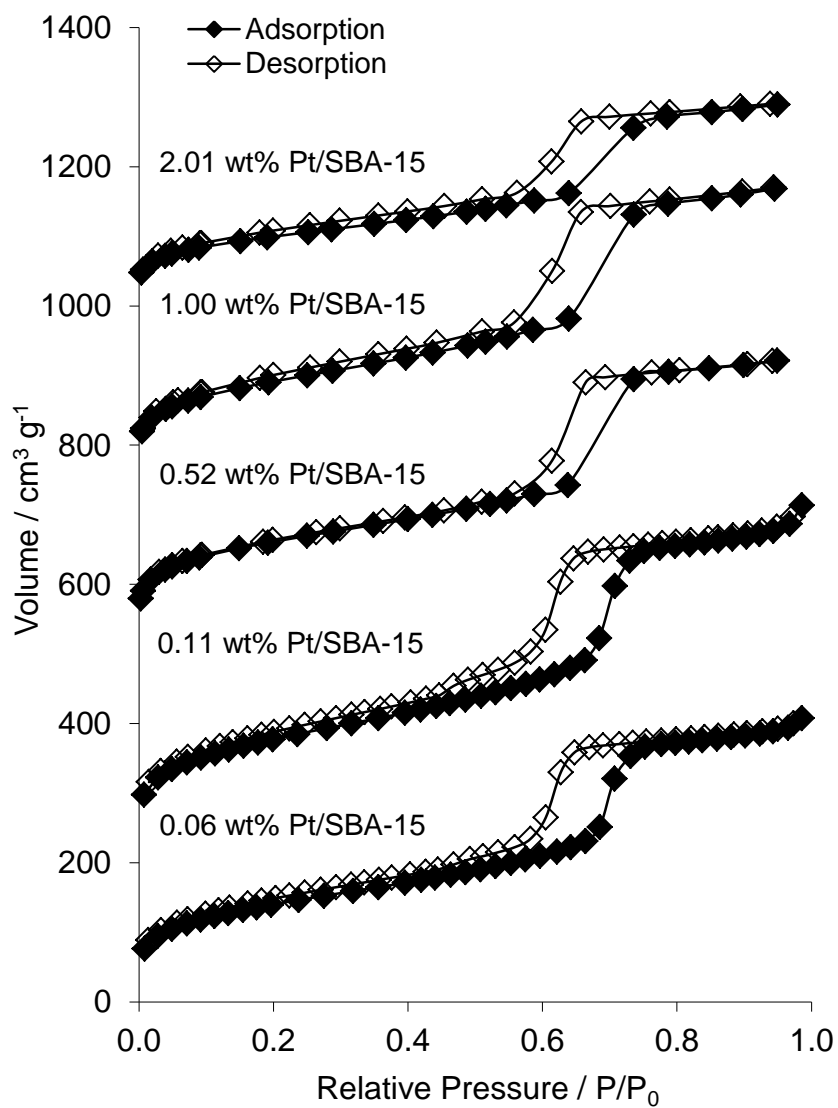
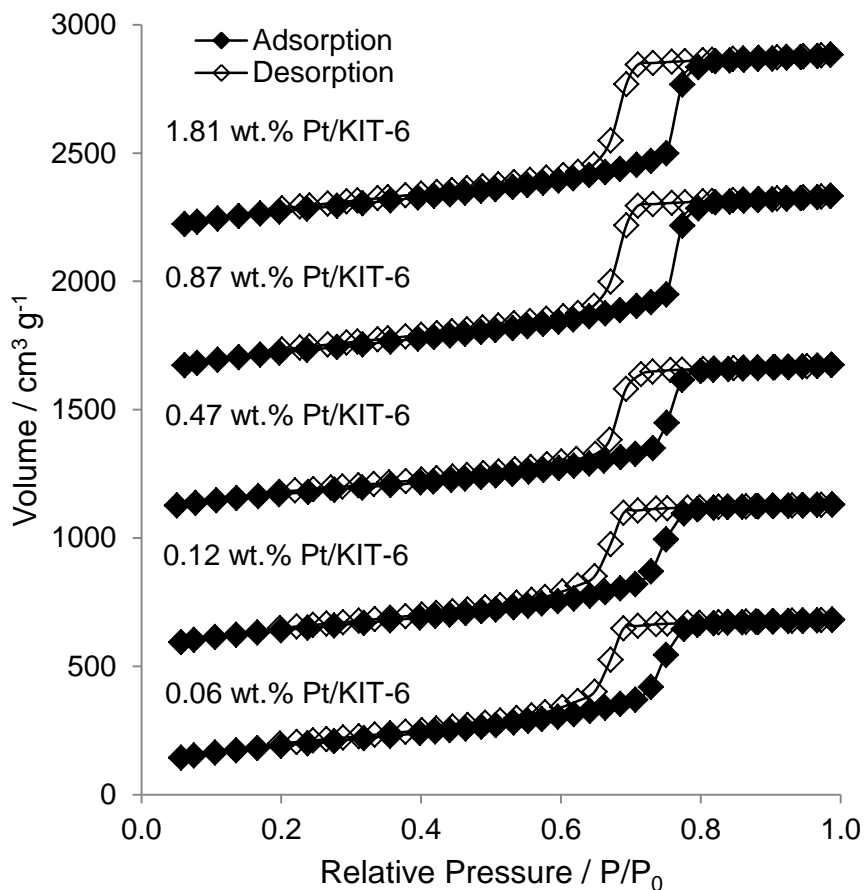


Figure 3.8 (a) – Stacked N<sub>2</sub> isotherm plot for Pt/amorphous silica series  
(Samples offset by 500 cm<sup>3</sup> g<sup>-1</sup> by metal loading for clarity)



**Figure 3.8 (b) – Stacked  $\text{N}_2$  isotherm plot for Pt/SBA-15 series**  
 (Samples offset by  $200 \text{ cm}^3 \text{ g}^{-1}$  by metal loading for clarity)



**Figure 3.8 (c) – Stacked N<sub>2</sub> isotherm plot for Pt/KIT-6 series**  
 (Samples offset by 500 cm<sup>3</sup> g<sup>-1</sup> by metal loading for clarity)

The isotherms of each material adhere closely to the original parent support. Hysteresis loops inherent to SBA-15 and KIT-6 mesoporous systems also retain their founding characteristics, highlighting the preservation of support hierarchical infrastructure after metal impregnation.

A decrease in BET support surface area is observed with increasing Pt loading (**Figure 3.9**). Due to the introduction of meso- and microporosity to SBA-15 and KIT-6 systems, the observed loss upon impregnation is more substantial, in comparison with the amorphous variant. Pore blocking within meso- and micropores can be blamed for this heightened loss of surface area. KIT-6 is expected to suffer a lowered percentage loss (*with respect to SBA-15*), as the introduction of interconnected mesopore architectures decreases the probability of total channel blocking with all pores accessible from multiple pathways. The likelihood of pore blockage increases with SBA-15, due to the long, parallel nature of said channels. Amorphous silica samples experience negligible surface area variances,

signifying potentially larger metal nanoparticles present only on the external support surface. Although alluded to in **Table 3.3**, the effects of support surface area on particle size and dispersion will be discussed in **Section 3.2.2.4**.

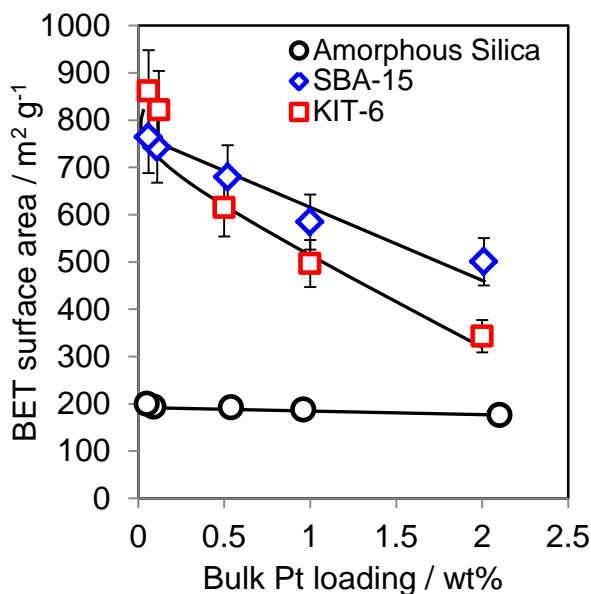


**Figure 3.9 – Tracking changes in BET support surface area with metal loading**

Earlier we stated that KIT-6 systems should display lowered surface area losses (*with respect to SBA-15*), however on closer inspection of **Figure 3.9** this does not appear to be the case. In order to explain this, the contribution of both meso- and microporous domains to the total surface area has been examined (**Figure 3.10**) through t-plot analysis.

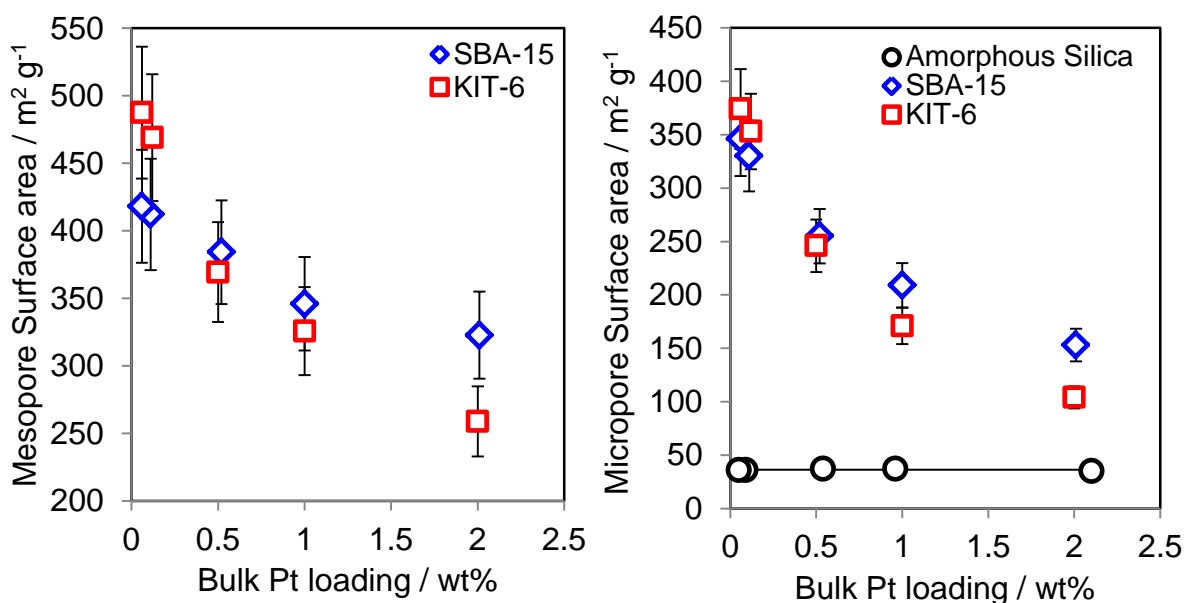


**Figure 3.10 – Changes in mesopore (Left) and micropore (Right) surface area with metal loading**



**Figure 3.10** clearly shows an inverse relationship between Pt loading and meso-/micropore surface areas for Pt/meso-silicas, with the latter demonstrating significantly diminished values. Pt impregnation results in a 56% and 72% decrease in support micropore surface area for SBA-15 and KIT-6 respectively (at 2 wt. % metal loading), followed by a 22% and 40% drop in mesopore surface area. This can be explained by an initial preference for Pt nucleation (and subsequent nanoparticle formation) in the micropores at sub-3nm nanoparticle sizes.<sup>14, 15</sup> Post-3nm Pt nanoparticles proceed to occupy the mesoporous domain, purely by steric factors alone, explaining the observed drop in mesopore surface area at bulk metal loadings >0.5 wt. %. The amorphous silica micropore surface area demonstrates negligible variation over all metal loadings, indicating Pt nanoparticle population at the support external surface exclusively.

No apparent change in average mesopore size is observed with Pt loading, as shown by the BJH pore size distribution plots in **Figure 3.11**. At bulk metal loadings <0.5 wt. %, SBA-15 and KIT-6 demonstrate a small peak at approx. 1.2-1.4 nm, indicative of micropores within the support walls. As metal loading increases, this peak disappears thus indicating the filling of micropores and further supporting evidence for **Figure 3.10**.

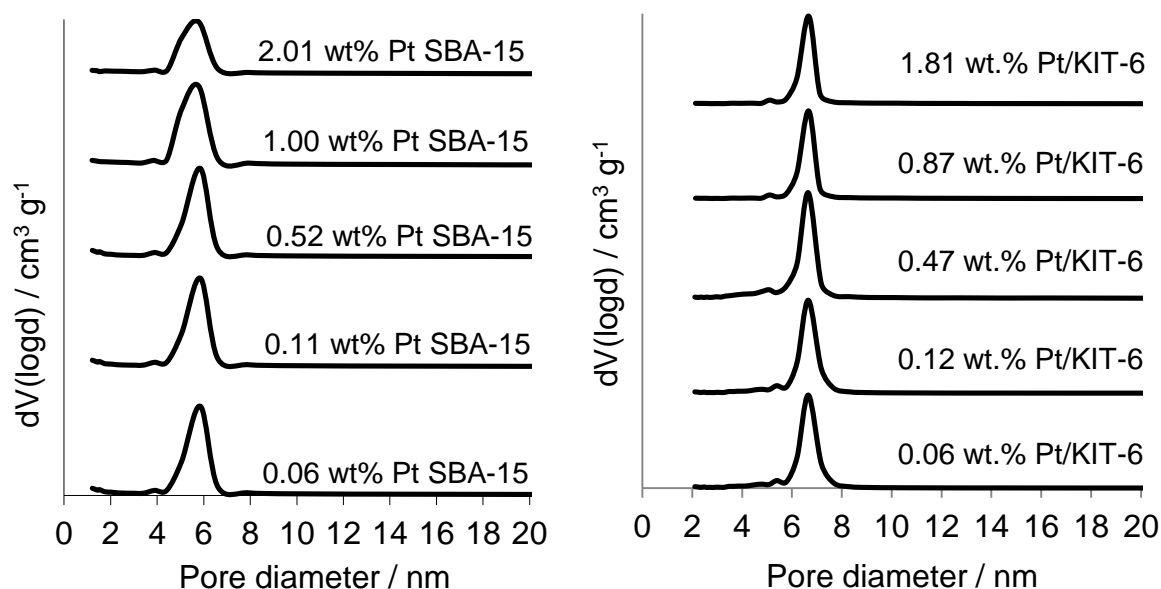


**Figure 3.11 – BJH pore size distributions for Pt impregnated SBA-15 (Left) and KIT-6 (Right). Offset for clarity**

### 3.2.2.4 Carbon monoxide pulse chemisorption

CO chemisorption was used to determine platinum dispersion values for all silica-based samples. The probe molecule, carbon monoxide, binds to platinum sites on the support surface in an atop fashion. A Pt:CO stoichiometry of 0.68 was applied to all calculations. This was theoretically derived, experimentally observed in the literature, from atop adsorption of CO forming a maximum  $\frac{7}{10}$  monolayer coverage. The presence of unfavourable repulsive lateral interactions between probe molecules prevents full monolayer saturation.<sup>16,17</sup>

**Table 3.4** – Dispersion and average Pt particle size calculated from CO titration

Support	Pt loading / wt. %	Dispersion / %	Average particle size / nm
aSiO <sub>2</sub>	2.10	10.0 (± 1)	15.6 (± 0.2)
aSiO <sub>2</sub>	0.96	14.7 (± 1)	11.7 (± 0.2)
aSiO <sub>2</sub>	0.54	20.0 (± 1)	7.7 (±0.2)
aSiO <sub>2</sub>	0.09	44.4 (± 1)	3.4 (± 0.2)
aSiO <sub>2</sub>	0.05	52.4 (± 2)	3.0 (± 0.2)
SBA-15	2.01	14.9 (± 1)	14.3 (± 0.2)
SBA-15	1.00	18.3 (± 1)	8.0 (± 0.2)
SBA-15	0.52	31.8 (± 1)	4.2 (± 0.2)
SBA-15	0.11	70.9 (± 2)	2.4 (± 0.2)
SBA-15	0.06	80.5 (± 3)	1.9 (± 0.2)
KIT-6	1.81	17.9 (± 1)	8.6 (± 0.2)
KIT-6	0.87	25.5 (± 1)	5.7 (± 0.2)
KIT-6	0.47	39.2 (± 1)	3.8 (± 0.2)
KIT-6	0.12	80.6 (± 3)	1.8 (± 0.2)
KIT-6	0.06	84.1 (± 3)	1.6 (± 0.2)

Metal dispersions were calculated using **Equation 2.6 (Chapter 2)**. Due to the versatility of this technique, additional Pt particle size data can be obtained via extrapolation from the total volume of chemisorbed CO and insertion of these values into **Equation 2.7 (Chapter 2)**. Average particle size and metal dispersion data for all samples can be found in **Table 3.4**.

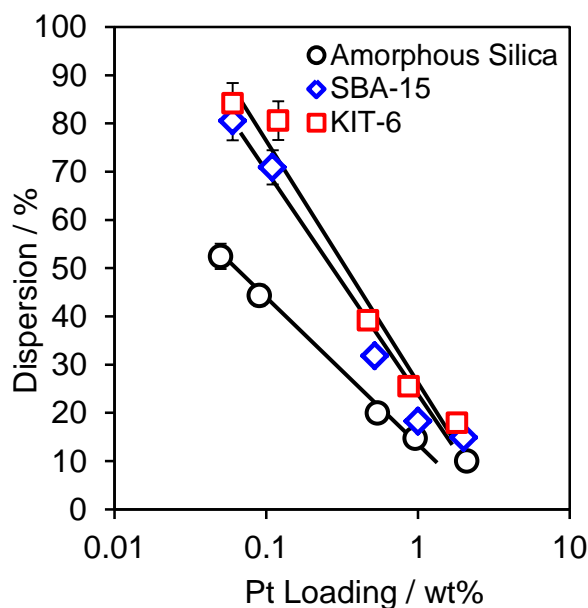


**Figure 3.12 – Influence of Pt loading and support architecture on Pt dispersion**

**Figure 3.12** highlights an inverse correlation between dispersion (*and thus particle size*) and metal loading across all samples. It can be stated that increasing support surface area, via the introduction of mesoporosity, plays a beneficial role in metal dispersion enhancement. Furthermore, the importance of internal support structure cannot be underestimated. For equivalent metal loadings, a clear decrease in particle size can be observed on transition from SBA-15 to KIT-6. Channel interconnectivity, inherent to KIT-6, affords modified diffusion characteristics for the metal precursor upon impregnation and subsequent post-treatment procedures. The possibility of multiple pathways through the support lowers the localised concentration of metal precursor, thus hindering nucleation and sintering phenomena. The probability of Pt nanoparticle migration is enhanced in SBA-15. The nature of the straight, non-connected channels affords two possible avenues for precursor introduction within said channels, thus encouraging greater odds for nucleation, explaining an increase in particle size for SBA-15 versus KIT-6.<sup>18,19</sup>

### 3.2.2.5 X-ray photoelectron spectroscopy (XPS)

XPS was used as the principle technique to quantify the surface oxidation state of the supported Pt nanoparticle samples. The Pt 4f XP spectra are shown in **Figure 3.13** for all three silica supports. Employing two different x-ray excitation sources (Mg versus Al  $K_{\alpha}$ ) provides a platform to determine the distribution of various surface oxidation states, utilising the different Pt 4f photoelectron sampling depths of each source.

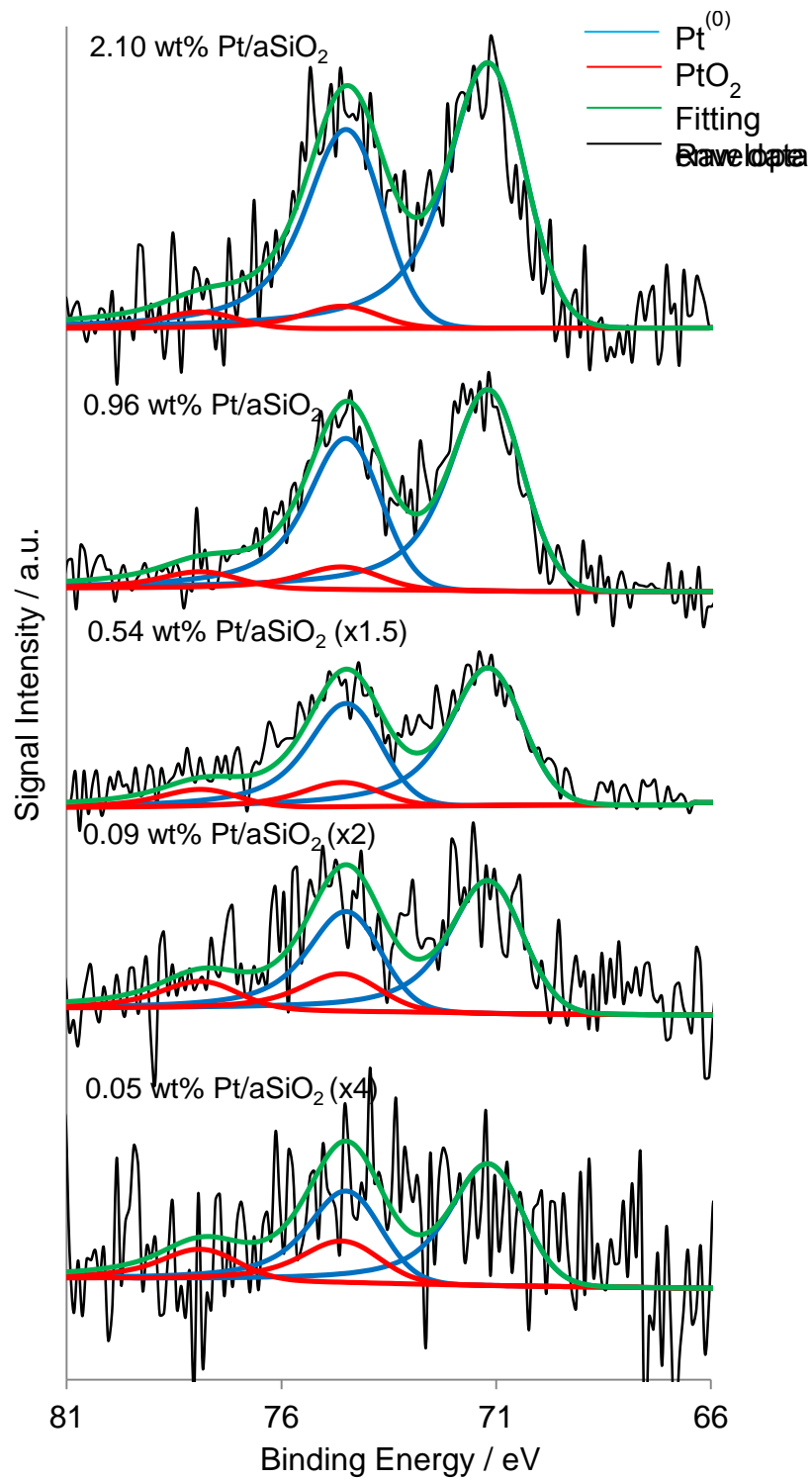


**Figure 3.13 (a) - Stacked Pt 4f XPS plot of Pt/amorphous silica series**

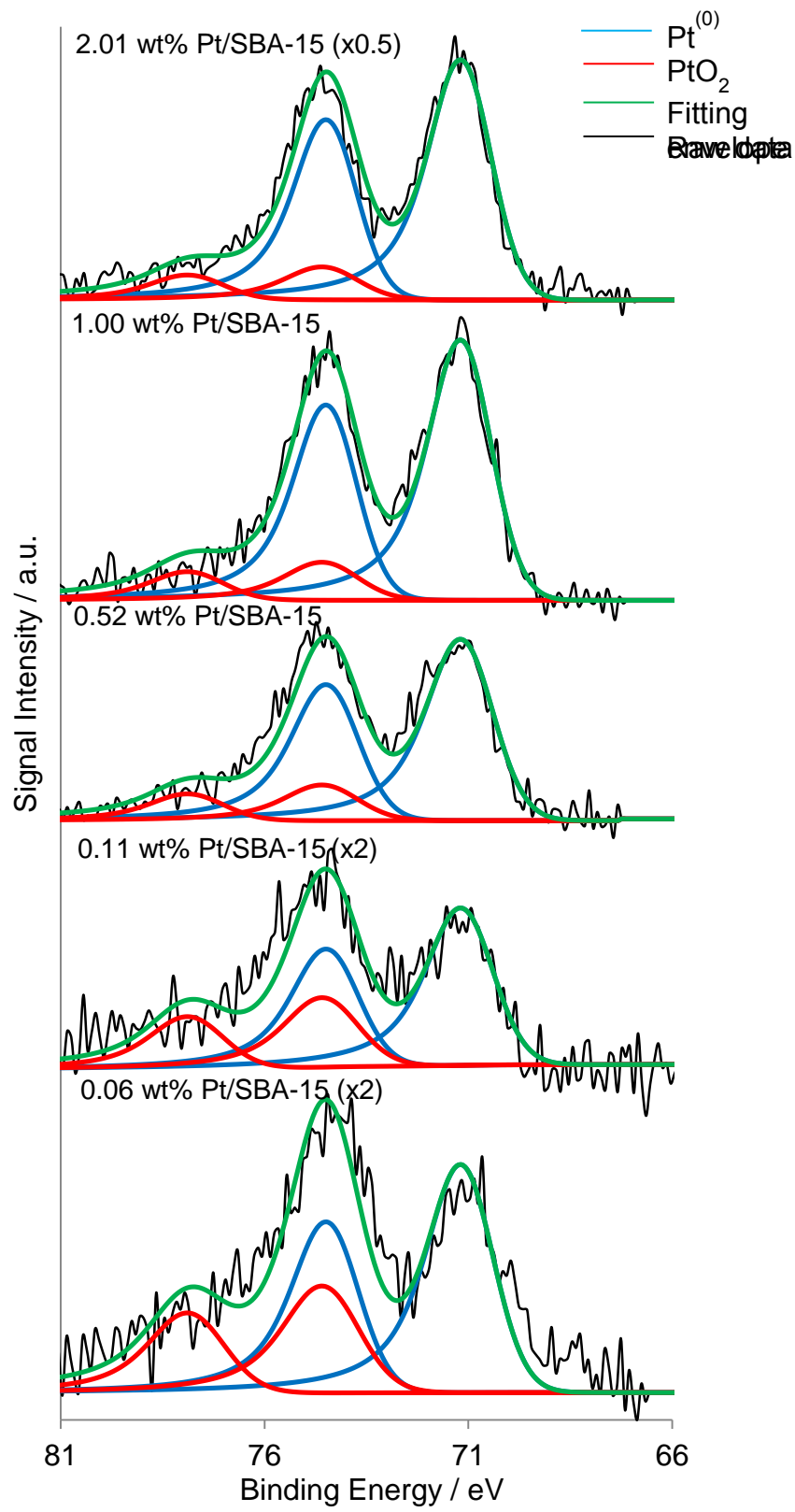
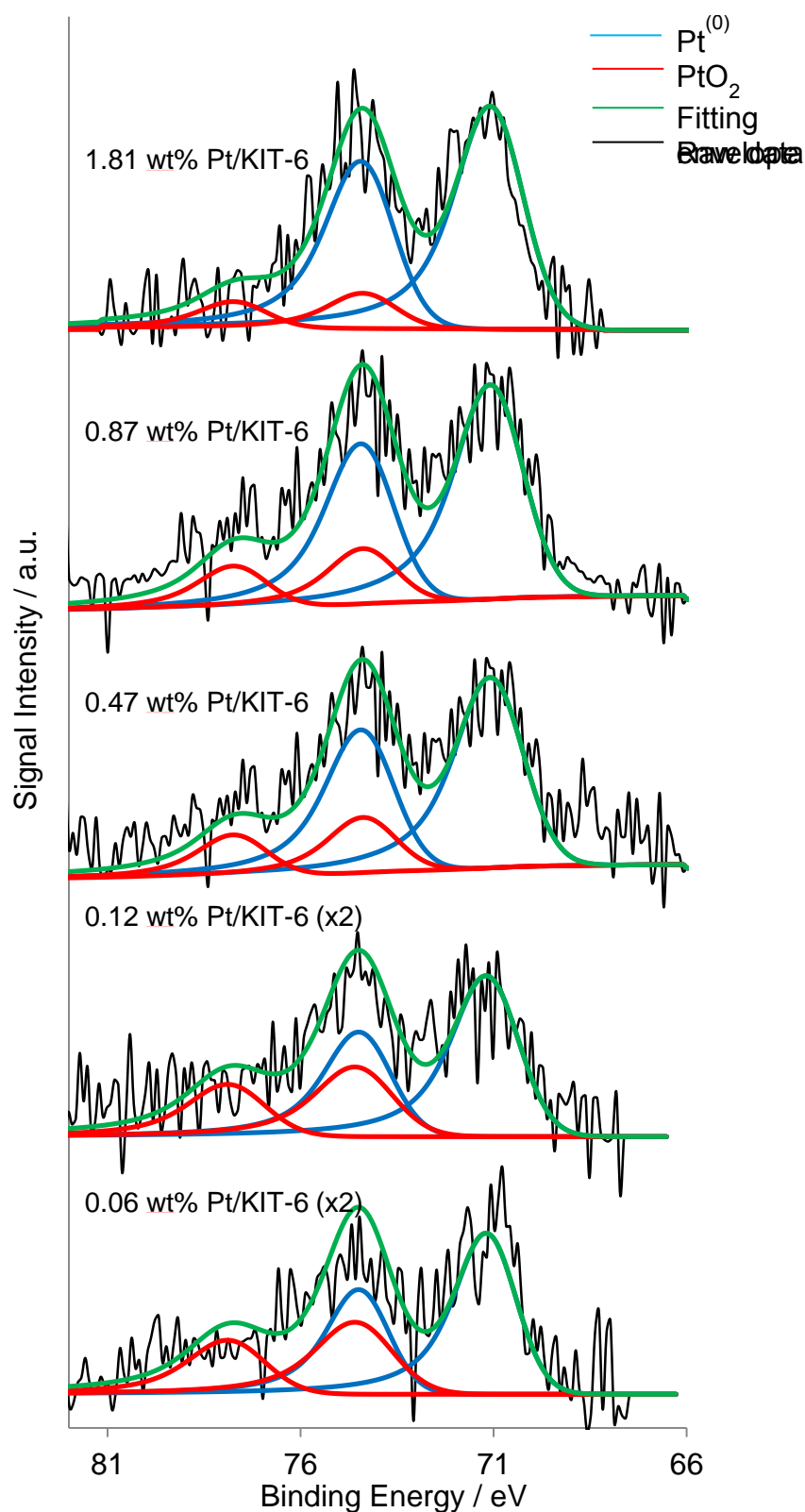


Figure 3.13 (b) - Stacked Pt 4f XPS plot of Pt/SBA-15 series



**Figure 3.13 (c) - Stacked Pt 4f XPS plot of Pt/KIT-6 series**

For all Pt/Silica X-ray photoelectron spectra, representative Pt 4f<sub>5/2,7/2</sub> doublet environments can be observed with a relative splitting of  $\pm 3.35$  eV<sup>20</sup>. Energy calibration and

background subtraction of each spectra to adventitious carbon has been applied (284.6 eV), with the Si region (103.4 eV) utilised as further verification. Comparative stacked plots of the Si 2p and O 1s regions for all parent supports show negligible changes in chemical environment or oxidation state population, thus evidencing physical characteristics to be the sole difference between silica families, *i.e.* surface area, mesoporosity and internal support architecture (**Appendix 1**). Decreasing metal loading sees the apparent introduction of an additional Pt environment shifted to higher energy. Increasing line broadening is witnessed as this component becomes more prominent, strengthening this deduction. An electron deficient, PtO<sub>2</sub>, species fits the observed binding energy for this component, and cannot be attributed to PtO due to the relative thermodynamic instability of this oxidation state under normal conditions.<sup>5</sup> **Figure 3.13** shows the apparent weighting of metallic Pt at 71.00 eV (indicated by a solid blue line on each plot) and PtO<sub>2</sub> at 74.4 eV (Indicated by a solid red line on each plot). Metallic Pt and PtO<sub>2</sub> standards were used to deduce the asymmetric line shape of each spectrum, assisting in peak identification for each species.

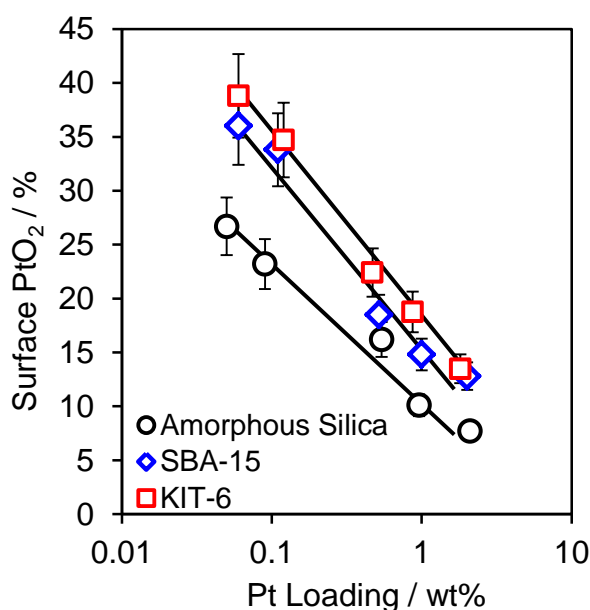


**Figure 3.14 – Influence of Pt loading and support architecture on surface PtO<sub>2</sub> content**

**Figure 3.14** shows an inverse correlation between surface PtO<sub>2</sub> content and metal loading for all silica systems. Augmented stabilisation of oxidic Pt species is observed upon introduction to high surface area supports with hierarchical architectures. As stated above, an increased support surface area provides more sites for initial nanoparticle nucleation, thus increasing Pt dispersion. This leads to a favourable decrease in surface energy, generating the PtO<sub>2</sub> phase in greater abundance.

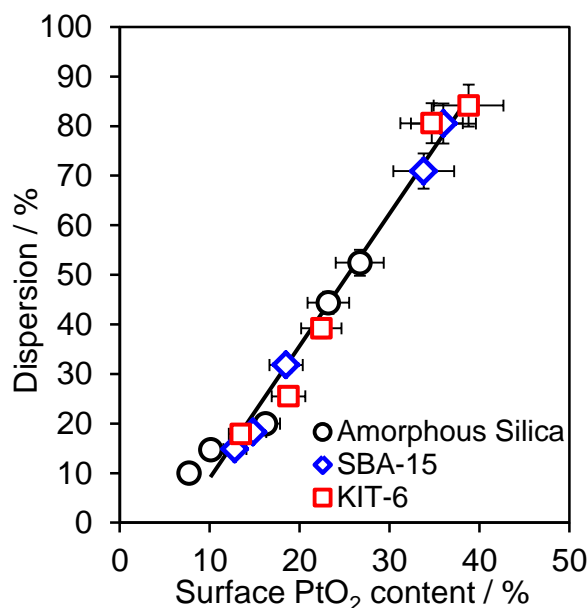


**Figure 3.15 – Relationship between surface PtO<sub>2</sub> content and metal dispersion**

A linear correlation between surface PtO<sub>2</sub> content (XPS) and metal dispersion (CO chemisorption) is demonstrated over mesoporous and amorphous silica families alike. Close scrutiny of **Figure 3.14** and **3.15** gives evidence for a Pt surface oxidation state heavily influenced by particle size.

The distribution of the PtO<sub>2</sub> phase was explored for the 0.1 wt. % Pt/amorphous silica sample via two different X-ray excitation sources (Mg versus Al K<sub>α</sub>). This technique offers two different Pt 4f photoelectron sampling depths, allowing for direct probing of PtO<sub>2</sub> thickness and determination of nanoparticle fine structure. A constant Pt<sup>(0)</sup> XP intensity signifies entirely homogeneous particles, however a variation in this intensity implies a core-shell structure. **Equations 3.1a** and **3.1b** allow for the calculation of the Pt<sup>(0)</sup> intensity for each excitation source, utilising the inelastic mean free path for the Pt 4f<sub>7/2</sub> photoelectrons ( $\lambda_{Pt} = 1.12 \text{ nm}^3$  and  $\lambda_{Pt} = 1.27 \text{ nm}^3$  for the Mg K<sub>α</sub> and Al K<sub>α</sub> respectively) and experimentally acquired intensities.

$$Intensity_{Pt}^{Actual \text{ Mg } K\alpha} = Intensity_{Pt}^{Bulk \text{ Pt}} \times \exp^{-\left[\frac{(number \text{ of } layers \times layer \text{ thickness})}{1.12}\right]} = 36.5 \text{ a. u.} \quad \text{Equation 3.1a}$$

$$Intensity_{Pt}^{Actual \text{ Al } K\alpha} = Intensity_{Pt}^{Bulk \text{ Pt}} \times \exp^{-\left[\frac{(number \text{ of } layers \times layer \text{ thickness})}{1.27}\right]} = 57 \text{ a. u.} \quad \text{Equation 3.1b}$$

As the proportion of metallic Pt is a function of the escape depth, it can be assumed that the nanoparticles comprise a Pt<sup>(0)</sup> core beneath a capping PtO<sub>2</sub> film, thus accounting for



the variation in Pt<sup>(0)</sup> intensities between excitation sources. Rearrangement of **Equations 3.1a** and **3.1b** into **Equations 3.2a** and **3.2b** allow an estimation of oxide thickness.

$$\frac{\text{Intensity}_{\text{Pt}}^{\text{Actual Mg Ka}}}{\text{Intensity}_{\text{Pt}}^{\text{Actual Al Ka}}} = \exp^{-\left[ \frac{(\text{number of layers} \times \text{layer thickness})}{1.11} - \frac{(\text{number of layers} \times \text{layer thickness})}{1.27} \right]} \quad \text{Equation 3.2a}$$

$$\ln \frac{36.5}{57} = - \left[ \frac{(\text{number of layers} \times \text{layer thickness})}{1.11} - \frac{(\text{number of layers} \times \text{layer thickness})}{1.27} \right] \quad \text{Equation 3.2b}$$

Using  $\alpha$ -PtO<sub>2</sub> unit cell parameters as a model, we assume a mean PtO<sub>2</sub> interlayer spacing of 0.255 nm:

$$\ln \frac{36.5}{57} = - \text{number of layers} \times \left[ \frac{(1.27 \times 0.255) - (1.11 \times 0.255)}{1.11 \times 0.255} \right]$$

Rearrangement yields **Equation 3.3**:

$$\text{Number of PtO}_2 \text{ layers} = \frac{0.45}{0.144} = 3 \quad \text{Equation 3.3: Estimation of oxide thickness}$$

These results seem to indicate a metal core-oxide shell fine structure. This is in line with typical Mott-Cabrera kinetics which predict a slow diffusion of oxygen into the bulk metal, with rapid formation of a surface metal oxide.<sup>21</sup> For the 0.1 wt. % Pt/amorphous silica sample, PtO<sub>2</sub> thickness is estimated at approximately 0.8 nm, equating to 3 crystalline oxide layers. As **Figure 3.14** and **3.15** establish the importance of nanoparticle size on surface PtO<sub>2</sub> content, one can hypothesise that as nanoparticle size increases, logically oxide layer thickness should decrease, due to decreasing surface oxide stability.

### 3.2.2.6 X-ray adsorption spectroscopy

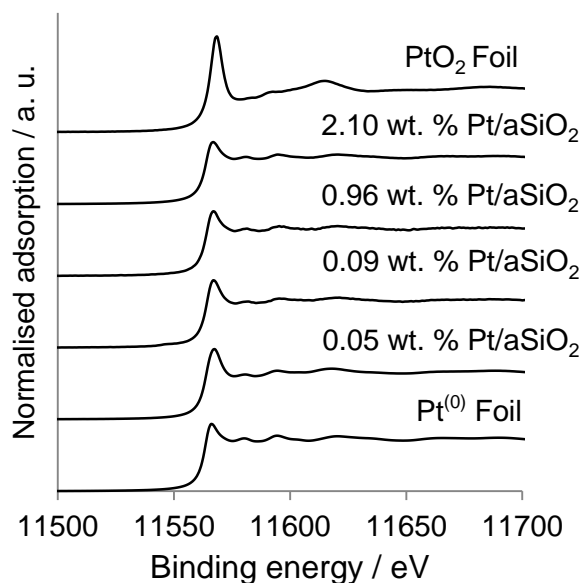


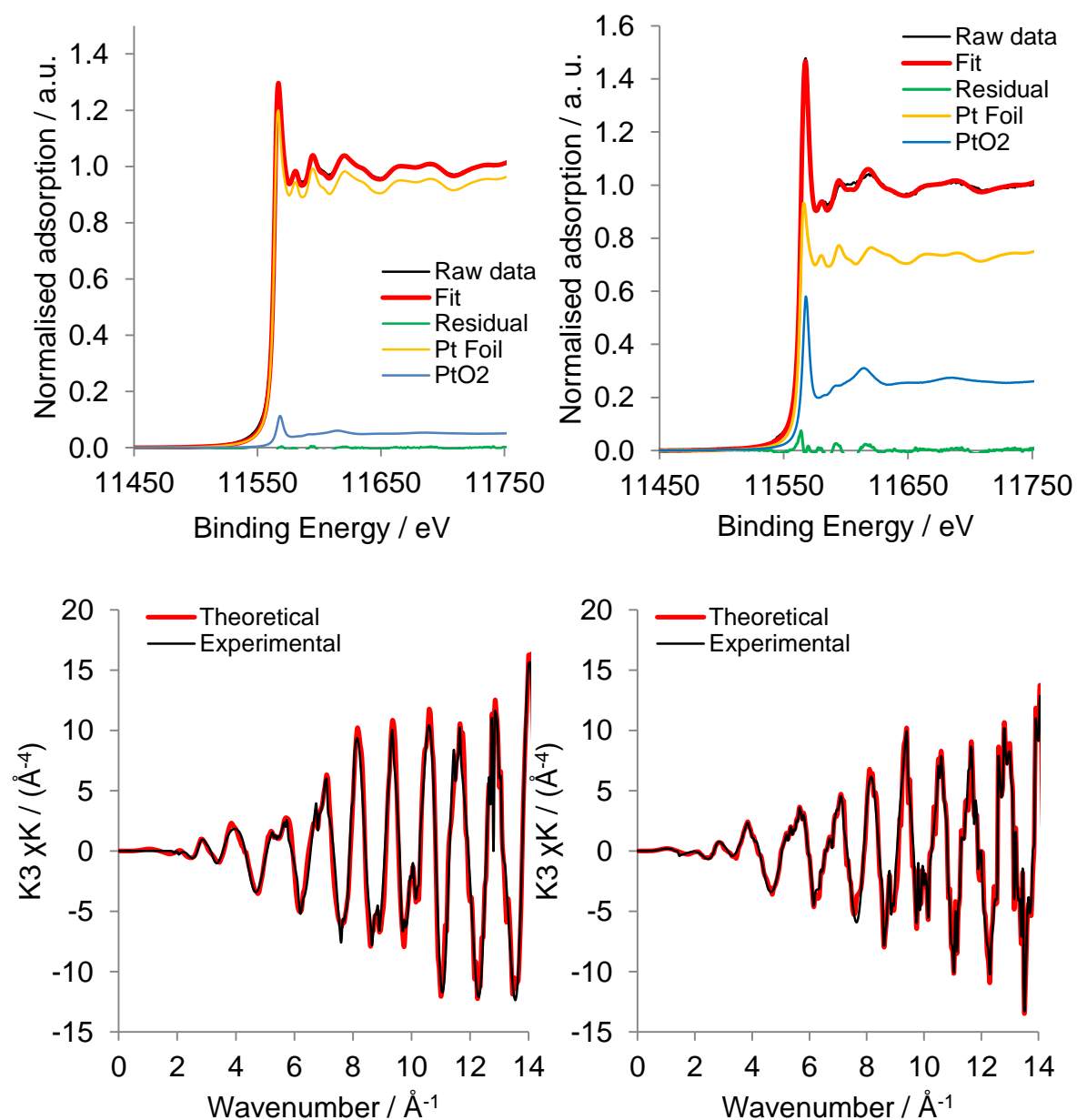
**Figure 3.16 – Stacked XAS normalised Pt L<sub>III</sub>-edge spectra Pt/amorphous silica series**

XAS is a powerful tool utilised to probe nanoparticle properties, including local environment, oxidation state and Pt coordination number.<sup>22</sup> **Figure 3.16** shows a background subtracted Pt L<sub>III</sub>-edge spectra for 2-0.05 wt. % loadings on amorphous silica, coupled with Pt<sup>(0)</sup> and PtO<sub>2</sub> standards for ease of comparison. Probing physical changes with XAS across Pt loading allows greater elucidation of catalyst behaviour for the oxidation and hydrogenation protocols discussed in this thesis. From previous studies, the Pd-catalysed selox of cinnamyl alcohol proceeds with greatest activity for materials with the lowest Pd loadings (highest fraction of surface PdO).<sup>23, 24</sup> Assuming this observation holds true for platinum, probing surface Pt oxidation state at low Pt loading (a regime where other techniques are less precise) permits accurate oxide content determination and hence greater certainty in TOF (Turnover frequency) quotation.

The background subtracted Pt L<sub>III</sub>-edge XANES regions indicate all samples exhibit metallic and oxidic character. As Pt loading decreases, oxidic character is shown to increase which is consistent with surface sensitive XPS values shown in **Figure 3.15**. Linear combination fitting of each normalised XANES region was employed to quantify total metal/surface oxide contribution. To aid in comparison, fits for the highest (2.10 wt.%) and lowest (0.05 wt.%) Pt/aSiO<sub>2</sub> samples can be found in **Figure 3.17**; values are quoted in **Table 3.5** showing excellent agreement with quoted XPS values.

**Table 3.5** – A direct comparison between surface PtO<sub>2</sub> determination using XPS and XANES

Support	Pt loading / wt. %	Surface PtO <sub>2</sub> content from XPS / %	Surface PtO <sub>2</sub> content from XANES / %
aSiO <sub>2</sub>	2.10	7.7	5.8
aSiO <sub>2</sub>	0.96	10.1	9.3
aSiO <sub>2</sub>	0.09	23.2	24.1
aSiO <sub>2</sub>	0.05	26.7	26.1



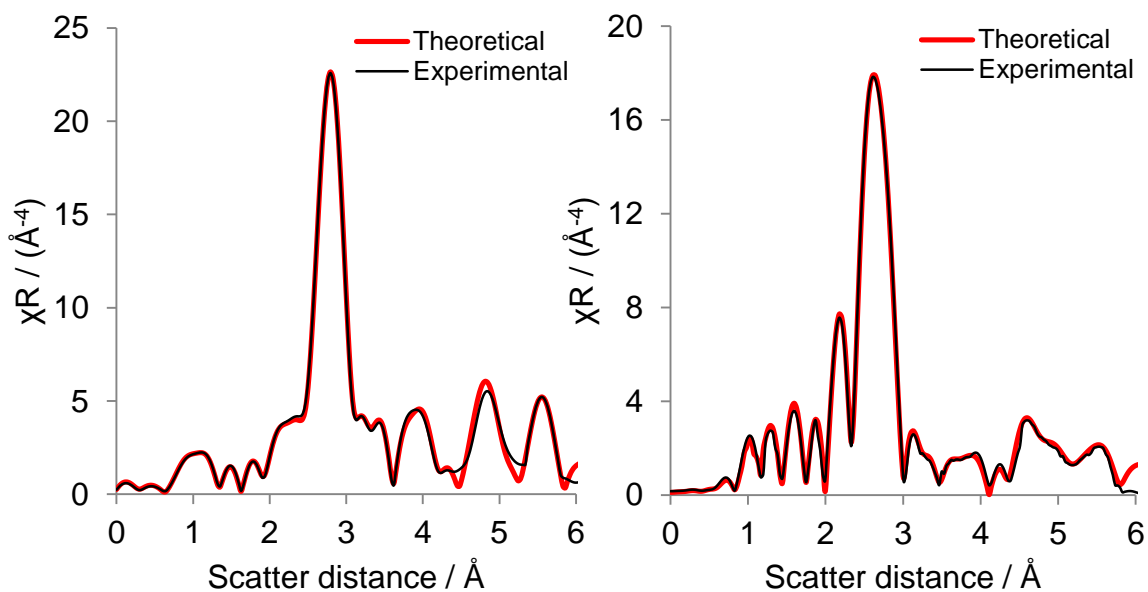


**Figure 3.17 – XANES fitting (top), EXAFS  $K^3$  weighted data (middle) and Fourier transform data (bottom) fittings for 2.10 wt. % (Left) and 0.05 wt. % Pt/aSiO<sub>2</sub> (Right)**

The EXAFS regions of Pt and PtO<sub>2</sub> foil standards were used to fit the  $Fm3m^{25}$  and  $Pnmm$  space groups respectively. In doing so, interatomic distances between neighbouring scatterers of metallic and oxidic character (i.e. coordination shell determination), Debye-Waller disorder factors and amplitude factors could be defined; these results are reported in **Table 3.6**. As previous XPS results have eluded to the presence of Pt<sup>(0)</sup> and Pt<sup>(IV)</sup> species, the combined usage of both standards permitted a model to be constructed, in which the relative contribution of each species could be adjusted (0-100 %) to produce the optimal fit. **Figure 3.17** reports the  $K^3$  weighted and Fourier transform fits for high and low Pt loading samples, with the corresponding coordination numbers, interatomic distances and Debye-Waller factors for the Pt/aSiO<sub>2</sub> series reported in **Table 3.6**. The Debye-Waller factor accounts for sample disorder such as thermal disorder within the structure (where lower values signify greater sample order). Fitting revealed increasing oxidic character with decreasing Pt loading/particle size (consistent with XPS analysis), however no sample was completely metallic or oxidic, thus indicating a combination from both species (XANES fitting further supports this conclusion). Pt<sup>(0)</sup> scattering species are present into the 3<sup>rd</sup> coordination shell. The extent of Pt population within coordination shells 1-3 are markedly lower than within the Pt<sup>(0)</sup> foil standard, thus indicating smaller Pt<sup>(0)</sup> containing nanoparticles. Pt<sup>(0)</sup> coordination number decreases with decreasing Pt loading, thus indicating decreasing nanoparticle size and increasing Pt<sup>(IV)</sup> character (consistent with previous XRD and XPS analysis). PtO<sub>2</sub> scattering species are shown to exclusively populate the 1<sup>st</sup> coordination shell. There is no

evidence for the presence of PtO<sub>2</sub> species in additional coordination shells, thus confirming previous dual-source XPS analyses – a Pt<sup>(0)</sup> core coated in a surface Pt<sup>(IV)</sup> oxide shell. Additionally, as Pt loading and nanoparticle size decrease, Pt<sup>(IV)</sup> population increases leading to an increase in surface PtO<sub>2</sub> thickness and surface oxide to metallic core ratio. This effect is predicted to be more substantial for low loading Pt nanoparticles, highly dispersed on mesoporous supports.

**Table 3.6** – Pt L<sub>III</sub>-edge EXAFS fitting parameters

Sample	CN1 Pt-Pt	CN2 Pt-Pt	CN3 Pt-Pt	CN4 Pt-Pt	CN1 Pt-O	Amplitude Factor
Pt <sup>(0)</sup> Foil	12	6	24	12	-	0.8258
2.10 wt.% Pt/aSiO <sub>2</sub>	10.27 (±0.51)	3.79 (±1.16)	8.35 (±1.54)	-	-	0.8258 / 0.7981
0.96 wt.% Pt/aSiO <sub>2</sub>	9.53 (±0.64)	3.02 (±1.20)	6.54 (±1.67)	-	-	0.8258 / 0.7981
0.09 wt.% Pt/aSiO <sub>2</sub>	7.66 (±0.71)	2.44 (±1.81)	4.07 (±2.15)	-	0.82 (±0.26)	0.8258 / 0.7981
0.05 wt.% Pt/aSiO <sub>2</sub>	7.09 (±0.67)	2.25 (±1.96)	3.96 (±2.18)	-	1.02 (±0.30)	0.8258 / 0.7981
PtO <sub>2</sub> Powder	2	-	-	-	4	0.7981

Sample	R1 Pt-Pt	R2 Pt-Pt	R3 Pt-Pt	R4 Pt-Pt	R1 Pt-O
Pt <sup>(0)</sup> Foil	2.76	3.91	4.79	5.53	-
2.10 wt.% Pt/aSiO <sub>2</sub>	2.765	3.91	4.789	-	2.015
0.96 wt.% Pt/aSiO <sub>2</sub>	2.763	3.91	4.786	-	2.016
0.09 wt.% Pt/aSiO <sub>2</sub>	2.762	3.91	4.785	-	2.015
0.05 wt.% Pt/aSiO <sub>2</sub>	2.762	3.91	4.786	-	2.016
PtO <sub>2</sub> Powder	3.04	-	-	-	2.02

Sample	σ1 Pt-Pt	σ2 Pt-Pt	σ3 Pt-Pt	σ4 Pt-Pt	σ1 Pt-O
Pt <sup>(0)</sup> Foil	0.0047 (±0.0005)	0.0061 (±0.0014)	0.0077 (±0.0010)	0.0228 (±0.0171)	-
2.10 wt.% Pt/aSiO <sub>2</sub>	0.0044 (±0.0006)	0.0046 (±0.0015)	0.0047 (±0.0010)	-	-
0.96 wt.% Pt/aSiO <sub>2</sub>	0.0046 (±0.0005)	0.0049 (±0.0009)	0.0055 (±0.0027)	-	-
0.09 wt.% Pt/aSiO <sub>2</sub>	0.0048 (±0.0004)	0.0061 (±0.0021)	0.0053 (±0.0023)	-	0.0088 (±0.0052)
0.05 wt.% Pt/aSiO <sub>2</sub>	0.0051 (±0.0005)	0.0068 (±0.0023)	0.0059 (±0.0029)	-	0.0085 (±0.0056)
PtO <sub>2</sub> Powder	0.0067 (±0.0006)	-	-	-	0.0050 (±0.0003)

CN = Coordination number, R = Interatomic distance from central Pt atom, σ = Debye-Waller factor, R-factor = Residual variance between the theoretical and experimental fits

### 3.2.3 Cinnamyl alcohol selox

The selective oxidation of cinnamyl alcohol,  $C_9H_{10}O$ , was used to probe the catalytic activity of all Pt/silica systems. The operational set-up and reaction conditions can be found in **Chapter 2**. Any deviations from this protocol are clearly stated. It must be noted that negligible conversion was observed for control experiments in the absence of supported platinum.

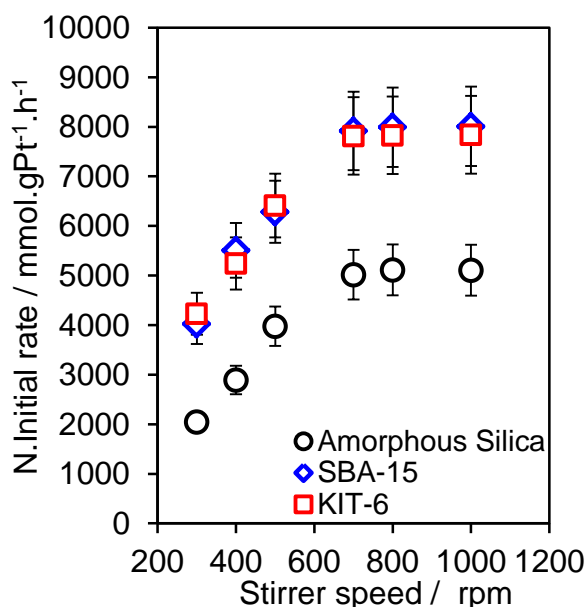


**Figure 3.18 – Influence of stirring rate on cinnamyl alcohol selective oxidation, normalised initial rates over approximate 0.10 wt. % Pt loading on various silica supports**

The elimination of external mass-transfer phenomena, such as reactant/product diffusion through the liquid-solid boundary of silica particles/in-pore diffusion for mesoporous systems, has been previously studied by our group and can be directly applied to this work with a high degree of reproducibility.<sup>14</sup> Agitation at stirrer speeds > 700 rpm were sufficient to eliminate external mass transport issues, ensuring the expressed reaction kinetics are “true” to catalytic activity (**Figure 3.18**).

#### 3.2.3.1 Active site heterogeneity

A hot filtration test was employed to rule out any possible homogeneously Pt-catalysed oxidation processes for these Pt/silica systems, using the most active 0.1 wt. % Pt loadings for each support. The reaction solution is filtered at reaction temperature, in order to minimise re-adsorption of Pt back onto the support,<sup>26</sup> without significantly disrupting reaction

kinetics if homogeneous processes do exist. A true heterogeneous catalyst should exhibit zero activity post-filtration. **Figure 3.19** demonstrates that catalyst removal through this procedure leads to a near instantaneous termination of substrate conversion, endorsing the postulation of a wholly heterogeneous catalyst.

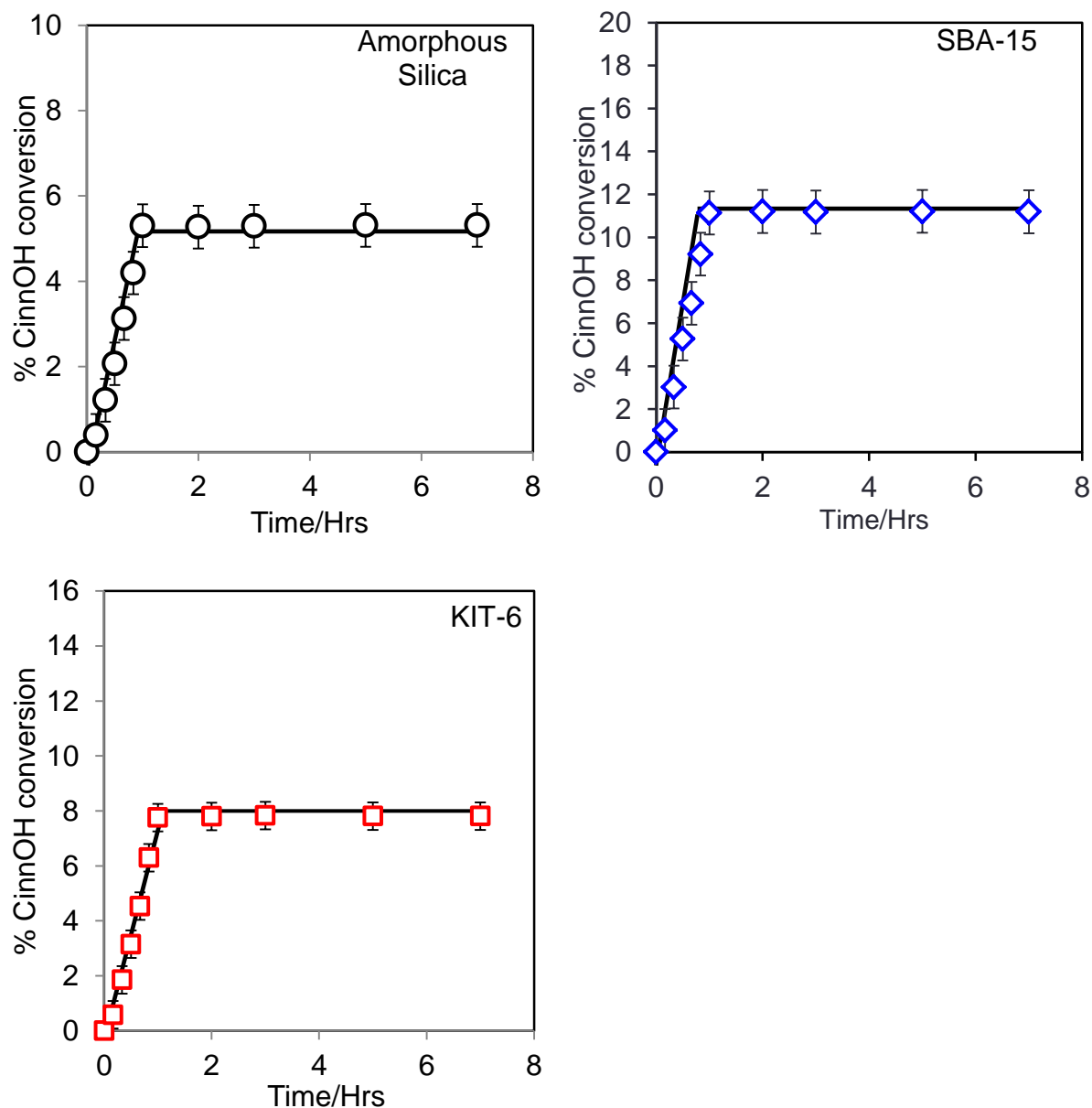


**Figure 3.19 – Hot filtration tests to determine the extent of Pt leaching in cinnamyl alcohol selective oxidation over 0.09 wt. % Pt/aSiO<sub>2</sub>, 0.11 wt. % Pt/SBA-15 and 0.12 wt. % Pt/KIT-6 (Catalyst removed after 60 minutes)**

### 3.2.3.2 Oxygen vs. air as primary oxidant

The catalytic activity for all three Pt/Silica families was gauged by contrasting changes in behaviour upon switching the main oxidant from air to pure O<sub>2</sub>. Artificial enhancement of support surface area, coupled with complimentary mesopore connectivity, plays a pivotal role in observed rate enhancements for Pt/SBA-15 and Pt/KIT-6 systems over the Pt/amorphous silica analogue. Irrespective of the applied oxidant, identical trends in activity enhancement apply, with Pt/SBA-15 and Pt/KIT-6 imparting a two-fold increase over the amorphous variant for both oxidants (**Figure 3.20**). It can be shown that selox activity is greatly impacted by support surface area and by extension, the level of connectivity within internal mesoporous architectures. As these two factors also control Pt dispersion and surface oxidation state density, with enhancements to reactant/substrate diffusion predicted through mesopore connectivity, these trends do not come as a surprise with previous studies reflecting this in the literature.<sup>14,27,28,29</sup> Cinnamyl alcohol selox reaction profiles for all three systems are shown in **Figure 3.21**, and show typical reaction behaviour for platinum group metal catalysts (PGM).

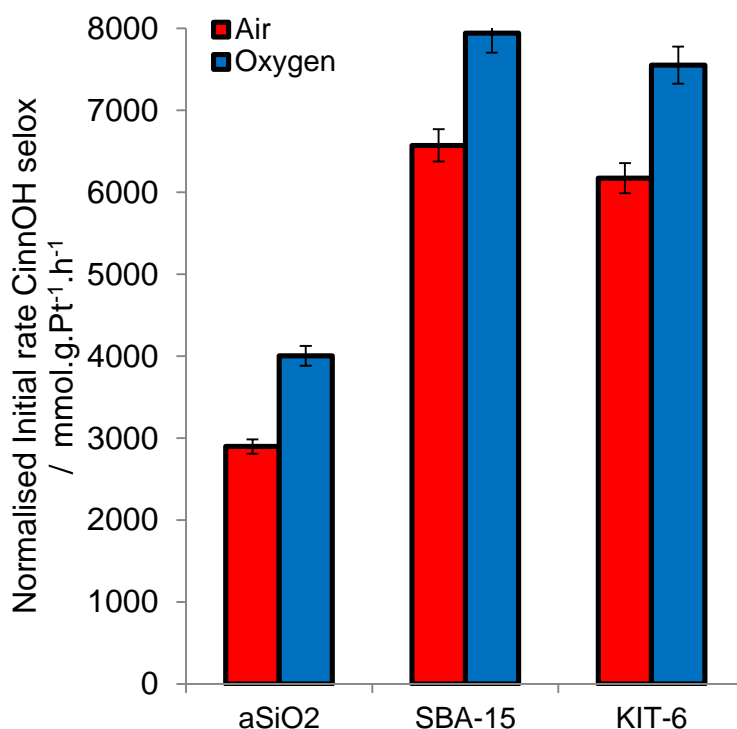


**Figure 3.20 – The effect of reaction atmosphere on cinnamyl alcohol initial activity over all three silica families at approximately 0.10 wt. % Pt loading**



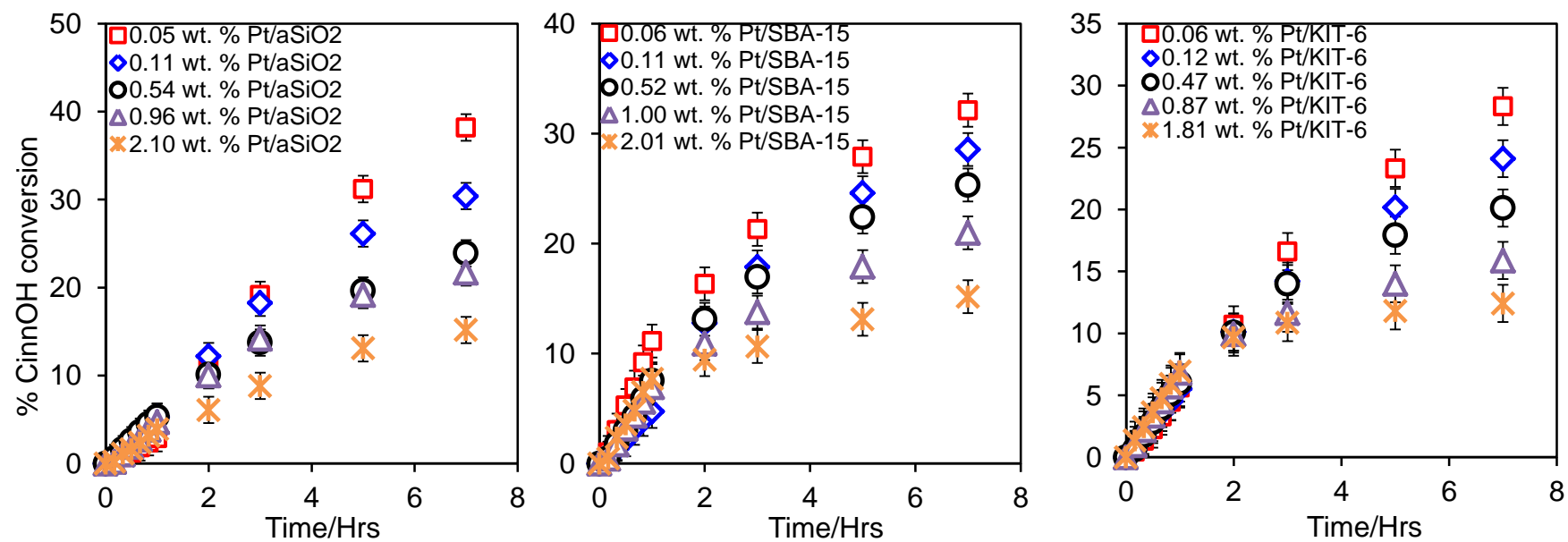
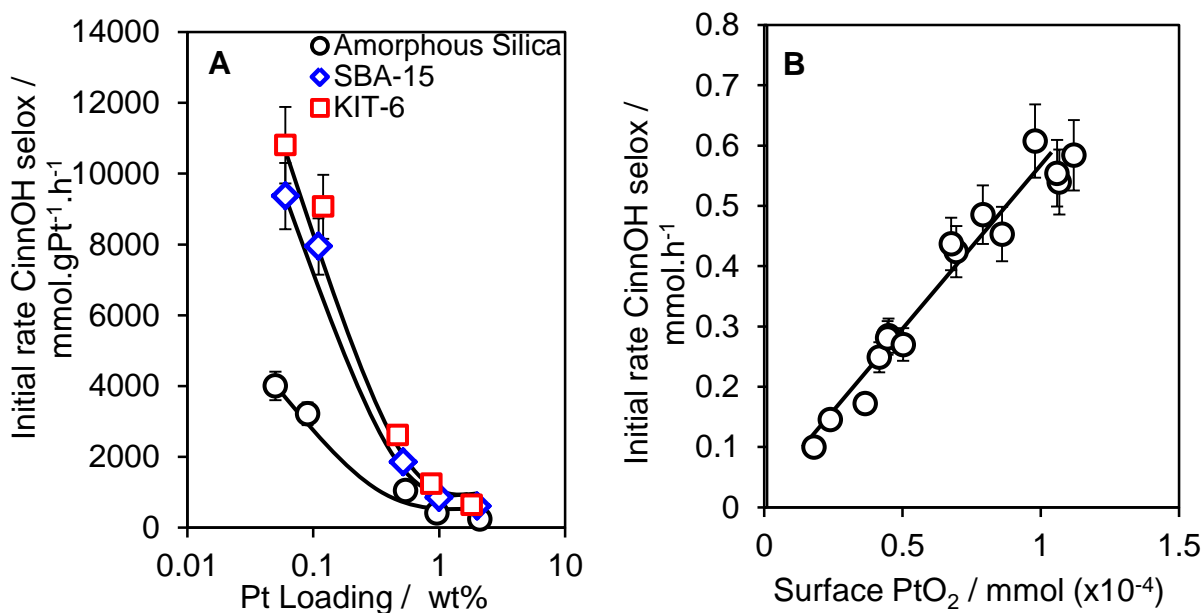


Figure 3.21 – Cinnamyl alcohol reaction profiles for amorphous silica (*Left*), SBA-15 (*Middle*) and KIT-6 (*Right*) series



**Figure 3.22 - Initial rate dependence of cinnamyl alcohol selox on (a) Pt loading and support architecture and (b) surface PtO<sub>2</sub> concentration**

**Figure 3.22(a)** highlights the discussed rate enhancement between amorphous and mesoporous silica systems under O<sub>2</sub> flow. Relative activity towards cinnamyl alcohol selox is apparent. Initial rates were determined from the linear portion of the conversion plot during the first hour of reaction time, chosen due to negligible catalyst deactivation at this point and with mass balances being calculated at > 97.5%. A clear, inverse correlation between activity and bulk metal loading is shown, again in fantastic agreement with other PGM nanoparticles in benzyl and allylic substrate oxidation.<sup>30,31,32</sup> Pt particle size, and by extension metal dispersion, is seen to dictate selox activity. There are drastic changes in particle size across the 0.05-2 wt. % loading range for all Pt/silica systems, accurate values shown in **Table 3.4**, accounting for the sudden increase in selox activity below the 3 nm size range. **Figure 3.22(b)** attempts to quantify the relationship between surface PtO<sub>2</sub> concentration and activity. A linear increase in activity with increasing surface oxide density suggests modulation of the predominant geometry and electronic properties of Pt nanoparticles at low size regimes. From dual anode XPS studies, we calculated oxide layer coverage of 0.8 nm for sub-3 nm Pt nanoparticles, however **Figure 3.21** indicates that this finding seems applicable across all Pt/silica families (at a similar size range). Highly dispersed Pt nanoparticles thus undergo preferential surface oxidation, in order to minimise total surface energy. This effect is highly dependent on particle size and dispersion, with larger Pt nanoparticles present in the metallic form and demonstrating diminished selox capacity. A strong support-activity functionality is

witnessed, ranging from  $\sim 4,000 \text{ mmol.gPt}^{-1}.\text{h}^{-1}$  for the best low area, amorphous Pt/SiO<sub>2</sub>,  $\sim 9,000 \text{ mmol.gPt}^{-1}.\text{h}^{-1}$  for high area mesoporous Pt/SBA-15, peaking at  $11,000 \text{ mmol.gPt}^{-1}.\text{h}^{-1}$  through pore interconnection in Pt/KIT-6. Tailoring support surface area and mesoporosity provides an avenue for promoting selox performance through augmented active site density and/or enhanced substrate diffusion.

So far the importance of particle size and metal dispersion has been established, with hints toward a probable active site for this reaction. In order to fully elucidate the nature of the active site under selox conditions, TOFs were calculated for all Pt/silica catalysts tested thus far. In recent years, the role of Pt<sup>(0)</sup> versus Pt<sup>(IV)</sup> in Pt-catalysed alcohol selox has been contested<sup>2,4,33</sup>. In order to clarify this ambiguity, calculation of TOFs to the normalised initial rates based on the concentration of either (i) surface PtO<sub>2</sub> in the as-synthesised catalysts (XPS), or (ii) the total surface Pt metal from complete surface reduction (CO chemisorption). In the absence of mass-transport limitations, positive identification of the true active species should yield a constant TOF, independent of silica support or Pt loading, with activity proportional to active site density. The presence of multiple active sites, mass-transport limitations and/or in-pore diffusion restrictions, will result in a variable TOF due to a non-linear complex interplay between each active component. These results are shown in **Figure 3.23**.

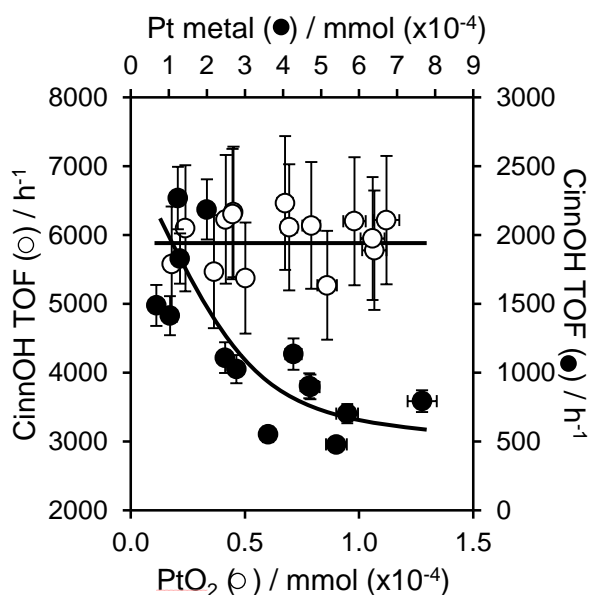


**Figure 3.23 – Cinnamyl alcohol aerobic selox turnover frequencies expressed as a function of surface Pt metal or PtO<sub>2</sub> content for Pt/aSiO<sub>2</sub>, Pt/SBA-15 and Pt-KIT-6 catalysts**

Increasing surface density of metallic Pt highlights a steady decay in TOF, whereas normalisation to surface  $\text{PtO}_2$  reveals a constant TOF of  $\sim 6000 \text{ h}^{-1}$ . Not only does this provide evidence of an oxide active site, but also shows that mass-transport and pore diffusion limitations are not apparent for this reaction regime. Initial rates are dictated purely by the amount of oxide present on each Pt nanoparticle, eliminating internal support structural effects. A result which is in excellent agreement with derived Pd/silica systems, which sport a similar TOF of  $\sim 5800 \text{ h}^{-1}$ .<sup>14,23</sup> This finding is interesting as it contrasts with earlier studies, which erroneously conclude that palladium is far superior to platinum in selox capability. It must be noted that Pt and Pd catalysts at similar metal loadings were used in this determination. Such comparisons are unfair as the relative molecular mass of Pt (195) is approximately double that of Pd (106), leading to a reported 50% decrease in quoted literature values.<sup>34,35</sup> We propose the rate-enhancements on switching from amorphous to mesoporous supports originate from the inherent stabilisation of  $\text{PtO}_2$  sites, with improved substrate diffusion through the support providing only negligible effect.

Catalytic selectivity towards the desired allylic aldehyde product is critical to the proposed commercial application of PGM-based selox catalysts. **Figure 3.24** shows representative selectivity plots for high and low Pt loadings, highlighting a high initial selectivity towards cinnamaldehyde ( $\sim 60\%$ ) over all Pt/silicas.

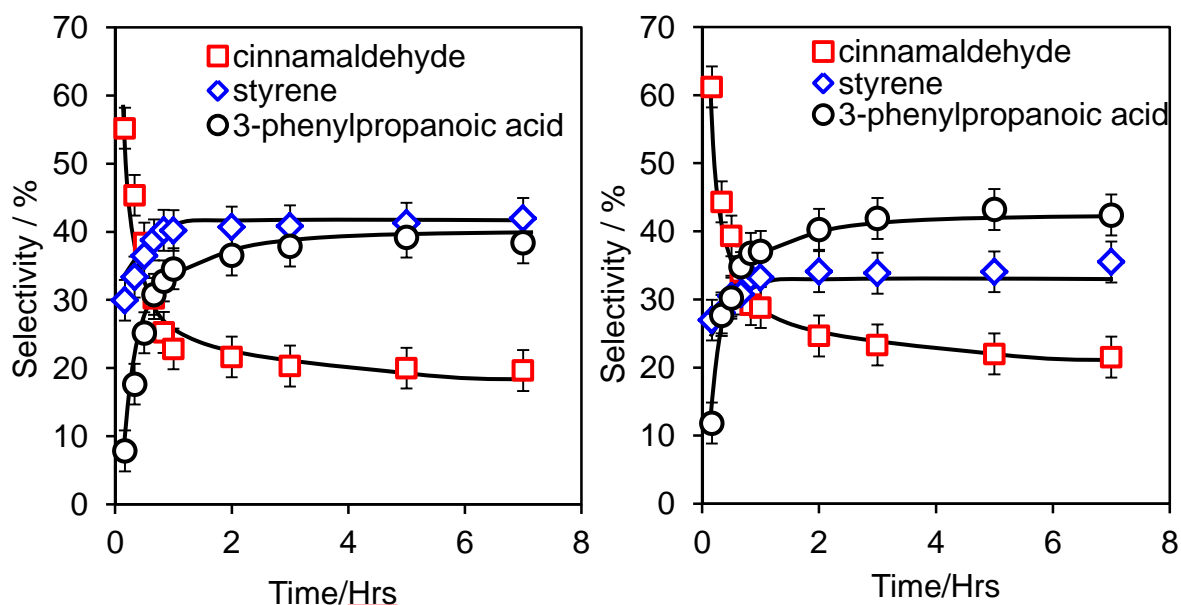


**Figure 3.24 – Representative selectivity profile as a function of reaction time showing major cinnamyl alcohol selox products over 2.10 wt. % (Left) and 0.09 wt. % Pt/aSiO<sub>2</sub> (Right) catalysts**

However, this high selectivity greatly diminishes to 25% during reaction, due to undesired styrene and 3-phenylpropanoic acid generation. The saturated carboxylic acid is likely to form via the hydrogenation of the C=C functionality, with subsequent over-oxidation yielding the carboxylic acid centre. Styrene must form via hydrogenolysis of the C-C bond. Direct comparison with Pd/Silica equivalents<sup>14,23</sup> indicate considerably higher levels of C=C centre hydrogenation over platinum, *again*, consistent with a known performance in platinum-catalysed liquid phase alkene hydrogenation.<sup>36</sup> The increasing generation of styrene during the cinnamyl alcohol selox of Pd and Pt/silicas demonstrates the presence of the metallic species,<sup>23,37</sup> thus indicating a potential *in-situ* reduction of surface PtO<sub>2</sub> active sites under reaction conditions.

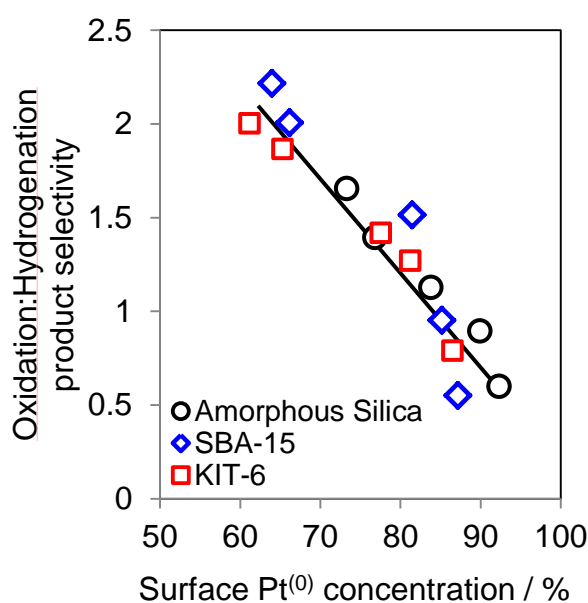


**Figure 3.25 – Detrimental impact of surface Pt<sup>(0)</sup> on selectivity to oxidation (cinnamaldehyde) versus hydrogenation (3-phenylpropanoic acid) products**

In order to determine the effect of zero-valent platinum species on the predominance of hydrogenation side-pathways within this reaction, the ratio of cinnamaldehyde to 3-phenylpropanoic acid was characterised as a function of surface Pt<sup>(0)</sup> concentration across all three Pt/silica analogues. **Figure 3.25** confirms a clear characteristic tendency towards hydrogenation versus oxidation products with an increasing extent of surface platinum reduction.

### 3.2.3.3 The role of catalyst pre-reduction on cinnamyl alcohol selox

The effect of an *in-situ* pre-reduction of Pt/silicas, prior to alcohol selox, was implemented to reinforce the postulation of a surface PtO<sub>2</sub> active site. Using previous literature arguments, the removal of any surface oxide should result in a substantial augmentation of catalytic activity and desired product selectivity.<sup>33</sup> If the hypothesis posed by this thesis is correct, catalytic performance should be greatly compromised.

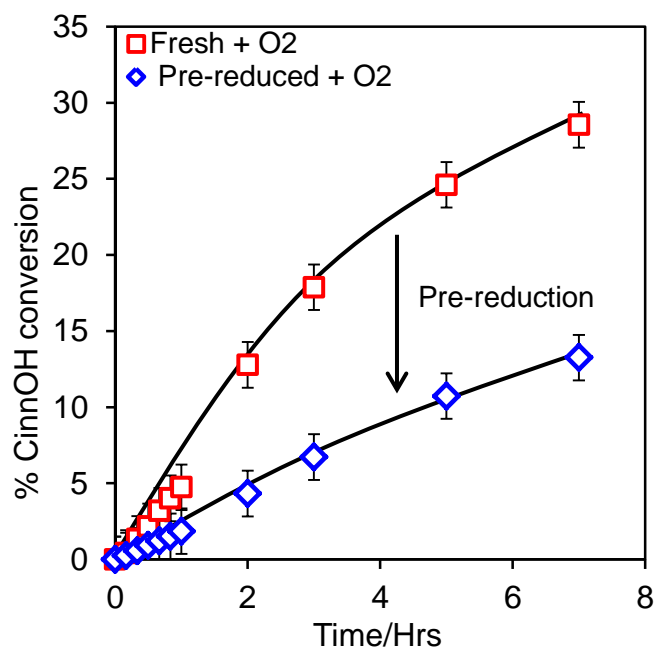


**Figure 3.26 – Cinnamyl alcohol selox reaction profiles over *in-situ* reduced 0.11 wt. % Pt/SBA-15 and control “fresh” catalyst under flowing O<sub>2</sub> (3 cm<sup>3</sup> min<sup>-1</sup>)**

**Figure 3.26** highlights the effect of pre-reduction on cinnamyl alcohol conversion over a 0.11 wt. % Pt/SBA-15 catalyst. Reduced catalysts were tested under flowing O<sub>2</sub> (3 cm<sup>3</sup> min<sup>-1</sup>) and catalytic activity compared against the corresponding unreduced samples (labelled fresh on the plot), in which N<sub>2</sub> was used instead of H<sub>2</sub> during *in-situ* treatments. Reactions were conducted in parallel.

This reaction plot provides a clear demonstration of the destructive effect of an *in-situ* reduction step. Substantial loss of catalytic performance is shown, although the introduction of flowing O<sub>2</sub>, *post-reduction*, allows the spontaneous regeneration of a small number of active sites, thus indicating that loss of oxide sites is not an inherently irreversible process. Control reactions with “fresh” samples gave equivalent activity and conversion parameters to those in the original study (**Figure 3.21**).

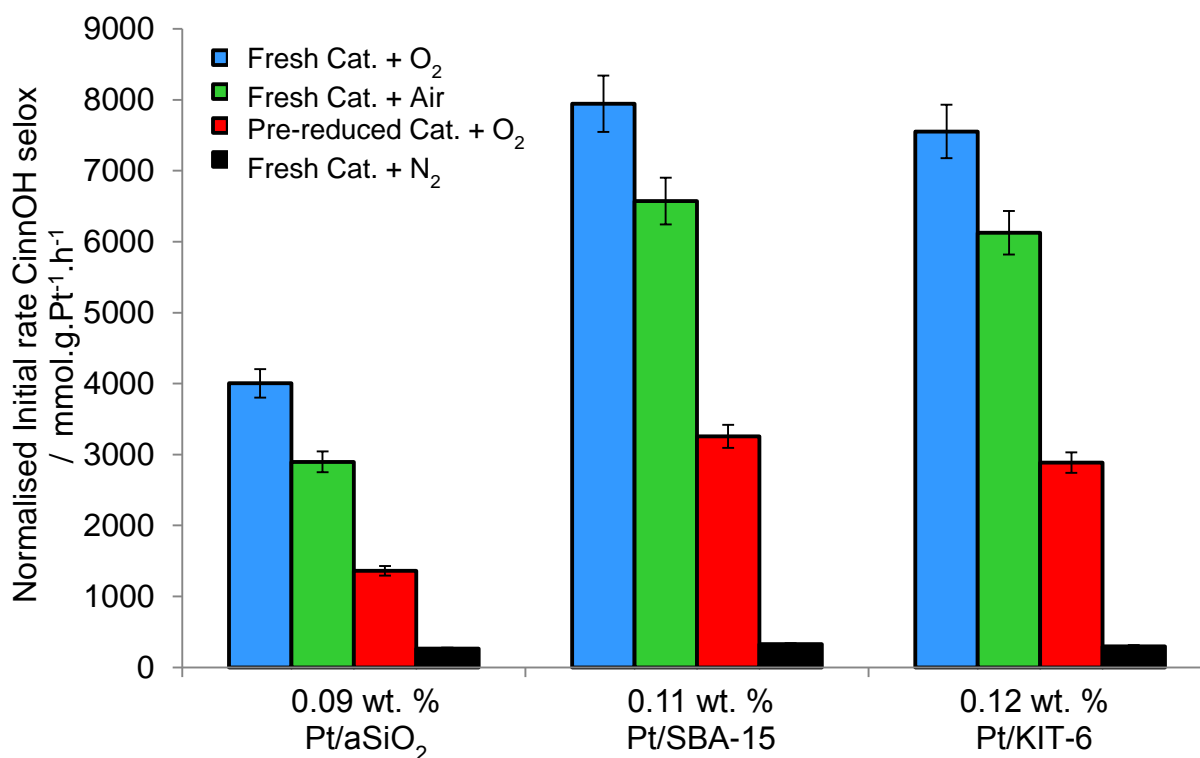


**Figure 3.27 – The effect of reaction atmosphere on cinnamyl alcohol initial activity over all three silica families at similar metal loadings**

The catalytic performance of Pt/silica catalysts in cinnamyl alcohol aerobic oxidation is greatly affected by the reaction atmosphere, illustrated by **Figure 3.27**. Initial rate determination highlights negligible catalytic activity under N<sub>2</sub> flow, with any conversion attributed to residual oxygen dissolved in the reaction solution. Catalysts under oxygen flow exhibit ~20-25% increased initial rates, wrt equivalent samples under air, possibly due to increased oxygen dissolution within the reaction solvent, increasing oxygen availability, thus hindering surface oxide deactivation. *In-situ* pre-reduction treatments show an adverse effect on activity, ~50% of all initial activity is lost. This effect becomes more severe as metal dispersion increases, demonstrating the following trend:

**KIT-6 > SBA-15 > Amorphous Silica**

Final cinnamyl alcohol conversions (*after 7 hours*) follow the same trend, with proportional losses of ~43%, 54% and 65% over “*fresh*” Pt-impregnated amorphous silica, SBA-15 and KIT-6 respectively.

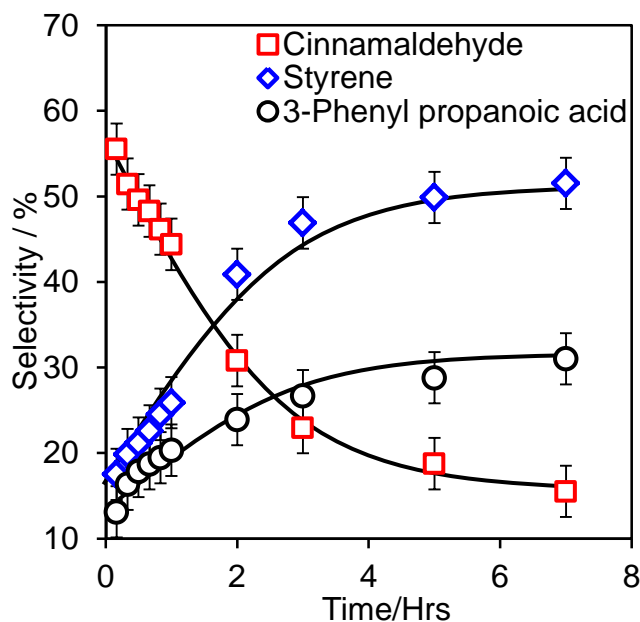


**Figure 3.28 – Representative selectivity profile as a function of reaction time showing major cinnamyl alcohol selox products over *in-situ* reduced 0.11 wt. % Pt/SBA-15 catalyst**

**Figure 3.28** highlights drastic changes in selectivity telemetry upon *in-situ* pre-reduction. The major products remain the same from Figure 3.24; however a 10% drop in cinnamaldehyde selectivity can be witnessed throughout the entire reaction. Interestingly, pre-reduction also diminishes 3-phenylpropanoic acid selectivity in favour of styrene formation. It is well known from the literature that metallic Pt promotes the hydrogenolysis pathway,<sup>38,39</sup> but it is unclear whether this reaction pathway is favoured due to the lack of hydrogen within the system (spilled over from –OH group conversion), thus inhibiting C=C hydrogenation pathways, or C-C scission being the predominant low-energy pathway under these conditions.

*In-situ* pre-reduction has been shown to impair catalytic activity for the selective oxidation of allylic alcohols, but also provides validation of a surface oxide active species. In tandem with poisoning phenomena, by CO and substrate adsorption to the catalyst surface, the *in-situ* reduction of PtO<sub>2</sub> surface species accounts for gradual catalyst deactivation.



### 3.2.4 Tailoring active species stability

Having identified surface  $\text{PtO}_2$  as the active species, the inherent stability and optimisation of this species is of paramount importance in the design of high efficiency Pt-based selox catalysts. The role of oxygen pressure on final product selectivity and substrate conversion levels allowed for further demonstration on the importance of the active species, demonstrated in **Figure 3.29**.

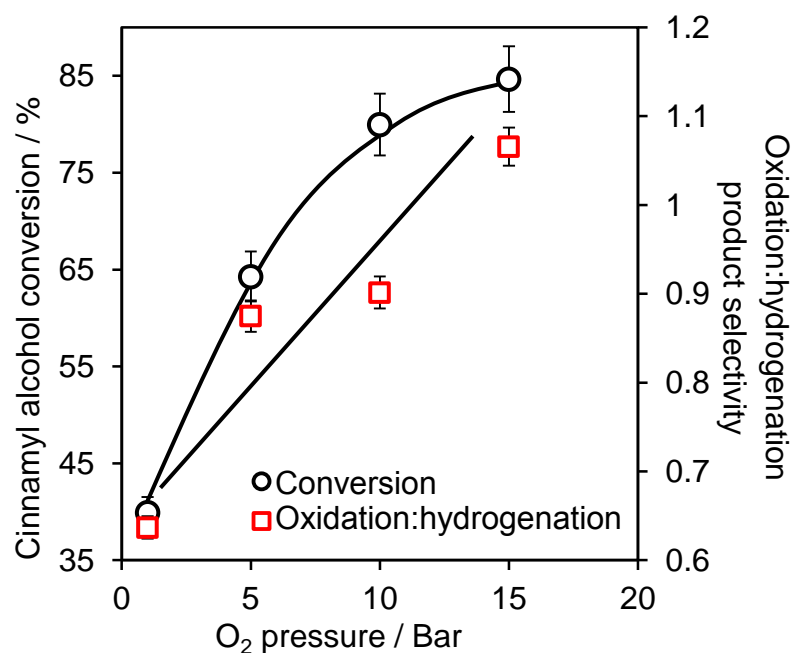


**Figure 3.29 – Influence of  $\text{O}_2$  reaction pressure on cinnamyl alcohol conversion and oxidation:hydrogenation product selectivity over a 0.05 wt.% Pt/aSiO<sub>2</sub> catalyst**

Increasing  $\text{O}_2$  partial pressure from 1 bar to 15 bar, increases substrate conversion by an additional 45% (over 7 hours), whilst increasing the oxidation:hydrogenation product selectivity from 0.6 to 1.1. An increased  $\rho\text{O}_2$  solubilises more oxygen within the reaction solution, and hence oxygen accessibility to the catalyst surface and substrate is substantially enhanced.<sup>40</sup> At raised pressures, surface  $\text{PtO}_2$  is far more stable due to an artificially elevated local oxygen concentration around each active site. When this is coupled with a lower affinity for the hydrogenation pathway, liberated H-species from  $-\text{OH}$  bond cleavage are readily converted into water and hence play a minimal part in on-stream active site deactivation. The possibility of surface  $\text{PtO}_2$  reduction still exists, but with increasing oxygen pressure, the likelihood of site re-oxidation is greatly improved.

XPS studies of “fresh” and spent catalyst, as seen in **Figures 3.30** and **3.31**, relate surface PtO<sub>2</sub> stability with O<sub>2</sub> pressure and allow on-stream deactivation to be monitored. Catalyst samples were analysed prior to reaction, to determine oxide content at  $t=0$ , with samples also drawn at  $t=0.5$  hours and  $t=7$  hours for reactions held at 1 and 10 bar O<sub>2</sub>.

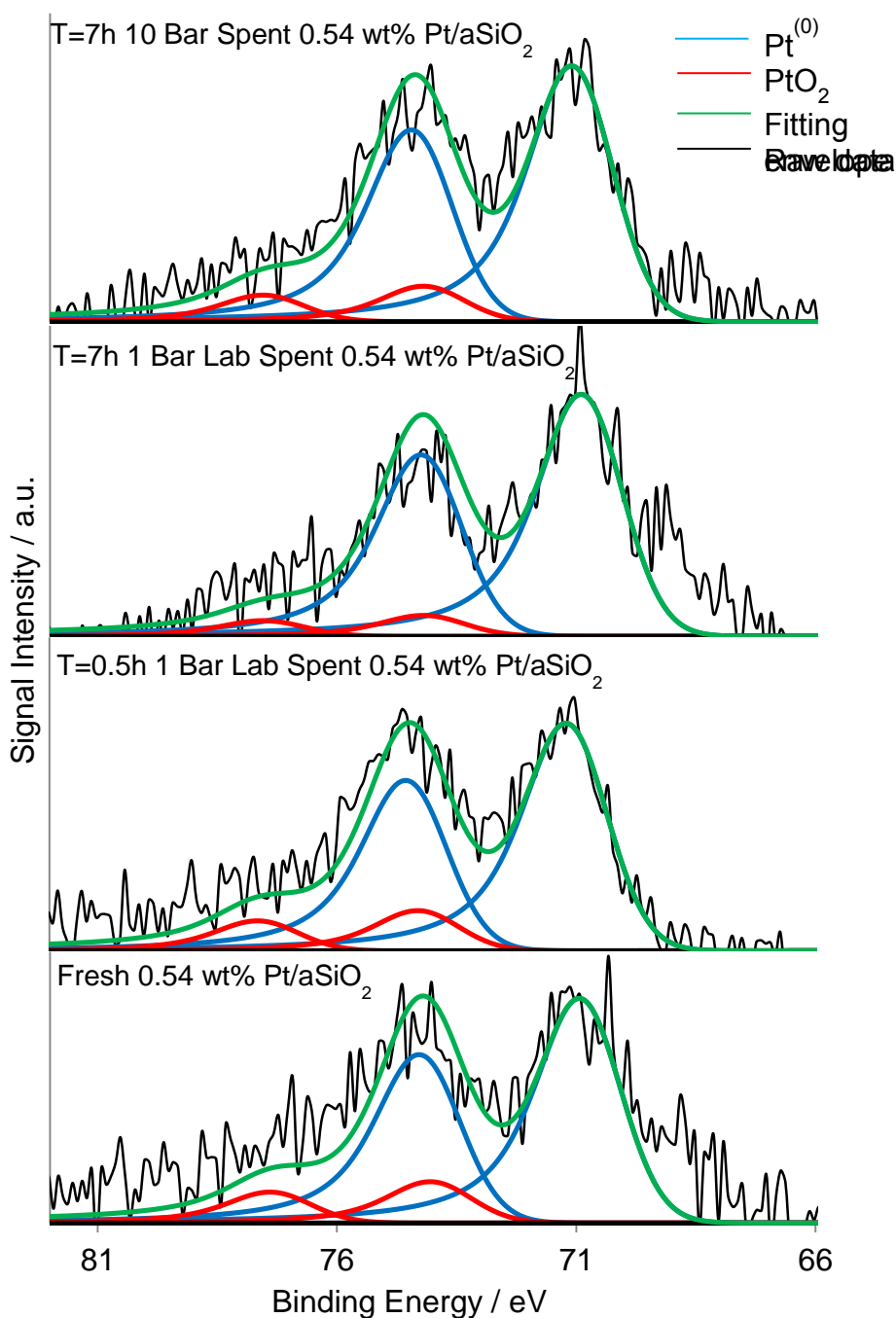


**Figure 3.30– Stacked Pt 4f XPS plots of fresh vs. spent Pt/aSiO<sub>2</sub> catalyst over variable reaction time and O<sub>2</sub> pressure.**

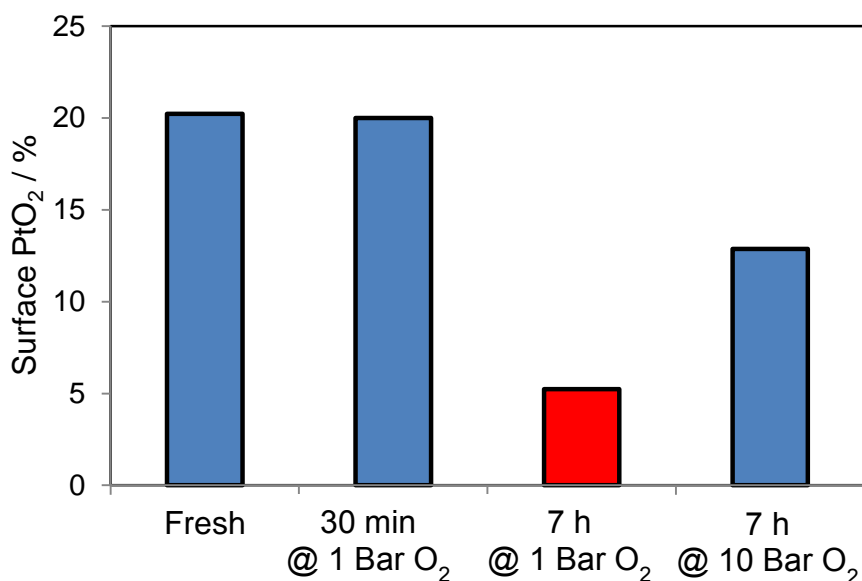
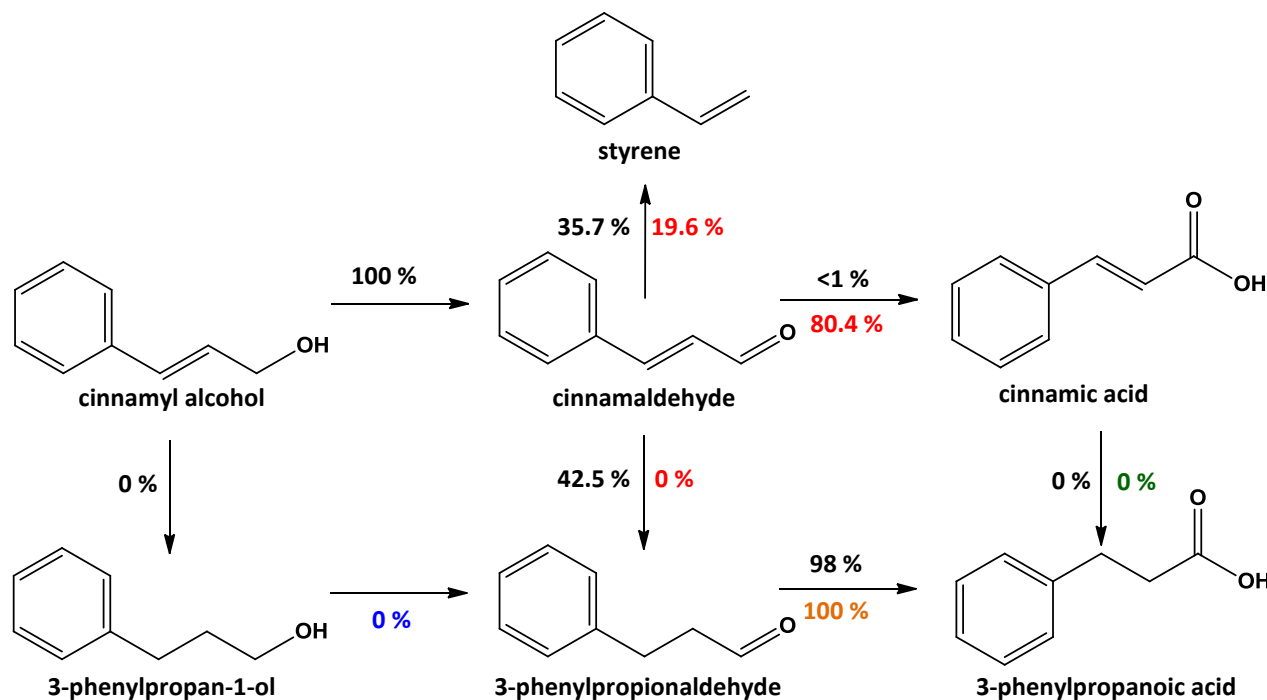


**Figure 3.31– Influence of cinnamyl alcohol reaction time and O<sub>2</sub> pressure on surface PtO<sub>2</sub> concentration for a 0.54 wt.% Pt/aSiO<sub>2</sub> catalyst**

Analysis of **Figures 3.30 and 3.31** confirm that the enhanced selox performance under O<sub>2</sub> high pressures can be directly related to an increased stabilisation of surface PtO<sub>2</sub> species. The *in-situ* PtO<sub>2</sub> reduction induced by cinnamyl alcohol conversion decreases surface oxide content from 20.5% during the early reaction stages, to approximately 5% over 7 hours under 1 bar O<sub>2</sub>. By comparison, increasing oxygen partial pressure results in a 13% PtO<sub>2</sub> surface population under 10 bar O<sub>2</sub> at an equivalent reaction time. As a note of interest, a negligible (<0.2%) loss in surface oxide content was observed after 0.5 hours, proving that utilisation of this timescale for TOF determination is a fair approximation. The catalyst active site can thus be assumed stable and functioning at optimal efficiency for the adopted reaction regime.

### 3.2.5 Mapping the reaction pathway

Understanding the role of reactive intermediates and by-product formation in cinnamyl alcohol oxidation, could provide a basis for targeted catalyst design for Pt-based systems in similar regimes.



**Scheme 1** – Reaction network for cinnamyl alcohol selox over a 0.05 wt. % Pt/SBA-15 catalyst at 90°C, 8.4 mmol substrate and 1 bar O<sub>2</sub>. Colour coded to indicate selectivity percentage when starting from indicated substrate. Black = **cinnamyl alcohol**; red = **cinnamaldehyde**; green = **cinnamic acid**; blue = **3-phenylpropan-1-ol**; and orange = **3-phenylpropionaldehyde**.

The reactivity of various intermediates were probed using the standard selox procedure, described in **Chapter 2**, with selectivity percentages quoted for each starting substrate, so the adopted reaction pathway can be directly observed. The focus of this chapter has been concerned predominantly with cinnamyl alcohol and the first step is shown to be oxidation to cinnamaldehyde with no direct C=C hydrogenation of the alcohol. The inherent instability of  $\alpha,\beta$ -unsaturation within reactively generated cinnamaldehyde yields an increased predominance towards hydrogenation (3-phenylpropionaldehyde) and decarbonylation (styrene) processes, leaving only 22% cinnamaldehyde remaining. The 3-phenylpropionaldehyde intermediate is itself extremely unstable and prone to over-oxidation to 3-phenylpropanoic acid. Over-oxidation of *in-situ* generated cinnamaldehyde to cinnamic acid is not apparent under our conditions. The initial oxidative dehydrogenation step permits the liberation and formation of surface hydrogen, actively promoting competing hydrogenation/hydrogenolysis pathways.

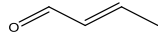
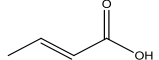
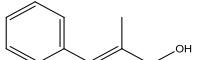
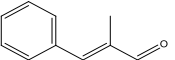


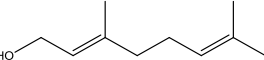
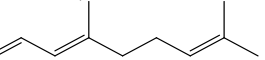
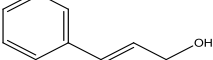
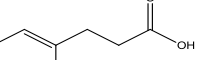
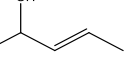
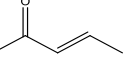
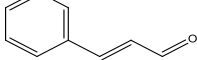
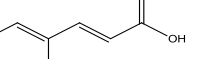
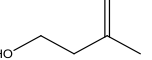
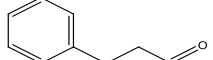
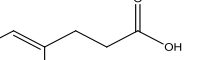
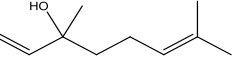
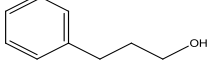
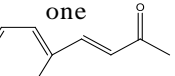
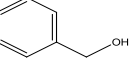
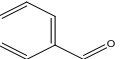
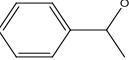
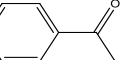
When the starting material is cinnamaldehyde, the pre-dominance of over-oxidation to cinnamic acid is apparent. The destabilising effect of surface hydrogen is not demonstrated here, with the absence of said species providing a very selective route towards maintaining internal  $\alpha,\beta$ -unsaturation in the final product. The presence of extended conjugated unsaturation imparts cinnamic acid with high stability, with respect to hydrogenation to 3-phenylpropanoic acid and decarbonylation to styrene, under mild oxidation conditions.

The high stability of C-H bonds adjacent to the hydroxyl group in 3-phenylpropan-1-ol prevents further conversion of this fully saturated substrate<sup>32</sup> under our conditions and can be deemed an inert component for all Pt/silica oxidations. 3-phenylpropanoic acid presents no observed reactivity due to the absence of any known reaction pathways under mild oxidation conditions.

Full reaction mapping for cinnamyl alcohol selox underlines the efficiency of platinum for targeted oxygen insertion and oxidative dehydrogenation reactions, in the formation of cinnamic acid and cinnamaldehyde respectively. Unfortunately, an exceptional efficiency for hydrogen transfer reactions has been exposed with the *in-situ* formation of surface hydrogen severely compromising final product selectivity, through loss of unsaturated functionality.

### 3.2.6 Alternative substrate selox

**Table 3.7** – Selox performance of 0.05 wt. % Pt/SBA-15 towards saturated and unsaturated oxygenates at 90°C.

Substrate	Primary product	C / %	S / %	Substrate	Primary product	C / %	S / %
Crotonaldehyde 	Crotonic Acid 	27	66	Trans-2-methyl-3-phenyl-2-propen-1-ol 	(E)-2-methyl-3-phenylacrylaldehyde 	13	68
Trans-hexen-1-ol 	Trans-hex-3-enal 	11	72	Geraniol 	(E)-3,7-dimethylocta-2,6-dienal 	6	100
Cinnamyl alcohol 	Hydrocinnamic acid 	38	42	3-Penten-2-ol 	(E)-Pent-3-en-2-one 	7	72
Cinnamaldehyde 	Cinnamic Acid 	31	80	3-Methyl-3-buten-1-ol 	n/a	0	0
Hydrocinnamaldehyde 	Hydrocinnamic acid 	58	95	Linalool 	Isomers	3	100
Hydrocinnamyl alcohol 	n/a	0	0	(E)-4-Phenylbut-3-en-2-one 	n/a	0	0
Benzyl alcohol 	Benzaldehyde 	30	92				
1-Phenyl ethanol 	Acetophenone 	25	100				

In order to determine the wider commercial viability for these systems, a 0.05 wt. % Pt/SBA-15 catalyst was screened against a range of alternate alcohols, aldehydes and ketones (**Table 3.7**). Promising activity was observed for the oxidation of several unsaturated primary alcohols and aldehydes, including 1-phenylethanol, benzyl alcohol, crotonaldehyde, hydrocinnamaldehyde and 2-methyl-3-phenyl-2-propen-1-ol, in stark contrast to the much diminished activity of secondary alcohols and ketones under our reaction conditions. The lack of reactivity for linalool, a *tertiary alcohol species*, was expected due to increased stability of a tertiary cation generated by enhanced hyperconjugation effects, in concert with the absence of a  $\beta$ -hydrogen species. Gamma methyl/alkyl C-H bond scission is typically more demanding and hence occurs with low frequency for this substrate.<sup>41</sup>

The binding of allylic alcohols is generally accepted to take place through the C=C and alkoxy groups. Through this transition state the proximity of the -C-H moiety to the Pt surface is artificially reduced, thus promoting oxidative dehydrogenation.<sup>42,43</sup> Stabilisation of the allylic aldehyde and ketone products proceeds through conjugation and resonance effects as facilitated by the allylic functionality. However, in such starting materials which do not possess a phenyl ring in close proximity to the C=C group, consistent diminished reactivity is exhibited. This is believed to occur due to much lowered extended-conjugation stabilisation in the absence of the phenyl ring. Additionally, repulsion of the phenyl ring from the Pt surface is often observed in the hydrogenation of cinnamaldehyde on Pt(111) facets.<sup>44,45</sup> It is understood that this steric repulsion decreases the C-H-Pt distance, and can thus explain the increased reactivity of aromatic allylic substrates over non-aromatic derivatives.<sup>33</sup>

The absence of the C=C moiety, induces a positive inductive effect in which the electron withdrawing effect of the hydroxyl oxygen is partially offset by the alkyl chain. Artificial stabilisation of the beta C-H species, strengthens the -C-H bond, *in comparison with allylic substrates*, and diminishes the rate of C-H bond cleavage.

### 3.3 Conclusion

Silica-supported Pt nanoparticles have demonstrated excellent activity in the liquid phase selective aerobic oxidation of cinnamyl alcohol to cinnamaldehyde under mild oxidation treatments. Fabrication of internal support structure, through the introduction of parallel 2D non-interconnected and 3D interconnected pore frameworks, enhances available support surface area favourably promoting platinum dispersion and permitting specific particle size control, in comparison with the low area amorphous silica.

Following the reaction kinetics of cinnamyl alcohol selox, in the presence of O<sub>2</sub> or via *in-situ* pre-reduction regimes, we have elucidated a PtO<sub>2</sub> active site predominantly responsible for catalyst activity in allylic alcohol selox. As catalyst activity presents a strong functionality with platinum dispersion, intricately linked to surface PtO<sub>2</sub> concentration, the implementation of mesoporous supports, increases surface active population and thus activity follows suit.

Product selectivity reflects a fine balance between oxidation and competing hydrogenation/hydrogenolysis pathways, where the latter is driven by *in-situ* hydrogen production and active site reduction. Methods for improving active site stability can aid in boosting catalytic activity over prolonged reaction timescales, and thus commercial viability. The simplicity and reproducibility of catalyst preparation, in conjunction with expressed activity towards alternate allylic substrates makes further development of these systems an attractive option.



### 3.4 References

1. A. F. Lee, C. V. Ellis, J. N. Naughton, M. A. Newton, C. M. Parlett and K. Wilson, *J Am Chem Soc*, 2011, 133, 5724-5727.
2. T. Mallat and A. Baiker, *Chemical Reviews*, 2004, 104, 3037-3058.
3. A. P. Markusse, B. F. M. Kuster, D. C. Koningsberger and G. B. Marin, *Catalysis Letters*, 1998, 55.
4. L. Durndell, C. M. Parlett, N. S. Hondow, K. Wilson and A. F. Lee, *Nanoscale*, 2013.
5. L. Ono, B. Yuan, H. Heinrich and B. R. Cuenya, *The Journal of Physical Chemistry C*, 2010, 114, 22119-22133.
6. N. Seriani, W. Pompe and L. C. Ciacchi, *The Journal of Physical Chemistry B*, 2006, 110, 14860-14869.
7. D. Zhao, Q. Huo, J. Feng, B. F. Chmelka and G. D. Stucky, *Journal of the American Chemical Society*, 1998, 120, 6024-6036.
8. T.-W. Kim, F. Kleitz, B. Paul and R. Ryoo, *Journal of the American Chemical Society*, 2005, 127, 7601-7610.
9. K. S. W. Sing, D. H. Everett, R. A. W. Haul, L. Moscou, R. A. Pierotti, J. Rouquerol and T. Siemieniewska, *Pure and Applied Chemistry*, 1985, 57, 603-619.
10. P. A. Webb, C. Orr and M. I. Corporation, *Analytical methods in fine particle technology*, Micromeritics Instrument Corporation, 1997.
11. N. Pernicone, *Cattech*, 2003, 7, 196-204.
12. J. Shen, X. Liu, S. Zhu, H. Zhang and J. Tan, *Materials Letters*, 2011, 65, 1179-1183.
13. G. A. Somorjai and Y. Li, *Introduction to Surface Chemistry and Catalysis*, John Wiley & Sons, 2010.
14. C. M. A. Parlett, D. W. Bruce, N. S. Hondow, M. A. Newton, A. F. Lee and K. Wilson, *ChemCatChem*, 2012, DOI: 10.1002/cctc.201200301, n/a-n/a.
15. C.-M. Yang, H.-A. Lin, B. Zibrowius, B. Spliethoff, F. Schüth, S.-C. Liou, M.-W. Chu and C.-H. Chen, *Chemistry of materials*, 2007, 19, 3205-3211.
16. B. Shan, Y. Zhao, J. Hyun, N. Kapur, J. B. Nicholas and K. Cho, *The Journal of Physical Chemistry C*, 2009, 113, 6088-6092.
17. R. Chen, Z. Chen, B. Ma, X. Hao, N. Kapur, J. Hyun, K. Cho and B. Shan, *Computational and Theoretical Chemistry*, 2012, 987, 77-83.
18. H. Araki, A. Fukuoka, Y. Sakamoto, S. Inagaki, N. Sugimoto, Y. Fukushima and M. Ichikawa, *Journal of Molecular Catalysis A: Chemical*, 2003, 199, 95-102.
19. A. Fukuoka, Y. Sakamoto, T. Higuchi, N. Shimomura and M. Ichikawa, *Journal of Porous Materials*, 2006, 13, 231-235.
20. NIST X-Ray Photoelectron spectroscopy database, <http://srdata.nist.gov/xps/>, Accessed March 2013, 2013.
21. N. Cabrera and N. Mott, *Reports on Progress in Physics*, 1949, 12, 163.
22. J. Als-Nielsen and D. McMorrow, *Elements of Modern X-ray Physics*, Wiley, 2001.
23. C. M. A. Parlett, D. W. Bruce, N. S. Hondow, A. F. Lee and K. Wilson, *ACS Catalysis*, 2011, 1, 636-640.
24. C. M. A. Parlett, P. Keshwalla, S. G. Wainwright, D. W. Bruce, N. S. Hondow, K. Wilson and A. F. Lee, *ACS Catalysis*, 2013, 3, 2122-2129.
25. Y. Waseda, K. Hirata and M. Ohtani, 1975.
26. S. Mandal, D. Roy, R. V. Chaudhari and M. Sastry, *Chemistry of materials*, 2004, 16, 3714-3724.
27. E. Ghedini, F. Menegazzo, M. Signoretto, M. Manzoli, F. Pinna and G. Strukul, *Journal of Catalysis*, 2010, 273, 266-273.
28. Y.-M. Liu, Y. Cao, N. Yi, W.-L. Feng, W.-L. Dai, S.-R. Yan, H.-Y. He and K.-N. Fan, *Journal of Catalysis*, 2004, 224, 417-428.

29. M. S. Holm, E. Taarning, K. Egeblad and C. H. Christensen, *Catalysis Today*, 2011, 168, 3-16.
30. A. F. Lee and K. Wilson, *Green Chemistry*, 2004, 6, 37.
31. C. P. Vinod, K. Wilson and A. F. Lee, *Journal of Chemical Technology & Biotechnology*, 2011, 86, 161-171.
32. A. F. Lee, J. J. Gee and H. J. Theyers, *Green Chemistry*, 2000, 2, 279-282.
33. T. Mallat, A. Baiker and L. Botz, *Applied catalysis A: General*, 1992, 86, 147-163.
34. R. Garcia, M. Besson and P. Gallezot, *Applied Catalysis A: General*, 1995, 127, 165-176.
35. P. Gallezot, *Catalysis Today*, 1997, 37, 405-418.
36. I. Pálincó, *Applied Catalysis A: General*, 1995, 126, 39-49.
37. D. Duca, P. Baranyai and T. Vidóczy, *Journal of computational chemistry*, 1998, 19, 396-403.
38. Y. Barron, G. Maire, J. M. Muller and F. G. Gault, *Journal of Catalysis*, 1966, 5, 428-445.
39. D. W. Blakely and G. A. Somorjai, *Journal of Catalysis*, 1976, 42, 181-196.
40. K. Fischer, *The Journal of Chemical Thermodynamics*, 2001, 33, 1285-1308.
41. X. Liu, R. J. Madix and C. M. Friend, *Chemical Society Reviews*, 2008, 37, 2243-2261.
42. A. F. Lee, Z. Chang, P. Ellis, S. F. Hackett and K. Wilson, *The Journal of Physical Chemistry C*, 2007, 111, 18844-18847.
43. J. Naughton, A. Pratt, C. W. Woffinden, C. Eames, S. P. Tear, S. M. Thompson, A. F. Lee and K. Wilson, *The Journal of Physical Chemistry C*, 2011, 115, 25290-25297.
44. X. Xiang, W. He, L. Xie and F. Li, *Catalysis Science & Technology*, 2013, DOI: 10.1039/C3CY00437F.
45. M. S. Ide, B. Hao, M. Neurock and R. J. Davis, *ACS Catalysis*, 2012, 2, 671-683.

## *Chapter 4*

### *Platinum-based selective hydrogenation of allylic aldehydes*

—

*An investigation of nanoparticle  
characteristics and support architecture  
on cinnamyl alcohol selectivity*

## 4.1 Introduction

**Chapter 3** evidences the crucial role of support structure on nanoparticle attributes. In the Pt-catalysed selective oxidation of allylic alcohols, strict control of surface PtO<sub>2</sub> population can lead to tunable catalytic activity.<sup>1</sup>

In this chapter, we apply these findings to cinnamaldehyde hydrogenation, the reverse reaction to the previous selective oxidation procedure. Catalytic activity will be compared over 4 variants of mesoporous silica (SBA-15, SBA-16, KIT-6 and TLCT-MM-SBA-15) in conjunction with a commercial, amorphous system (aSiO<sub>2</sub>). Catalytic activity is predicted to increase with particle size and Pt<sup>(0)</sup> density, however the introduction of mesoporous domains and enhanced support order may lead to unusual activity-selectivity observations. It was deemed beneficial to study two additional mesoporous systems, SBA-16 and true liquid crystal templated macroporous-mesoporous SBA-15 (TLCT-MM-SBA-15), with SBA-16 used as a basis of comparison with KIT-6 in **Chapter 3**. SBA-16 possesses a 3-D interconnected mesopore network (akin to KIT-6), body centred cubic close-packed spherical pores, with each pore connected to 8 nearest neighbours and the expression of an *Im3m* unit cell.<sup>2</sup> With regards to TLCT-MM-SBA-15, the generation of macropores within the SBA-15 architecture is predicted to benefit internal mass diffusion kinetics through a more open support structure.<sup>3</sup> Retaining the mesopore domains, characteristic to SBA-15, should permit similar levels of metal dispersion enhancement to those expressed in **Chapter 3**.

## 4.2 Results and Discussion

### 4.2.1 Characterisation of polystyrene spheres – Scanning electron microscopy

The emulsion polymerisation protocol devised by Vaudreuil *et al*<sup>4</sup> was used to produce mono-disperse polystyrene spheres, as the basis for a hard template for SBA-15 macropore incorporation. SEM was used to establish the successful synthesis of mono-dispersed polystyrene spheres. **Figure 4.1** confirms a successful synthesis, with spherical morphologies exclusively synthesised and a narrow mean bead diameter of 343 ( $\pm$  22) nm, thus confirming relatively good mono-dispersity. All values are in excellent agreement with reported literature values under similar synthesis conditions.<sup>3</sup>

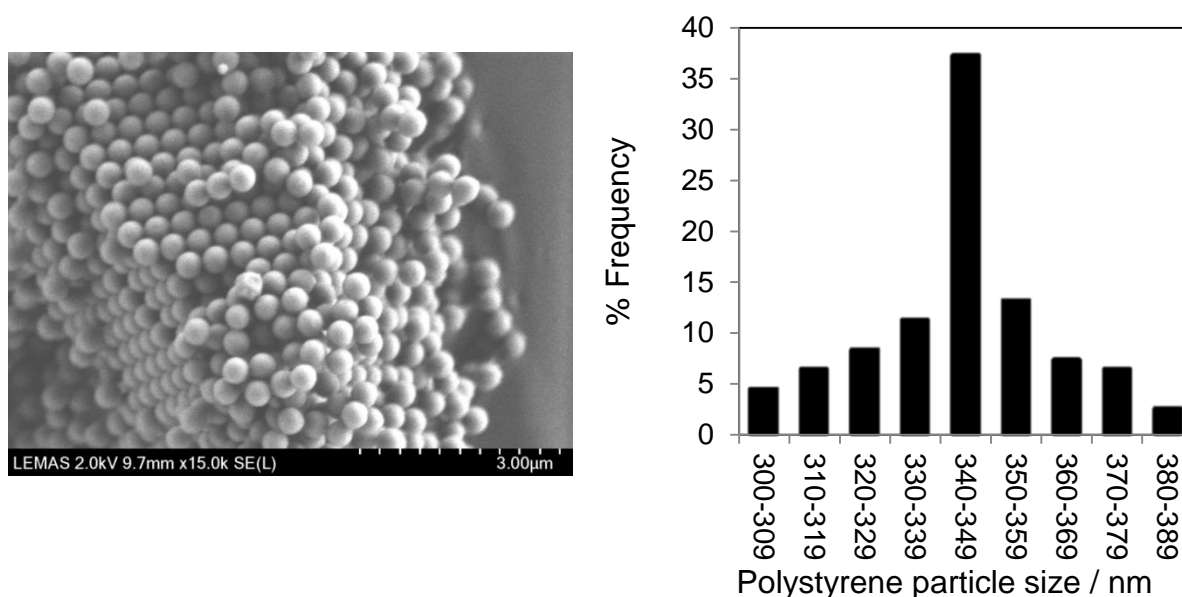


**Figure 4.1 – SEM image of synthesised polystyrene spheres and associated particle size distribution (200 particles)**

## 4.2.2 Characterisation of parent SBA-16 and TLCT-MM-SBA-15 supports

SBA-16 and TLCT-MM-SBA-15 were synthesised using methodologies developed by Zhao *et al.*<sup>5</sup> and Lee *et al.*<sup>3</sup> Successful synthesis was verified using a variety of characterisation techniques.

### 4.2.2.1 Powder x-ray diffraction

The successful formation of SBA-16 ( $Im3m$ ) and TLCT-MM-SBA-15 ( $P6mm$ ) pore architectures can be confirmed via the indexing of major peaks apparent in the associated low angle powder XRD spectra (**Figure 4.2**). All reflections observed at low angle can be associated with well-defined pore structures and long-range support order. This analysis permits the calculation of the unit cell lattice parameter, which strictly adhere to reported literature values.<sup>2, 3, 6</sup> **Table 4.1** shows the physical properties of parent SBA-16 and TLCT-MM-SBA-15, with alternate supports included for ease of comparison. It must be noted that macropore ordering within the support framework was undetectable via traditional low angle powder diffraction, due to the extremely large repeat unit distances between each macropore.

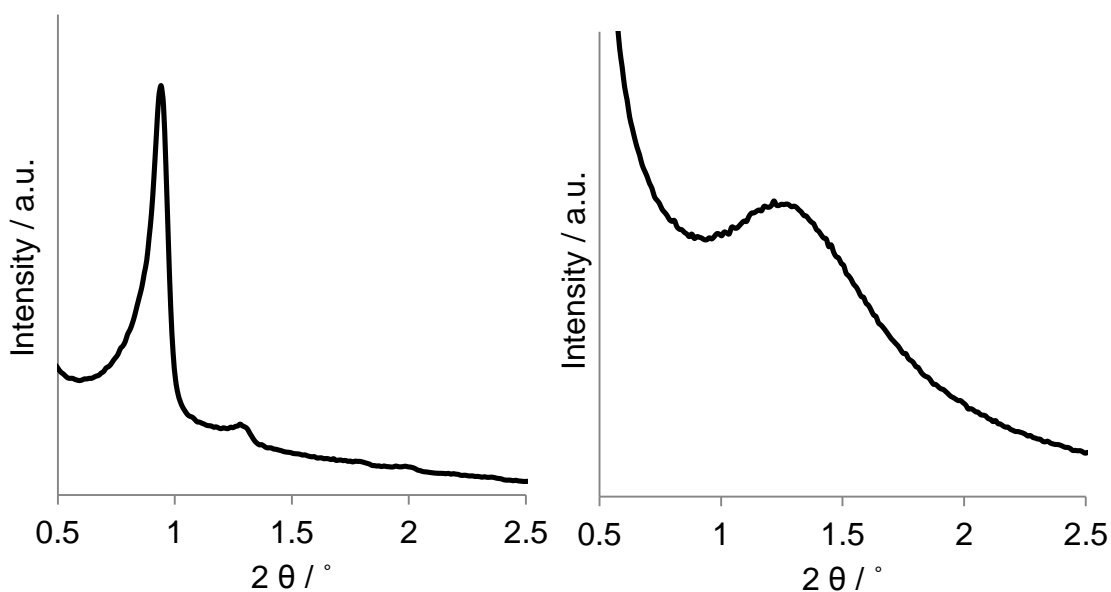


**Figure 4.2 – Low angle XRD patterns of parent SBA-16 (Left) and TLCT-MM-SBA-15 (Right) supports**

**Figure 4.2** clearly demonstrates the expected diffraction pattern for the  $Im3m$  space group. In the case of SBA-16, the principle peak is indexed as the  $d_{110}$  reflection, but it must also be noted that smaller  $d_{200}$  and  $d_{211}$  can be observed. The as-synthesised TLCT-MM-SBA-15 demonstrates a broadened SBA-15  $d_{100}$  reflection only. Under close scrutiny, a moderate shift in peak position to a higher angle can be observed, with respect to SBA-15 (**Chapter 3 Figure 3.2**). This shift can be attributed to a decrease in  $d_{100}$  spacing, yielding the observed drop in cell parameter and pore spacing values (via unit cell contraction). As a consequence of a contracted unit cell, the reported mesopore diameter and pore wall thickness also sport diminished values to those of parent SBA-15. The addition of macropores to SBA-15 leads to a substantial decrease in observable peak intensity. This can be explained by a disruption to the established mesopore network of the parent SBA-15 resulting in a lower number of pore repeat units. Due to a drop in total peak intensity, it is not possible to observe the additional  $d_{110}$  and  $d_{200}$  reflections of the  $P6mm$  space group, inherent to the hexagonally packed SBA-15 unit cell. HRTEM was used to provide concrete evidence for the successful generation of this architecture and for subsequent cell parameter calculations (**Section 4.2.2.3**).

**Table 4.1** - Textural properties of parent silica supports

Sample	Surface area / m <sup>2</sup> g <sup>-1(a)</sup>	Mesopore diameter / nm <sup>(b)</sup>	Micropore surface area / m <sup>2</sup> g <sup>-1(c)</sup>	Cell Lattice parameter / nm <sup>(d)</sup>
aSiO <sub>2</sub>	208 (± 25)	31.3	37 (± 4)	n/a
SBA-15	882 (± 88)	5.7	441 (± 41)	9.0 (± 0.2)
KIT-6	918 (± 92)	6.4	485 (± 49)	22.2 (± 0.2)
SBA-16	776 (± 78)	3.4	510 (± 51)	13.5 (± 0.2)
TLCT-MM-SBA-15	524 (± 52)	3.4	81 (± 9)	7.0 (± 0.2)

<sup>a</sup>N<sub>2</sub> BET, <sup>b</sup>BJH desorption isotherm, <sup>c</sup>N<sub>2</sub> t-plot, <sup>d</sup>Low angle XRD via Bragg's law

#### 4.2.2.2 Nitrogen porosimetry

Evaluation by N<sub>2</sub> porosimetry further confirms the successful generation of SBA-16 and TLCT-MM-SBA-15. The expected Type IV isotherms with inherent hysteresis for both materials are presented in **Figure 4.3**, and are characteristic for mesoporous materials.<sup>2, 7, 8</sup> The presence of ink-bottle pore openings within the internal architecture of SBA-16 leads to type H2 hysteresis. This pore morphology increases liquid nitrogen surface tension around the pore opening, leading to disfavoured evaporation at higher P/P<sub>0</sub>, with respect to SBA-15 and KIT-6.<sup>9</sup> As previously established for SBA-15, TLCT-MM-SBA-15 exhibits a Type IV isotherm and H1 hysteresis, inherent to the preservation of SBA-15 mesostructure and pore uniformity.<sup>10</sup> A second hysteresis is shown for this material at higher pressures due to the incomplete filling/emptying of the macropores. BET and BJH treatments have been used to calculate surface area and pore diameters respectively and can be found in **Table 4.1**. All readings adhere to literature stated values for these materials, under similar preparation conditions. Amorphous, SBA-15 and KIT-6 supports discussed in **Chapter 3** have been included for ease of comparison.

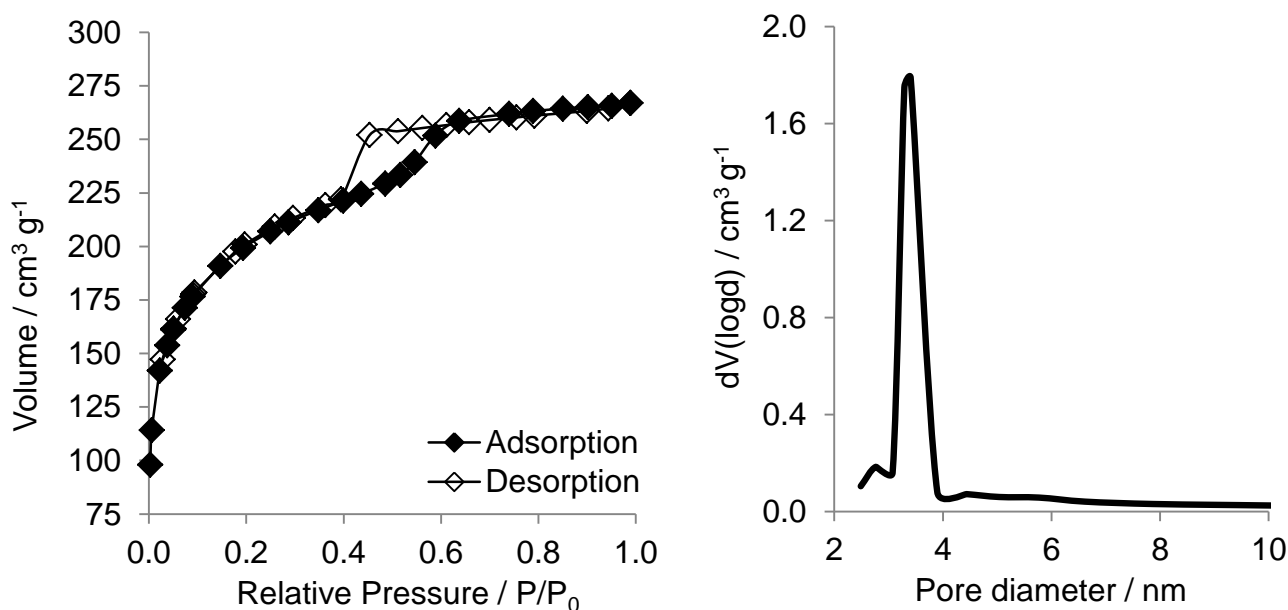


**Figure 4.3 (a) – Isotherm plot (Left) and BJH pore size distribution (Right) of parent SBA-16 support**

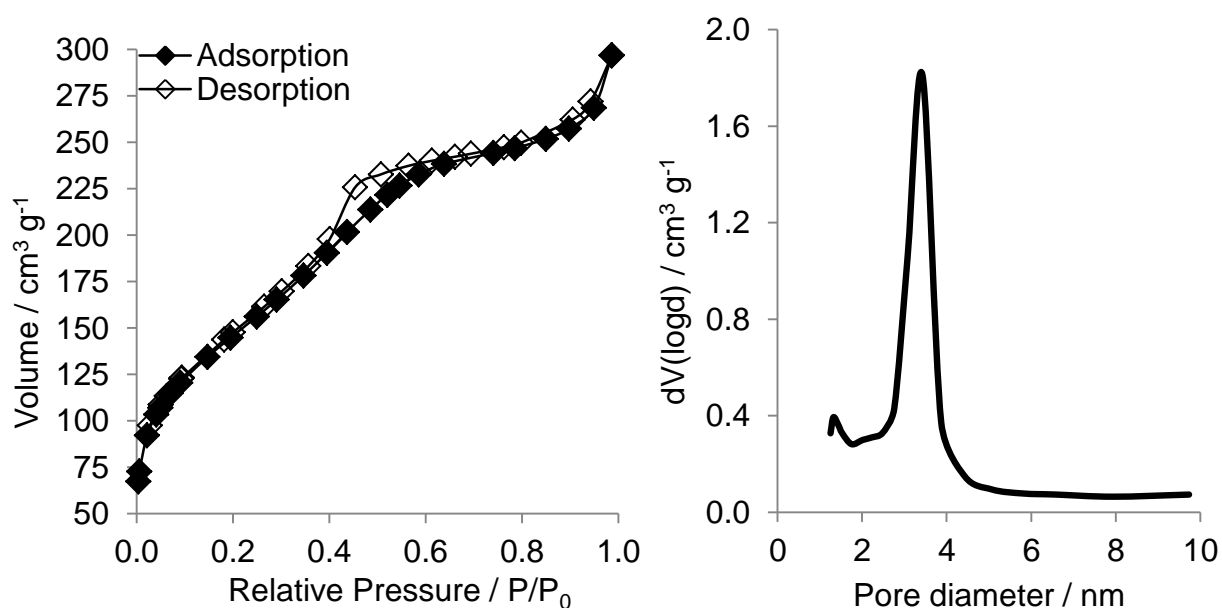


**Figure 4.3 (b) – Isotherm plot (Left) and BJH pore size distribution (Right) of parent TLCT-MM-SBA-15 support**

Narrow pore size distributions for SBA-16 and TLCT-MM-SBA-15 are clearly shown and presented in **Figure 4.3**. The BJH values for SBA-16 are markedly decreased, in comparison with SBA-15 and KIT-6, which may be attributed to the tri-block copolymer (Pluronic F127) used in this synthesis protocol. The resulting spherical pore structure and ink bottle openings could account for the observed drop in total surface area. The as-synthesised TLCT-MM-SBA-15 demonstrates diminished microporosity values (t-plot),<sup>8, 11</sup> thus resulting



in a BET-derived surface area drastically lower than SBA-15. Although TLCT-MM-SBA-15, SBA-15 and KIT-6 were synthesised using an identical P123 surfactant template, the mesopore diameter displayed for TLCT-MM-SBA-15 shows a clear reduction. This observation can be explained by the removal of the hydrothermal treatment in TLCT synthetic protocols;<sup>12</sup> thus altering pore-swelling dynamics. Additionally, the presence of the polystyrene bead-macropore template restricts the formation and swelling of the mesophase to cavities around said template, thus explaining the smaller mesopore size, unit cell parameter and fall in XRD peak intensity (**Figure 4.2**).

**Table 4.1** shows all supports contain a high degree of microporosity; in the order of KIT-6 > SBA-16 > SBA-15 >> TLCT-MM-SBA-15. There are two approaches for the artificial modification of microporosity within mesoporous materials; (i) addition of co-surfactants/additives<sup>13</sup> and (ii) control of hydrothermal step conditions.<sup>14</sup> As TLCT-MM-SBA-15 was synthesised using a TLCT methodology, the substantially reduced microporosity of 81 vs. 441 m<sup>2</sup> g<sup>-1</sup> for SBA-15 can be explained through the removal of the hydrothermal step from traditional mesoporous material syntheses. Alternatively, increasing hydrothermal temperature has been shown to destabilise the interaction between polyethylene oxide chains of neighbouring micelles in SBA-15 and thus discourage micropore formation (described in more detail in **Chapter 1**).<sup>14</sup> Increasing the temperature at this stage or foregoing this step completely can lead to partial inhibition of micropore formation.<sup>15-17</sup> The incorporation of a hard macroporous template (PS beads) within SBA-15 could be an additional factor preventing the facile formation of micropores, theoretically lowering the potential for polyethylene oxide chain interactions between micelles – a key interaction inherent to “softer” surfactant-based templating methods for mesoporous materials.<sup>14, 18</sup> Literature micropore values of 1-1.4 nm have been reported for all 4 classes of porous silica investigated;<sup>14, 19, 20</sup> the values reported here agree with these findings. Average mesopore diameters of 3.4 nm and 3.6 nm for SBA-16<sup>2, 21</sup> and TLCT-MM-SBA-15<sup>3</sup> respectively; remain true to previously reported literature values. It must be noted that due to the ink-bottle nature inherent to SBA-16 mesopore entrances, quoted N<sub>2</sub> porosimetry mesopore values are often underestimated by 1-2 nm. This can be attributed to changes in capillary evaporation of N<sub>2</sub> from said pores with respect to gradual changes in mesopore diameter.<sup>2, 21</sup>

### 4.2.2.3 Transmission electron microscopy – As synthesised supports

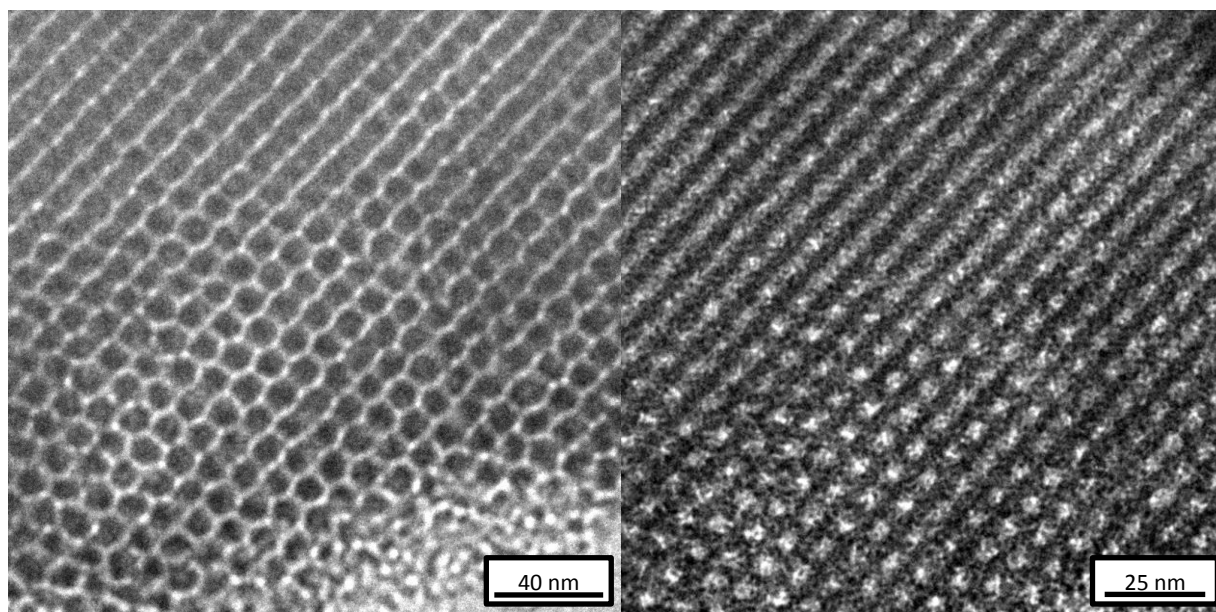


Figure 4.4 (a) – Representative HRTEM images of SBA-16

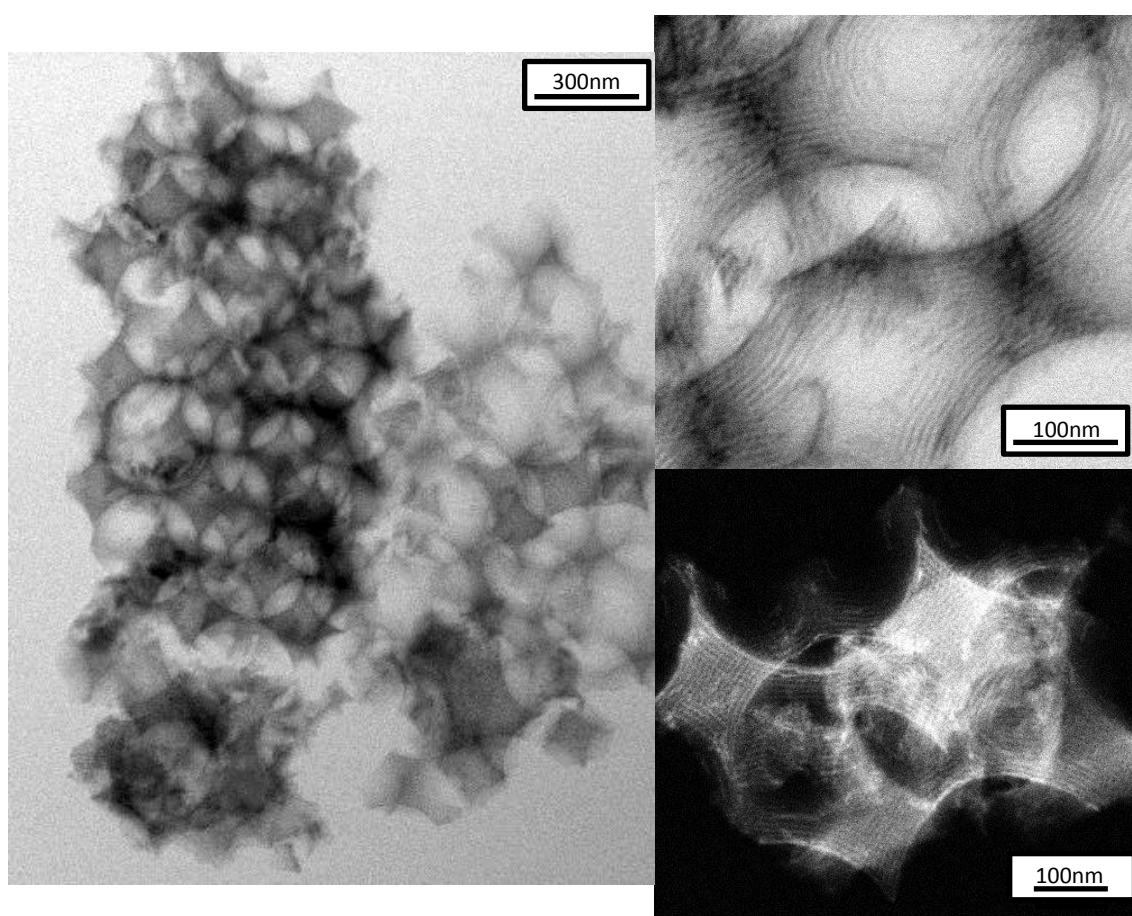


Figure 4.4 (b) – Representative HRTEM images of TLCT-MM-SBA-15

Representative TEM images of SBA-16 and TLCT-MM-SBA-15 are shown in **Figure 4.4** (Images of SBA-15 and KIT-6 are shown in **Chapter 3 Figure 3.5**). SBA-16 clearly displays the cubic structure inherent to the  $Im3m$  space group.<sup>7</sup> The hexagonal pore structure and channels inherent to the  $P6mm$  space group are clearly visible in the TLCT-MM-SBA-15 structure.<sup>3</sup> Additionally, successful incorporation of macropores within the parent SBA-15 structure is shown, thus confirming the synthesis of hierarchical macroporous-mesoporous silica. An average macropore diameter of 330 ( $\pm$  22 nm) is consistent with previous HRTEM imaging of the polystyrene hard template utilised (**Figure 4.1**). Average pore diameters, determined from measurement of approx. 150 pores, produced values of 5.8 ( $\pm$  0.3 nm) and 4.0 ( $\pm$  0.3 nm) for SBA-16 and TLCT-MM-SBA-15 respectively, in close agreement with obtained porosimetry values. This combination of TEM and BJH analyses for SBA-16 provides an effective way to differentiate the contribution of narrow ink-bottle pore openings and the differing internal mesopore channel structure to the overall support architecture.

**Figure 4.4** (b) highlights the breakup of the mesopore channels via macropore incorporation into the SBA-15 structure. It is interesting to observe the resultant concentric reconstruction of these mesopores within the macropore network. An explanation for this highly-organised geometric arrangement arises from the self-assembly of Pluronic P123 block copolymer and silica precursor around the bead template - stimulated by hydrogen-bonding and electrostatic interactions.<sup>3, 22, 23</sup>

### 4.2.3 Characterisation of Pt impregnated supports

Upon successful characterisation of each support, we proceeded with Pt impregnation using the incipient wetness protocol, aiming for bulk Pt loadings of 2-0.05 wt. %.

#### 4.2.3.1 Energy dispersive x-ray analysis

**Table 4.2** – A comparison of targeted and actual bulk platinum loadings

Support	Targeted loading / wt. %	Calculated loading <sup>a</sup> / wt. %
SBA-16	2.00	1.87
	1.00	0.89
	0.50	0.47
	0.10	0.11
	0.05	0.05
TLCT-MM-SBA-15	2.00	1.94
	0.50	0.48
	0.10	0.16

<sup>a</sup>EDX analysis

As demonstrated in **Chapter 3**, excellent correlation can be seen between targeted and attained bulk Pt loadings, providing further evidence for the validity and reproducibility of this synthetic protocol.

### 4.2.3.2 Powder x-ray diffraction

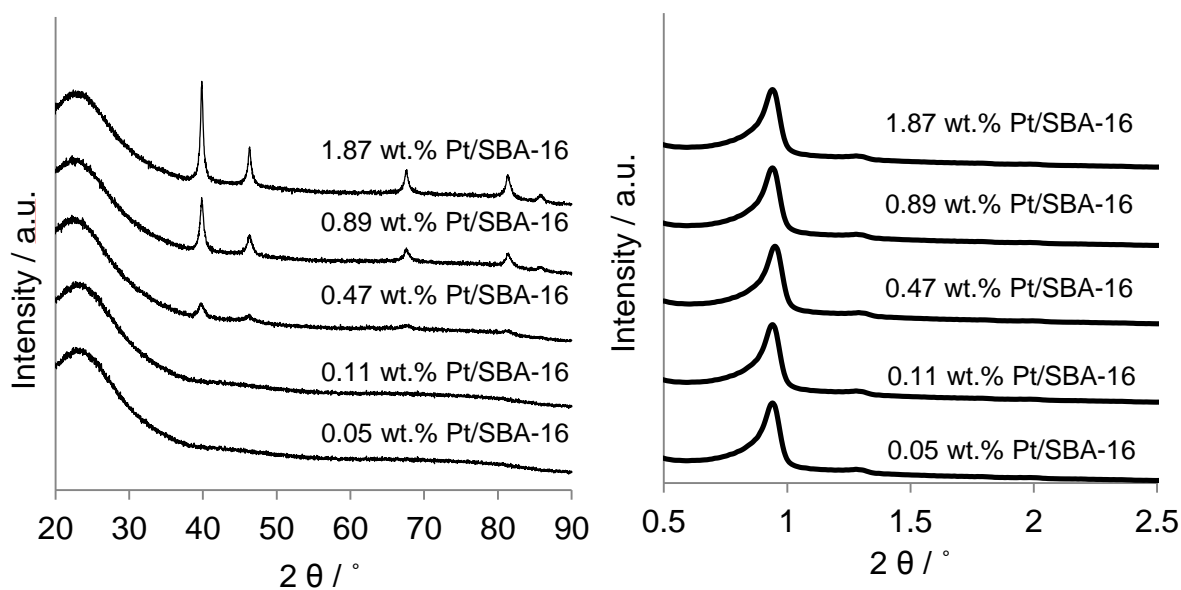


**Figure 4.5 (a) – Stacked wide angle (Left) and low angle (Right) XRD plots for Pt/SBA-16**

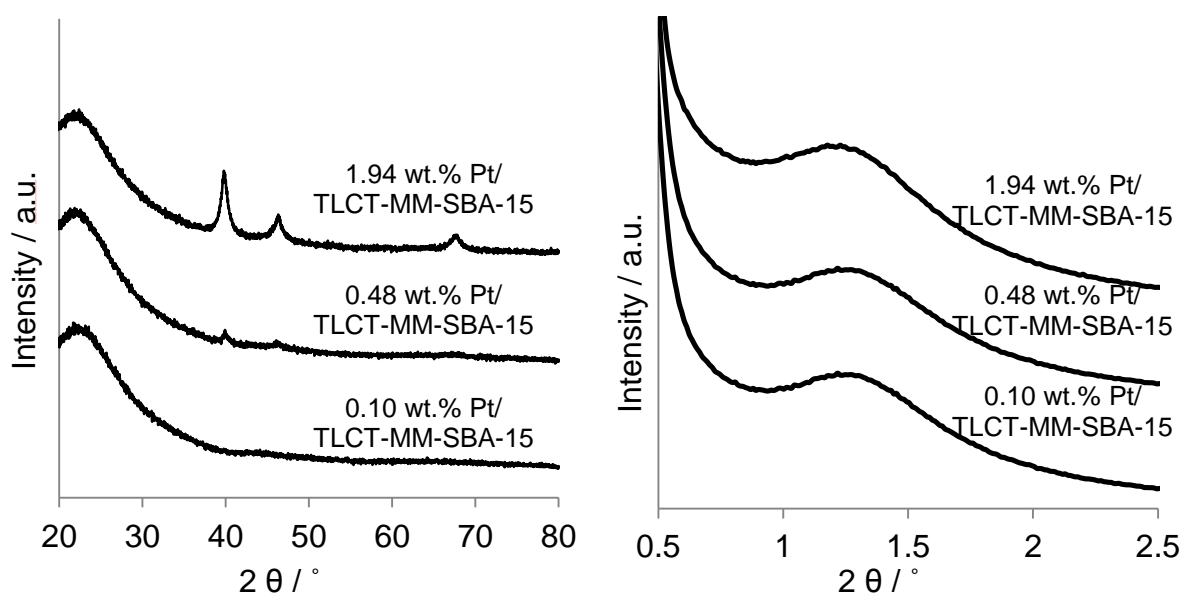


**Figure 4.5 (b) – Stacked wide angle (Left) and low angle (Right) XRD plots for Pt/TLCT-MM-SBA-15**

Pt-impregnated SBA-16 and TLCT-MM-SBA-15 show a similar Pt nanoparticle size versus loading dependency, as demonstrated for Pt-impregnated silica in **Chapter 3**. The four major reflections are distinct, highlighting the successful generation of highly ordered Pt crystallites on the support surface. As shown with previous studies, diffraction patterns due to Pt could not be observed at bulk metal loadings  $<0.45$  wt. %. Pt impregnation onto either support surface shows no observable change in support long-range order. No apparent shift in

peak position, shape or intensity from the parent support low angle diffraction patterns are observed and cell unit parameters are within error of parent support values, thus proving a conservation of mesopore structure (**Figure 4.5**). Pt nanoparticle sizes calculated via a combination of wide angle XRD diffraction patterns and the Scherrer equation are displayed in **Table 4.3**.

**Table 4.3** – Pt nanoparticle size calculated from Pt(111) reflection

Support	Pt loading / wt. %	Pt particle size / nm
SBA-16	1.87	13.7
	0.89	11.9
	0.47	7.5
TLCT-MM-SBA-15	1.94	9.8
	0.48	4.8

### 4.2.3.3 Nitrogen porosimetry

Figure 4.6 shows the stacked N<sub>2</sub> isotherms for the Pt/SBA-16 and Pt/TLCT-MM-SBA-15 series.

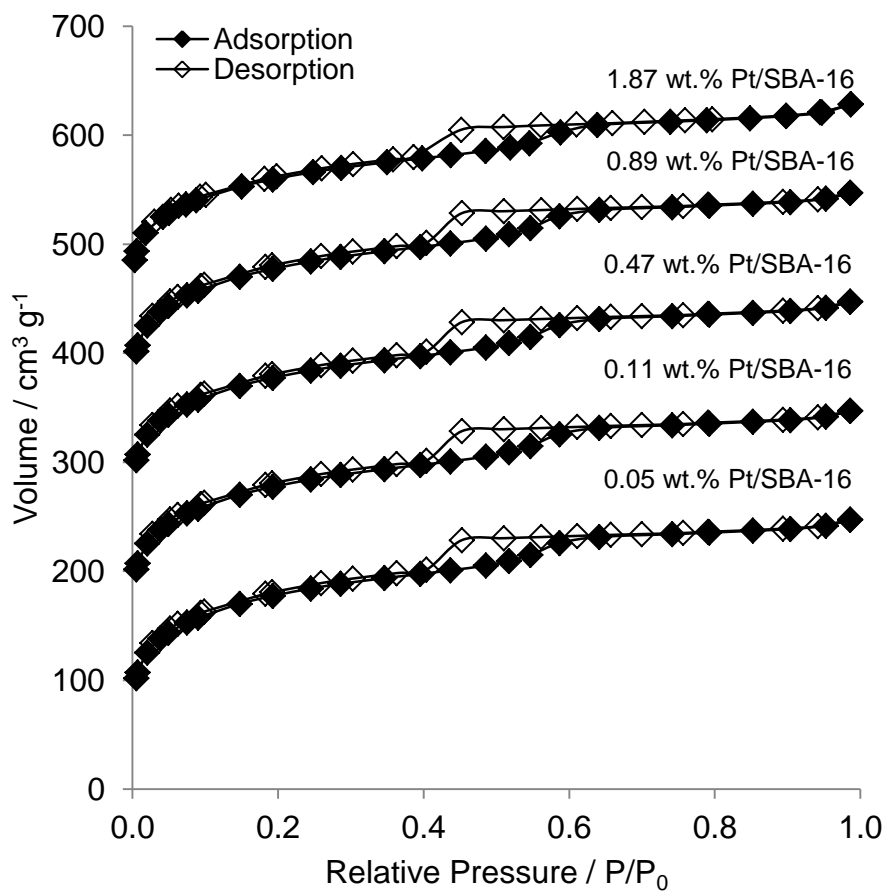
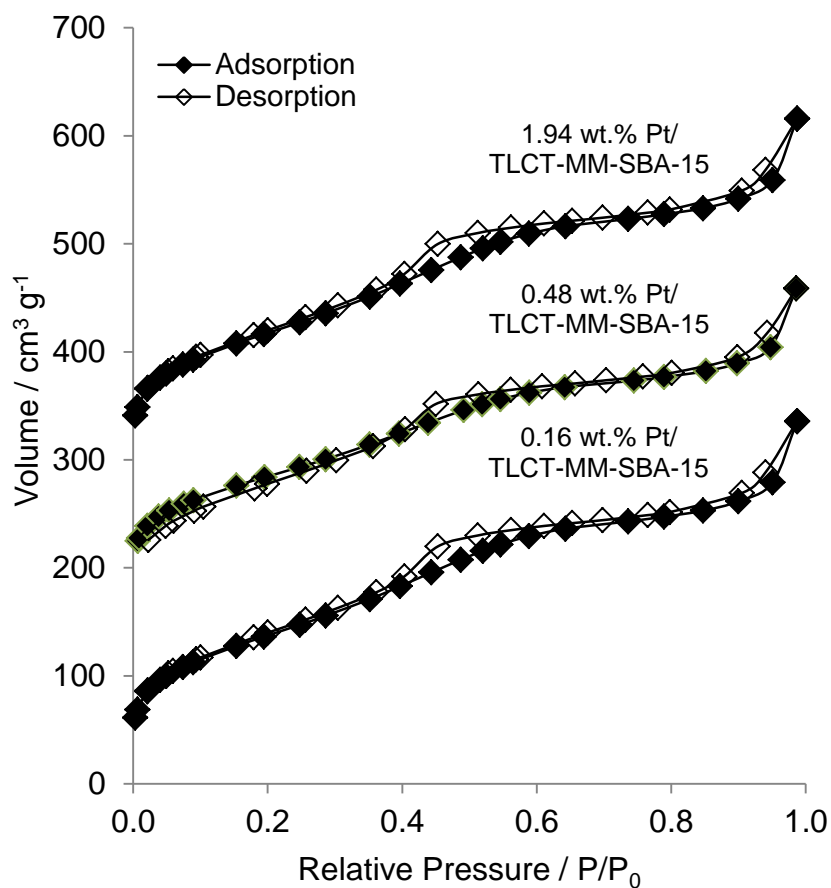


Figure 4.6 (a) – Stacked N<sub>2</sub> isotherm plot for Pt/SBA-16 series  
(Samples offset by 100 cm<sup>3</sup> g<sup>-1</sup> by metal loading for clarity)



**Figure 4.6 (b) – Stacked N<sub>2</sub> isotherm plot for Pt/TLCT-MM-SBA-15 series**

(Samples offset by 150 cm<sup>3</sup> g<sup>-1</sup> by metal loading for clarity)

As seen in **Chapter 3**, the characteristic hysteresis and isotherm shape of the parent material is preserved upon metal impregnation – underlining negligible pore collapse or change in support infrastructure.



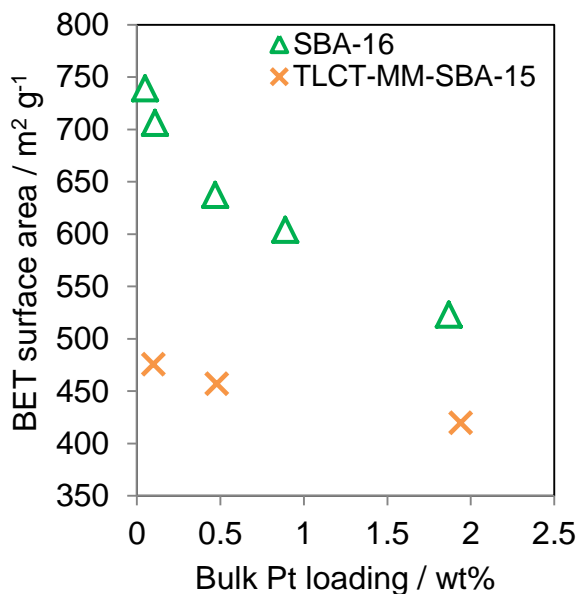


**Figure 4.7 – Tracking changes in BET support surface area with metal loading**

An inverse relationship between BET surface area and metal loading was established for mesoporous silica's in **Chapter 3 (Figure 3.9)**. Studies on the Pt/SBA-16 series highlighted a similar trend to those exhibited by Pt/KIT-6 materials. Contrasting with the observed relationship, the Pt/TLCT-MM-SBA-15 series sports much lower losses in surface area relative to the other mesoporous silica families (**Figure 4.7**). Similar to findings in **Chapter 3**, diminishing surface areas with metal loading arise due to increasing losses in microporosity (**Figure 3.10**).

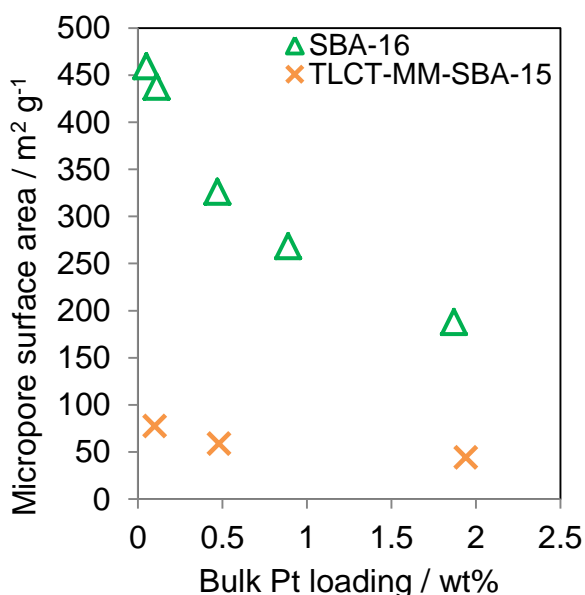


**Figure 4.8 – Changes in micropore surface area with metal loading**

**Figure 4.8** illustrates the contribution of support microporosity towards total BET surface area. Both SBA-16 and TLCT-MM-SBA-15 demonstrate the aforementioned inverse association between microporosity and Pt loading, however the lowered microporosity of TLCT-MM-SBA-15 results in a dampened expression of this effect, thus supporting the increased preservation of BET surface area in **Figure 4.7**.

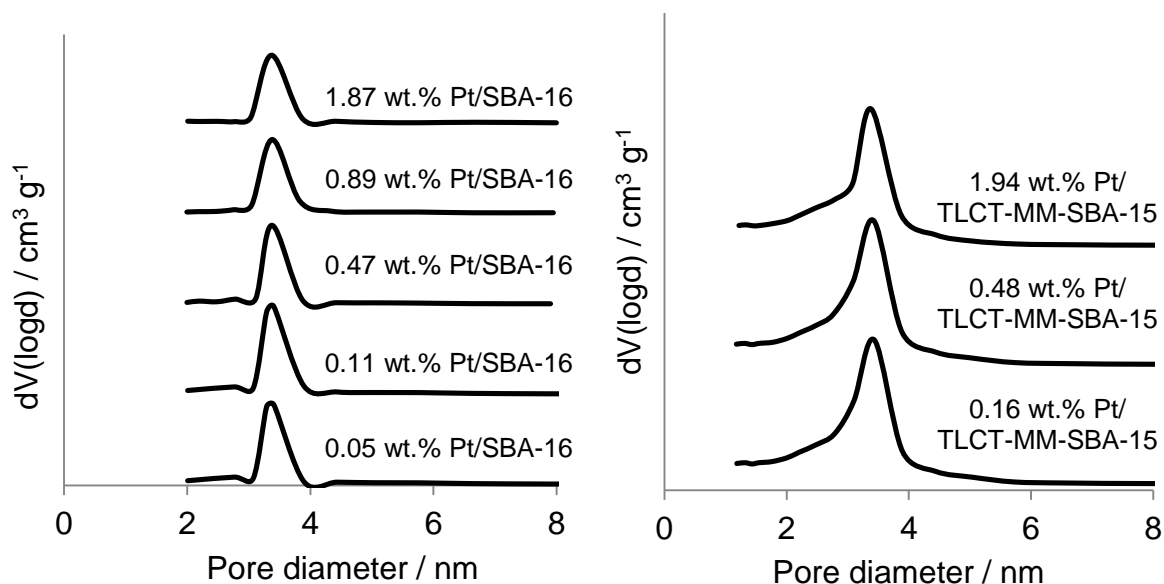


**Figure 4.9 – BJH pore size distributions for Pt/SBA-16 and Pt/TLCT-MM-SBA-15.**

#### Offset for clarity

BJH pore size distribution plots in **Figure 4.9** show no observable change in average mesopore size for either support class with Pt loading, further reinforcing support and pore structure stability.

#### 4.2.3.4 Carbon monoxide pulse chemisorption

CO pulse chemisorption measurements over Pt/SBA-16 and Pt/TLCT-MM-SBA-15 show an identical inverse correlation in particle size and dispersion as metal loading increases. These observations are consistent with those obtained for the Pt/silica systems probed in **Section 3.2.2.4**.

**Table 4.4** – Dispersion and average Pt particle size calculated from CO titration

Support	Pt loading / wt. %	Dispersion / %	Average particle size / nm
SBA-16	1.87	12.8 ( $\pm$ 1)	13.4 ( $\pm$ 0.2)
	0.89	16.9 ( $\pm$ 1)	11.0 ( $\pm$ 0.2)
	0.47	28.7 ( $\pm$ 1)	5.1 ( $\pm$ 0.2)
	0.11	66.8 ( $\pm$ 2)	2.4 ( $\pm$ 0.2)
	0.05	74.5 ( $\pm$ 2)	2.0 ( $\pm$ 0.2)
TLCT-MM-SBA-15	1.94	15.3 ( $\pm$ 1)	12.1 ( $\pm$ 0.2)
	0.48	29.4 ( $\pm$ 1)	4.8 ( $\pm$ 0.2)
	0.16	60.4 ( $\pm$ 2)	2.7 ( $\pm$ 0.2)

**Figure 4.7** and **Table 4.4** highlight the benefits of mesopore incorporation into support architecture on expressed particle size and dispersion for the Pt/SBA-16 series, in direct comparison with amorphous silica. However, poorer dispersion values for this series are quoted when in comparison with KIT-6 and SBA-15. This may be attributed to the ink-bottle pore opening for this material. Decreased diffusion of the Pt precursor, during the impregnation step, may lead to the enhanced nucleation and formation of larger Pt nanoparticles which as a consequence leads to pore blockage and significant drops in surface area. In regimes where Pt loading is  $< 0.11$  wt.%, overall dispersion and particle size values approach those reported for SBA-15 and KIT-6 series (at similar metal loadings), supporting the proposal of a Pt precursor diffusion problem. It has been reported in the literature, that the use of chloride-based Pt precursors sport higher particle sizes (and hence lower metal dispersions) with respect to nitrate-based analogues.<sup>24-26</sup> The presence of the  $\text{Cl}^-$  ion provides a site for initial nucleation, thus promoting nanoparticle growth (a method often used for the genesis of morphologic control of Pt nanoparticles).<sup>27-29</sup> An affinity to generate large metallic crystallites, in conjunction with a narrow ink-bottle opening could explain the reported drop in metal dispersion over SBA-16 materials at high metal loading.

Impregnation of Pt onto TLCT-MM-SBA-15 generates metal dispersions comparable with those reported for SBA-15 and KIT-6 series, suggesting that BET surface area in conjunction with enhanced mesopore accessibility can lead to the successful generation of small, discrete Pt nanoparticles. The incorporation of a continuous, interpenetrating macropore-mesopore network (**Figure 4.4 (b)**) and lowered mesopore channel length, aids in the distribution of the Pt precursor through the material during Pt impregnation. This

principle has been used to increase the metal dispersions of Pd<sup>8</sup> and Ir<sup>30</sup> over macroporous-mesoporous supports versus their mesoporous counterparts.

#### 4.2.3.5 Transmission electron microscopy – Pt-impregnated materials

HRTEM analysis of Pt-impregnated SBA-16 and TLCT-SBA-15 (approx. 2 wt. %) was conducted, in order to supplement nanoparticle size determination via existing XRD and CO chemisorption analyses. Representative TEM images for both samples are shown in **Figure 4.10**.

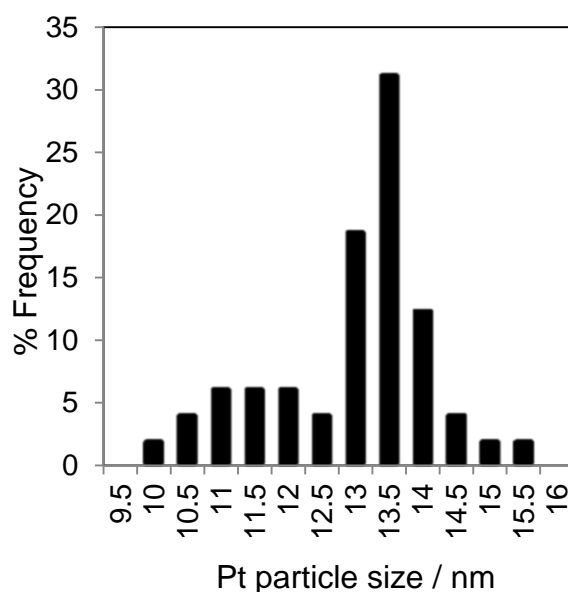
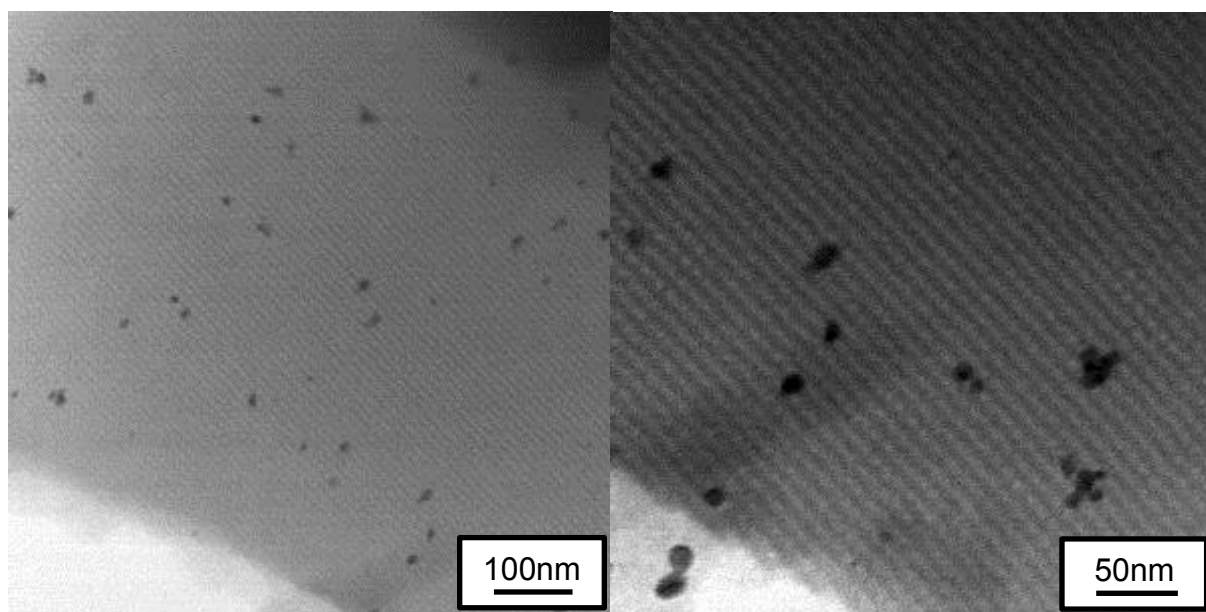


**Figure 4.10 (a) – Representative HRTEM images of approx. 2 wt. % Pt/SBA-16 and particle size distribution for 70 particles**

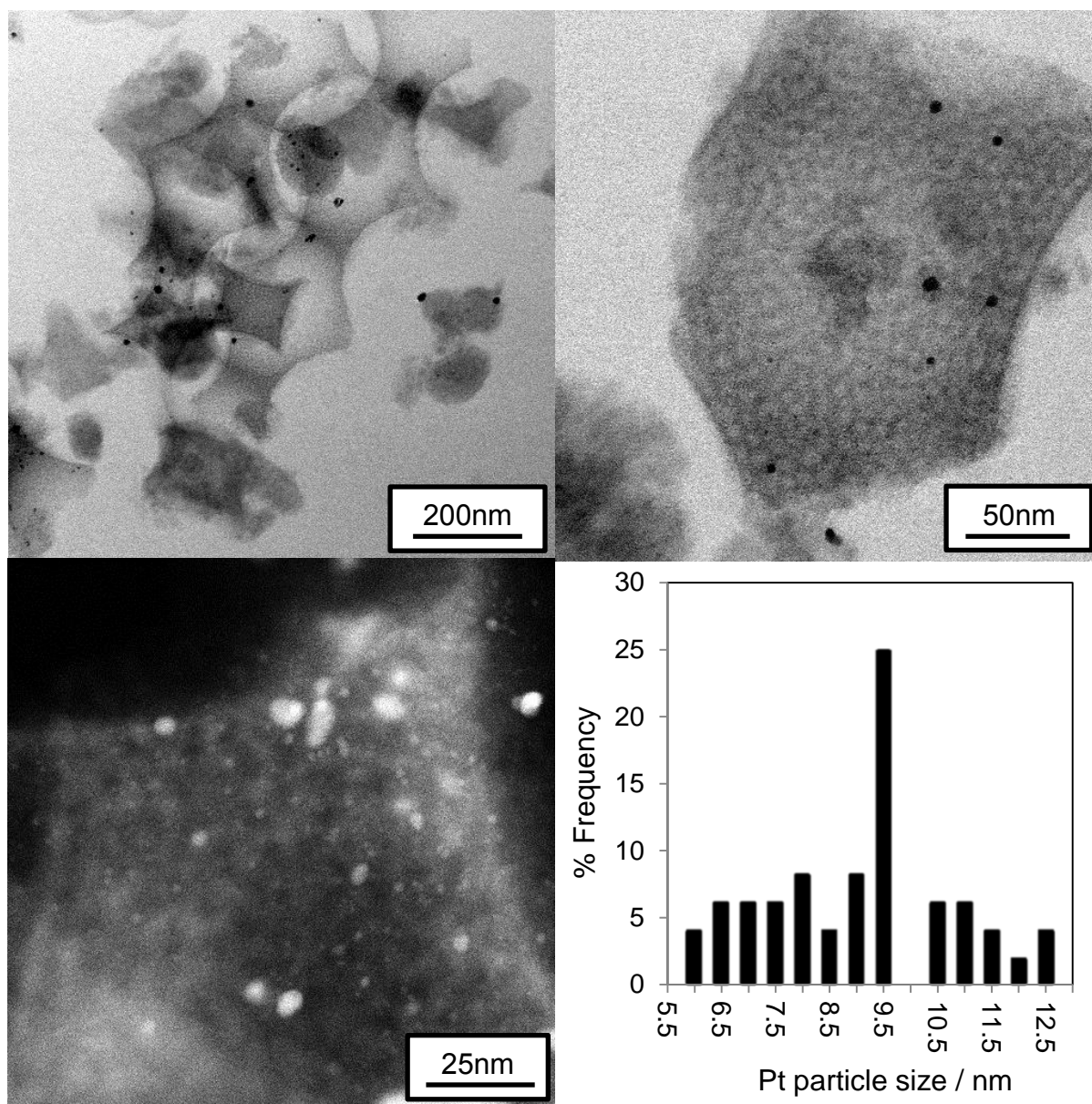


**Figure 4.10 (b) – Representative HRTEM images of approx. 2 wt. % Pt/TLCT-MM-SBA-15 and particle size distribution for 50 particles**

There is an excellent agreement in particle size determination for Pt-impregnated SBA-16 and TLCT-MM-SBA-15 materials, when using CO chemisorption, HRTEM and XRD in tandem. 2 wt. % Pt/SBA-16 reported an average particle size of  $13.4 \pm 0.6$  nm using the three techniques - with a narrow size distribution. HRTEM and XRD analysis of 2 wt. % Pt/TLCT-MM-SBA-15 demonstrates a slightly larger particle size distribution of  $9.5 \pm 1.1$  nm; however the smaller Pt nanoparticle size over macroporous SBA-15 (with respect to mesoporous analogues) highlights the beneficial effect of macropore introduction on Pt precursor diffusion - demonstrating enhanced nanoparticle stabilisation and thus affording greater Pt dispersion. This finding is consistent with Pd systems on a similar material.<sup>8</sup>

#### 4.2.3.6 X-ray photoelectron spectroscopy (XPS)

The surface oxidation state of Pt impregnated SBA-16 and TLCT-MM-SBA-15 samples were probed using XPS analysis. Identical peak positions and fitting parameters for the Pt<sup>(0)</sup> and PtO<sub>2</sub> species, identified in **Chapter 3**, were also applied here. The XPS spectra for both supports are shown in **Figure 4.11**.

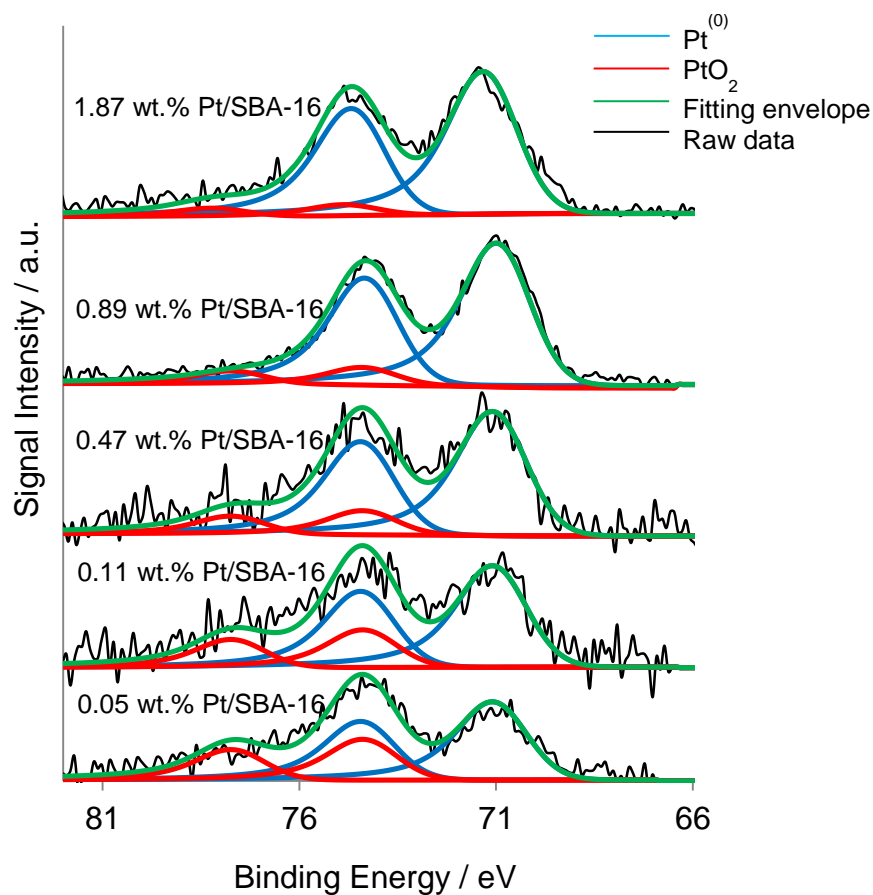


**Figure 4.11 (a) - Stacked Pt 4f XPS plot of Pt/SBA-16 series**

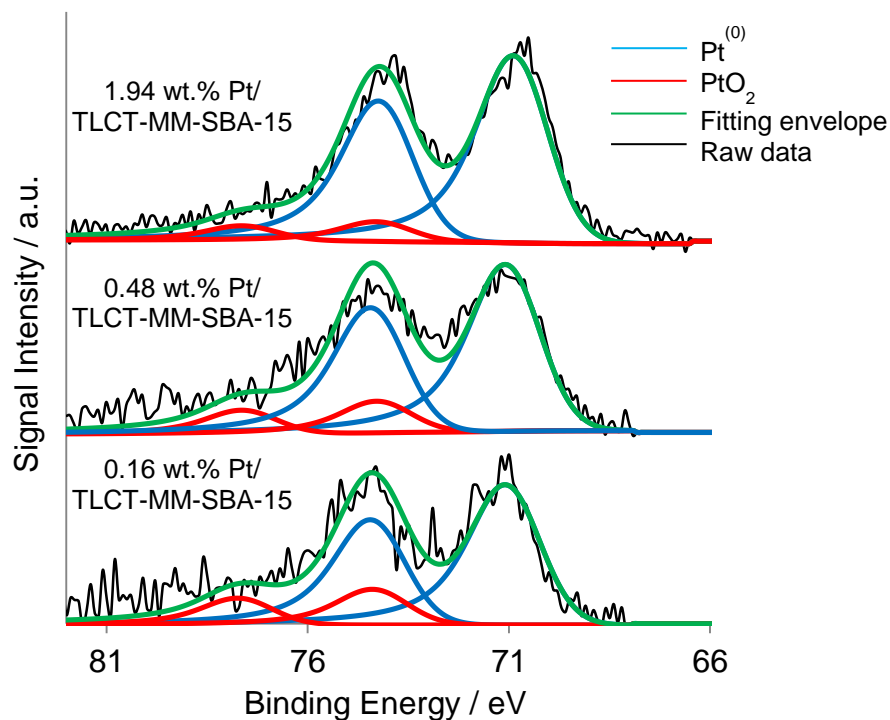


**Figure 4.11 (b) - Stacked Pt 4f XPS plot of Pt/TLCT-MM-SBA-15 series**

**Figure 4.12** illustrates the relationship between PtO<sub>2</sub> content and Pt loading for Pt-impregnated SBA-16 and TLCT-MM-SBA-15 materials (Pt/SBA-15 has been included as a point of comparison).

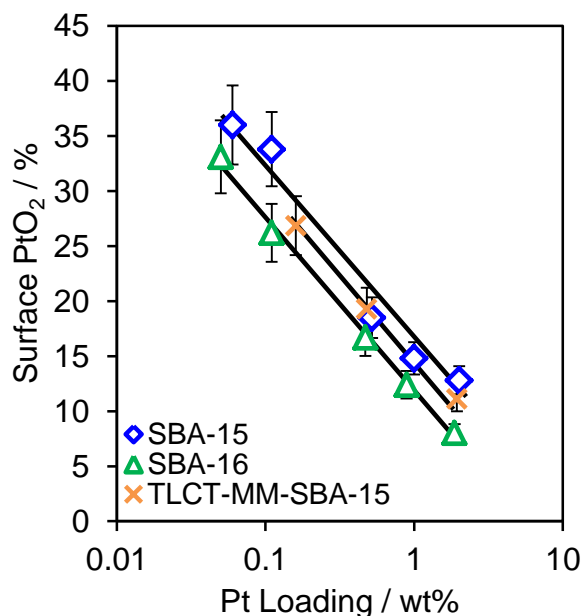


**Figure 4.12 – Influence of Pt loading and support architecture on surface PtO<sub>2</sub> content**

The inverse correlation between Pt loading and oxide content from **Chapter 3** is maintained for Pt impregnation on SBA-16 and TLCT-MM-SBA-15. As seen in **Table 4.4**, Pt-impregnated SBA-16 exhibits diminished PtO<sub>2</sub> content (on comparison with KIT-6 and SBA-15), which can be attributed to a moderate increase in Pt particle size for this series. A direct comparison of TLCT-MM-SBA-15 and SBA-15 highlights a greater PtO<sub>2</sub> dependence of these materials with respect to bulk loading; than SBA-16, reflecting the greater metal dispersions afforded by these hierarchical structures.

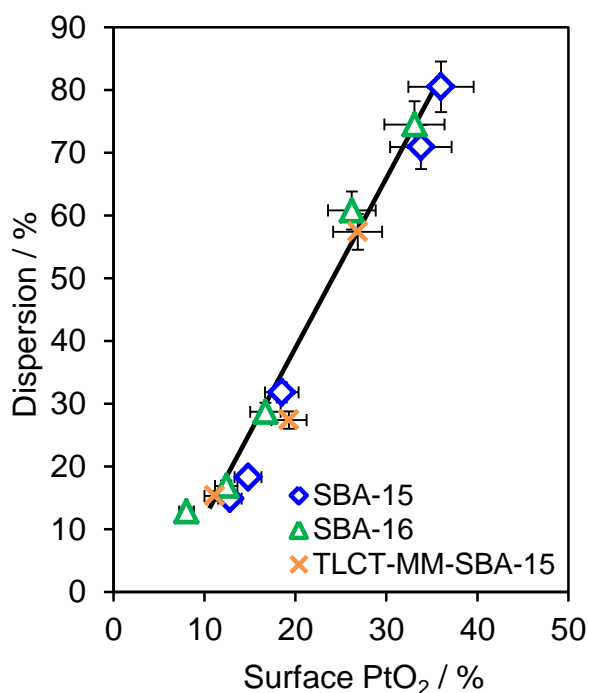


**Figure 4.13 – Relationship between surface PtO<sub>2</sub> content and metal dispersion**

As shown in **Figure 4.13**, surface PtO<sub>2</sub> content (XPS) and metal dispersion (CO chemisorption) demonstrates the same linear correlation identified in **Chapter 3 Figure 3.15**. As this dependence is observed across all studied macro-mesoporous, mesoporous and amorphous silica analogues, it can be stated that Pt dispersion dictates expressed surface PtO<sub>2</sub> content for this family of materials (weakly-interacting, non-reducible silica).



## 4.2.4 Cinnamaldehyde hydrogenation

The selective hydrogenation of cinnamaldehyde,  $C_9H_8O$ , was used to probe the catalytic activity of all Pt/silica systems. The operational set-up and reaction conditions can be found in **Chapter 2**. Any deviations from this protocol are clearly stated. It must be noted that negligible conversion was observed for control experiments in the absence of supported platinum or  $H_2$ .

In order to measure “true” reaction kinetics in the absence of external mass-transfer limitations; such as  $H_2$  solubility in the chosen solvent and substrate diffusion within pores/channels of the investigated mesoporous systems; the effect of stirrer speed on observed catalyst activity was investigated. Equivalent 2 wt. % Pt/silica’s were used to ascertain the optimal stirrer speed for subsequent investigations. Results are shown in **Figure 4.14**. Initial rates have been normalised to account for total mass of Pt present.

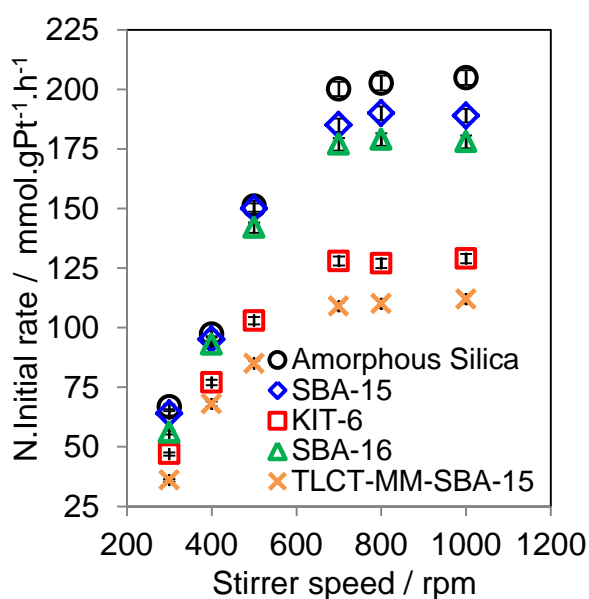


**Figure 4.14 – Influence of stirring rate on cinnamaldehyde hydrogenation, normalised initial rates over approximate 2 wt. % Pt loading on various silica supports**

A clear plateau in normalised initial rates at stirrer speeds  $> 700$  rpm shows this regime to be sufficient to overcome mass-transport limitations. Scrutiny of this preliminary test presents early indications that hydrogenation activity is highly diminished ( $\sim 150$ - $225$   $h^{-1}$ ) when compared with cinnamyl alcohol selox ( $\sim 5000$ - $8000$   $h^{-1}$ )<sup>1</sup> for the same materials. This may be attributed to the lower solubility of  $H_2$  versus  $O_2$  in organic solvents under our “mild” conditions<sup>31, 32</sup> or different structure-activity relationships.

**Figure 4.15** shows the reaction profiles for all five Pt/silica series, utilising the established stirring regime. All catalysts show activity towards cinnamaldehyde hydrogenation, with increasing substrate conversion with Pt loading. Substrate conversion increased in a linear fashion over the first 60 minutes (for all catalysts), before slowing (never reaching total conversion), thus indicating the presence of on-stream deactivation phenomena.

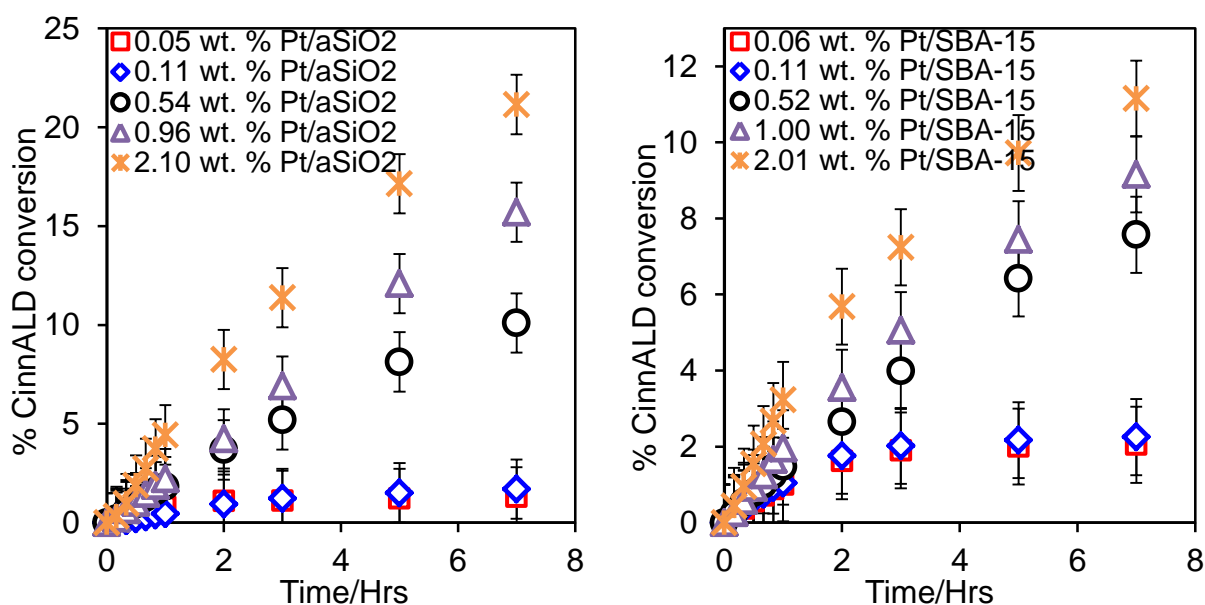


**Figure 4.15 (a) - Cinnamaldehyde hydrogenation reaction profiles for amorphous silica (Left) and SBA-15 (Right) series under ambient conditions**

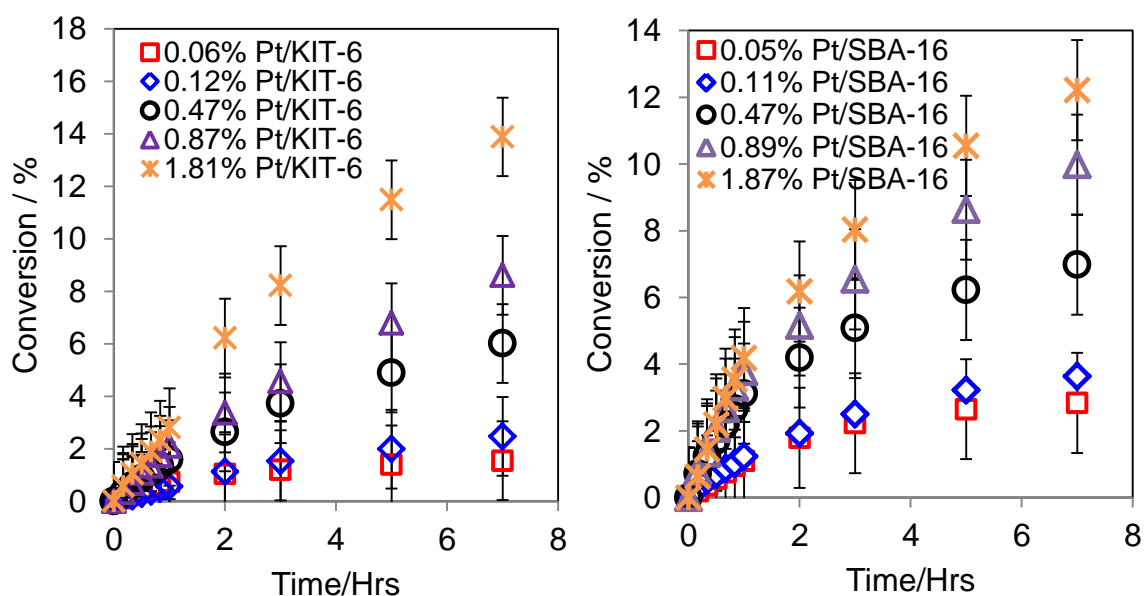


**Figure 4.15 (b) - Cinnamaldehyde hydrogenation reaction profiles for KIT-6 (Left) and SBA-16 (Right) series under ambient conditions**

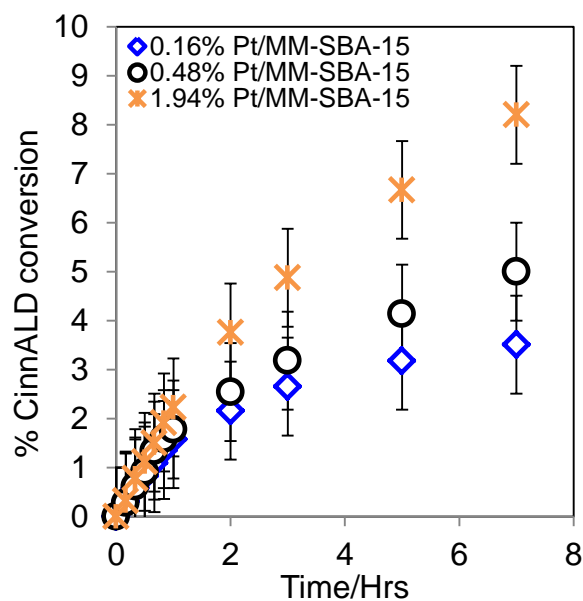


**Figure 4.15 (c) - Cinnamaldehyde hydrogenation reaction profile for TLCT-MM-SBA-15 series under ambient conditions**

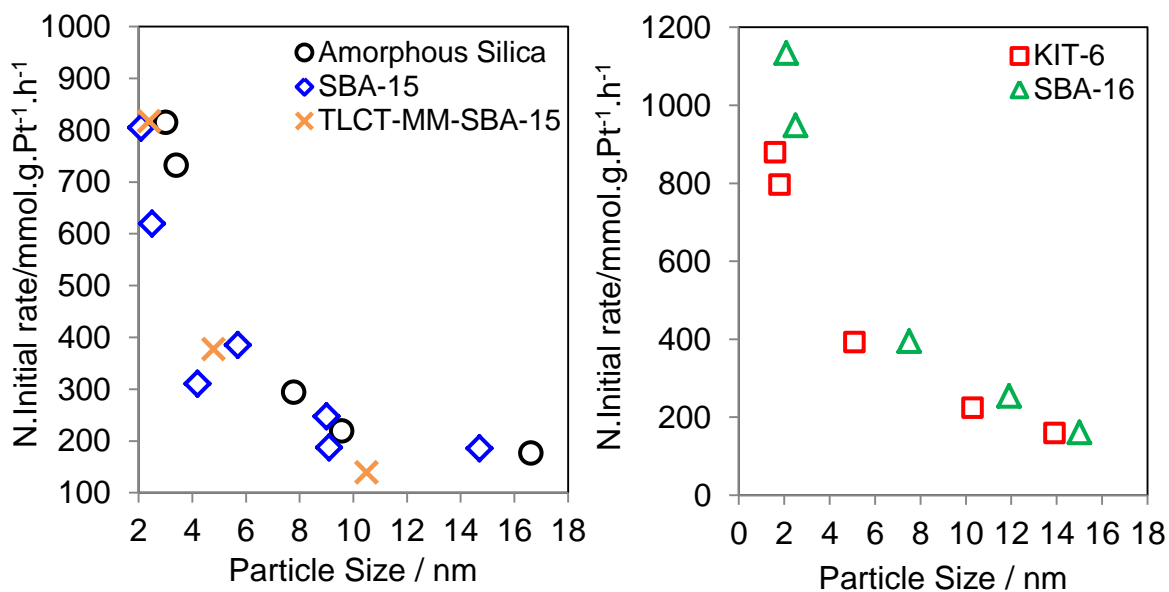


**Figure 4.16 (a) – Initial rate dependence of cinnamaldehyde hydrogenation at 1 bar as a function of Pt particle size (Supports separated for clarity)**

**Figure 4.16 (a)** highlights a dramatic fall in CinnALD hydrogenation initial rates with increasing nanoparticle size, exhibiting an inverse proportionality with Pt particle diameter for all supports. This is to be expected if reactivity is controlled solely by geometric platinum surface area, ignoring local surface atom coordination number or electronic structure.

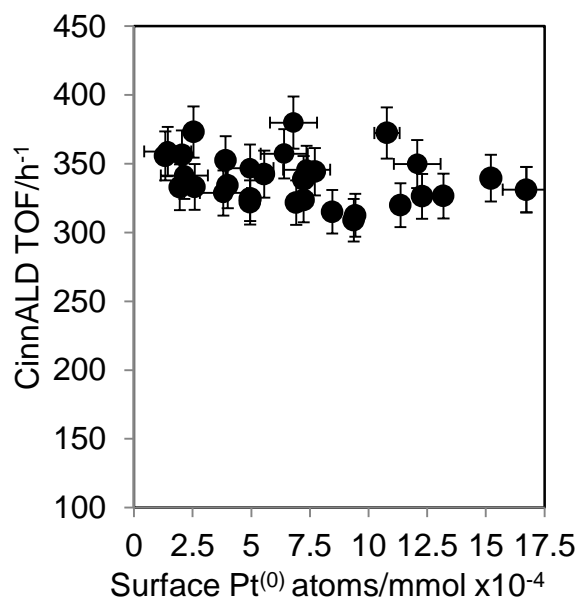


**Figure 4.16 (b) - Turnover frequencies for cinnamaldehyde hydrogenation**

Structure insensitivity is confirmed through the calculation of the corresponding TOFs for CinnALD hydrogenation (**Figure 4.16 (b)**), derived through the normalisation of the initial rate to Pt<sup>(0)</sup> atom surface density - determined via CO chemisorption and XPS. Altering Pt particle size or internal support architecture exhibits negligible effect, where a common TOF of  $\sim 345 \text{ h}^{-1} (\pm 25)$  at 1 bar H<sub>2</sub> for all catalysts are shown. This structure insensitivity is also reported in the literature for platinum and ruthenium nanoparticles supported on carbon nanofibers (CinnALD hydrogenation at atmospheric pressure), in which TOFs ranging between  $200\text{-}350 \text{ h}^{-1}$  were reported.<sup>33</sup> Recent work by Zaera *et al.*, reports TOFs increasing from  $396\text{-}1836 \text{ h}^{-1}$  with increasing Pt particle size over a narrow range of 1.3-2.4 nm (room temperature hydrogenation of CinnALD at 10 bar H<sub>2</sub> over Pt/Aerosil catalysts), seemingly in direct contrast to this work.<sup>34</sup> However, HRTEM was used as an indirect method to quote surface Pt atom density, and hence derive TOFs. Additional empirical evidence provided by a combination of XPS, XRD and CO chemisorption measurements could offer a more accurate surface active species and nanoparticle size quantification, thus leading to greater accuracy in activity determination in their study. Considering the systematic behavior of Pt/silica catalysts investigated in this work, no solid evidence is shown that cinnamaldehyde hydrogenation is favored purely over the flat surfaces present on larger platinum nanoparticles (*i.e.* CinnALD conversion is still observed on small, coordinatively unsaturated Pt nanoparticles). The inverse proportionality of CinnALD hydrogenation initial rate with respect to particle size is consistent with a direct correlation between activity and geometric

surface Pt atom density. This also suggests that all catalysts undergo rapid *in-situ* reduction to form similar, metallic platinum surface species.

In **Figure 4.17**, the catalyst:substrate ratio was varied and the effect on initial rate and TOF calculated.

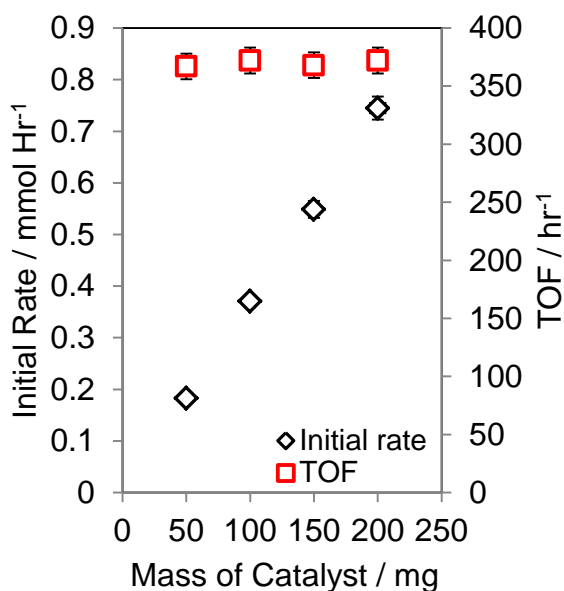


**Figure 4.17 – Influence of catalyst:substrate ratio on cinnamaldehyde hydrogenation initial rate and turnover frequency**

Cinnamaldehyde hydrogenation initial rates increased with catalyst mass, but upon normalisation to Pt<sup>(0)</sup> surface atom density, the calculated TOF demonstrated a clear independence to the amount of catalyst. Furthermore, the TOF value of ~368 h<sup>-1</sup> is within error to the value experimentally determined in **Figure 4.16**, providing greater evidence to Pt structural insensitivity for this substrate.

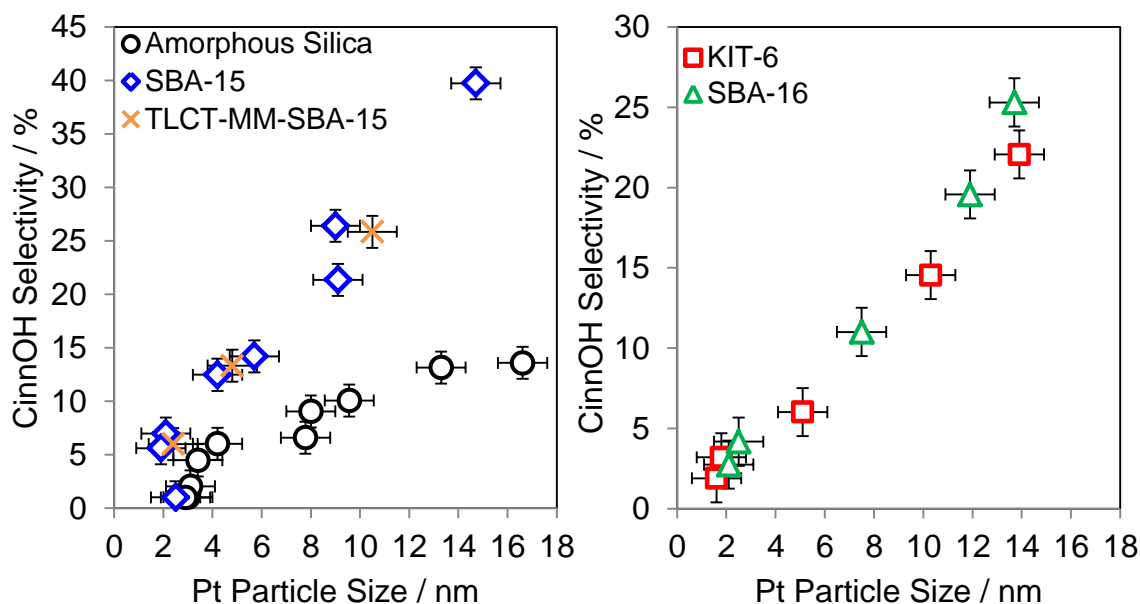


**Figure 4.18 - Cinnamyl alcohol selectivity over amorphous silica, SBA-15 and TLCT-MM-SBA-15 (Left); KIT-6 and SBA-16 (Right) supported platinum catalysts for CinnALD hydrogenation after 7 hrs as a function of Pt particle size (1 Bar H<sub>2</sub>)**

The selectivity towards CinnOH has been shown to track linearly with particle size, rising from < 2% for the smallest nanoparticles across all supports (2 nm) to 14% and 40% for 15 nm particles on amorphous silica and SBA-15 respectively (**Figure 4.18**). Interestingly, the incorporation of macropores into the SBA-15 architecture shows very little destabilising influence on the established linear relationship between Pt particle size and CinnOH selectivity over SBA-15 supported catalysts; any reduction in overall selectivity produced as a result of lowered nanoparticle size (aka enhanced dispersion values). Continuing this theme, progression from a non-interconnecting (SBA-15) to a 3D interpenetrating network (SBA-16 and KIT-6) seems to have little detrimental effect on CinnOH selectivity. The discussed linear relationship is preserved, CinnOH selectivity decreases to approx. 30% for 15 nm particles (SBA-16 supported materials). In order to explain this slight drop in CinnOH selectivity, **Figure 4.19** shows the product selectivity progression as a function of CinnALD conversion over Pt impregnated amorphous silica, SBA-15, KIT-6 and TLCT-MM-SBA-15 (SBA-16 have been omitted, as it demonstrates similar trends in reaction behaviour to KIT-6).

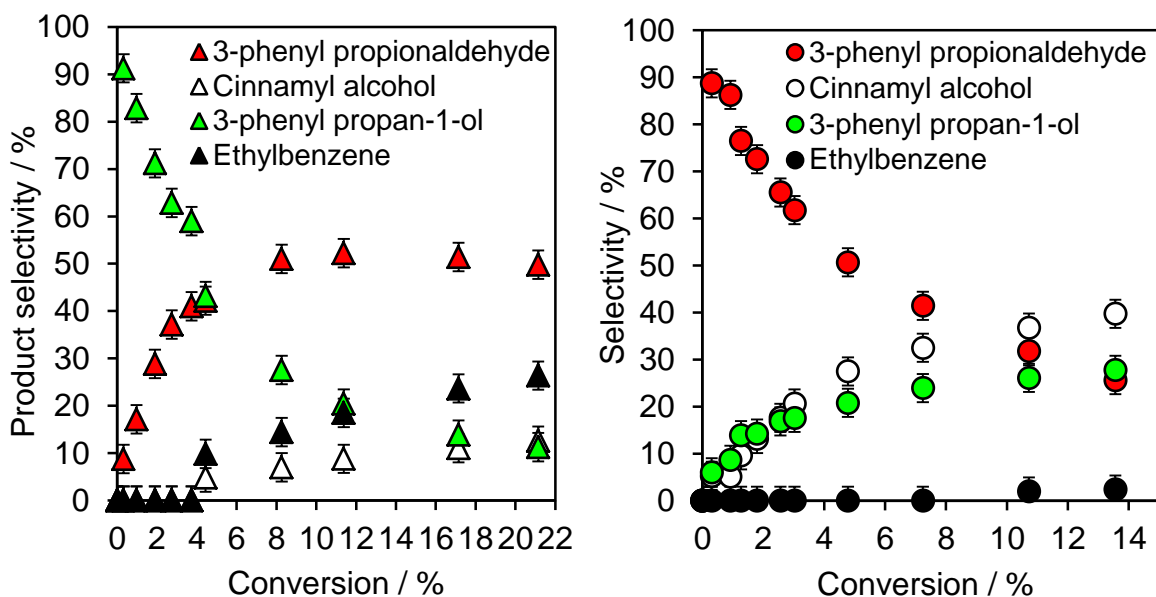


**Figure 4.19 (a) - Evolution of product selectivity as a function of CinnALD conversion over approx. 2 wt. % Pt/amorphous silica (Left) and Pt/SBA-15 (Right) catalysts**

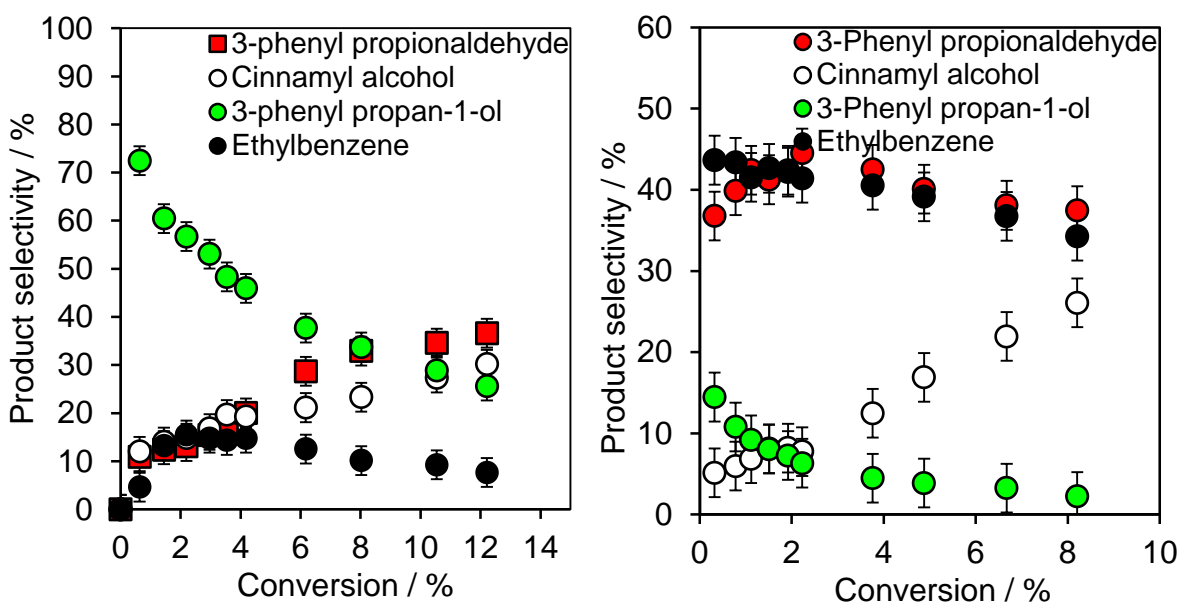


**Figure 4.19 (b) - Evolution of product selectivity as a function of CinnALD conversion over approx. 2 wt. % Pt/KIT-6 (Left) and Pt/TLCT-MM-SBA-15 (Right) catalysts**

Competition between C=C hydrogenation, decarbonylation and unsaturated alcohol formation is evident across all silica families. Major side-products include 3-phenylpropionaldehyde, 3-phenylpropan-1-ol and ethylbenzene. The high selectivity to the saturated aldehyde for all systems demonstrates that unwanted C=C hydrogenation competes directly with C=O hydrogenation. Ethylbenzene is formed as a by-product of 3-phenyl propionaldehyde and/or 3-phenylpropan-1-ol hydrogenolysis (**Figure 4.19**). Particle size

dependency on CinnOH selectivity is in accordance with previous literature findings for Ru,<sup>35-37</sup> Co<sup>38</sup> and Pt catalysts.<sup>39-41</sup> In these studies, an increase in Pt(111) facet density versus coordinatively unsaturated edge and corner sites over larger nanoparticles is given as the origin to this enhancement. The close approach of the C=C functionality is suggested to be sterically hindered over Pt(111), leading to a promotion in the C=O hydrogenation pathway.<sup>39, 42-45</sup> Extended Hückel calculations by Delbecq and Sautet back this postulation, showing the presence of extended Pt(111) facets to strongly destabilise the di- $\sigma_{CC}$  CinnALD adsorption mode and thus encourage C=O hydrogenation, through adsorption in the di- $\sigma_{CO}$  mode. As particle size decreases, stepped and Pt(100) facet population increases. Subsequent stabilisation of a co-planar  $\eta^4$  di- $\sigma_{CO}+\pi_{C=C}$  and/or trihapto  $\pi_{C=C+(O)}$  CinnALD binding mode, favours C=C hydrogenation.<sup>46</sup>

Closer scrutiny of **Figure 4.19** shows some interesting similarities and differences between the hierarchical supports in this reaction. Focussing on SBA-15 versus TLCT-MM-SBA-15, both materials exhibit an increasing selectivity towards the desired unsaturated alcohol product. This may reflect the greater substrate-product diffusion kinetics permitted by SBA-15 substructures versus the amorphous analogue. However, TLCT-MM-SBA-15 sports consistently higher ethylbenzene and saturated aldehyde selectivities (approx. 40%), formed through decarbonylation and C=C hydrogenation respectively. 2 wt. % Pt/TLCT-MM-SBA-15 nanoparticles show a greater dispersion, and hence lower particle size (10 nm), than their SBA-15 counterparts (15 nm). This change in geometric configuration leads to a lowering of Pt(111) facet density, explaining a lower CinnOH selectivity but also the increased expression of the “undesired” reaction pathways - as edge, corner and Pt(100) facet population increases over smaller nanoparticles. The observed rise in CinnOH and 3-phenylpropan-1-ol with CinnALD conversion over Pt/SBA-15 is consistent with previous literature studies over oxide supported Pt<sup>47</sup> and Ir/C<sup>48</sup> catalysts. C=C hydrogenation is preferentially favoured over these catalysts, but as surface crowding due to strongly bound adsorbates occurs,<sup>49</sup> this pathway is promptly switched off during the early stages of CinnALD hydrogenation.

In the case of SBA-16/KIT-6 materials, the interconnection of mesopore channels does permit the generation of CinnOH in moderate selectivity (approx. 25%) – “out of pore” diffusion of *in-situ* formed CinnOH aided by this interconnectivity. However, saturated aldehyde selectivity also tracks with directly with CinnOH production (saturated alcohol and



ethylbenzene selectivities also demonstrate high values), so we can state that for this family of materials, C=O versus C=C hydrogenation are truly in competition. As nanoparticle sizes are comparable for SBA-15 and SBA-16, we cannot attribute this change to geometric effects exclusively. One possible explanation is that mesopore interconnectivity, which usually promotes in-pore diffusion, can also promote secondary reaction in this case. The formation of CinnOH or 3-phenylpropionaldehyde takes place as the principle first reaction, diffusion from the Pt surface occurs, followed by consecutive adsorption onto Pt elsewhere. This explains the formation of the saturated alcohol and ethylbenzene side-products. From **Figure 4.19(b)**, we see saturated alcohol selectivity decrease with conversion, followed by a significant decrease in ethylbenzene production. At low conversion and reaction time, the number of Pt nanoparticles available for secondary reaction is relatively high, but as the reaction proceeds and a greater number of CinnALD substrate molecules diffuse into the mesopores, substrate crowding at each active site lowers the probability of secondary adsorption thus explaining the observed drop in 3-phenylpropan-1-ol and ethylbenzene production.

In contrast, Pt/aSiO<sub>2</sub> demonstrates very low selectivity towards CinnOH, in favour of the saturated aldehyde and decarbonylation pathways. Interestingly, 3-phenylpropan-1-ol is the favoured initial product before a switching of reaction pathways towards 3-phenylpropionaldehyde and CinnOH synthesis. In order for this to occur, the C=O bond in the saturated aldehyde must be rapidly hydrogenated over the fresh catalyst, becoming less prevalent as adsorbates accumulate on the catalyst surface and as catalyst *in-situ* reduction takes place. The dramatic decrease in CinnOH selectivity (when compared with SBA-15) cannot be explained by Pt nanoparticle geometric effects and so must be due to an additional factor (i.e. support surface character).

#### 4.2.4.1 Probing the reaction pathway

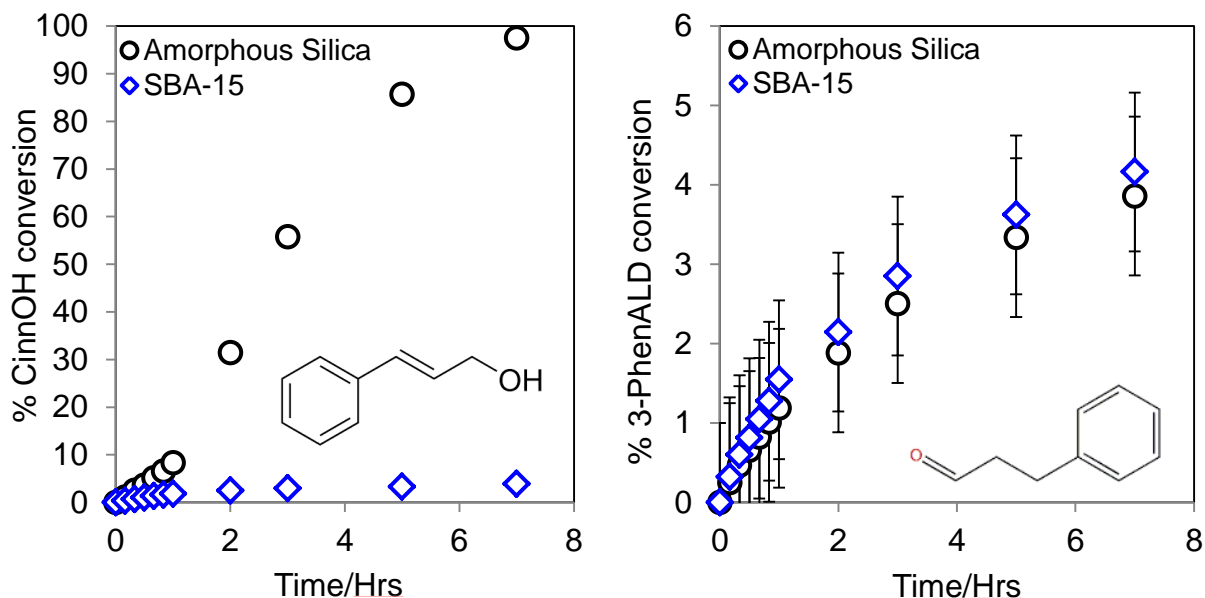


**Figure 4.20 – Cinnamyl alcohol (Left) and 3-phenylpropionaldehyde (Right) hydrogenation over approx. 2 wt. % silica supported platinum catalysts at 1 bar H<sub>2</sub>**

In order to fully analyse the CinnALD hydrogenation reaction pathway, the hydrogenations of CinnOH and 3-phenylpropionaldehyde were probed. As shown by **Figure 4.18**, Pt impregnated on hierarchical silica demonstrates structure sensitivity towards CinnOH selectivity with Pt nanoparticle size; in the order of 5 (for SBA-15) and 2.5 times greater (SBA-16, KIT-6 and MM-TLCT-SBA-15), respectively, than the amorphous silica supported analogues. As CinnALD hydrogenation takes place with a mutual TOF over all supports, any difference in CinnOH selectivity cannot be easily attributed to mass-transport issues through hierarchical support structure. If mass-transport issues were present, one would expect *in-situ* formed CinnOH to be more easily removed over Pt/aSiO<sub>2</sub> catalysts, where the reaction occurs predominantly on the external surface area, and thus a higher selectivity to this product should be observed. However, our findings allude to the description of CinnOH selectivity as a function of the rate of C=O (versus C=C) hydrogenation for the CinnALD starting material and the secondary hydrogenation of the allylic alcohol product to 3-phenylpropan-1-ol.

To understand this, **Figure 4.20** demonstrates a crucial support dependence for the hydrogenation of CinnOH over amorphous silica and SBA-15 supported Pt nanoparticles, at a size (15 nm) and metal loading (approx. 2 wt. %) region where the most striking comparisons in CinnALD hydrogenation behavior have previously been noted (**Figures 4.18 and 4.19**).

The selective hydrogenation of 3-phenylpropionaldehyde, formed via C=C hydrogenation of CinnALD, presents identical rates of conversion over 2 wt. % amorphous silica and SBA-15 catalysts. This shows saturated aldehyde selectivity is determined only by the rate of CinnALD C=O versus C=C hydrogenation, as the rate of removal of this saturated aldehyde is similar over both catalyst families. Since CinnALD selectivity towards 3-phenylpropionaldehyde is lower across all hierarchical supports (27-37%) versus amorphous silica (51%), the choice of support does seem to influence the rates of C=O versus C=C hydrogenation, and thus the rate of CinnOH production. For both supports, 3-phenylpropionaldehyde hydrogenation produces 3-phenylpropan-1-ol and ethylbenzene as the only products, confirming the operation of C=O hydrogenation and hydrogenolysis pathways respectively. The observed limited reactivity of Pt/SBA-15 towards CinnOH hydrogenation does come as a surprise and may reflect an external influence on the adopted substrate adsorption mode. The differing reactivity of the hierarchical silica's towards the selective hydrogenation of CinnALD dictates unsaturated alcohol product selectivity - which is strongly influenced by their interaction with the starting material.

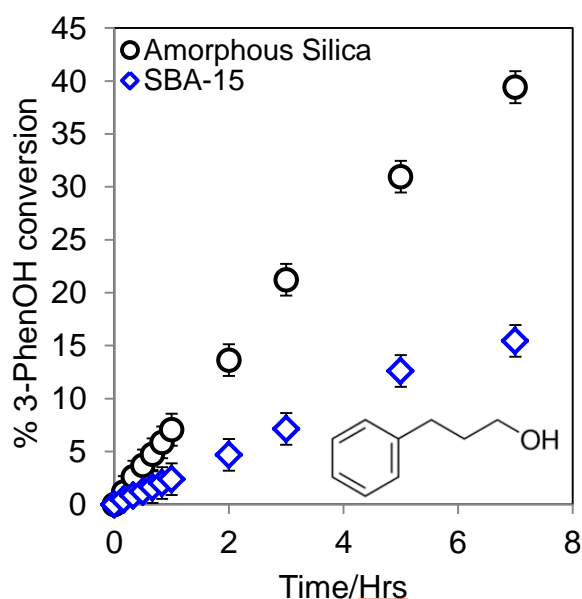
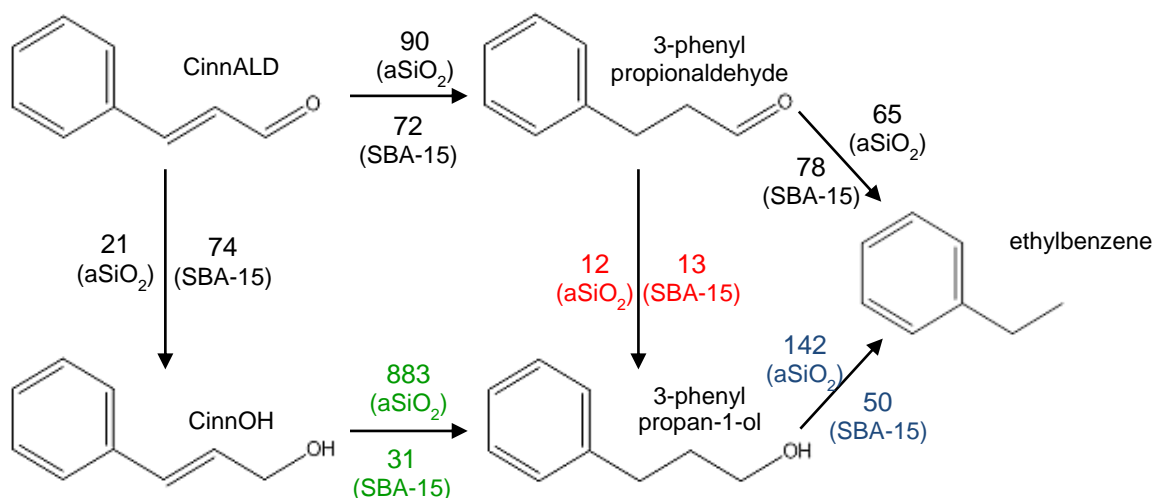


**Figure 4.21 – 3-phenylpropan-1-ol hydrogenation over approx. 2 wt. % silica supported platinum catalysts at 1 bar H<sub>2</sub>**

In **Figure 4.21**, we conduct the hydrogenation of 3-phenylpropan-1-ol to confirm the presence of the hydrogenolysis pathway within the CinnALD hydrogenation reaction scheme. As demonstrated in the hydrogenation of CinnOH, Pt impregnated on amorphous silica also outperforms Pt/SBA-15 in the hydrogenation of the saturated alcohol. For both materials, ethylbenzene is the predominant product; confirming the origin of hydrogenolysis products in

the main reaction scheme. The promotion of this pathway over Pt/aSiO<sub>2</sub> catalysts, in tandem with the CinnOH hydrogenation pathway, explains the low overall selectivity towards CinnOH. Reactively formed CinnOH, undergoes sequential C=C and hydrogenolysis reactions over Pt. An effect not explainable by geometric effects alone, as size and Pt loading for the screened materials are similar. DFT calculations using allylic aldehyde hydrogenation over model Pt(111) surfaces by Laref and co-workers, showed selectivity toward unsaturated alcohols is determined principally by the strength of their binding.<sup>50</sup> The role of H<sub>2</sub> pressure, Pt nanoparticle *in-situ* structure and support surface characteristics will be probed in future sections to reveal the origin of this behaviour.



**Scheme 1** - Kinetic network for CinnALD hydrogenation for approx. 2 wt. % Pt/aSiO<sub>2</sub> and Pt/SBA-15 catalysts (Black = **cinnamaldehyde**; red = **3-phenylpropionaldehyde**; green = **cinnamyl alcohol**; and blue = **3-phenylpropan-1-ol**. Values refer to the initial rates of each step in mmol.h<sup>-1</sup>.g<sub>Pt</sub><sup>-1</sup>)

**Scheme 1** gives a pictorial representation of the main and by-product pathways in operation for CinnALD hydrogenation. The initial rates for each step have been shown and colour coded for each starting material. The difference in reactivity between the two supports is clearly evident, supporting previous conclusions reporting amorphous silica to favour C=C hydrogenation of CinnALD and CinnOH; and SBA-15 to be more selective towards CinnOH production - inhibiting subsequent transformation to unwanted side products. It is interesting to note that theoretically methanol and formic acid are also potential side products for cinnamaldehyde hydrogenation, however these components elute at similar times to anisole on the GC trace; making it difficult to accurately quantify these components.

#### 4.2.4.2 Effect of H<sub>2</sub> pressure

Figure 4.22 shows the effect of H<sub>2</sub> pressure on CinnALD hydrogenation, focussing on CinnOH selectivity and expressed TOF for all silica supports.

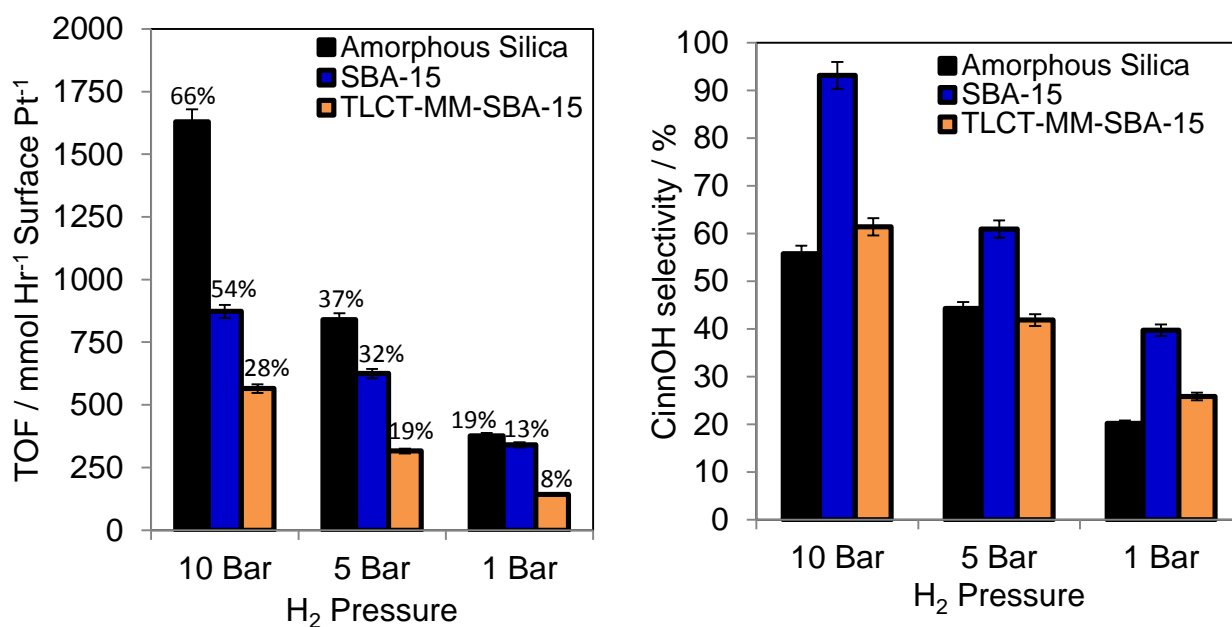


Figure 4.22(a) – H<sub>2</sub> pressure dependence of CinnALD hydrogenation over amorphous silica, SBA-15 and TLCT-MM-SBA-15 at approx. 2 wt. % Pt. Percentage values inset represent 7 hr conversions

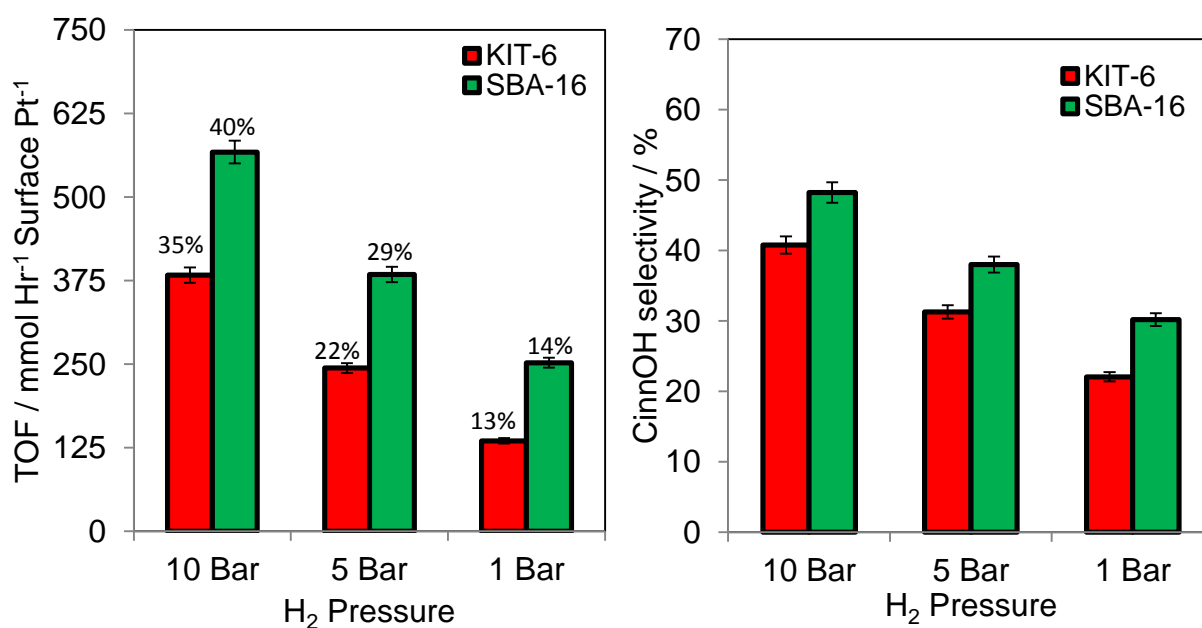
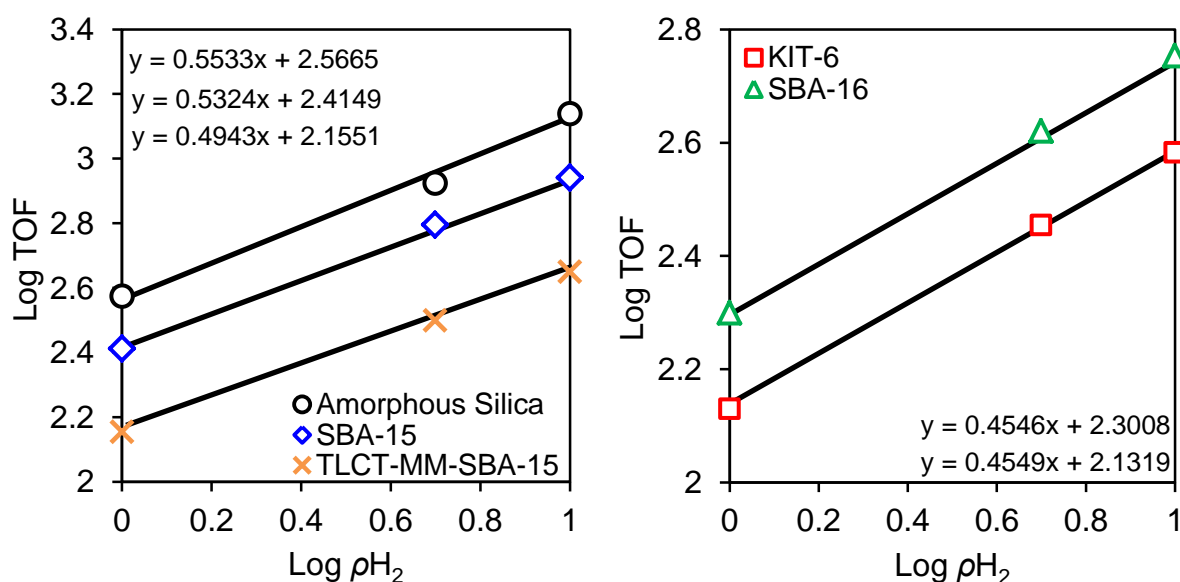


Figure 4.22(b) – H<sub>2</sub> pressure dependence of CinnALD hydrogenation over KIT-6 and SBA-16 at approx. 2 wt. % Pt. Percentage values inset represent 7hr conversions

Positive reaction orders with respect to hydrogen pressure are usually shown for liquid phase catalytic hydrogenation.<sup>51-54</sup> Higher solubility in the liquid phase, grants increased availability of atomic hydrogen over catalytic active sites, an effect derived from “Henry’s law.” At 1 bar H<sub>2</sub>, all catalysts reported CinnALD conversion levels < 20%, in order to increase H<sub>2</sub> solubility within these systems (and hence improve activity), the impact of hydrogen pressure upon CinnALD hydrogenation was therefore investigated over the most selective approx. 2 wt. % Pt silica catalysts in a stirred batch autoclave under a constant hydrogen pressure at 1, 5 and 10 bar respectively. **Figure 4.22** shows the expected increase in initial rate, TOF and final CinnALD conversion for all screened catalysts, as hydrogen pressure increases. Similar observations have been noted in the literature, atmospheric<sup>40</sup> versus high pressure (48 bar)<sup>33</sup> CinnALD hydrogenation, using Pt supported on carbon nanofibers, reported a promotion in TOFs from approx. 200 to 828 h<sup>-1</sup> with increasing H<sub>2</sub> pressure.



**Figure 4.23 – Relationship between  $p_{H_2}$  and reaction order over amorphous silica, SBA-15 and TLCT-MM-SBA-15 (Left); KIT-6 and SBA-16 (Right) supported platinum catalysts for CinnALD hydrogenation (approx. 2 wt. %)**

**Figure 4.23** shows Pt-impregnated amorphous silica behaves with a minor increase in pressure sensitivity, than the hierarchical silica’s; the reaction order in  $p_{H_2}$  ranges from 0.45 to 0.55 over all supports. This value is close to the expected 0.5 value, suggesting that the rate determining step involves the reaction of the CinnALD substrate with a single hydrogen adatom – formed from the dissociative adsorption of molecular H<sub>2</sub> over Pt. Consistent with the aforementioned study using reduced platinum nanoparticles over deoxygenated carbon

nanofibers at ambient pressure.<sup>33</sup> A positive reaction order in  $p_{H_2}$  shows that vacant surface sites are available for the dissociative chemisorption of hydrogen at these pressure ranges, with no surface saturation occurring. The atomic hydrogen produced can take part in the two competing CinnALD hydrogenation pathways (C=O versus C=C) to yield CinnOH or 3-phenylpropionaldehyde, as shown by the variability of product selectivity with support choice at comparable  $p_{H_2}$  (Figures 4.22 and 4.24).

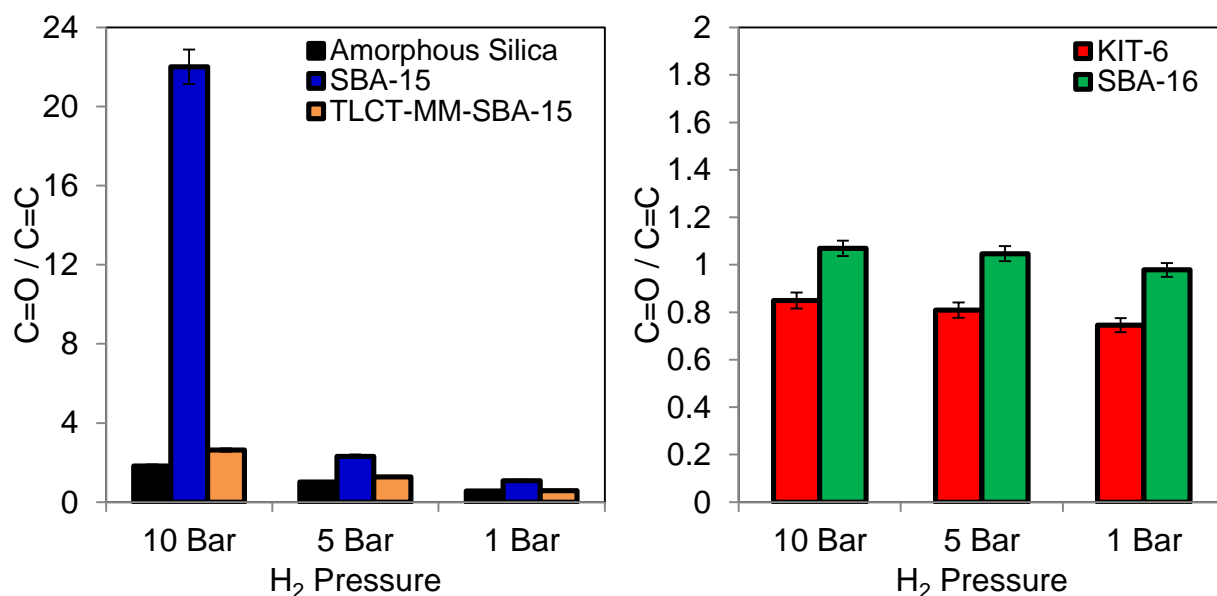


**Figure 4.24 – H<sub>2</sub> pressure dependence on C=O versus C=C hydrogenation pathways during CinnALD hydrogenation over approx. 2 wt. % Pt supported on silica**

Figures 4.22 and 4.24 show that hydrogen pressure has a greater effect on product selectivity than on activity. CinnALD hydrogenation to CinnOH is promoted over all support architectures, with increasing H<sub>2</sub> pressure. This promotion is most evident over 2 wt. % Pt/SBA-15, where CinnOH selectivity surpassed 90% at 10 bar, with trace amounts of 3-phenylpropionaldehyde reported as the only side-product. Staggeringly, this corresponds to a 22-fold increase in the ratio of CinnOH to 3-phenylpropionaldehyde production. Selectivity also rose across 2 wt. % Pt impregnated on amorphous silica and TLCT-MM-SBA-15 to 56% and 61% respectively. In both cases, the hydrogenolysis of 3-phenylpropan-1-ol to ethylbenzene exhibited diminished selectivity, highlighting suppression of this pathway at increasing  $p_{H_2}$ . The lower conversion and CinnOH selectivity values for Pt-impregnated TLCT-MM-SBA-15 versus SBA-15 can be explained by the decreased particle size of TLCT-MM-SBA-15 impregnated Pt nanoparticles (10.5 nm versus 14.7 nm). However, as the linear correlation between Pt particle size and CinnALD conversion/CinnOH selectivity

has been maintained, one would expect Pt/TLCT-MM-SBA-15 under a comparable particle size regime to match or outperform those values quoted for 2 wt. % Pt/SBA-15, due to an improvement in substrate-product diffusion kinetics afforded by the presence of a highly ordered macro-mesopore architecture.<sup>3,6</sup>

The incorporation of mesoporosity into the silica framework yielded greater  $pH_2$  sensitivity and superior CinnOH production ability. It was believed that this reaction behaviour could be improved further via the interconnection of the mesopore channels into a 3D interconnecting framework (KIT-6 and SBA-16), enhancing substrate-product diffusion kinetics and hydrogen availability at each Pt active site. As stated before, increasing hydrogen pressure has a positive influence on CinnALD conversion (and by extension TOFs), but due to the smaller, more highly dispersed Pt nanoparticles generated by SBA-16 and KIT-6 supports, the overall promotion in activity and conversion (TOF = 385 h<sup>-1</sup> and 567 h<sup>-1</sup> (SBA-16 and KIT-6 respectively) versus 873 h<sup>-1</sup> (SBA-15)) falls far short of those sported by Pt/SBA-15. Most shockingly, the ratio of C=O to C=C hydrogenation demonstrates only a small shift towards preferential C=O hydrogenation with increasing pressure. Increased C=C hydrogenation occurs through the total suppression of the hydrogenolysis route to ethylbenzene, caused by surface crowding at higher H<sub>2</sub> pressures (an effect also exhibited by amorphous and SBA-15 derived silica analogues). The lack of distinction between the CinnOH and 3-phenylpropionaldehyde reaction pathways for SBA-16 and KIT-6 materials comes as a surprise. At present, we have no immediate explanation for this observed change in reaction behaviour. From a geometric perspective, smaller Pt nanoparticles on 3D interconnected SBA-16 and KIT-6 yield a lower surface population of flat, extended Pt(111) facets thus partially accounting for a drop in CinnOH selectivity, but as the difference in nanoparticle size between Pt/SBA-15 (14.7 nm) and Pt/KIT-6/SBA-16 (13.9 nm and 13.7 nm respectively) is  $\leq 1$  nm, additional factors must be apparent. Probing of support surface characteristics and *in-situ* nanoparticle structure may provide an answer.

#### 4.2.4.3 Active site heterogeneity

A hot filtration test was used in **Chapter 3 section 3.2.3.1** to exclude any contribution to the observed selective oxidation activity through homogeneous processes. The same procedure is applied here for the hydrogenation scheme, using the most active 2 wt. % Pt loading for each support.



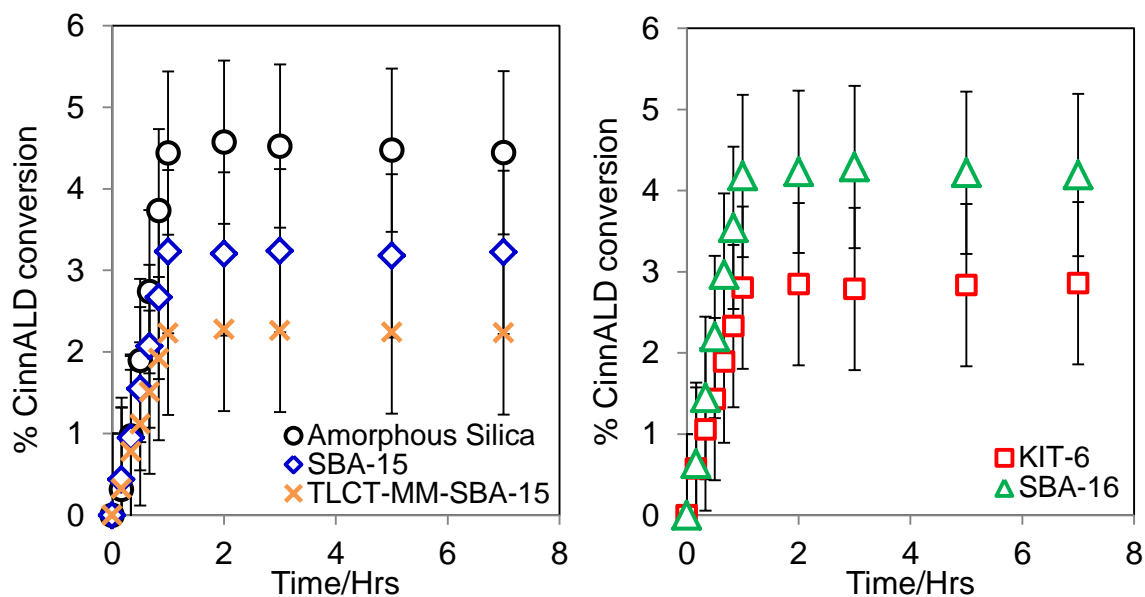


**Figure 4.25 – Hot filtration tests to determine the extent of Pt leaching in cinnamaldehyde hydrogenation for approx. 2 wt. % Pt on aSiO<sub>2</sub>, SBA-15, KIT-6, SBA-16 and TLCT-MM-SBA-15 materials (Catalyst removed after 60 minutes)**

Figure 4.25 demonstrates that substrate conversion ceases upon catalyst removal, thus verifying the generation of a truly heterogeneous material.

#### 4.2.5 Extended characterisation of Pt impregnated silica supports

In order to determine the origin of the CinnOH selectivity enhancement over Pt impregnated SBA-15 analogues, and the subsequent shift in reaction behaviour over 3D interconnected hierarchical silica, a range of extended characterisation techniques were utilised to probe support surface characteristics, reagent binding parameters and *in-situ* Pt morphology.

##### 4.2.5.1 *In-situ* XRD

*In-situ* XRD was used to investigate the role of H<sub>2</sub> pressure on Pt nanoparticle structure at reaction temperature (90°C). The overall procedure operates in an identical fashion to traditional XRD analyses. The sample is housed in a specialised “Anton Parr XRK 900 Reactor *in-situ* Chamber”, which permits gas phase delivery, at a range of 1-7 bar (correct at time of writing), in tandem with controlled temperature ramping/control (max. 700 °C). It is believed that elevated H<sub>2</sub> pressures may promote Pt nanoparticle restructuring, leading to subtle variations in Pt particle size, geometry or exposed facet population.

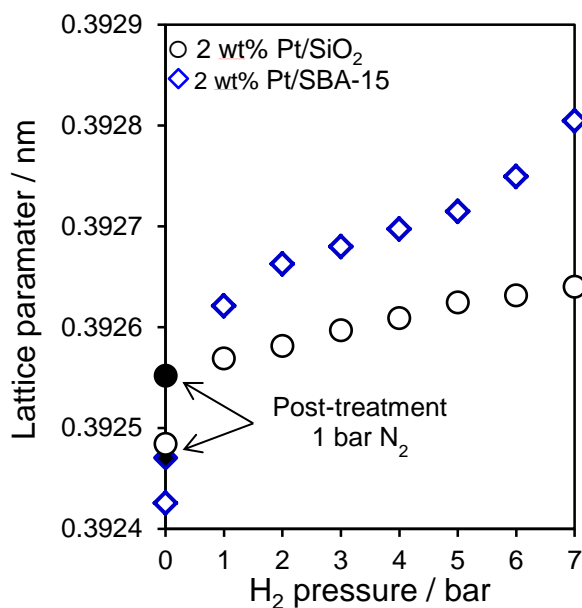


**Figure 4.26 – Hydrogen pressure dependence of fcc platinum lattice parameter of approx. 2 wt. % silica supported platinum catalysts at room temperature**

*In-situ* XAS measurements conducted by Mistry and co-workers discovered that discrete 1 nm platinum clusters experienced a transformation in adopted surface geometry, progressing from 2D  $\rightarrow$  3D over  $\gamma$ -Al<sub>2</sub>O<sub>3</sub>; as  $p_{H_2}$  increased from 1 to 21 bar at room temperature.<sup>55</sup> In this study, Pt (111) bilayers were proposed to form cuboctahedra, forming new Pt (100) facets with the overall loss of approx. 70% (111) facets.<sup>56</sup> As previously eluded to earlier, extended Hückel calculations by Delbecq and Sautet highlight the favourability of the di- $\sigma_{CO}$  cinnamaldehyde adsorption mode over Pt (111) facets, and thus C=O hydrogenation promotion as a result, whereas Pt (100) facets tend towards a co-planar  $\eta_4$  mode, favourable for C=C adsorption.<sup>46</sup> In this case, the hydrogen pressure-induced shift from (111) to (100) facets, proposed by Mistry et al, would serve to lower selectivity to cinnamyl alcohol. Taking the core principles of this work, *in-situ* powder XRD of silica supported approx. 2 wt. % Pt catalysts was conducted between 1 and 7 bar H<sub>2</sub> pressure - to determine if Pt nanoparticle restructuring is possible during elevated pressure CinnALD hydrogenation. **Figure 4.26** shows a small, but systematic fcc platinum lattice expansion ( $\sim 0.0004$  nm  $\pm$  0.1%) was observed over Pt/aSiO<sub>2</sub> and Pt/SBA-15 catalysts, with the overall expansion being greater for the SBA-15 supported nanoparticles. However, this expansion was proved to be reversible upon removal of H<sub>2</sub>. In comparison with work reported by Mistry et al, the observed fcc expansion was a factor of ten smaller than those observed via the *in-situ* XAS study of Pt/  $\gamma$ -Al<sub>2</sub>O<sub>3</sub> materials.

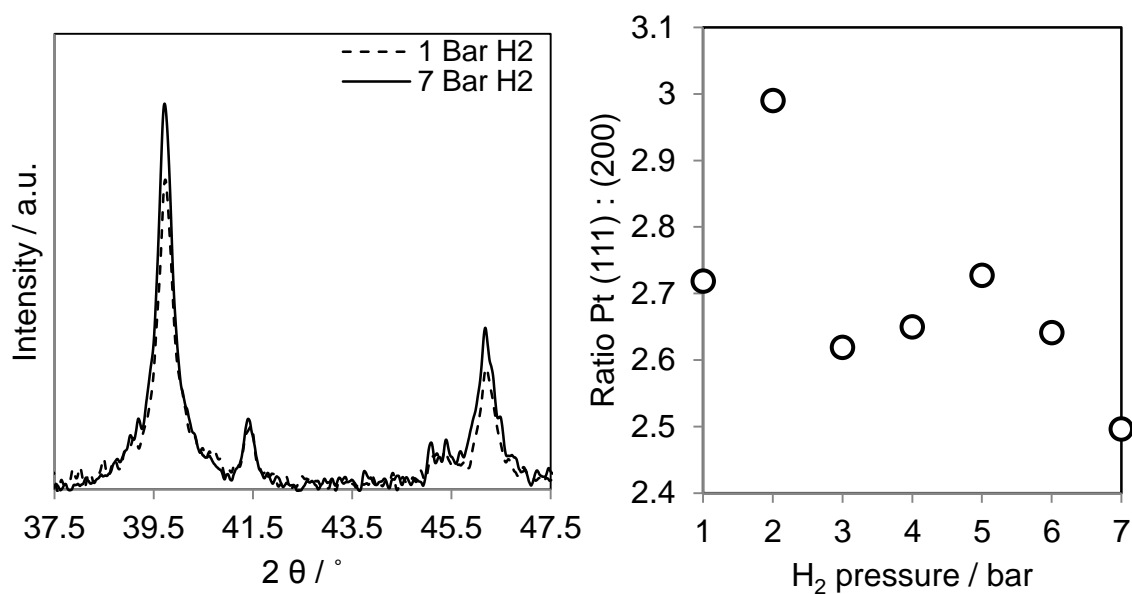
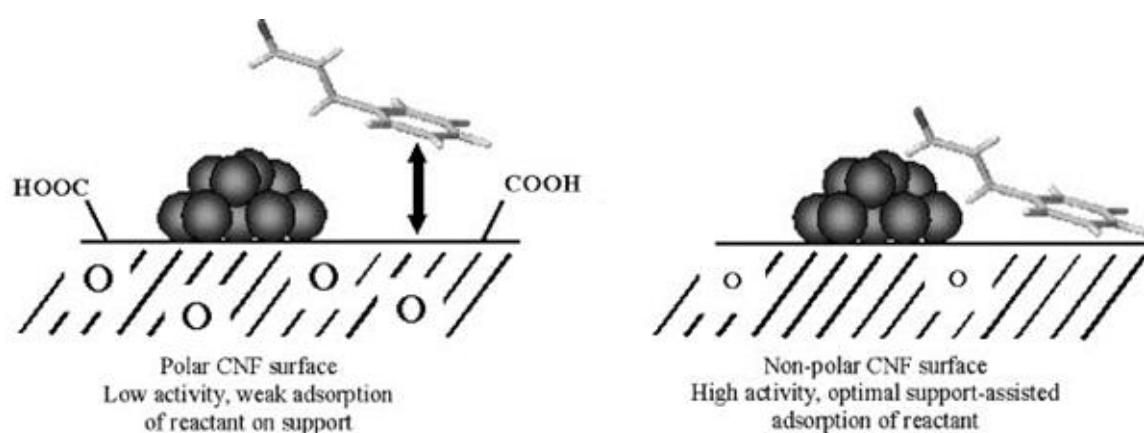


**Figure 4.27 – Hydrogen pressure independence Pt (111):(200) x-ray reflections over approx. 2 wt. % Pt/SBA-15 catalysts**

**Figure 4.27** shows the XRD pattern of approx. 2% Pt/SBA-15 at atmospheric and 7 bar H<sub>2</sub>, the ratio of Pt (111):(200) x-ray reflections are independent of the applied H<sub>2</sub> pressure, which suggests hydrogen does not prompt major changes in particle size or shape for this work (the following observation can also be applied to the amorphous silica material). This is expected when bearing in mind that our 2 wt. % catalysts contain dramatically larger particles of approximately 15 nm (versus 1 nm for Pt/  $\gamma$ -Al<sub>2</sub>O<sub>3</sub>), which thermodynamics calculations advocate the existence of Pt nanoparticles in a stable decahedra configuration.<sup>57, 58</sup> Separate studies by Isobe *et al*<sup>59</sup> and Hakamada *et al*<sup>60</sup> show an observable Pt lattice expansion of 2-4% from combinatorial experimental and first principles calculations, due to the formation and adsorption of surface hydride species. A similar level of expansion is observed during the selective chemisorption of hydrogen over strained sub-5 nm Pt nanoparticles,<sup>61-63</sup> where hydrogen weakens metal-support interactions, thus relaxing Pt-Pt bond distances for smaller nanoparticles, tending towards bulk Pt values (2.7 nm).<sup>64</sup> As the magnitude of our reported lattice expansions are much diminished with regards to these studies, it can be stated that the observed selectivity enhancements observed at heightened hydrogen partial pressures is not due to hydrogen-induced Pt restructuring.

#### 4.2.5.2 Diffuse reflectance infrared fourier transform

There have been several studies postulating a support effect on CinnALD hydrogenation rate and CinnOH selectivity for Pt nanoparticles on carbon<sup>33, 65</sup> and oxide supports. High temperature annealing of carbon nanofibers was hypothesised to produce a non-polar carbon surface in which the direct adsorption of the CinnALD aromatic ring onto said support was favoured (**Scheme 2**). In this regime, hydrogenation arose due to spillover hydrogen from adjacent Pt nanoparticles; with a consequential 100-fold increase in activity. However, this exhibited promotion in activity follows significantly diminished CinnOH selectivity, when compared with the more polar, oxygen-rich and acidic analogues.



**Scheme 2** - CinnALD adsorption over carbon nanofiber-supported Pt nanoparticles – Elucidation of activity and selectivity effects over polar (*Left*) and non-polar surfaces (*Right*) – Modified from reference 33

In contrast, Ji et al studied the hydrogenation of CinnALD over Pt/graphene-based catalysts, which demonstrated higher selectivity towards CinnOH than traditional “Vulcan carbon” materials<sup>65</sup> (expressing increased surface polarity relative to graphene),<sup>66</sup> the author attributes this to a higher proportion of Pt<sup>(0)</sup> present on graphene surfaces. Studies on Lewis acidic K10 montmorillonite and Al-SBA-15/Al<sub>2</sub>O<sub>3</sub> supports, by Szöllösi<sup>67</sup> and Handjani<sup>47</sup> respectively, show an increased selectivity towards CinnOH; ascribed to increased support acidity. Preferential adsorption of the polar C=O function at acidic sites adjacent to Pt nanoparticles switches the preferred reaction pathway from C=C to C=O hydrogenation, favouring the unsaturated alcohol. **Figure 4.28** represents an attempt to elucidate an origin for the differing reactivity of Pt/aSiO<sub>2</sub> and hierarchical silica catalysts, shown in **Figures**

4.22-4.24, through direct probing of support surface polarity. DRIFT spectra of parent support and approx. 2 wt. % Pt catalysts were compared.

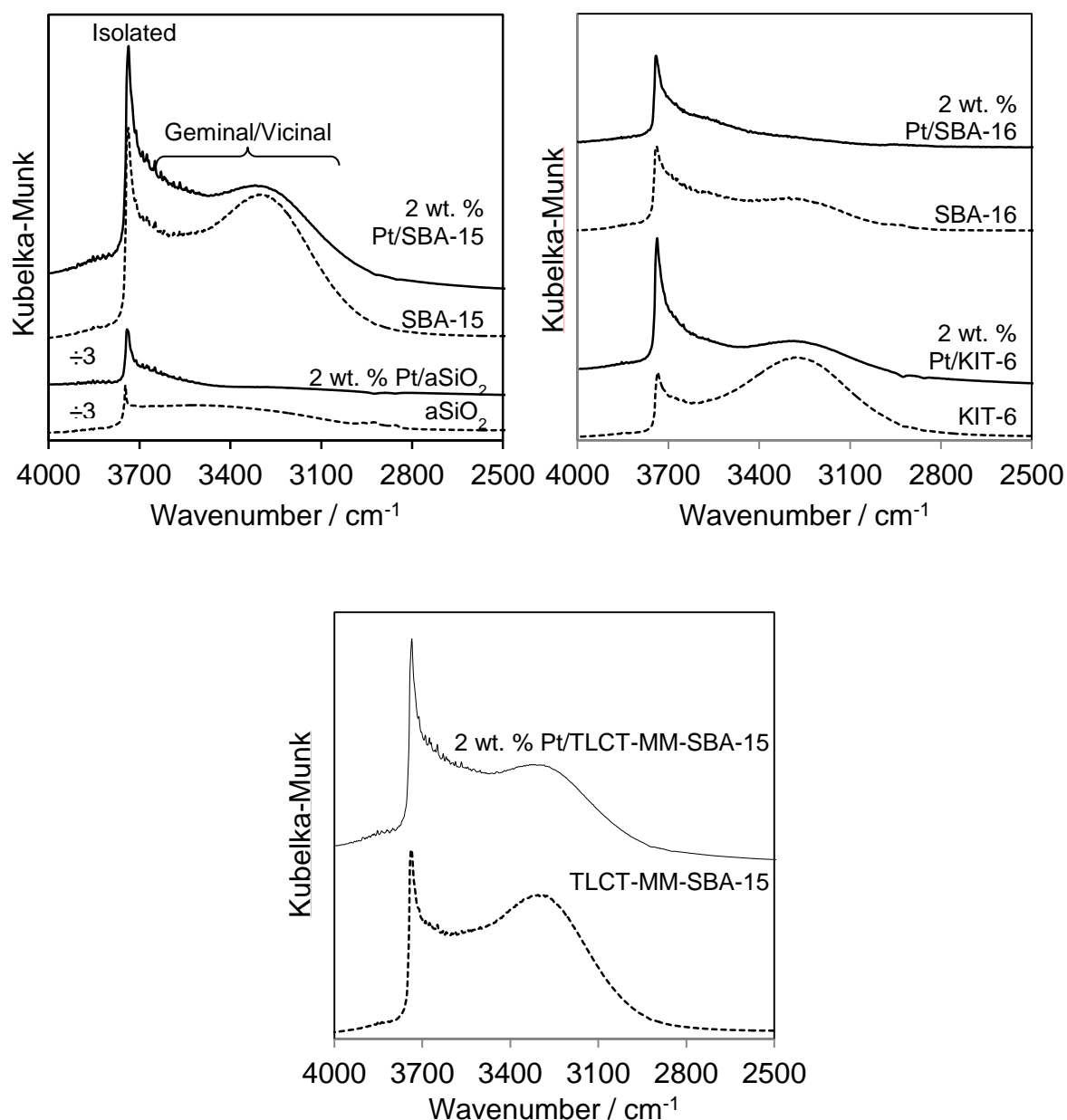
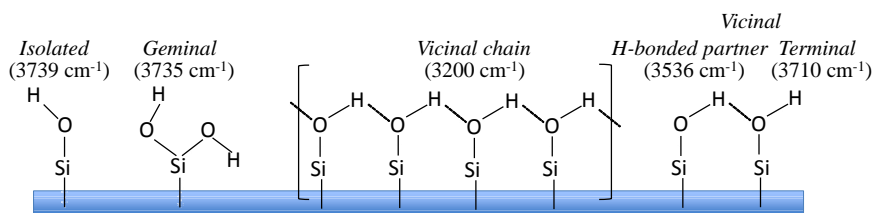


**Figure 4.28 – In vacuo DRIFT spectra of 2 wt. % silica-supported platinum catalysts**

**Scheme 3** shows a pictorial representation of the three major silanol groups present on our silica supports (isolated, geminal and vicinal). Support hydrophilicity is imparted predominantly by regions of vicinal silanol groups hydrogen-bonded into an extended chain<sup>68</sup> (three stretching frequencies for such groups are observed at 3200 cm<sup>-1</sup> (chain), 3536 cm<sup>-1</sup> (hydrogen-bonding between two Si-O centres) and 3710 cm<sup>-1</sup> (chain-terminus silanol group)). Differentiation between vicinal, geminal and isolated silanol groups through DRIFT analysis

is a facile process, due to distinguishable fingerprint stretching frequencies for each group (reported in **Scheme 3**).



**Scheme 3** – Schematic representation of silanol functionalities with associated stretching frequencies. Modified from reference 77

On close observation of **Figure 4.28**, the hierarchical silica supports show a more substantial enhancement in surface silanol density and coordination mode than values expressed for amorphous  $\text{SiO}_2$  (3.0 vs. 1.6  $\text{mmol.g}^{-1}$  for SBA-15 and a $\text{SiO}_2$  respectively). This promotion seems to arise due to a substantial increase in geminal/vicinal silanol group population for mesoporous systems, whereas amorphous silica displays isolated silanols exclusively. Surface silanol density exhibits the following trend:



Increasing silanol density affords increased support surface polarity. Previous physicochemical analyses of Pt supported nanoparticles on silica, show negligible differences in the established trends for surface oxidation (XPS), crystallite phase (XRD) and size/dispersion (TEM/CO chemisorption) parameters. Knowing this, it can be suggested that the observed promotion in CinnOH selectivity at 1-10 bar CinnALD hydrogenation is intimately linked with support polarity. It is interesting to note that the above trend in surface silanol density can be directly applied, in the same order, to the enhancement in CinnOH production. Amorphous silica, whose hydrophobicity is imparted purely by the presence of isolated surface silanols,<sup>69</sup> reports the lowest yield in CinnOH. The molecular orientation of CinnALD and/or reactively formed hydrogenation products is predicted to favour CinnOH and CinnALD molecular adsorption modes which require the close approach of the aromatic phenyl ring to the support surface for hydrophobic materials. Such adsorption modes position the C=C functionality within close proximity to the Pt-support perimeter, thus favouring C=C hydrogenation. Conversely, the enhanced hydrophilicity of the hierarchical supports promotes a molecular re-orientation of CinnALD and associated hydrogenation products, in which the apolar phenyl ring is repelled from the support surface. This favours adsorption

configurations where the C=O functionality is immediate to the support with the molecular plane orientated away from the surface (**Figure 4.29 (Right)**), thus favouring C=O to C-OH transformation.

In order to fully verify the above findings, an *in-situ* ATR study for the adsorption of our reactant molecule, cinnamaldehyde, from an 0.84 M anisole solution was conducted over catalyst films of approx. 2 wt. % Pt/aSiO<sub>2</sub> and Pt/SBA-15 at 90 °C. This allows for a close measure of CinnALD adsorption modes under the actual reaction conditions used for our catalytic studies (discussed previously). Hydrogen was not added to the substrate-catalyst film mixture to minimise complications/additional IR signatures arising from reactively formed hydrogenation products. Additional studies were also conducted at room temperature, in which it was discovered that vibrational spectra over both catalyst films were temperature independent between room temperature (approx. 25 °C at time of measurement) and 90 °C (**Figure 4.29**).

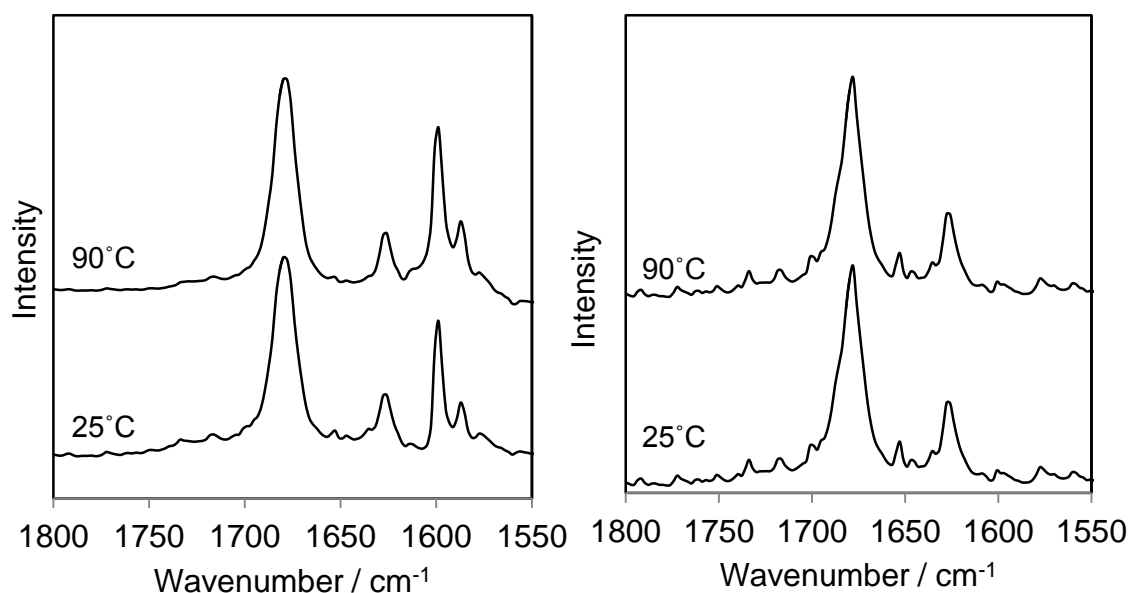


**Figure 4.29 – *In-situ* ATR-IR spectra confirming the temperature independence of approx. 2 wt. % Pt/aSiO<sub>2</sub> (Left) and 2 wt. % Pt/SBA-15 (Right) catalyst films under flowing cinnamaldehyde/anisole solution at 25 °C and 90 °C**

**Figure 4.30** displays the attained vibrational spectra for the approx. 2 wt. % Pt/aSiO<sub>2</sub> and Pt/SBA-15 films and a direct comparison with the calculated vibrational spectra of the “free” CinnALD substrate molecule (annotations for the most important vibrational modes have been included for greater clarity).

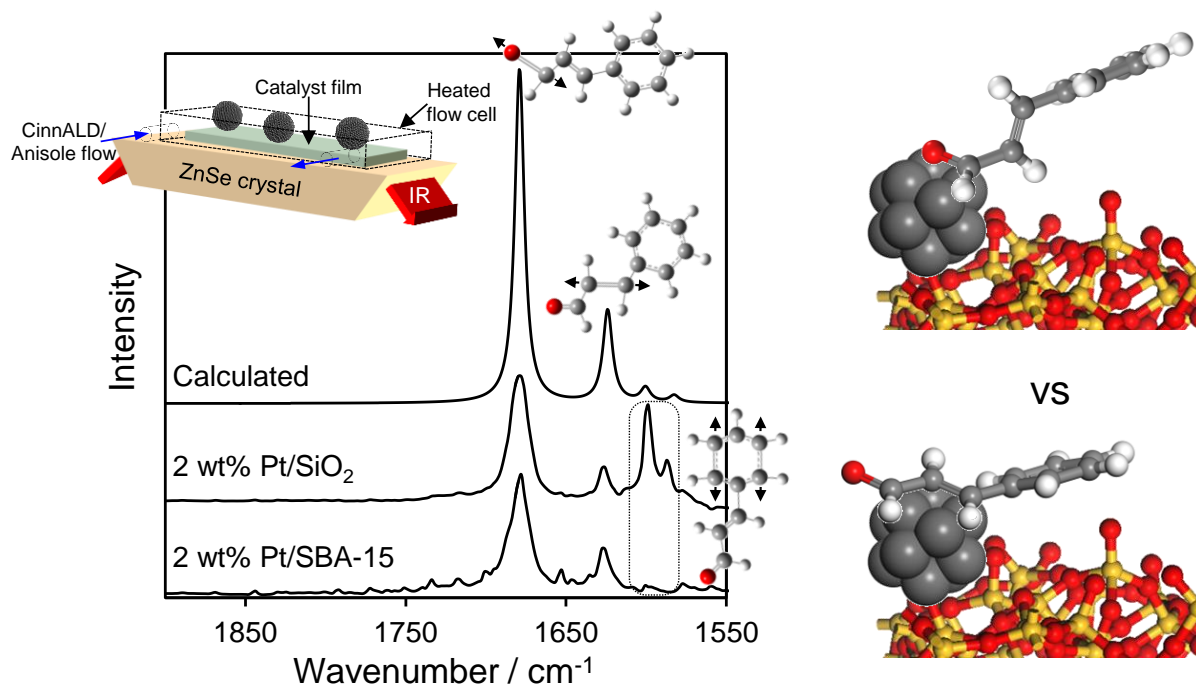


**Figure 4.30 – *In-situ* ATR-IR spectra of approx. 2 wt. % Pt impregnated silica catalyst films under flowing cinnamaldehyde/anisole solution at 90 °C (Left) and an illustration of unfavorable aromatic-surface interaction arising from adoption of di- $\sigma_{C=C}$  versus di- $\sigma_{C=O}$  CinnALD adsorption on Pt nanoparticles over a polar SBA-15 surface (Right)**

Both catalyst films yielded the characteristic  $\nu_{C=O}$  and symmetric  $\nu_{C=C}$  bands, inherent to the parent CinnALD, at  $1678\text{ cm}^{-1}$  and  $1624\text{ cm}^{-1}$  respectively. A key difference is demonstrated in the aromatic C=C stretching regime, where bands at  $1600\text{ cm}^{-1}$  and  $1594\text{ cm}^{-1}$ , present in the parent spectra and Pt/aSiO<sub>2</sub>, are absent from Pt nanoparticles dispersed over the more polar SBA-15 support. As a consequence of **Figure 4.27** and now with further compelling evidence from these *in-situ* studies, the omission of the two aromatic C=C stretches validates the proposed molecular re-orientation of the CinnALD aromatic functionality away from the support as surface polarity increases – thus providing an explanation for decreased C=C hydrogenation over SBA-15 support equivalents.



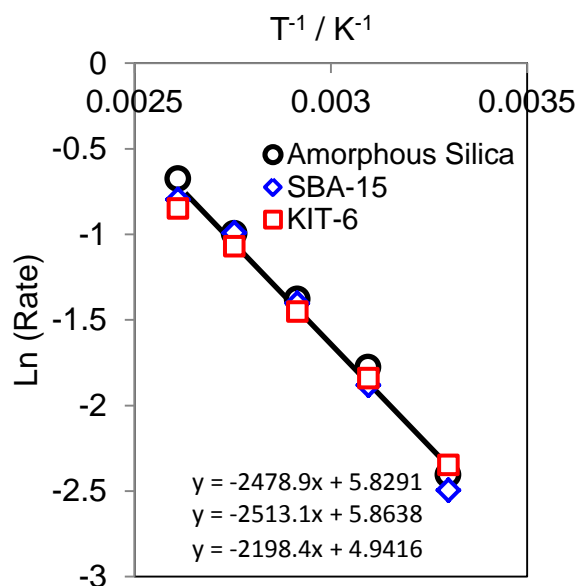


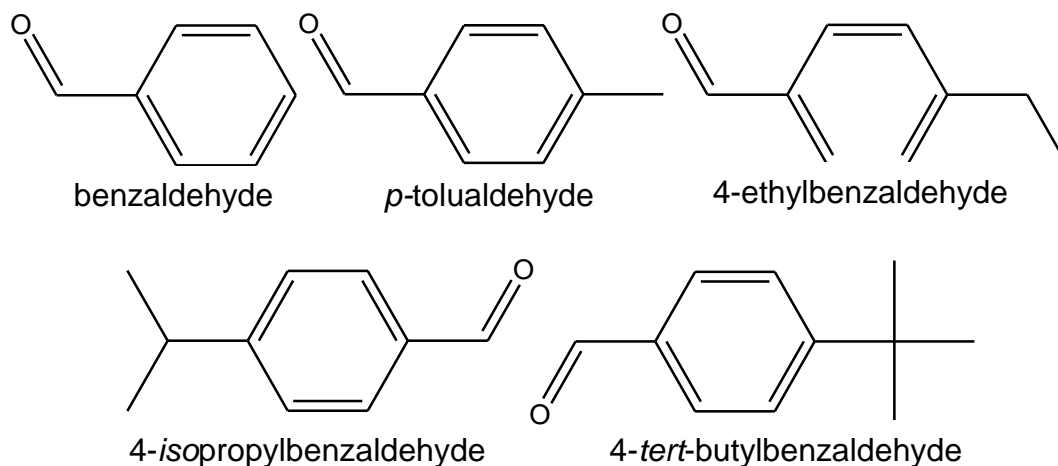
**Figure 4.31 – Arrhenius plots for CinnALD hydrogenation over approx. 2 wt. % Pt impregnated on amorphous, SBA-15 and KIT-6 silica's at 1 bar  $H_2$**

The activation energy for CinnALD hydrogenation was probed for approx. 2 wt. % Pt-impregnated SBA-15, KIT-6 and amorphous silicas (**Figure 4.31**). A common activation energy of  $20 \pm 0.6 \text{ kJ.mol}^{-1}$  was reported over the three materials, thus reinforcing previous aforementioned studies suggesting differing catalytic selectivity through modified CinnALD adsorption over each support, rather than the presence of different hydrogenation active sites and altered internal support structure (*i.e.* 2D SBA-15 versus 3D KIT-6).

In conclusion, increasing  $p_{H_2}$  leads to a radical shift in CinnALD hydrogenation pathways from C=C and hydrogenolysis regimes to the more desirable C=O transformation. A combination of *in-situ* XRD and DRIFT studies examines and proves that the enhancement in CinnOH selectivity shown over more polar Pt/SBA-15 materials is a function of the molecular reorientation of the phenyl functionality away the support surface, due to repulsion of this group by surface germinal and extended vicinal silanol chains – promoting di- $\sigma_{C=O}$  adsorption and subsequent C=O hydrogenation. This finding holds true for the silica materials screened in this line of work, but it was noted that in the case of graphene-supported Pt nanoparticles,  $\pi$ - $\pi$  interactions between CinnALD and the support yielded higher selectivity towards the C=O pathway.<sup>65</sup> This seems to be in direct contradiction with this work but may suggest different adsorption geometries could be present for Pt nanoparticles supported on carbon versus the oxide surfaces examined here.

## 4.2.6 Alternate Substrates

### 4.2.6.1 Substituted benzaldehydes



**Scheme 4** – Chemical structure of screened benzylic aldehydes

Using identical 2 wt. % Pt-impregnated amorphous silica and SBA-15 catalysts, the favourability of support polarity on selective C=O hydrogenation of aromatic aldehydes was tested further through the hydrogenation of increasingly complex benzylic aldehydes at 1 bar H<sub>2</sub> and 90 °C. The structures of the screened substrates are given in **Scheme 4**. **Figure 4.32** reviews the catalytic performance (conversion and alcohol selectivity) for both catalyst families after 7 hour reaction under standard conditions. As demonstrated for the CinnALD substrate, Pt/SBA-15 clearly outperforms Pt/aSiO<sub>2</sub> with respect to C=O versus C=C hydrogenation and hydrogenolysis pathways for all benzaldehyde-based substrates. The literature speculates the stabilisation of adsorbed  $\pi$ -complexed aromatic systems through electron-donation by alkyl substituents, thus inferring high barriers to ring (C=C) hydrogenation.<sup>70, 71</sup> Using this argument, we can rationalise the superior selectivity observed towards alkyl-substituted benzylic alcohols, *with increased substitution*, compared to benzyl alcohol.

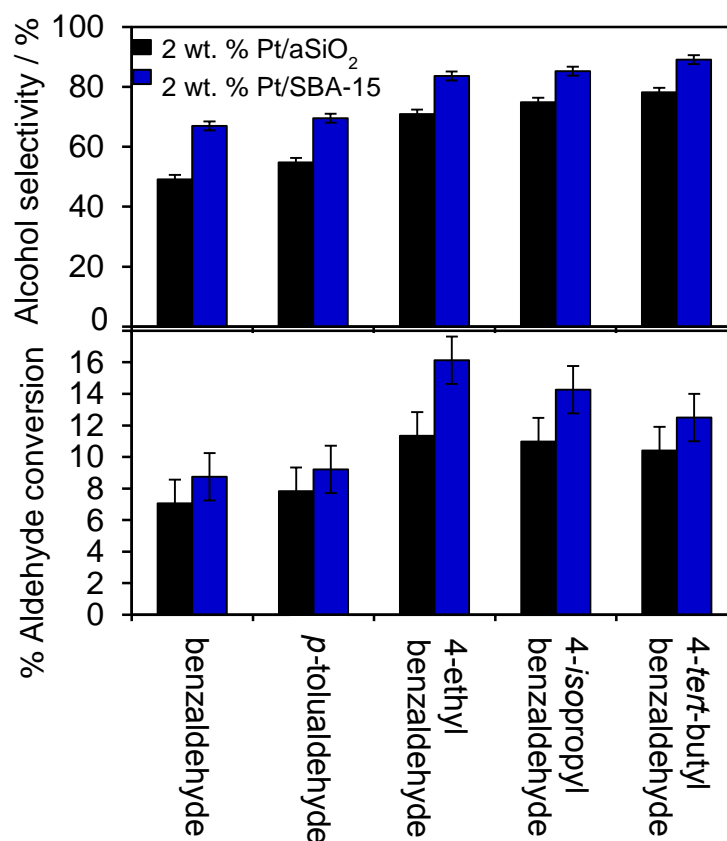
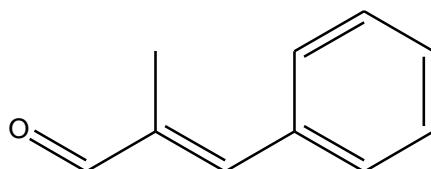


**Figure 4.32 – Performance of approx. 2 wt. % Pt/SBA-15 and 2 wt. % Pt/aSiO<sub>2</sub> catalysts for the hydrogenation of substituted benzaldehydes**

In contrast to previous cinnamaldehyde hydrogenations, Pt/SBA-15 expressed greater activity towards all screened benzylic aldehydes than Pt/aSiO<sub>2</sub>. We can attribute this to a secondary effect of the more polar SBA-15 surface, in which less polar aromatic-based products are subject to faster desorption kinetics over SBA-15 (due to increased aromatic-silanol group repulsion) and thus are removed from the support surface with greater efficacy. **Figure 4.32** illustrates the importance of electron-donating alkyl substituents on the hydrogenation of benzaldehyde derivatives. An observed acceleration of benzaldehyde hydrogenation is witnessed over both silica supports as the electron-donating ability of its substituents increases. This work is complimentary with findings by Li and co-workers for the hydrogenation of *para*-substituted benzaldehydes via mesopolymer-entrapped Pt nanoparticles, in which a similar effect is discussed.<sup>72</sup> Previous work by Han and co-workers showed the hydrogenation of benzaldehyde to be hampered by the electron-donating effect of O and N-based substituents for Pt supported on MgAl<sub>2</sub>O<sub>4</sub> basic supports.<sup>73</sup> The radically different nature of these basic materials could introduce an entirely new substrate adsorption mode or active site, thus altering the reaction kinetics for this reaction versus our reported

Pt/silica materials. Additionally, gas phase hydrogenation of o-tolualdehyde over Ni/SiO<sub>2</sub> also proved to be slower than benzaldehyde.<sup>70</sup> The higher activity observed for our materials suggests increasing carbonyl activation, tracking with electron donation enhancements from alkyl substituents, is beneficial for the hydrogenation of benzylic aldehydes.

#### 4.2.6.2 $\alpha$ -methyl-trans-cinnamaldehyde hydrogenation



**Scheme 5** – Chemical structure of  $\alpha$ -methyl-trans-cinnamaldehyde

The above investigations have provided concrete evidence that destabilisation of the C=C adsorption mode of CinnALD relative to C=O; and the electronic activation of the C=O functionality (through alkyl group to aromatic electron donation), can lead to a favourable increase in desired alcohol product selectivity (CinnOH and benzylic alcohols respectively), in Pt/silica catalysed hydrogenation processes. We propose that artificially increasing the steric hindrance around the CinnALD alkene functionality for a fixed particle size and support polarity, should enhance the formation of the desired unsaturated alcohol – through destabilisation of the di- $\sigma_{CC}$  or  $\eta^4$  di- $\sigma_{CO} + \pi_{C=C}$  adsorption modes.<sup>46</sup>  $\alpha$ -methyl-*trans*-cinnamaldehyde (2-methyl-3-phenylpropenal) hydrogenation was examined over high and low-loading Pt nanoparticles supported on amorphous silica and the more polar SBA-15. The resulting selectivity to  $\alpha$ -methyl-*trans*-cinnamyl alcohol versus 2-methyl-3-phenylpropanol/2-methyl-3-phenylpropionaldehyde was compared to values recorded for CinnALD hydrogenation to CinnOH versus 3-phenylpropan-1-ol/3-phenylpropionaldehyde – **Figure 4.33** highlights any expressed change in selectivity for C=O versus C=C hydrogenation upon steric encumbrance of the C=C centre.

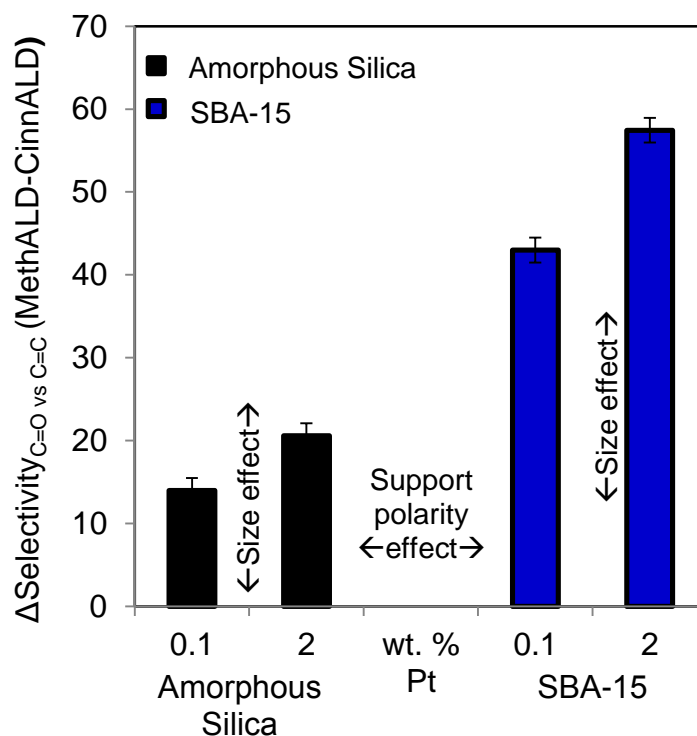


**Figure 4.33 - Influence of methyl substitution alpha to the carbonyl in CinnALD for the rates of C=C versus C=O hydrogenation over large and small Pt nanoparticles supported on silica analogues**

**Figure 4.33** clearly shows methyl substitution to significantly enhance C=O hydrogenation to the desired unsaturated alcohol product. A decrease of 15-55 % in saturated aldehyde/alcohol product generation, and hence the C=C hydrogenation pathway, was observed over all screened catalysts. C=O hydrogenation enhancement was shown to be approx. 10 % greater for larger nanoparticles, consistent with the added steric hindrance around the C=C centre, thus impeding a close approach of the alkene functionality to larger, extended platinum surfaces. The impact of silica hydrophilicity seems to be far more significant, with selectivity to  $\alpha$ -methyl-trans-cinnamyl alcohol improved by ~30 % over the polar SBA-15 relative to amorphous silica.

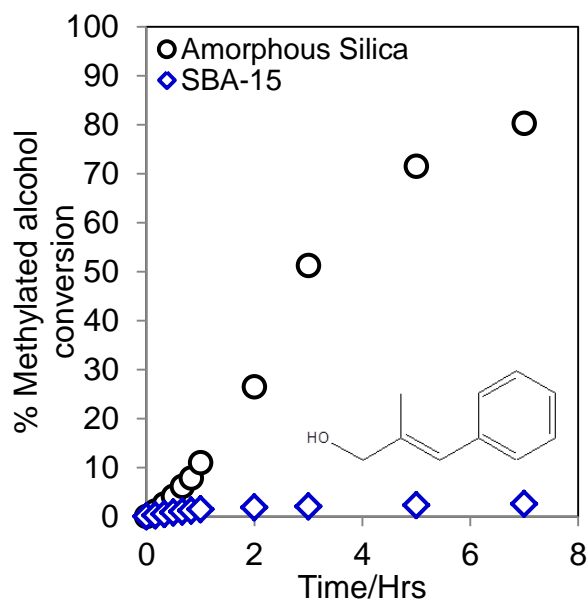
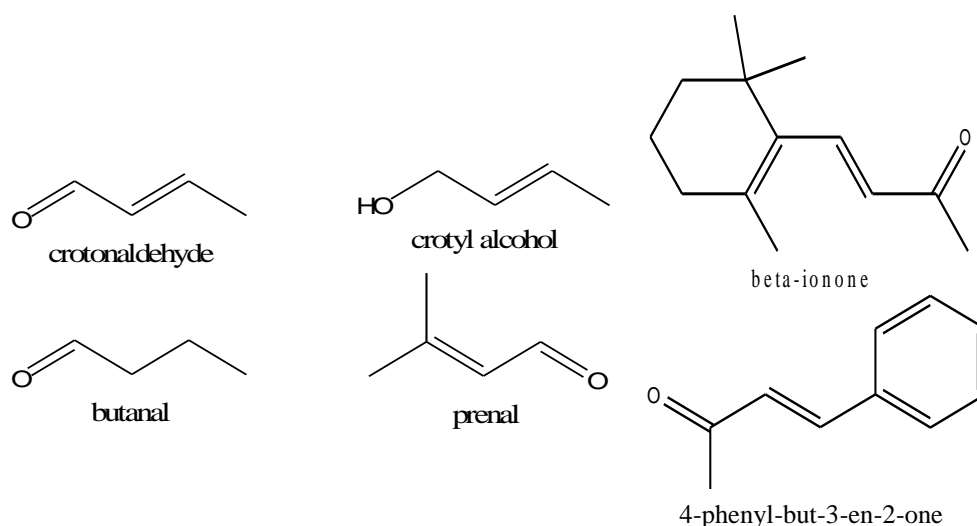


**Figure 4.34 –  $\alpha$ -methyl-*trans*-cinnamyl alcohol hydrogenation over approx. 2 wt. % silica supported platinum catalysts at 1 bar H<sub>2</sub>**

The hydrogenation of  $\alpha$ -methyl-*trans*-cinnamyl alcohol, shown by **Figure 4.34**, reflects a very similar trend to an analogous study using CinnOH as the starting reagent (**Figure 4.20**). Substrate conversion levels for amorphous silica and SBA-15 dispersed 2 wt. % Pt nanoparticles are proportionally 10% diminished to that study, consistent with steric hindrance preventing ease of access to Pt facets. Most importantly, the relative inability of SBA-15-supported Pt to hydrogenate the C=C functionality to the same degree as Pt/aSiO<sub>2</sub>, highlights the combined importance of steric hindrance around the alkene group and beneficial phenyl ring repulsion by surface silanols on C=O activation and unsaturated alcohol selectivity in the original CinnALD study.

#### **4.2.6.3 Preliminary studies into ketone and derivative aliphatic aldehyde hydrogenation**

In a preliminary study, crotonaldehyde (CrotALD) and several of its key reaction intermediates were screened; in tandem with a commercially applied ketone ( $\beta$ -ionone) and the ketone alternative of our original substrate (CinnALD); to test the versatility and general applicability of the hydrogenation effects uncovered in this chapter. **Scheme 6** gives the chemical structure of these substrates for ease of comprehension.



**Scheme 6** – Chemical structure of screened CroTALD derivatives (*Left*) and ketones (*Right*)

**Table 4.5** summarizes conversion and selectivity values (C=O versus C=C hydrogenation) for all **Scheme 6** substrates - screened using approx. 2 wt. % Pt impregnated on amorphous and SBA-15 silicas respectively.

**Table 4.5** – Catalytic performance of allylic substrates and aromatic ketones under ambient conditions

Substrate	% Product selectivity				Conversion	
	2 wt. % Pt/aSiO <sub>2</sub>		2 wt. % Pt/SBA-15		2 wt. % Pt/aSiO <sub>2</sub>	2 wt. % Pt/SBA-15
	Alcohol	C=C	Alcohol	C=C		
<b>Allylic derivatives</b>						
<b>Crotonaldehyde</b>	2.2	97.8	7.6	92.4	33.4	24.2
<b>Crotyl alcohol</b>	n/a	100	n/a	100	93.2	68.4
<b>Butanal</b>	100	n/a	100	n/a	6.8	0.5
<b>Prenal</b>	3.7	96.3	12.4	87.6	20.3	11.4
<b>Aromatic ketones</b>						
<b><i>β</i>-ionone</b>	0.7	91.2	15.9	79.2	33.7	51.7
<b>4-phenyl-but-3-en-2-one</b>	0.0	92.6	2.3	90.9	6.4	1.6

**Note** – Selectivity and conversion values quoted after 7hrs reaction time

Under our mild conditions, both ketone substrates show a remarkable resistance to C=O hydrogenation, favoring C=C pathways. Stability to heterogeneously catalyzed C=O hydrogenation is not uncommon or unexpected; as Noyori reports the absence of heteroatoms adjacent to the C=O functionality, in tandem with geometric constraints prevents labile conversion of this group.<sup>74</sup> It must be noted that Noyori *et al* study the effect of Ru-based

homogeneous catalysts, in which catalysis revolves around a single active site – It is expected that the effect of steric constraints around the carbonyl centre would be drastically decreased for heterogeneous-based, larger metal nanoparticle catalysts. There is one example of Pt-catalysed enantioselective hydrogenation of various ketones by Exner et al,<sup>75</sup> who use chiral modifiers to dictate final product selectivity through substrate binding mode control. In this study, it is clearly shown that selective C=O ketone hydrogenation is possible through strict adsorption mode control, however more rigorous hydrogen pressures are employed than for our study (50 bar H<sub>2</sub>) and substrate conversion levels are not stated, so a true comparison with our materials is not possible. Due to stability inferred by extended conjugation and steric effects around the ketone group, 4-phenyl-but-3-en-2-one exhibits low conversion levels over both silica catalysts. A loss of ring aromaticity in  $\beta$ -ionone (in comparison with the studied cinnamaldehyde derivatives) lowers the total stability of the ketone centre, causing an escalation in substrate conversion levels (approx. 5 and 32-fold increase of Pt/aSiO<sub>2</sub> and Pt/SBA-15 respectively). The aforementioned support polarity effect on C=O selectivity for benzylic aldehyde and cinnamaldehyde derivatives seems to apply here, with Pt/SBA-15 posting higher desired C=O selectivity values for both ketone substrates. Ring methylation in  $\beta$ -ionone is an excellent example of electronic C=O activation and substrate adsorption mode modification over polar surfaces, where we ascribe the promotion in alcohol selectivity to be imparted by a partial deactivation of C=C centric binding modes.

Removal of the aromatic functionality from cinnamaldehyde yields crotonaldehyde. The decreased steric bulk of this substrate yields a positive promotion in substrate conversion levels over both catalysts. However, due to the decreased hydrophobicity and geometric complexity of this allylic system, the alkene functionality is permitted greater exposure to Pt active sites, thus accounting for decreased unsaturated alcohol selectivity (when compared with cinnamaldehyde values).<sup>46, 76</sup> The observed favorability of C=O hydrogenation over Pt/SBA-15 is still maintained, showing that a partial repulsion of hydrophobic alkene functionalities still exists, even if it is severely diminished. Prenal represents methylation of the C=C group and gives positive evidence to the previous observation. Increased steric bulk leads to an apparent drop in conversion over both Pt/silica catalysts, however this follows a 1.6 x factor increase in C=O selectivity – consistent with a change in substrate binding mode and/or aldehyde group electronic activation through –CH<sub>3</sub> electron donation. In **Figure 4.20**, we identified a stark difference in cinnamyl alcohol hydrogenation over Pt-impregnated aSiO<sub>2</sub> and SBA-15 catalysts; evidencing SBA-15 catalysts to be less active towards cinnamyl



alcohol conversion. Screening of crotyl alcohol expresses a similar effect. The removal of the phenyl ring in this study, permits increased conversion of the unsaturated allylic alcohol, with butanal produced as the exclusive product. The relative inability of both Pt catalysts to hydrogenate butanal highlights the critical importance of the C=C functionality in substrate binding. Comparing cinnamaldehyde and crotonaldehyde systems, it is clear that the presence of aromaticity has a strong effect on the adopted binding mode, with support characteristics dictating substrate reaction pathway activation. For both substrates, polar Pt/SBA-15 has a negative influence on binding modes that require flat adsorption over Pt facets.<sup>46</sup> This in turn favors C=O hydrogenation, whilst enhancing the rate of unsaturated alcohol product removal – preserving the desired product.

We can tentatively state that the effects of support polarity and size-controlled selectivity on preferential C=O hydrogenation can be applied to other unsaturated carbonyl substrates. A full study should be conducted on allylic and ketone derivatives before it can be said with total certainty, but these preliminary studies do show great promise.

### 4.3 Conclusion

In this chapter we demonstrate the successful generation of SBA-16 and TLCT-MM-SBA-15. Strong evidence shows that the liquid phase, selective hydrogenation of CinnALD to CinnOH using silica supported Pt nanoparticles has strong catalyst physicochemical and applied reaction parameter dependence. CinnALD activity is structure-insensitive with respect to metallic platinum, yielding a constant TOF of  $\sim 350 \text{ h}^{-1}$ , but structure sensitive to CinnOH selectivity – high CinnOH product generation requires large metal terraces which favour C=O versus C=C hydrogenation. Support polarity plays a major role in product determination. A clear trend is observed, in which increasing surface polarity, enhances C=O hydrogenation to the desired unsaturated alcohol whilst inhibiting subsequent hydrogenation to 3-phenylpropan-1-ol. This effect is most pronounced when comparing highly polar SBA-15, with extended vicinal/geminal silanol groups, versus the weakly hydroxylated amorphous, low area silica. *In-situ* ATR-IR spectroscopy associates a change in CinnALD orientation over higher polarity supports as the origin to increased unsaturated alcohol selectivity. The efficient removal of reactively formed cinnamyl alcohol by a hydrophilic SBA-15 surface prevents subsequent secondary reaction of the C=C functionality. The versatility of this reaction model was further tested through the first systematic study of alkyl-

substituted benzylic aldehydes, reporting a similar selective carbonyl promotion over SBA-15 versus more hydrophobic amorphous silica.

As expected, increasing hydrogen pressure from 1-10 bar permitted an enhancement in CinnALD hydrogenation over all silica supports. However perhaps unexpectedly, high  $p_{H_2}$  pressures also induced a significant switch in adopted CinnALD reaction pathway from dominant C=C hydrogenation (1 bar) to C=O hydrogenation (10 bar) over all supports and Pt loadings. This effect is the most dramatic for Pt/SBA-15, reporting a >90 % preference to the C=O hydrogenation pathway. As there is no solid evidence for any apparent change in Pt morphology or oxidation state, this promotion likely arises due to the effects of surface crowding upon CinnALD adsorption - less sterically-demanding  $\eta_2$  di- $\sigma_{CO}$  binding is favoured over di- $\sigma_{CC}$  and  $\eta_4$  di- $\sigma_{CO} + \pi_{C=C}$  modes. Methylation of the CinnALD alkene functionality supports this hypothesis, with increased C=O versus C=C bond hydrogenation with respect to CinnALD as steric hindrance around the C=C bond is artificially increased. This is particularly evident over the polar SBA-15 support, where it has been previously established that close approach of the aromatic and methylated alkene functions is clearly disfavoured.

To put succinctly, the platinum-catalysed chemoselective hydrogenation of unsaturated aldehydes requires optimisation of metal particle size versus support dispersion enhancements *and* support surface polarity, in tandem with high hydrogen pressures in order to achieve best selectivity to the desired unsaturated alcohols.

## 4.4 References

1. L. Durdell, C. M. Parlett, N. S. Hondow, K. Wilson and A. F. Lee, *Nanoscale*, 2013.
2. T.-W. Kim, R. Ryoo, M. Kruk, K. P. Gierszal, M. Jaroniec, S. Kamiya and O. Terasaki, *The Journal of Physical Chemistry B*, 2004, 108, 11480-11489.
3. J. Dhainaut, J.-P. Dacquin, A. F. Lee and K. Wilson, *Green Chemistry*, 2010, 12, 296-303.
4. S. Vaudreuil, M. Bousmina, S. Kaliaguine and L. Bonneviot, *Advanced Materials*, 2001, 13, 1310-1312.
5. D. Zhao, Q. Huo, J. Feng, B. F. Chmelka and G. D. Stucky, *Journal of the American Chemical Society*, 1998, 120, 6024-6036.
6. C. M. Parlett, P. Keshwala, S. G. Wainwright, D. W. Bruce, N. S. Hondow, K. Wilson and A. F. Lee, *ACS Catalysis*, 2013, 3, 2122-2129.
7. P. Van Der Voort, M. Benjelloun and E. F. Vansant, *The Journal of Physical Chemistry B*, 2002, 106, 9027-9032.
8. C. M. A. Parlett, P. Keshwala, S. G. Wainwright, D. W. Bruce, N. S. Hondow, K. Wilson and A. F. Lee, *ACS Catalysis*, 2013, 3, 2122-2129.
9. P. I. Ravikovitch and A. V. Neimark, *Langmuir*, 2002, 18, 9830-9837.
10. P. A. Webb, C. Orr and M. I. Corporation, *Analytical methods in fine particle technology*, Micromeritics Instrument Corporation, 1997.
11. S. G. Wainwright, C. Parlett, R. A. Blackley, W. Zhou, A. F. Lee, K. Wilson and D. W. Bruce, *Microporous and Mesoporous Materials*, 2013, 172, 112-117.
12. J. Y. Ying, C. P. Mehnert and M. S. Wong, *Angewandte Chemie International Edition*, 1999, 38, 56-77.
13. D. Li, X. Guan, J. Song, Y. Di, D. Zhang, X. Ge, L. Zhao and F.-S. Xiao, *Colloids and Surfaces A: Physicochemical and Engineering Aspects*, 2006, 272, 194-202.
14. A. Galarneau, H. Cambon, F. Di Renzo, R. Ryoo, M. Choi and F. Fajula, *New journal of Chemistry*, 2003, 27, 73-79.
15. A. Galarneau, H. Cambon, F. Di Renzo and F. Fajula, *Langmuir*, 2001, 17, 8328-8335.
16. C.-M. Yang, B. Zibrowius, W. Schmidt and F. Schüth, *Chemistry of materials*, 2003, 15, 3739-3741.
17. C.-M. Yang, H.-A. Lin, B. Zibrowius, B. Spliethoff, F. Schüth, S.-C. Liou, M.-W. Chu and C.-H. Chen, *Chemistry of materials*, 2007, 19, 3205-3211.
18. C. G. Göltner, B. Smarsly, B. Berton and M. Antonietti, *Chemistry of Materials*, 2001, 13, 1617-1624.
19. A. Silvestre-Albero, E. Jardim, E. Bruijn, V. Meynen, P. Cool, A. Sepulveda-Escribano, J. Silvestre-Albero and F. Rodriguez-Reinoso, *Langmuir*, 2008, 25, 939-943.
20. M. Choi, F. Kleitz, D. Liu, H. Y. Lee, W.-S. Ahn and R. Ryoo, *Journal of the American Chemical Society*, 2005, 127, 1924-1932.
21. Y. Sakamoto, M. Kaneda, O. Terasaki, D. Y. Zhao, J. M. Kim, G. Stucky, H. J. Shin and R. Ryoo, *Nature*, 2000, 408, 449-453.
22. J. S. Yun, M.-Y. Seong and S.-K. Ihm, *Journal of Physics and Chemistry of Solids*, 2008, 69, 1129-1132.
23. N. D. Petkovich and A. Stein, *Hierarchically Structured Porous Materials: From Nanoscience to Catalysis, Separation, Optics, Energy, and Life Science*, 2011, 55-129.
24. J. T. Miller, M. Schreier, A. J. Kropf and J. R. Regalbuto, *Journal of Catalysis*, 2004, 225, 203-212.
25. B. Bachiller-Baeza, A. Guerrero-Ruiz and I. Rodriguez-Ramos, *Applied Catalysis A: General*, 2000, 192, 289-297.
26. Z. C. Zhang and B. C. Beard, *Applied Catalysis A: General*, 1999, 188, 229-240.
27. K. Bratlie, H. Lee, P. Yang and G. A. Somorjai, *Nano Letters*, 2007, 7.
28. P. Yang, C.-K. Tsung, J. Kuhn and G. A. Somorjai, *J Am Chem Soc*, 2009, 131.

29. H. Lee, S. E. Habas, S. Kweskin, D. Butcher, G. A. Somorjai and P. Yang, *Angewandte Chemie*, 2006, 118, 7988-7992.
30. I. J. Jang, H. S. Shin, N. R. Shin, S. H. Kim, S. K. Kim, M. J. Yu and S. J. Cho, *Catalysis Today*, 2012, 185, 198-204.
31. E. Wilhelm, R. Battino and R. J. Wilcock, *Chemical reviews*, 1977, 77, 219-262.
32. E. Brunner, *Journal of Chemical & Engineering Data*, 1985, 30, 269-273.
33. M. L. Toebes, T. Alexander Nijhuis, J. Hájek, J. H. Bitter, A. Jos van Dillen, D. Y. Murzin and K. P. de Jong, *Chemical engineering science*, 2005, 60, 5682-5695.
34. Y. Zhu and F. Zaera, *Catalysis Science & Technology*, 2014, DOI: 10.1039/C3CY01051A.
35. S. Galvagno, G. Capannelli, G. Neri, A. Donato and R. Pietropaolo, *Journal of molecular catalysis*, 1991, 64, 237-246.
36. L. Mercadante, G. Neri, C. Milone, A. Donato and S. Galvagno, *Journal of Molecular Catalysis A: Chemical*, 1996, 105, 93-101.
37. B. Coq, P. Kumbhar, C. Moreau, P. Moreau and M. Warawdekar, *Journal of molecular catalysis*, 1993, 85, 215-228.
38. Y. Nitta, K. Ueno and T. Imanaka, *Applied catalysis*, 1989, 56, 9-22.
39. W. O. Oduro, N. Cailuo, K. M. Yu, H. Yang and S. C. Tsang, *Phys Chem Chem Phys*, 2011, 13, 2590-2602.
40. A. J. Plomp, H. Vuori, A. O. I. Krause, K. P. de Jong and J. H. Bitter, *Applied Catalysis A: General*, 2008, 351, 9-15.
41. A. K. Prashar, S. Mayadevi and R. Nandini Devi, *Catalysis Communications*, 2012, 28, 42-46.
42. S. C. Tsang, N. Cailuo, W. Oduro, A. T. S. Kong, L. Clifton, K. M. K. Yu, B. Thiebaut, J. Cookson and P. Bishop, *ACS Nano*, 2008, 2, 2547-2553.
43. P. Gallezot and D. Richard, *Catalysis Reviews*, 1998, 40, 81-126.
44. M. Englisch and J. Lercher, *Journal of Molecular Catalysis A: Chemical*, 1997, 121.
45. R. Zheng, M. D. Porosoff, J. L. Weiner, S. Lu, Y. Zhu and J. G. Chen, *Applied Catalysis A: General*, 2012, 419-420, 126-132.
46. P. Sautet and F. Delbecq, *Journal of Catalysis*, 1995, 152.
47. S. Handjani, E. Marceau, J. Blanchard, J.-M. Krafft, M. Che, P. Mäki-Arvela, N. Kumar, J. Wärnå and D. Y. Murzin, *Journal of Catalysis*, 2011, 282, 228-236.
48. J. Breen, *Applied Catalysis A: General*, 2004, 268, 267-274.
49. T. Vergunst and J. Moulijn, *Catalysis Today*, 2001, 66.
50. S. Laref, F. Delbecq and D. Loffreda, *Journal of Catalysis*, 2009, 265, 35-42.
51. U. K. Singh and M. A. Vannice, *Applied Catalysis A: General*, 2001, 213, 1-24.
52. M. Shirai, T. Tanaka and M. Arai, *Journal of Molecular Catalysis A: Chemical*, 2001, 168.
53. J. McCarty and H. Wise, *Journal of Catalysis*, 1979, 57, 406-416.
54. R. Rao, A. Dandekar, R. Baker and M. Vannice, *Journal of Catalysis*, 1997, 171, 406-419.
55. H. Mistry, F. Behafarid, S. R. Bare and B. Roldan Cuenya, *ChemCatChem*, 2014, 6, 348-352.
56. A. Barnard, *Computer Physics Communications*, 2011, 182, 11-13.
57. F. Baletto and R. Ferrando, *Reviews of modern physics*, 2005, 77, 371.
58. Y. Xia, Y. Xiong, B. Lim and S. E. Skrabalak, *Angewandte Chemie International Edition*, 2009, 48, 60-103.
59. Y. Isobe, M. Yamauchi, R. Ikeda and H. Kitagawa, *Synthetic Metals*, 2003, 135, 757-758.
60. M. Hakamada, T. Furukawa, T. Yamamoto, M. Takahashi and M. Mabuchi, *MATERIALS TRANSACTIONS*, 2011, 52, 806-809.
61. D. Ramaker, B. Mojet, M. G. Oostenbrink, J. Miller and D. Koningsberger, *Physical Chemistry Chemical Physics*, 1999, 1, 2293-2302.
62. A. Ankudinov, J. Rehr, J. Low and S. R. Bare, *Physical review letters*, 2001, 86, 1642.
63. Y. Lei, J. Jelic, L. C. Nitsche, R. Meyer and J. Miller, *Topics in Catalysis*, 2011, 54, 334-348.
64. J. M. Ramallo-López, G. F. Santori, L. Giovanetti, M. L. Casella, O. A. Ferretti and F. G. Requejo, *The Journal of Physical Chemistry B*, 2003, 107, 11441-11451.

65. X. Ji, X. Niu, B. Li, Q. Han, F. Yuan, F. Zaera, Y. Zhu and H. Fu, *ChemCatChem*, 2014, 6, 3246-3253.
66. S. Senthil Kumar, J. Soler Herrero, S. Irusta and K. Scott, *Journal of Electroanalytical Chemistry*, 2010, 647, 211-221.
67. G. Szollosi and M. Bartok, *Journal of Catalysis*, 1998, 179, 619-623.
68. A. A. Christy, *Vibrational Spectroscopy*, 2010, 54, 42-49.
69. O. Isaienko and E. Borguet, *Langmuir*, 2013, 29, 7885-7895.
70. M. A. Keane, *Journal of Molecular Catalysis A: Chemical*, 1997, 118, 261-269.
71. M. Vasiur Rahaman and M. Albert Vannice, *Journal of catalysis*, 1991, 127, 267-275.
72. S. Li, T. Boucheron, A. Tuel, D. Farrusseng and F. Meunier, *Chemical Communications*, 2014, 50, 1824-1826.
73. M. Han, H. Zhang, Y. Du, P. Yang and Z. Deng, *Reaction Kinetics, Mechanisms and Catalysis*, 2011, 102, 393-404.
74. R. Noyori and T. Ohkuma, *Angewandte Chemie International Edition*, 2001, 40, 40-73.
75. C. Exner, A. Pfaltz, M. Studer and H. U. Blaser, *Advanced Synthesis & Catalysis*, 2003, 345, 1253-1260.
76. M. Grass, R. Rioux and G. Somorjai, *Catal Lett*, 2009, 128, 1-8.
77. L. Durdell, C. M. Parlett, N. S. Hondow, M.A. Isaacs, K. Wilson and A. F. Lee, *Scientific Reports*, Pending.

## *Chapter 5*

### *Conclusions and Further work*

## 5.1 Conclusions

From the beginning, this project was split into two fields of study; (I) the selective oxidation of cinnamyl alcohol to cinnamaldehyde and (II) the selective hydrogenation of cinnamaldehyde to cinnamyl alcohol (the reverse pathway to (I)).  $\alpha$ ,  $\beta$ -unsaturated derivatives were chosen as the target substrates, due to their inherently complex structure and high industrial relevance.<sup>1, 2</sup> The proximity of aromatic ring and alkene functionalities adjacent to the target alcohol/aldehyde group in these substrates present complex thermodynamic and reactivity issues. Mesoporous silicas as catalyst support materials were deemed beneficial due to well-defined synthetic protocols present in the literature<sup>3-5</sup> and the “*weakly-interacting nature*” of the materials themselves.

### 5.1.1 Cinnamyl alcohol selective oxidation

The successful production of mesoporous silicas with two-dimensional non-interconnecting (SBA-15) and three-dimensional interpenetrating mesopore structure (KIT-6) allowed the role of support architecture and physical properties on Pt nanoparticle characteristics to be explored. The introduction of mesoporosity yielded a substantial increase in BET surface areas, over control amorphous, commercial silica. This permitted the formation of highly dispersed, catalytically active Pt nanoparticles. Recorded nanoparticle dispersions increased as mesopore interconnectivity increased (KIT-6 versus SBA-15), highlighting an apparent upturn in metal precursor solution permeability through interconnected mesopores; thus greatly aiding the generation of catalytically active species. Pt activity displayed a direct correlation with metal dispersion for the selective oxidation of cinnamyl alcohol. Pt/KIT-6 exhibited superior activity to Pt/SBA-15; however both mesoporous materials outperformed Pt impregnated on the low surface area, commercial support – thus reinforcing the beneficial effect of mesoporosity. In recent years, the role of Pt<sup>(0)</sup> versus Pt<sup>(IV)</sup> in Pt-catalysed alcohol selox has been fiercely contested.<sup>6, 7</sup> In order to clarify this ambiguity, TOF calculations normalised to initial rates based on the concentration of either (i) surface PtO<sub>2</sub> or (ii) total surface Pt metal from complete surface reduction was conducted, evidencing a non-fluctuating TOF for surface PtO<sub>2</sub>. As the active species is independent to nanoparticle size and structure, any differences in catalyst activity, *with metal loading*, can be attributed to changes in total active site density (**Figure 5.1** replicated from **Chapter 3 Figure 3.22**). Reaction atmosphere was deemed a crucial factor in active site stability; selective oxidation conducted in pure O<sub>2</sub> expressed greater substrate conversion and

activity values than in air and lowered catalyst deactivation levels at comparable time periods. XPS of spent catalyst samples confirmed a greater preservation of the PtO<sub>2</sub> active site for experiments conducted in O<sub>2</sub>. Catalyst deactivation can therefore be attributed to loss of active site density, through *in-situ* reduction and irreversible substrate adsorption. Catalyst pre-reduction, prior to reaction, was shown to dramatically decrease previous observed activity values (up to 50%), with decarbonylation becoming the dominant reaction pathway.

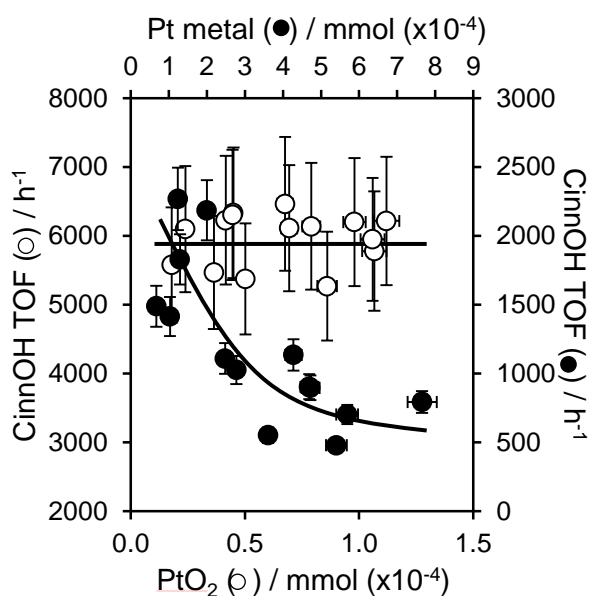


**Figure 5.1– Cinnamyl alcohol aerobic selox turnover frequencies expressed as a function of surface Pt metal or PtO<sub>2</sub> content for Pt/aSiO<sub>2</sub>, Pt/SBA-15 and Pt-KIT-6 catalysts**

The importance of support surface area and hierarchical architecture cannot be understated for the Pt-catalysed selective oxidation of cinnamyl alcohol. Genesis of PtO<sub>2</sub> centres with high dispersion and density is mandatory for the promotion of selective oxidation performance and catalyst utility.

Due to the presence of kinetically labile hydrogenation by-products (present under oxidation conditions), elucidation of the catalytic behaviour of this material under hydrogenation conditions was probed. Platinum is a well-known hydrogenation catalyst and so greater understanding of the catalytic performance of these materials, in the presence of hydrogen, can provide an avenue to greater understanding and optimisation of catalytic performance in both schemes of work.



### 5.1.2 Cinnamaldehyde selective hydrogenation

In addition to the three silica variants examined for the Pt-catalysed oxidation of cinnamyl alcohol, SBA-16 and TLCT-MM-SBA-15 silica supports were also studied for the liquid phase hydrogenation of cinnamaldehyde. It was deemed necessary to compare the influence of pore architecture for silica variants with three-dimensional mesoporosity (KIT-6 and SBA-16) on Pt nanoparticle physicochemical characteristics and hydrogenation kinetics. It was proposed that the addition of ordered macroporosity to SBA-15, would aid in Pt precursor solution and substrate-product diffusion; thus forming more highly dispersed Pt nanoparticles, whilst enhancing substrate-product throughput. Liquid phase, cinnamaldehyde hydrogenation activity was found to be *structure-insensitive* with respect to metallic platinum, yielding a constant TOF  $\sim 350 \text{ h}^{-1}$ . Desired cinnamyl alcohol selectivity was shown to be structure-sensitive; requiring large, extended Pt (111) facets for appreciable unsaturated alcohol formation. The influence of  $p\text{H}_2$  for this reaction scheme was remarkable. Although it does not come as any surprise that catalyst activity and conversion increased as  $\text{H}_2$  pressure increased (from 1 to 10 bar). A significant switch over in adopted C=C to C=O hydrogenation as the dominant pathway was evidenced over all supports, with the effect expressed with greatest intensity at high Pt loading (**Figure 5.2** replicated from **Chapter 4 Figure 4.21**). It is believed that elevated pressures, leads to greater steric crowding on the support surface, thus altering the cinnamaldehyde binding mode to an atop C=O configuration – minimising steric constraints.<sup>8,9</sup>

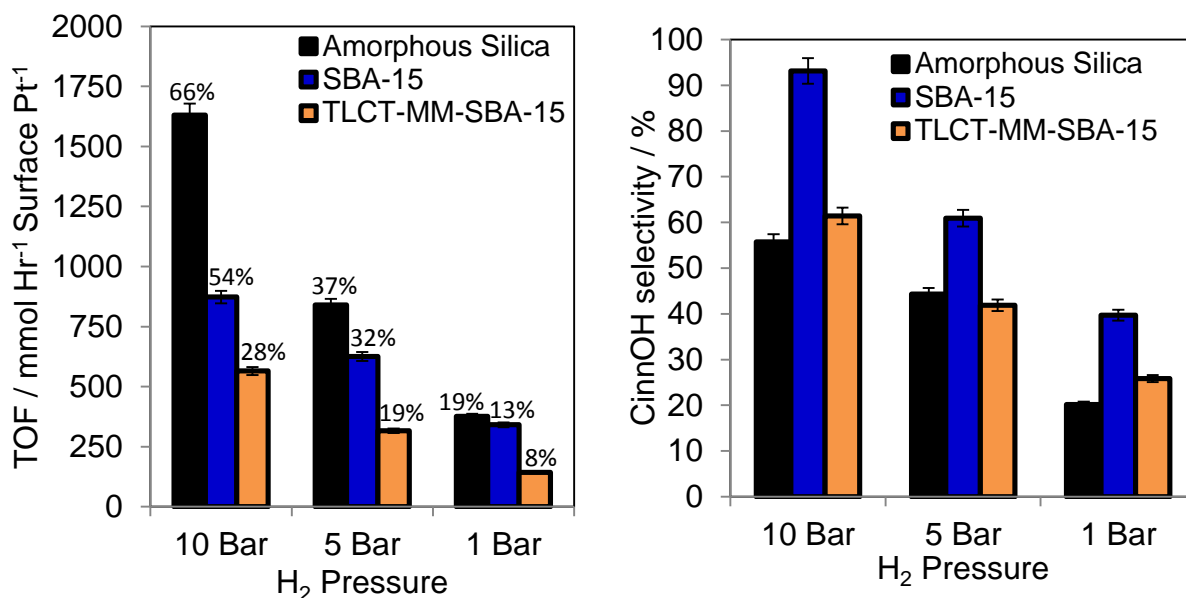


**Figure 5.2– H<sub>2</sub> pressure dependence of CinnALD hydrogenation over amorphous silica, SBA-15 and TLCT-MM-SBA-15 at approx. 2 wt. % Pt. Percentage values inset represent 7hr conversions**

The interplay between support polarity and Pt geometric size over high surface area silica supports proved to be an interesting battleground. As shown in **Chapter 3**, the incorporation of mesoporosity into support internal structure led to higher support surface areas; thus more highly dispersed Pt nanoparticles and smaller Pt crystallites. However, unsaturated alcohol formation is shown to be a function of Pt particle size and so the higher evidenced cinnamyl alcohol selectivities expressed for all hierarchical silicas does not fit into this model. Fortunately, a combination of *in-situ* ATR-IR and DRIFT studies uncovered a difference in support polarity between hierarchical and amorphous, low surface area commercial silicas, in which the former silicas contained a higher population of vicinal/geminal silanol species conferring dramatically increased surface polarity (**Figure 5.3** replicated from **Chapter 4 Figure 4.27**). Increased surface polarity gave rise to a preferential shift in CinnALD adsorption mode from  $\eta_4$  di- $\sigma_{CC}$  and  $\eta_4$  di- $\sigma_{CO} + \pi_{C=C}$  to  $\eta_2$  di- $\sigma_{CO}$ , repelling the cinnamaldehyde aromatic functionality from the support surface and favouring C=O versus C=C hydrogenation. Pt particle size and support polarity effects could also be applied to the liquid phase hydrogenation of benzaldehyde derivatives. In this case, the activation of the C=O functionality by ring-alkyl substituents played an additional role in desired alcohol product formation.

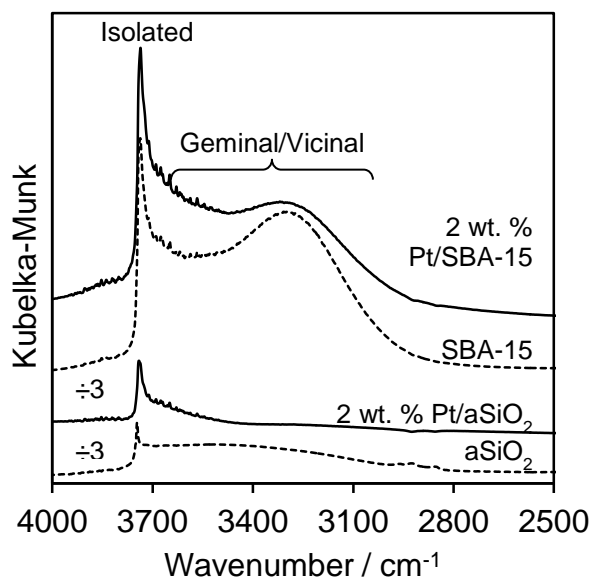


**Figure 5.3– In vacuo DRIFT spectra of 2 wt. % silica supported platinum catalysts**

Tuning support polarity, in conjunction with Pt nanoparticle size, has led to a new method of substrate adsorption control - permitting total dictation of functional group transformation. For the selective, liquid phase hydrogenation of cinnamaldehyde, Pt impregnated on polar supports with large, extended Pt (111) facets at elevated  $p_{H_2}$  ( $\geq 10$  bar) are required for the preferential formation of cinnamyl alcohol.

### 5.1.3 Future work

In **Chapter 3**, we identified the role of *in-situ* reduction on  $PtO_2$  active site degeneration and the subsequent negative effect portrayed on final conversion and product selectivity values. In theory, removal of reactively generated H adatoms from  $CinnOH \rightarrow CinnALD$  conversion could lead to a greater preservation of the active site and superior catalyst lifetime. Furthermore, removal of said species may increase the catalyst selectivity to cinnamaldehyde, by minimising the observed C=C side hydrogenation reactions observed. Two possible avenues to explore are: (I) Conducting Pt-catalysed cinnamyl alcohol selective oxidations under flow conditions could permit tuning of substrate residence time; such that the conversion of alcohol to aldehyde step is permitted but subsequent side reactions do not have time to occur. Drawbacks with this approach include the cost of initial outlay for flow reactor apparatus and as alcohol to aldehyde conversion is the rate determining step (RDS) for this reaction, there is no way to predict if it is possible to deactivate the labile hydrogenation/hydrogenolysis pathways at any residence time once the RDS has occurred.

(II) The introduction of additives as sacrificial protecting agents or hydrogen scavengers to protect PtO<sub>2</sub> active site integrity.

In the liquid phase, hydrogenation of cinnamaldehyde (*and benzylic substrates*), it was identified that the presence of extended, flat Pt (111) facets and highly polar support surfaces were beneficial for overcoming the thermodynamic drive compelling C=C hydrogenation, switching to the less favoured C=O pathway. Suggestions for additional work include *in-situ* or post-synthetic modification of existing silica supports to enhance surface vicinal/geminal hydroxyl density or overall polarity. In work similar to Tsang and co-workers,<sup>10</sup> selective capping of Pt nanoparticle edge and corner sites could lead to an increase in C=O hydrogenation, through inhibition of adsorption modes requiring the C=C centre bound directly to these coordinatively unsaturated facets. Finally, the generation and subsequent impregnation of pre-formed Pt nanoparticles with strictly controlled facets and size (cube, cuboctahedral, tetrahedral etc.) onto supports of known behaviour could permit further elucidation of size and facet-controlled reactivity in commercially relevant hydrogenation procedures.

## 5.2 References

1. J. Cocchiara, C. S. Letizia, J. Lalko, A. Lapczynski and A. M. Api, *Food Chem Toxicol*, 2005, 43, 867-923.
2. S.-S. Cheng, J.-Y. Liu, K.-H. Tsai, W.-J. Chen and S.-T. Chang, *Journal of Agricultural and Food Chemistry*, 2004, 52, 4395-4400.
3. D. Zhao, J. Feng, Q. Huo, N. Melosh, G. H. Fredrickson, B. F. Chmelka and G. D. Stucky, *Science*, 1998, 279, 548-552.
4. T.-W. Kim, F. Kleitz, B. Paul and R. Ryoo, *Journal of the American Chemical Society*, 2005, 127, 7601-7610.
5. J. Dhainaut, J.-P. Dacquin, A. F. Lee and K. Wilson, *Green Chemistry*, 2010, 12, 296-303.
6. T. Mallat and A. Baiker, *Chemical Reviews*, 2004, 104, 3037-3058.
7. L. Durndell, C. M. Parlett, N. S. Hondow, K. Wilson and A. F. Lee, *Nanoscale*, 2013.
8. T. Vergunst and J. Moulijn, *Catalysis Today*, 2001, 66.
9. P. Sautet and F. Delbecq, *Journal of Catalysis*, 1995, 152.
10. S. C. Tsang, N. Cailuo, W. Oduro, A. T. S. Kong, L. Clifton, K. M. K. Yu, B. Thiebaut, J. Cookson and P. Bishop, *ACS Nano*, 2008, 2, 2547-2553.

## *Chapter 6*

## *Appendix*

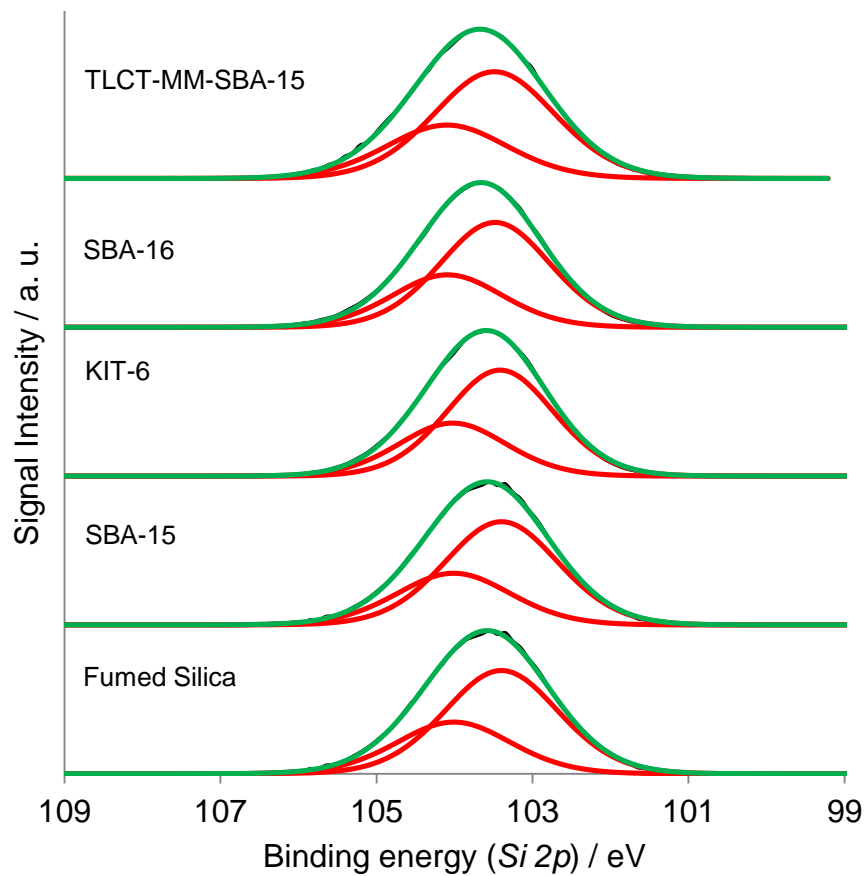


**Figure 6.1- Stacked Si 2p XPS plot of all parent silica supports**

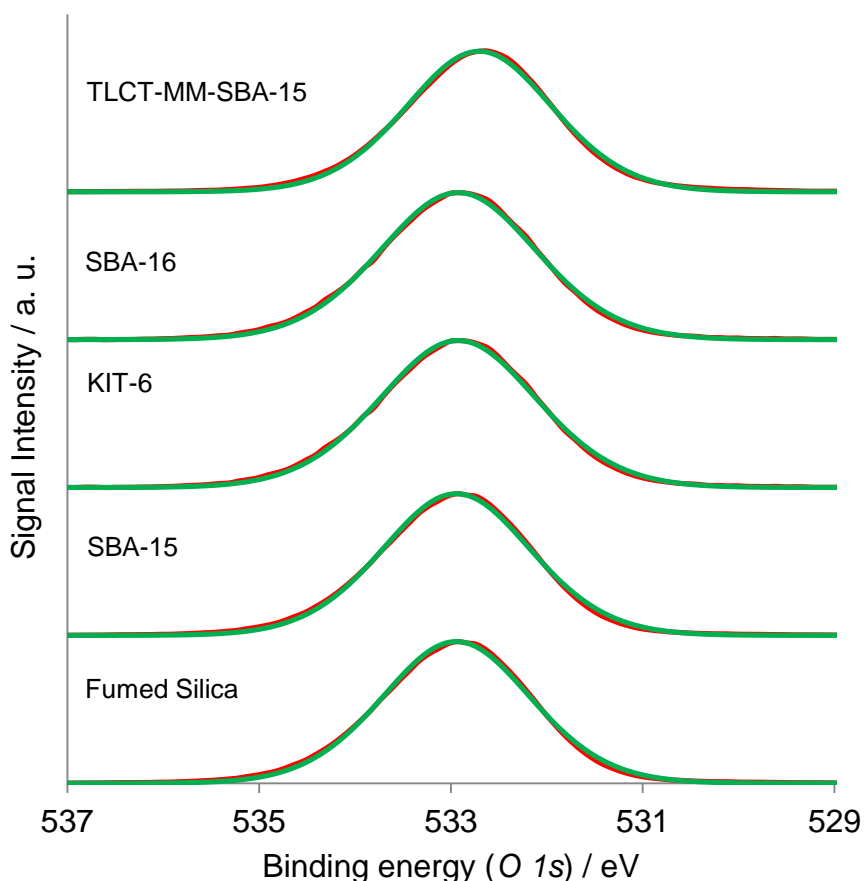


**Figure 6.2- Stacked O 1s XPS plot of all parent silica supports**

**Figures 6.1** and **6.2** show stacked plots of the Si 2p and O 1s regions for the parent silica supports studied in this thesis. Although the physical properties for each support may differ (i.e. BET surface area, microporosity, unit cell structure or extent of porosity etc.), as all materials show negligible change in electronic environment we can exclude differences in support electronic configuration from arguments where altered reaction behaviour in oxidation and hydrogenation protocols is exhibited.